LBL-36683
UC-404

Lawrence Berkeley Laboratory
UNIVERSITY OF CALIFORNIA

Engineering Division

Low Temperature Carrier Transport Properties in Isotopically Controlled Germanium

K. Itoh
(Ph.D. Thesis)

December 1994

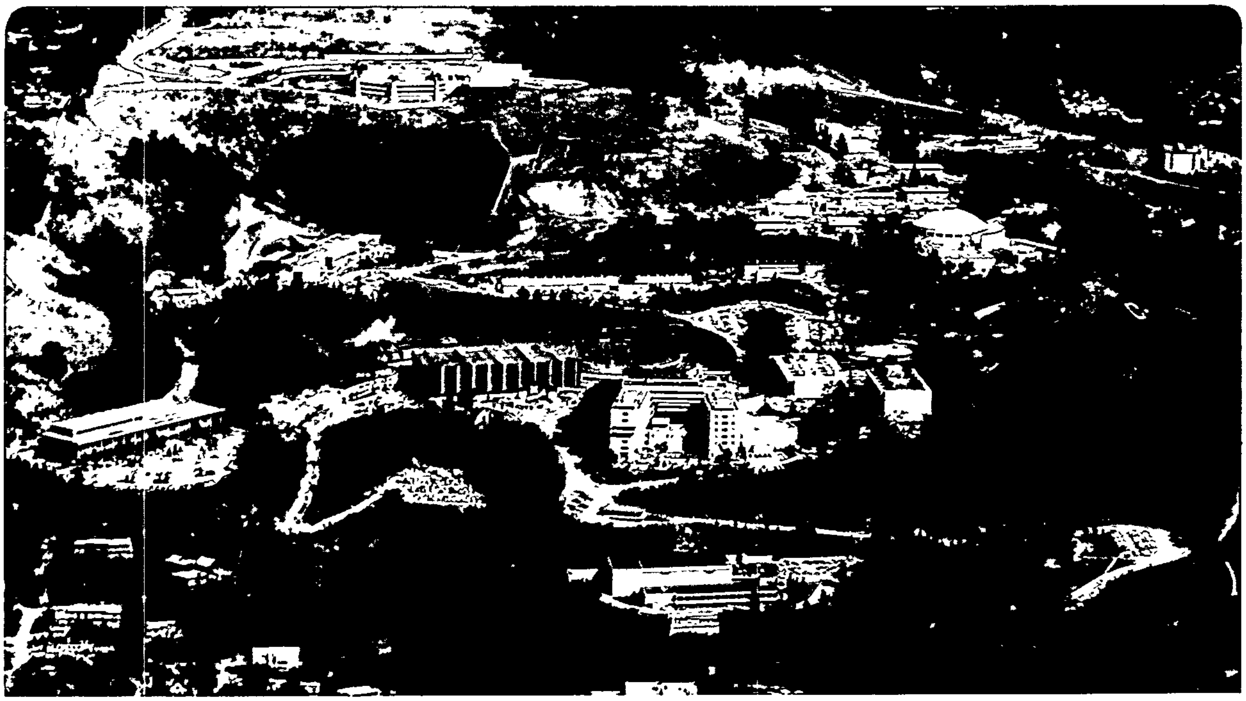

Prepared for the U.S. Department of Energy under Contract Number DE-AC03-76SF00098

DISCLAIMER

This document was prepared as an account of work sponsored by the United States Government. While this document is believed to contain correct information, neither the United States Government nor any agency thereof, nor The Regents of the University of California, nor any of their employees, makes any warranty, express or implied, or assumes any legal responsibility for the accuracy, completeness, or usefulness of any information, apparatus, product, or process disclosed, or represents that its use would not infringe privately owned rights. Reference herein to any specific commercial product, process, or service by its trade name, trademark, manufacturer, or otherwise, does not necessarily constitute or imply its endorsement, recommendation, or favoring by the United States Government or any agency thereof, or The Regents of the University of California. The views and opinions of authors expressed herein do not necessarily state or reflect those of the United States Government or any agency thereof, or The Regents of the University of California.

This report has been reproduced directly from the best available copy.

Lawrence Berkeley Laboratory is an equal opportunity employer.

LBL-36683
UC-404

Low Temperature Carrier Transport Properties in Isotopically Controlled Germanium

Kohei Itoh
Ph.D. Thesis

Materials Science and Mineral Engineering Department
University of California, Berkeley

and

Engineering Division
Lawrence Berkeley Laboratory
University of California
Berkeley, CA 94720

December 1994

This work was supported by the U.S. National Science Foundation Center for Particle Astrophysics, Grant No. ADT-8809616 through the U.S. Department of Energy under Contract No. DE-AC03-76SF00098.

Abstract

Low Temperature Carrier Transport Properties in Isotopically Controlled Germanium

by

Kohei Itoh

Doctor of Philosophy in Engineering -

Materials Science and Mineral Engineering

University of California at Berkeley

Professor Eugene E. Haller, Chair

Investigations of electronic and optical properties of semiconductors often require specimens with extremely homogeneous dopant distributions and precisely controlled net-carrier concentrations and compensation ratios. The previous difficulties in fabricating such samples are overcome as reported in this thesis by growing high-purity Ge single crystals of controlled ^{74}Ge and ^{70}Ge isotopic compositions, and doping these crystals by the neutron transmutation doping (NTD) technique. The resulting net-impurity concentrations and the compensation ratios are precisely determined by the thermal neutron fluence and the [^{74}Ge]/[^{70}Ge] ratios of the starting Ge materials, respectively. This method also guarantees unprecedented doping uniformity.

Using such samples we have conducted four types of electron (hole) transport studies probing the nature of (1) free carrier scattering by neutral impurities, (2) free carrier scattering by ionized impurities, (3) low temperature hopping conduction, and (4) free carrier transport in samples close to the metal-insulator transition. We have also performed infrared absorption spectroscopy studies of compensated Ge samples, investigating the line broadening mechanism due to random electric fields arising from ionized impurity centers.

In the study of neutral impurity scattering, we find excellent agreement between the low temperature experimental mobility and phase shift calculations for the hydrogen atom scaled to shallow impurities in semiconductors.

In the ionized impurity scattering study, none of the theories we have tested so far explains our low temperature experimental mobilities in highly compensated Ge (K>0.3). We discuss possible problems associated with the theories, in particular, the treatment of the screening mechanism.

In the study of low temperature hopping conduction, we show results of temperature dependent resistivity measurements as a function of both the net-carrier concentration and the compensation ratio. These results are compared with the theoretical prediction of variable range hopping conduction.

A transport study of samples close to the metal-insulator transition allows us to probe the nature of this important phenomenon. Our NTD isotopically engineered samples with extreme dopant uniformity are ideal systems to re-examine some of the previously published results. Our results suggest that one of the most controversial findings reported recently is most likely an artifact arising from inhomogeneous dopant distribution.

Lastly, we discuss low-temperature infrared absorption spectroscopy studies of p-type Ge:Ga,As samples as a function of the compensation ratio. The observed Ga impurity absorption peaks broaden linearly with the ionized impurity concentration due to the quadrupole interactions between Ga bound holes and the electric field gradients. Experimental linewidths are quantitatively compared to existing theories of electric field broadening. We find excellent agreement with the theory which is based on the correlated distribution of ionized impurity centers.

Acknowledgment

The five and a half years of my graduate studies could not have been carried out to my satisfaction without the help and support of many people. I would above all like to express my heartfelt thanks to my advisor Eugene Haller. His contribution both to my research and to my development as a scientist has been truly invaluable. His encouragement and advice at every step of my research, from the growth of crystals to the careful reading of every publication I wrote, have been deeply appreciated. I must also thank Bernard Sadoulet for his support and continuous interest in this work. His careful review of this thesis has significantly improved the contents. The theoretical analysis of the transport studies presented in Sec.4 has been conducted under a guidance of Wladek Walukiewicz. The countless discussions I had with him have been one of the most enjoyable aspects of my studies. The careful reading of this thesis by Eicke Weber is also greatly appreciated.

None of the isotope engineering work described in this thesis would have been possible without the generosity of Valeri Ozhogin of Kurchatov Institute of Atomic Energy in Moscow who made isotopically enriched Ge available. His pure curiosity towards science was the key to the establishment of the collaboration between U.S. and Russian National Laboratories. John Farmer of the Research Reactor Facility at University of Missouri has been the neutron transmutation doping expert in this work. More than fifty thermal neutron irradiations have been conducted by him.

I have benefited from working with a number of knowledgeable and kind staff members in our research group. Bill Hansen came up with the idea of the simple crystal growth system described in this thesis. Many of my semiconductor processing skills have been developed through his lessons, which always started from "you don't even know how to do this?!" Jeff Beeman has contributed to the design, construction, and repair of experimental equipment, and Dick Davis has been an invaluable source of practical help for me.

It has been very fortunate for me to be able to meet many excellent researchers around the world through the research described in this thesis. Many interactions especially with Gordon Davies at Kings College, London, Manuel Cardona and his co-workers at Max-Planck Institute, Stuttgart, Jim Wolfe and his students at University of Illinois, Champaign, and Anant Ramdas and his students at Purdue University, Indiana, have been very enjoyable.

I have been most impressed by the enthusiasm and quality of students I met throughout my graduate studies at Berkeley. All students in our research group have contributed to this work in one way or another. I'd like to especially thank James Heyman, Jeff Wolk, and Bill Knowlton for their significant contributions to my graduate career. Tom Shutt, Alan Cummings and Walter Stockwell at Physics Department, UC Berkeley kindly helped me with low temperature measurements involving their dilution refrigerator.

Having come from abroad, I have experienced much hardships during my first two years at Berkeley. My struggle was overcome through the support of my best friends, Oscar Dubon, Amy Moll, John Birmingham, and John O'Brien. They really made my life at Berkeley different.

Finally, it is most important to acknowledge the members of my family. The long path of my personal development began with my parents Koichi and Naoko Itoh. Their non-imposing style of education and continuous interest in their son have been the most precious gifts to me. I must thank for the finical support I received from my grandfather Eikichi Itoh and my father. Since 1991, my wife Yuko has been the main source of my happiness. Now with our happy son Ryohei, it is hard to imagine a life better than we currently enjoy at Berkeley.

I would like to thank for the financial support provided by the US NSF Center for Particle Astrophysics ADT-8809616. This work was also supported in part by the

Lawrence Berkeley Laboratory Director's Research and Development program, and in part by US NASA contract W17605 through interagency agreement with the US DOE contract DE-AC03-76SF00098.

Table of Contents

Appendixes

Chapter 1 Introduction

1.1 Isotopes

An atom consists of a highly localized nucleus (radius~10^{-12}cm) and delocalized orbital electrons (radius>10^{-9}cm).* This model of an atom was first proposed by Rutherford in 1911.[1] Around the same time Thomson [2] studied the deflection of a beam of charged neon ions by magnetic and electric fields. Measurements of the extent of the deflection permitted the calculation of q/m, the ratio of the charge of the ions to their mass. As a result, Thomson showed that the inert gas neon contained atoms of two different mass numbers 20 and 22. This was one of the first experiments to show the existence of isotopes. Although Thomson's paper was first to appear in the formal literature, historians seem to agree that the discovery of isotopes occurred during work on radioactive elements.[3] Studies of the various radioactive substances present in uranium and thorium minerals showed that there were several radioactive species which were chemically indistinguishable from each other, but which differed in their radioactive decay properties.[4-9] In 1907 McCoy and Ross [4] showed the first experimental evidence of these chemically inseparable substances. Between 1913 and 1914, Soddy [5], Richards and Lembert [7], Hönigschmid and Horovitz [8], and Curie [9] independently performed experiments to show that those atoms were chemically identical but differed in atomic weight. This lead Soddy [5] to suggest the name "isotopes", meaning "the same place" in the periodic table. The invention of mass spectroscopy in 1919 by Aston [10, 11] led to the discovery of a large spectrum of isotopes in the periodic table. It was found that the mass numbers of all isotopes were nearly integers when the mass of oxygen was taken as 16. These experimental findings triggered the extensive research efforts to clarify the physical origin of the mass differences between various isotopes. One possibility, which had been suggested by Rutherford in 1920 [12], was that an electron and a proton might be in such close proximity as to form a hypothetical neutral particle "neutron". Rutherford's

---

* For example the Bohr radius of hydrogen is 5.3Å.

suggestion was confirmed experimentally by Chadwick in 1932.[13, 14] He observed the emission of electrically neutral particles due to the decay of polonium during the bombardment of beryllium with α particles. Immediately after the discovery of the neutron, the new particle was incorporated into theories of the structure of nuclei[15], for it was clear that nuclei of any mass and charge could in principle be constructed from a suitable number of neutrons and protons. The number of protons is equal to the positive electrical charge units of the nucleus and hence to the atomic number Z. The mass of the atom is given by the mass number A=Z+N (N: number of neutrons) of the nucleus, since the mass of an electron is 1/1836 of the mass of a proton or a neutron and is negligible. It is now a common practice in physics to use the symbol ${}^{A}_{Z}X$ for the description of an isotope, e.g., ${}^{1}_{1}H$, ${}^{2}_{1}H$ for hydrogen and deuterium, respectively, etc.

Now we shall look at the stable isotopes of the elements. We use the term "stable" isotopes as opposed to "unstable" or "radioactive" isotopes. The mass spectra of the elements have been investigated in detail and the isotopic composition of the elements has been tabulated in a reference book entitled "Table of Isotopes"[16] According to the Table of Isotopes, there are 284 stable isotopes* divided among 83 elements when Z up to 92 is considered. No stable isotopes for Z=43, 61, 84-89, and 91 exist. Twenty elements, about one quarter of all, are mono-isotopic. The relative abundance of an isotope is very close to constant in nature, i.e., independent of the source of the sample that is measured. An examination of the values of Z and A shows that in the stable nuclei, with the exception of ${}^{1}H$ and ${}^{3}He$, the number of neutrons is always greater than or equal to the number of protons. This means there is always at least one neutron for each proton. This property of the stable isotopes is shown in Fig.1.1, in which the number of neutron N=A-Z is plotted against Z. It can be also seen in Fig.1.1 that elements with large Z tend to have lager

---

* Stable isotopes defined here include eight naturally occuring feebly radioactive elements with extremely long half lives (${}^{40}K$, ${}^{87}Rb$, ${}^{115}In$, ${}^{147}Sm$, ${}^{176}Lu$, ${}^{187}Re$, ${}^{150}Nb$, and ${}^{138}La$) and four nuclear reaction products (${}^{232}Th$, ${}^{234}U$, ${}^{235}U$, and ${}^{238}U$) which are radioactive but they occur in sufficient amounts and with very weak activity that they can be handled in the same way as the stable isotopes.

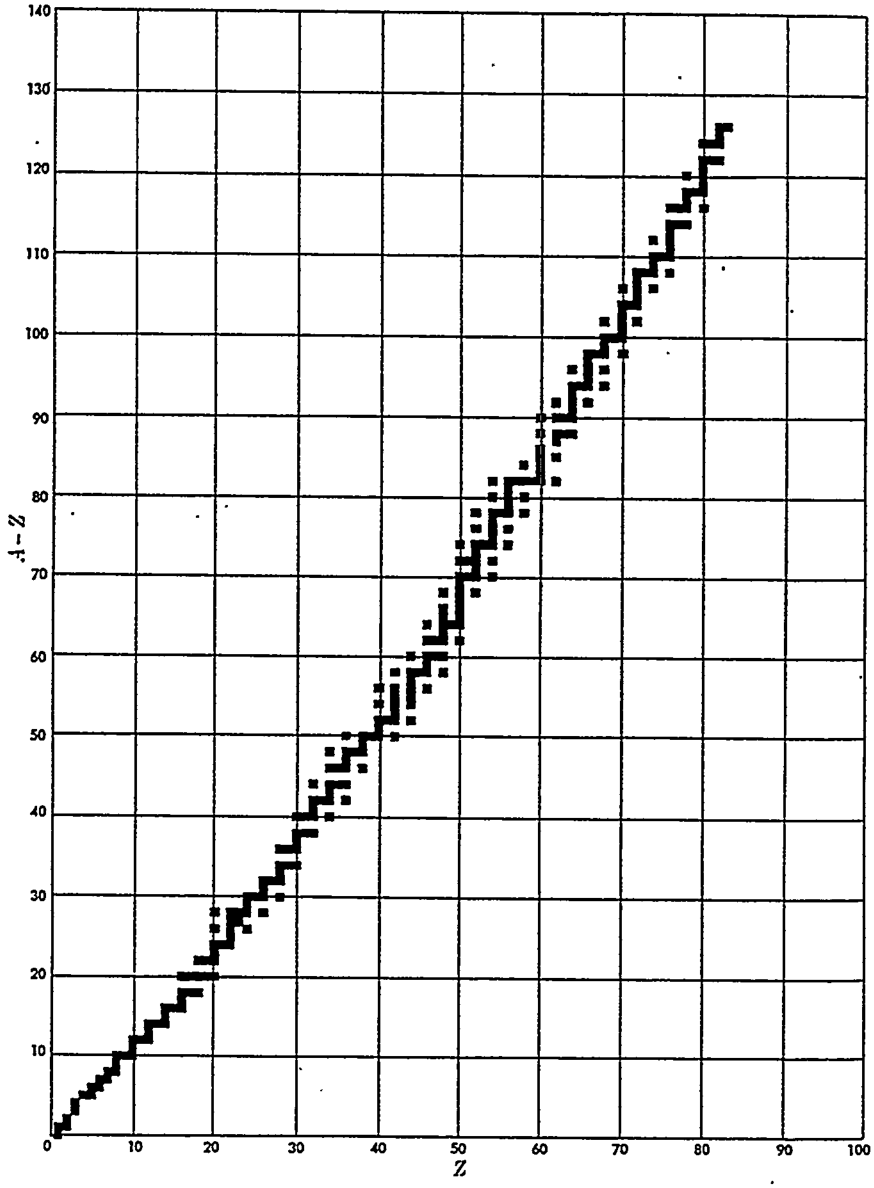

Fig.1.1 Chart of the stable nuclides

number of stable isotopes, though there are some exceptions like mono-isotopic Au with Z=79. There are several other striking "rules" in the table of stable isotopes. The numbers of nuclides with the various combinations of even and odd atomic and mass numbers are listed in Table 1.1. Nuclides of even Z are much more numerous than those of odd Z. Nearly all nuclides of even A are much more numerous than those of odd A. Most elements with less than three stable isotopes have odd Z. Of the 20 mono-isotopic elements, 19 elements have odd Z, with beryllium being the only exception. 19 of 21 elements with two stable isotopes have odd Z as well as odd A (helium and carbon are two exceptions). On the other hand elements with even Z tend to have more than two stable isotopes. The regularities that have been described are closely connected to nuclear stability and must eventually be understood by nuclear theory, in particular, in terms of the strong forces between nucleons.[17, 18]

Table 1.1 Isotope statistics

	Number of elements	Odd A	Even A	Total	Average number of isotopes per element
Odd Z	40	53	8	61	1.5
Even Z	43	57	166	223	5.2
Total	83	110	174	284	3.4

We shall now discuss how the existence of isotopes has been contributing to the progress of physics of solids*. Fajans [19] was one of the first scientists who proposed the possibility of an "isotope shift" in physical properties of solids which depend on the frequencies of atomic and molecular vibrations. In 1932 the first discovery of deuterium (^{2}H) was made from the vibrational frequency shift in the atomic spectroscopy.[20] Later the isotope shift of molecular vibrational frequencies became the key for the spectroscopic

---

* We shall limit our discussion to the vibrational related properties of stable isotopes.

determination of various molecular structures.[21, 22] All forms of matters used by scientists and engineers before invention of the isotope separation process in 1938 [23] consisted of stable isotopes in fixed concentration ratios. The first isotope separation process due to Clusius and Dickel [23] involved a series of simple thermal diffusion columns in which isotopes were separated via different diffusion length. The first isotopes separated by them were ^{35}Cl and ^{37}Cl. More recently, other isotope separation methods such as the electromagnetic "mass spectroscopy" [24] and the gaseous centrifuge systems [25] have been developed. The availability of enriched isotopes immediately had an tremendous impact on science. The experimental observation of the isotope shift of the critical temperature T_c in isotopically enriched superconductor Hg by Maxwell [26] and Reynolds et al. [27] showed the importance of the electron-phonon interactions in superconductivity. This observation led the way towards the definitive theory of the superconductivity known as the Bardeen-Cooper-Schrieffer or "BCS theory".[28] Today, isotope substitution is widely used in an effort to clarify the superconducting mechanism in high T_c oxide materials. The first report on an isotopically enriched semiconductor crystal was published by Geballe and Hull in 1958.[29] They grew an isotopically enriched ^{74}Ge crystal and compared its thermal conductivity to that of natural Ge. More recently the local structure of light impurities in semiconductors have been determined from the shift in the impurity local vibrational mode frequencies when masses (i.e., isotopes) of the impurity or the host crystal are changed.[30-32]

The above mentioned references contain only a small portion of the extensive efforts spent on isotope related research over the past 80 years. Unstable or radioactive isotopes which we have so far neglected may have been used in a wider range of applications than stable isotopes. The radioactive isotope tracer method has substantially contributed to many fields of science including physics, chemistry, biology, medicine, etc. Nuclear medical treatments involve a variety of radio-isotopes. It is clear that today's state of science could not have been achieved without the significant role isotopes have played.

1.2 Isotope Effects in Semiconductors

There has been a dramatic surge in interest in the effects of the isotopic composition on the physical properties of semiconductors over the past five years. Following the end of the US-Soviet cold war, former Soviet Union's massive isotope separation facilities that had been developed in previous years for the isotope separation of uranium and plutonium for the atomic weapon development were turned into isotope separators for scientific research. As a result, it became possible for western researchers to obtain a variety of enriched isotopes and to establish scientific collaborations with scientists of the former Soviet Union. In western countries separated isotopes of many elements have been available from the Oakridge National Laboratory and other suppliers for a few decades. However, due to the extremely high price of separated semiconductor isotopes (upto tens of US$ per milligram!), the ^{74}Ge enriched crystal of Geballe and Hull mentioned in the previous section had remained to be the only isotopically enriched elemental semiconductor in western countries until the end of the cold war.

All elemental and most compound semiconductors and their alloys contain elements which consist of more than one stable isotope. The most commonly used semiconductor silicon is composed of the three isotopes $^{28}_{14}$Si, $^{29}_{14}$Si and $^{30}_{14}$Si with abundances of 92.23%, 4.67% and 3.10%, respectively. The important compound semiconductor GaAs consists of mono-isotopic $^{75}_{33}$As and the two Ga isotopes $^{69}_{31}$Ga and $^{71}_{31}$Ga with abundances of approximately 60% and 40%, respectively. The semiconductor of interest to this thesis Ge consists of five stable isotopes: $^{70}_{32}$Ge (20.5%), $^{72}_{32}$Ge (27.4%), $^{73}_{32}$Ge (7.8%), $^{74}_{32}$Ge (36.5%), and $^{76}_{32}$Ge (7.8%). Other stable isotopes important from a semiconductor material's point of view are listed in Table 3.1 The information contained in the first two columns, the isotopes and their natural abundances, illustrates the very large number of possible isotopic compositions which can be formed, at least in principle, when we consider binary compound or ternary and quaternary alloy semiconductors.

Most physical properties of semiconductor crystals depend to some degree on their isotopic composition.[33] There are at least four distinctive sources of isotope effects in semiconductors.

(1) The shift in the crystalline and impurity vibrational frequencies due to the change in the atomic mass. This causes the isotope shift of all frequency dependent properties such as the lattice constant, specific heat, electronic band gap, and local vibrational mode of light impurities.

(2) The effect due to the random distribution or "disorder" of isotopes. This so called "isotope disorder effect" changes the lifetime of phonons, and affects the phonon scattering rate, i.e., the thermal conductivity.

(3) The differences in nuclear reactions associated with different nuclei. This property can be utilized for doping of semiconductors with specific dopants via the neutron transmutation doping technique which will be explained in detail in Sec.1.3 and Sec.2.

(4) The nuclear spin may change as well between different isotopes. This affects the certain magnetic properties of solids.

In the following two sections (Sec.1.2.1 and Sec.1.2.2), I will review published research results probing all of the above mentioned isotope effects in bulk semiconductors. The utilization of new semiconductor structures, isotope superlattices, will be introduced at the end (Sec.1.2.3). Brief descriptions of semiconductor characterization techniques which will appear in the followings sections are given in Appendix A.

1.2.1 Phonons and Related Properties

In this section I shall describe the experimentally studied isotope effects on phonon dependent properties. With a few exceptions, most experiments we are going discuss were performed on isotopically controlled germanium (Ge) and diamond* (C). The following

---

* We shall treat diamond as a wide-gap semiconductor.

dependence of the phonon frequency ω on mass M is given by a simple "spring and ball" model:

$$\omega \propto M^{-1/2}. \tag{1.1}$$

Fig.1.2 shows the phonon dispersion relationship for single crystal Ge as a typical example of a three dimensional crystal with diamond structure. We see a total of four branches: longitudinal optical (LO), longitudinal acoustic (LA), transverse optical (TO), and transverse acoustic (TA) modes (with each of the TO and TA branches being doubly degenerate). Only the inelastic neutron scattering technique allows the investigation of the phonon dispersion relation spanning the whole Brillouin zone, i.e. $0 \leq k \leq \pi/a$ (a: lattice constant) in various crystallographic directions. However, for the $k=0$ and $k=\pi/a$ cases, Raman spectroscopy and photoluminescence (PL) techniques, respectively, allow highly accurate phonon frequency measurements. These two techniques have been widely applied to measure the isotope shift in phonon frequencies.

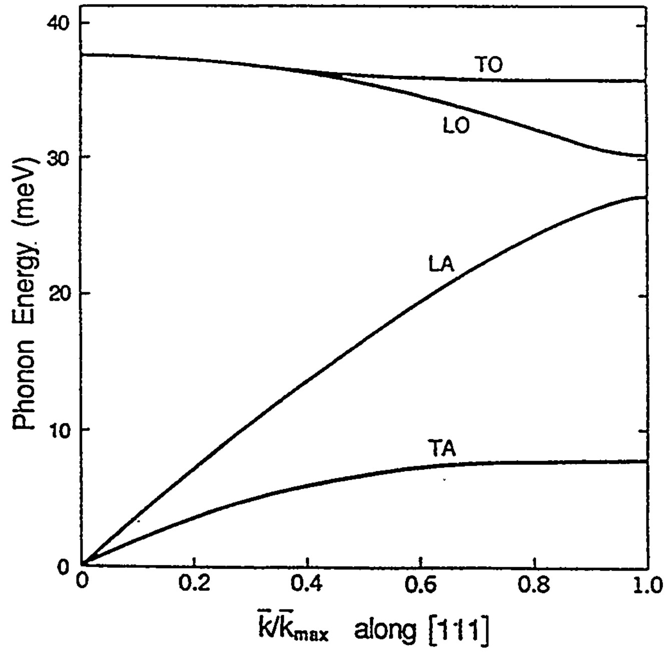

Fig.1.2 Phonon dispersion relations in the [111] direction in germanium at 80 K. The two TA phonon branches are horizontal at the zone boundary position, $\left(\vec{k} = \frac{\pi}{a}, \text{L-point}\right)$. The LO and TO branches are degenerate at the center of the Brillouin zone $\left(\vec{k} = 0, \Gamma\text{-point}\right)$; this also is a consequence of the crystal symmetry of Ge. The results were obtained by Nilsson and Nelin [34] using inelastic neutron scattering.

1.2.1.1 Isotope and Isotope Disorder Effects on Phonon Frequencies in Germanium

Extensive Raman spectroscopy studies on isotopically controlled Ge crystals were performed by the members of Cardona's group at the Max-Planck-Institute in Stuttgart, Germany.[35-38] Fig.1.3 shows the superimposed Raman spectra of Ge of natural isotopic composition (^{Nat}Ge) and isotopically enriched Ge samples recorded at T=90K.[36] The positions of the peaks obey the $M^{-1/2}$ law (Eq.1.1) with two almost negligible corrections: (i) ~0.5% shift due to the isotopic disorder contributes to an additional **k**-dependent phonon self-energy and (ii) <0.06% shift due to the anharmonicity of the lattice vibration. What is striking in Fig.1.3 is that the width of peaks in all spectra, including that of ^{Nat}Ge which contains five isotopes in complete disorder, is very similar (~1cm^{-1}). The spectrum of ^{Nat}Ge contains only one peak at the frequency corresponding to the average mass number of ^{Nat}Ge 72.59. It is interesting to ask ourselves why the ^{Nat}Ge Raman spectrum exhibits this one (M=72.59) sharp peak rather than one broader peak resulting from the superposition of the five peaks due to five Ge stable isotopes. The answer to this question is given by Fuchs et al. [36, 37] and Cardona et al. [39, 40] using Anderson's theory of localization.[41] If we express the relative mass fluctuations $\Delta M/\overline{M}$ in the form of a frequency bandwidth $\left(\Delta M/\overline{M}\right)\omega_0 = 12\ \text{cm}^{-1}$ with ω_0 being the angular optical phonon frequency at $\vec{k} = 0$ and compare it with the bandwidth of the optical phonons in the first Brillouin zone $\Delta\omega_0 \sim 100\ \text{cm}^{-1}$, we see that the mass fluctuation bandwidth is much smaller than the intrinsic optical phonon bandwidth. Under these circumstances phonons do not become localized but remain spread out over a large number of unit cells, leading to a close to perfect linear averaging of the various isotope masses. Another interesting point to notice is the linewidths of Raman peaks arising from different isotopic crystals. In simple terms the widths of peaks in all spectra are almost the same, but a careful inspection in fact reveals that the line-width of ^{70}Ge is slightly larger than that of ^{Nat}Ge. In order to understand this puzzling results, we have provided Cardona's group with a specially

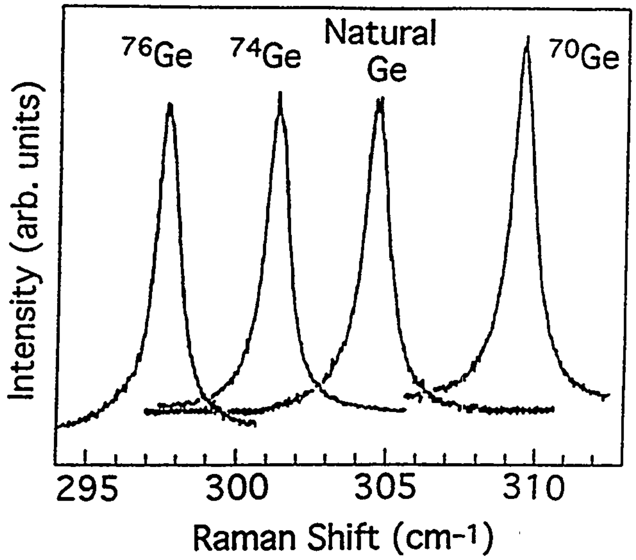

Fig.1.3 Raman spectra of the L-phonon of several Ge isotopes and natural Ge at 90K.[36]

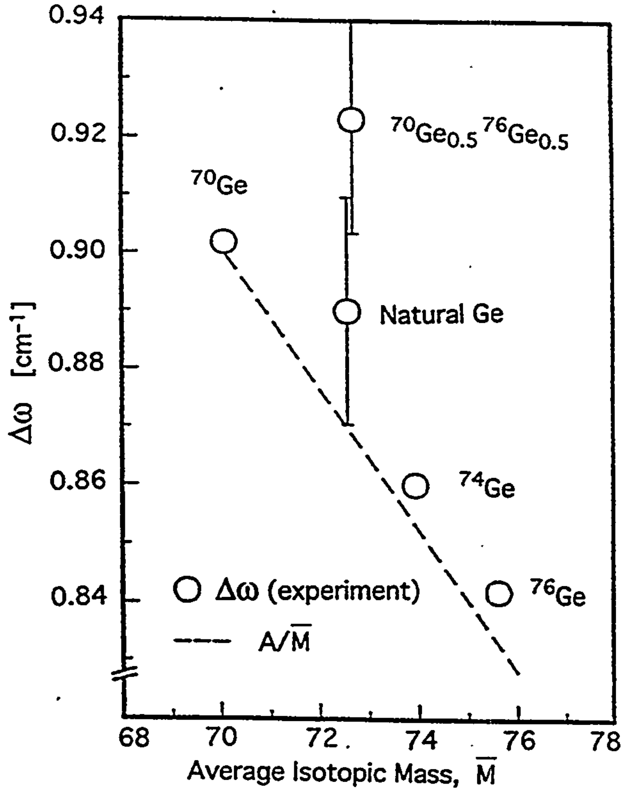

Fig.1.4 Full width at half maximum of the Raman lines shown in Fig.1.2 and of a $^{70}Ge_{0.5}/^{76}Ge_{0.5}$ sample.[36] The dashed line represents the M^{-1} dependence for isotopically pure samples.

grown Ge crystal consisting 50%-^{70}Ge and 50%-^{76}Ge. This results in the largest possible isotope disorder one can create using stable Ge isotopes. In Fig.1.4 we show the width as a function of average masses in all samples mentioned above. One finds that the widths $\Delta\omega_0$ of the Raman peaks in mono-isotopic crystals have a simple dependence $\propto M^{-1}$. Raman linewidths for the isotopically disordered ^{Nat}Ge and $^{70/76}$Ge alloy are slightly broader than the M^{-1} proportional widths of mono-isotopic crystals because of the isotopic disorder effect. The physical origin of this M^{-1} dependence is due to the phonon lifetime τ dominated by the anharmonic decay into two phonons. Time resolved measurements have yielded lifetimes of 6 ps, i.e., with a relation $\Delta\omega_0\,\tau \approx 1$, one finds $\Delta\omega_0 = 1\text{cm}^{-1}$ which is in good agreement with the observed widths.[36] This natural line-width (or lifetime) is caused by anharmonic interactions leading to the decay of an optical phonon at **k**=0 into two phonons. At the low temperature where these Raman experiments with natural and isotopically enriched Ge were conducted, the rate for anharmonic decay (τ^{-1}) is proportional to the square of amplitudes of the two phonons created in the process:

$$\tau^{-1} = \Delta\,\omega_0 \propto \langle u_1^2\rangle\langle u_2^2\rangle = \frac{\hbar^2}{4M^2\omega_1\omega_2}\,. \tag{1.2}$$

Using Eq.1.1 $\omega \propto M^{-1/2}$ we find

$$\Delta\,\omega_0 \propto M^{-1}\,. \tag{1.3}$$

Photoluminescence studies of several isotopically enriched Ge crystals were reported by Davies et al. [42, 43] and Etchegoin et al.[44, 45] PL involves the radiative recombination of an electron and a hole forming an exciton. A free exciton is an electron-hole pair that is free to move around within a crystal. The photon energy E_{FE} emitted in the decay of a free exciton for the case of an indirect semiconductor is given by,

$$E_{FE} = E_g - E_X - \hbar\,\omega \tag{1.4}$$

where Eg is the indirect energy gap, E_X the exciton binding energy, $\hbar\omega$ the energy of the Brillouin zone boundary phonons whose emission is necessary in order to conserve the momentum.

When excitons are bound to impurities or defects, they are called bound excitons. The energy E_{BE} for bound exciton luminescence is given by,

$$E_{BE} = E_g - E_X - E_B \ (-\hbar\omega) \tag{1.5}$$

where E_B is the binding energy of the exciton to the impurity or defect. Bound exciton recombination can occur without phonons because this process does not require conservation of **k** due break down of the crystal symmetry by the impurity or defect. Since E_X and E_B are not expected to exhibit an isotope shift, one can determine the isotope shift of E_g directly by comparing E_{BE} of a particular *no phonon assisted* ($\hbar\omega=0$) bound exciton recombination for the crystals of different isotopes. That is $\Delta E_{BE}=\Delta E_g$ since E_X and E_B are constant in Eq.1.5. As it will be explained in detail, the isotope shift of the band gaps was precisely determined by Davies et al. [43, 46] using the bound exciton PL analysis just explained. Once the isotopic dependence of E_g is determined, one can find the isotope shift of the zone boundary phonon $\hbar\omega$ from the shift of the free exciton energy E_{FE} and Eq.1.4. Isotope shifts of the zone boundary TA,LA, and TO phonon frequencies obtained in this manner obey the $\propto M^{-1/2}$ law (Eq.1.1) very well.[42]

Diamond

As shown in Table 3.1, there are two stable carbon isotopes ^{12}C and ^{13}C. It is interesting to point out that natural carbon is already a 98.89% ^{12}C enriched material. Banhozer and Anthony [47] at General Electric have developed a system which allows to grow large, gem quality diamonds of controlled isotopic compositions (anywhere between 99.96%-^{12}C and 99%-^{13}C). Using these diamonds, Hass et al. [48, 49] have performed a Raman spectroscopy study of the isotopic disorder effect on **k**=0 optical phonons. They analyzed the frequencies and line-widths of optical phonon peaks as a function of the ^{13}C concentrations, and found quantitative agreement with the theoretical curves calculated using the coherent potential approximation (CPA).[50] The M^{-1} dependence of the Raman peak widths (life time effect) was observed only for widths of nearly pure ^{12}C and ^{13}C. Widths of ^{12}C-^{13}C alloys are wider due to the isotope disorder effect.

PL studies of isotopically enriched ^{12}C and ^{13}C films were performed by Collins et al.[51, 52] After correcting for the isotope shift of the energy gap, they also have observed the $M^{-1/2}$ proportionality of the phonon frequencies at the Brillouin zone boundary.

1.2.1.2 Heat Capacity

The heat capacity of an insulator at constant volume C_V is generally given by the Debye formula [53],

$$C_v = \frac{3\,k_D^3}{2\,\pi^2} \int_0^{\Theta_D/T} \frac{x^4\, e^x\, dx}{(e^x - 1)^2} \quad \text{with } x = \frac{\hbar\, c\, k}{k_B\, T} \tag{1.6}$$

where k_D is the radius of a sphere in reciprocal space which contains precisely N allowed vectors (N: number of Bravais lattice sites in the crystal), Θ_D is the Debye temperature, and c is the phonon velocity, and k is the wave vector. Θ_D is defined as,

$$\hbar\, c\, k_D = \hbar\, \omega_D = k_B\, \Theta_D \tag{1.7}$$

where ω_D is the Debye frequency. In the low temperature region ($T<0.2\ \Theta_D$), Eq.1.6 becomes,

$$C_v = \frac{234\, k_D^3}{6\,\pi^2}\left(\frac{T}{\Theta_D}\right)^3 k_B. \tag{1.8}$$

Because the Debye temperature of Ge is ~370 K, Eq.1.8 is valid below ~77 K. The isotope shift of the heat capacity between ^{70}Ge and ^{74}Ge can be estimated by the shift of the Debye frequency, ω_D. Since $\omega_D \propto M^{-1/2}$ and $\Theta_D \propto M^{-1/2}$, one finds $C_V \propto M^{3/2}$ from Eq. 1.8. Therefore we expect the fractional difference of the heat capacities $C_V(^{70}\text{Ge})$ and $C_V(^{74}\text{Ge})$ to be,

$$\frac{C_v(^{74}\text{Ge})}{C_v(^{70}\text{Ge})} - 1 = \left(\frac{74}{70}\right)^{\frac{3}{2}} = 8.7\ \% \tag{1.9}$$

To our knowledge, there has been no data published on the isotope shift of heat capacity in Ge up to date. Heat capacity measurements on isotopically controlled semiconductors allow us to probe the isotope and isotope disorder effects on acoustic phonons with frequencies near k=0. This study may be important for the understanding of the thermal conductivity (which depends on the acoustic phonon properties) in isotopically controlled semiconductors.

1.2.1.3 Thermal Conductivity

The thermal conductivity of dielectrics is given by

$$\kappa = \frac{1}{3} C_v c L , \tag{1.10}$$

with C_v = specific heat, c = phonon velocity and L = phonon mean-free path. L is limited by phonon scattering from defects, impurities, isotope disorder, or sample boundaries. Because each scattering mechanism has a different temperature dependence, one can gain valuable information about these scattering processes from the temperature dependence of the thermal conductivity. Pomeranchuk suggested the importance of isotope scattering as early as 1942.[54]

Germanium

The thermal conductivity of isotopically enriched ^{74}Ge and ^{Nat}Ge was measured as a function of temperatures by Geballe and Hull.[29] Open circles in Fig.1.5 are the experimentally measured thermal conductivities by Geballe and Hull. At low temperatures (T<5K), κ shows the T^3 dependence in both ^{74}Ge and ^{Nat}Ge. This is known as the Casimir regime [55] in which phonon scattering occurs only at sample boundaries. The T^3 dependence comes from T^3 dependence of C_v at low temperatures. At higher temperatures, one has to include other scattering mechanisms in the calculation of κ. Theoretical calculations for Geballe and Hull's experiment were performed by Callaway [56] who included isotope scattering, normal three phonon processes, umklapp processes, and boundary scattering. The solid lines in Fig.1.5 are theoretical calculation due to Callaway. The agreement between the theory and experiment is reasonable.

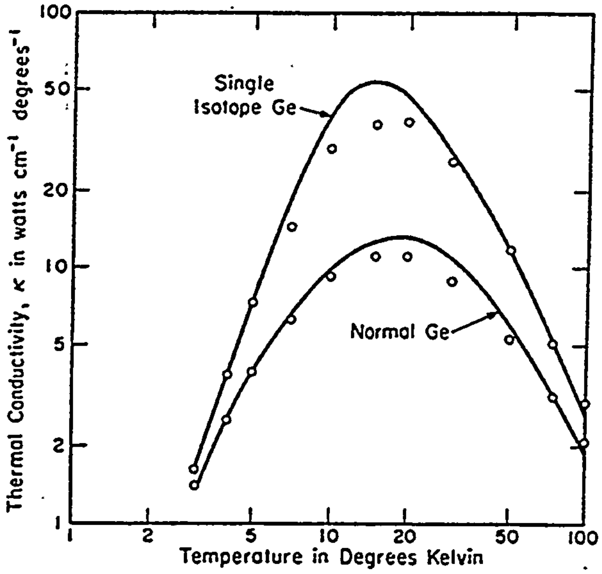

Fig.1.5 Thermal conductivity of Ge. The open circles represent experimental points taken by Geballe and Hull.[29] The solid lines are the theoretically curves represent Callaway's theory.[56]

Diamond

The highest degree of isotopic enrichment so far obtained in diamond is ^{12}C 99.96% which is much higher than that of Ge (^{74}Ge 96.8%). The thermal conductivity is predicted to be extremely sensitive to the isotopic enrichment when the degree of isotopic purity is so high (>99%). Callaway's theory [56] predicts an almost 150% increase in κ at room temperature when 1.1% ^{13}C atoms are removed from natural diamond.

Fig.1.6 shows the thermal conductivity in isotopically controlled diamonds measured by Anthony et al. [57], Olson et al. [58] and Wei et al.[59] The thermal conductivity κ=410Wcm^{-1}K^{-1} at T=104K for a 99.9% ^{12}C is the highest κ measured in any solids. Wei et al. fitted their data with Callaway's model [56] using four independent scattering processes mentioned in the previous section on Ge. The fits are represented by solid curves in Fig.1.6. According to the fit for the 99.9% ^{12}C diamond, κ is predicted to rise

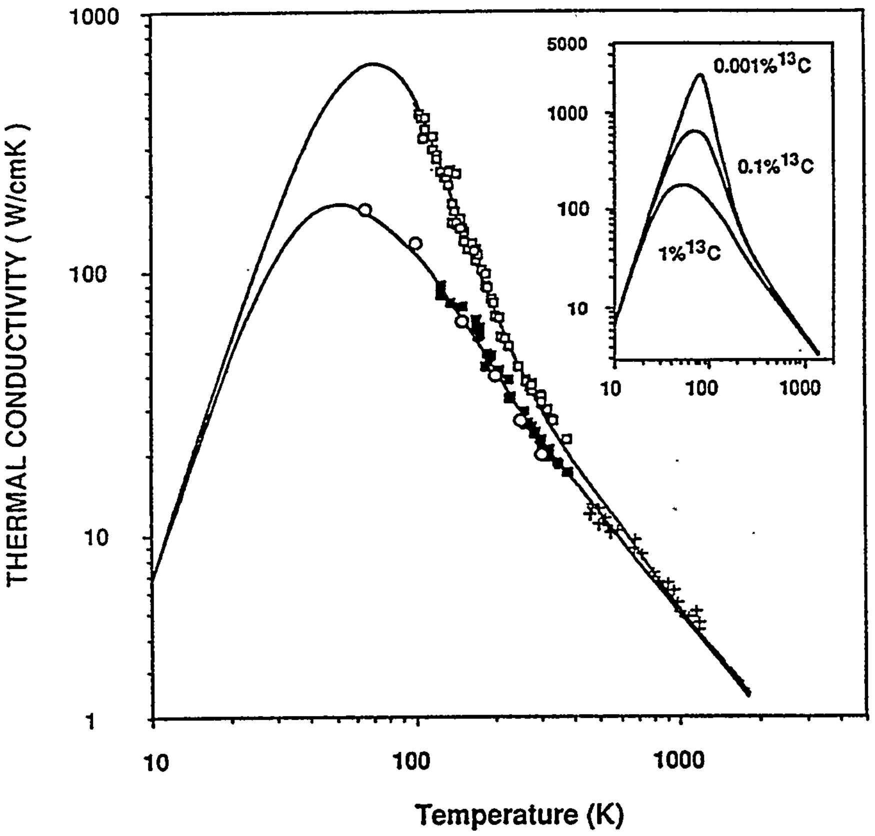

Fig.1.6 Thermal conductivity of natural abundance (1.1% ^{13}C) diamond (filled squares), isotopically enriched (0.1% ^{13}C) diamond (open squares), together with the low temperature data of Slack [62] (circles) and the high temperature data of Olson et al. [58] (crosses). The solid curves are the result of fitting the Callaway theory [56] to the data, using the same set of fitting parameters. The inset shows the calculated thermal conductivity corresponding to 1%, 0.1%, and 0.001% ^{13}C concentrations according to the Callaway theory. (Adapted from Wei et al.[59]).

to values as high as 2000Wcm^{-1}K^{-1} around 80K, which by factor of two larger than Geballe's theoretical prediction [60] of 1000Wcm^{-1}K^{-1} at 77K. It should be pointed out that the very complicated experimental method and analysis had to be employed for all of the above mentioned measurements because of the small size of the diamond specimens.

Therefore the accuracy of the results are not as well defined as normal thermal conductivity data that are obtained with a large specimen.

However, there in no doubt about the isotopically enriched diamond being the world most efficient heat conductor. For this reason the isotopically enriched diamonds are used very recently as monochromators for synchrotron radiation where the heating and the subsequent broadening of the spectrum is a persistent problem due to the high incident radiation density.[61]

1.2.1.4 Lattice Constants and Bulk Modulus

Imagine one atom of mass M oscillates in each of the periodically placed parabolic potential wells of a crystal. These parabolic wells arise from electrostatic forces between atoms. According to this classical picture of the lattice vibration (harmonic approximation), an isotope shift of the lattice constant should not occur because the change in M only changes the amplitude of the oscillation but not the average distances between the atoms. Thus the isotope shift of the lattice constant must originate in the quantum mechanical anharmonic terms which affect the shape of the potential wells making them asymmetric around the center position. In this case replacement of M with a heavier mass leads to a decrease in the lattice constant.

Germanium

Buschert et al.[63] have studied the isotope effect on the lattice constant for the same enriched ^{74}Ge crystal which was studied by Geballe and Hull.[29] Their highly sensitive x-ray technique allowed for measurements of the order of 1ppm relative lattice constant changes. The expression for the relative changes in the lattice constant a_0 with isotopic mass at low temperatures ($e^{-\hbar\omega/k_BT} \ll 1$) is given by:[63]

$$\frac{\Delta a}{a} = -\frac{C_v}{a^3}\frac{\Delta M}{M}\left(\gamma_0 \hbar\, \omega_0 + \frac{3}{4}\gamma_a k_B \Theta_D\right) \qquad (1.11)$$

where $\gamma_0 = 1.12$ and $\gamma_a = 0.40$ are the Grüneisen parameters for optical and acoustical phonon modes in Ge, $\Theta_D = 374$K is the Debye temperature, and the optical phonon energy

$\hbar\,\omega_0 = 37.3$ meV. Buschert et al. [63] evaluated the above equation for a 95.8% enriched ^{74}Ge crystal in comparison with a natural Ge crystal. Eq.1.11 predicts a 12 ppm and a 6 ppm reduction in a_0 for T=0K and T=300K, respectively. Buschert et al. [63] found experimentally reductions of a 14.9 ppm and 6.3 ppm at T=77 K and at T=300 K, respectively. Though this agreement between theory and experiment is considered adequate, a more complete set of experimental results may be obtained by evaluating several isotopically enriched Ge.

Diamond

Holloway et al. [64] have performed lattice parameter measurements for several isotopically mixed diamonds. The experimentally obtained lattice constants are proportional to the atomic fraction of ^{13}C. Values of a_0 for the two pure isotopic diamonds are ~3.56715Å for 0%-^{13}C and ~3.56661Å for 100%-^{13}C. This measurement by Holloway et al. [64] confirmed that ^{13}C diamond has the largest atomic density of any known solid.

The decrease in lattice constant of diamonds with increasing ^{13}C content has led to the speculation that ^{13}C diamonds may be harder than their natural counterparts.[47] In an elegant experiment Ramdas et al. [65] have determined the elastic moduli of highly enriched ^{13}C diamond using Brillouin shifts in inelastically scattered monochromatic radiation from LA phonons traveling along the <100> and the <111> crystal orientations. These measurements show that the elastic moduli are 0.5% higher for ^{13}C diamonds as compared to natural diamonds. Based on the dependence $c_{11} \propto H^{7/4}$ (H:hardness) [66] Ramdas et al. supported their claim that ^{13}C diamonds are the hardest terrestrial material.

1.2.1.5 Band Gaps

The temperature dependence of the energy gap $E_g(T)$ of semiconductors is generally given by: [51, 52, 66]

$$E_g(T) = E' + \int d\omega\, f(\omega)\, \{n(\omega,T) + \frac{1}{2}\} - s\,(c_{11} + 2\,c_{12})\,\Delta V(T)\,/\,3V \qquad (1.12)$$

where $n(\omega,T)$ is the Bose-Einstein occupation number, $f(\omega)d\omega$ the difference in the electron-phonon coupling for the conduction band minimum and the valence band maximum for the modes in the frequency range between ω and $\omega+d\omega$, s the change in the energy per unit compressional hydrostatic stress, c_{11} and c_{12} the elastic constants, and $\Delta V(T)/V$ the fractional volume expansion. At 0K, the energy gap is:

$$E_g\,(T=0) = E' + \frac{1}{2}\int d\omega\, f(\omega) \qquad (1.13)$$

In Eq.1.12, the second term is a contribution from the electron-phonon interaction whereas the third is a contribution from the lattice constant. Since both quantities are dependent on the isotope mass, the energy gap of the semiconductor itself exhibits an isotope shift.

Germanium

The expression "band gap" usually refers to the minimum band gap in the E-**k** space. Ge is a indirect semiconductor with the conduction band minimum at the L point in the Brillouin zone and the valance band maximum at the Γ point. The minimum gap energy is 0.66eV at room temperature. Davies et al. [43, 46] and Etchegoin et al. [44] have reported photoluminescence (PL) studies of isotope shift of E_g for natural and several highly enriched, high quality single crystal of Ge. As explained in the germanium part of Sec.1.2.1.1, the isotope shift of E_g can be found by comparing the energy E_{BE} of no-phonon (NP) bound exciton lines between various isotopically enriched Ge crystals. Fig.1.7 shows the typical PL spectra of Cu doped ^{70}Ge and ^{74}Ge crystals taken by Davies et al.[43, 46] Fig.1.8 shows the no phonon (NP) Cu and P bound exciton PL energies E_{BE} as a function of the average mass number A of the host Ge atom. No phonon means $\hbar\omega=0$ in Eq.1.5. From Fig.1.8, Davies et al. [43, 46] obtained:

$$dE_g\,/\,dA \;=\; d\,E_{NP}\,/\,dA \;=\; 0.35 \pm 0.02 \text{ meV/amu}. \qquad (1.14)$$

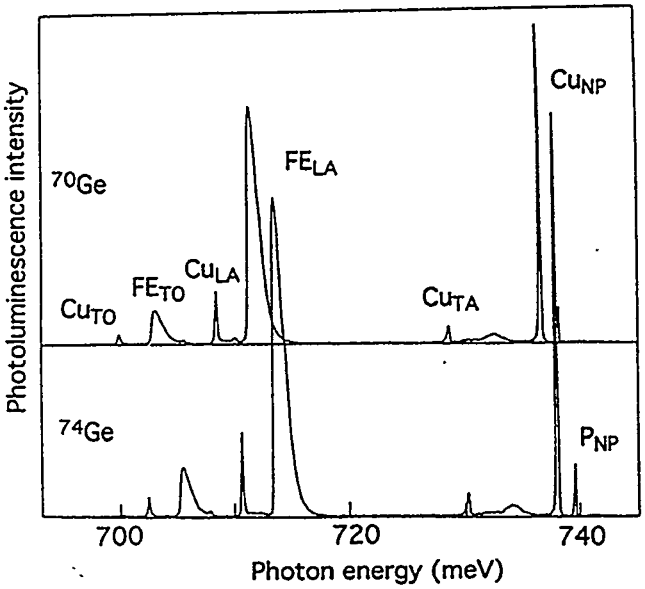

Fig.1.7 Luminescence from the decay of free excitons and excitons bound to Cu acceptors and P donors in ^{70}Ge and ^{74}Ge at 4.2K. The subscripts indicate the L-point phonons assisting in the exciton decay. The impurity bound excitons can decay without emission of a phonon (NP).[43, 46]

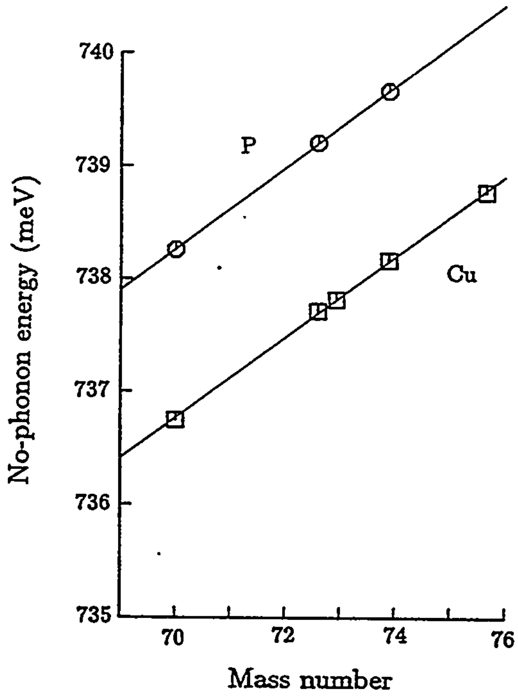

Fig.1.8 Energies of the no-phonon lines of excitons bound to Cu acceptors (squares) and P donors (circles).[43, 46]

A very similar result was also obtained by Etchegoin et al.[44] The isotope shift of E_g for Ge has been calculated by Zollner et al.[67] They found $dE_g/dA=0.48$meV which is in reasonable agreement with the experimental result Eq.1.14. About 2/3 of this E_g change is due to the second term in Eq.1.12 (electron-phonon interaction term), while the rest (1/3) comes from the third, lattice constant related term.

Measurements of the direct bandgap at the Γ point (k=0) in the Brillouin zone have also been performed by Davies et al.[68] They used low temperature optical absorption measurements with very thin samples of Ge single crystals with natural composition and of three different, highly enriched isotopes. They found

$$dE_{dg}/dA = 0.49 \pm 0.03 \text{ meV/amu} \tag{1.15}$$

for the temperature extrapolated to zero. Parks et al. [69] have used piezo- and photo-modulated reflectivity spectra of four monoisotopic and one natural Ge crystals. Their findings were exactly same as those of Davies et al.[68] Parks *et al.* [69] also determined the isotope mass dependence of the sum of the direct gap and the split-off valence band (Δ_0) and found $d(E_{dg}+ \Delta_0)/dA=0.74$ meV/amu. The experimentally measured direct band energy is a factor of ~3.2 smaller that the prediction of Zollner et al.'s calculations.[67]

Diamond

Collins et al. [51, 52] have measured the isotope shift of the indirect energy gap between natural diamond (^{Nat}C) and ^{13}C diamonds using PL. They measured the energy shift of boron bound exciton peaks between ^{Nat}C and ^{13}C which is due to the shift of the band gap. As a result of the isotope substitution, the energy gap of ^{13}C increased by ~13.6 meV over that of natural diamond (98.9%-^{12}C).[51, 52] The absolute shift of the gap ~13.6meV between ^{12}C and ^{13}C is much lager than the shift of 1.75meV between ^{70}Ge and ^{76}Ge. This is due to the one order of magnitude difference in E_g between C and Ge (the room temperature E_g for C and Ge are ~5.47eV and ~0.66eV, respectively).

1.2.1.6 Local Vibrational Mode (LVM) Spectroscopy

We mentioned in Sec.1.1 that the vibrational eigen frequencies of molecules are affected by the mass (isotope) of constituting atoms. Many molecular structures were determined from the quantitative analysis of the isotope shift of vibrational Eigen-frequencies. It was also mentioned in the same section that the local atomic configurations near a variety of light impurities have been determined by isotope substitution of impurities.[30, 31]

In this section we shall describe the LVM study of oxygen in Ge in which isotope substitution of host semiconductor lattice sites (not impurities) were performed in collaboration with the members of the Ramdas group at Purdue University.[32] Oxygen atoms in Ge occupy interstitial sites forming pseudo ^{x}Ge-O-^{y}Ge molecules. One of the three fundamental vibrational modes of this CO_2 molecule-like structure is the "wag" mode (ν_3).[21] High resolution studies of ^{Nat}Ge:O show eleven infrared absorption lines, each one split into several components whose relative intensities depend on temperature. The eleven lines result from the different isotope (mass) combinations of ^{x}Ge and ^{y}Ge. Combinations with identical linear mass averages (e.g. ^{72}Ge/^{74}Ge and ^{73}Ge/^{73}Ge) lead to the same oxygen vibrational frequencies.[21]

The complexity of such spectra can be reduced very significantly through the use of isotopically pure (or at least highly enriched) crystals. Fig.1.9 shows two spectra which were recently reported by us.[32] We used oxygen doped natural and four highly enriched Ge crystals. The reduction from eleven to one LVM line is significant because it allows a quantitative study of the line width and of the coupling between ν_3 and the other modes as a function of temperature. The splitting is a result of the nonlinear superposition of the ν_2 and the ν_3 modes. The low frequency ν_2 modes can be thermally populated already near liquid helium temperature. We were able to precisely determine the bond angle=110° and the Ge-O bond length=1.4948Å of the pseudo Ge-O-Ge molecule.

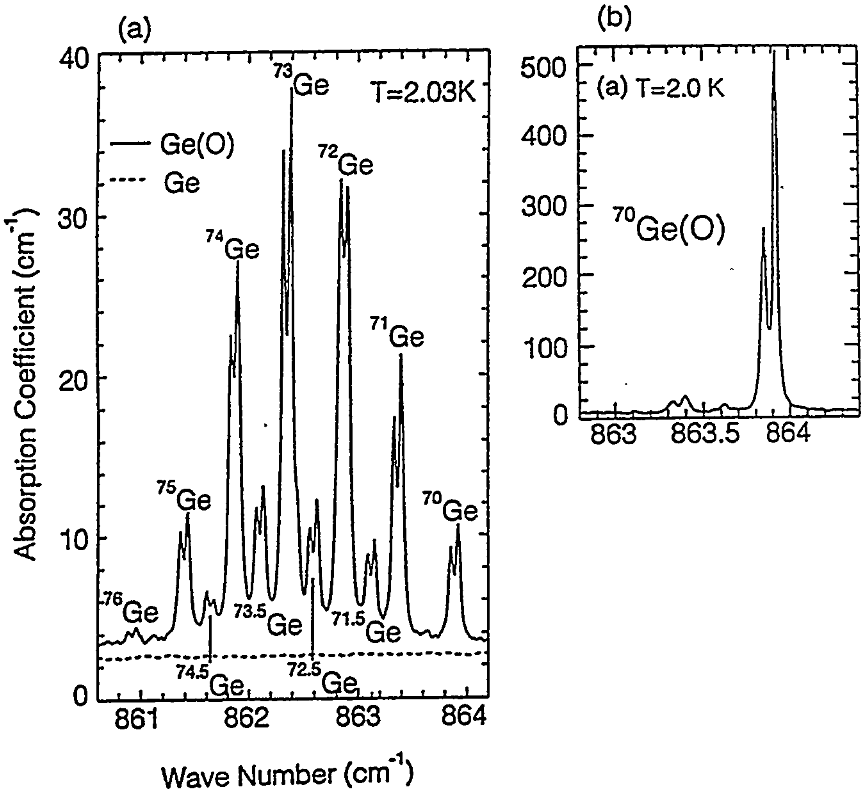

Fig.1.9 (a) Spectrum of the Ge$_2$O pseudo molecules in natural Ge at 2.05 K. Eleven lines split by ν_2-ν_3 coupling excitations correspond to the distinct isotopic mass combinations of the two Ge atoms in the quasi molecule. An oxygen free sample produced the dashed line. The lines labeled ^{75}Ge and ^{71}Ge are caused by traces of ^{74}Ge in ^{76}Ge and ^{72}Ge in ^{70}Ge, respectively. The spectrum was obtained with an oxygen doped highly enriched sample of ^{70}Ge.

1.2.2 Nuclear Structure Related Isotope Effects

Most of the mass related isotope effects so far discussed are subtle (with clear exceptions of thermal conductivity in diamonds and O vibrational modes in Ge). Much larger isotope effects due to nuclear properties are introduced in this section.

1.2.2.1 Neutron Transmutation Doping (NTD)

By far the largest effects due to isotopic composition occur after the capture of a thermal neutron by the nucleus of a specific isotopes. The new nucleus is either stable and the element remains unchanged or it decays transmuting into a new element which may act as a dopant. This neutron transmutation doping (NTD) is one of the major foci of this thesis. A brief introduction and an in depth description of this technique is given in Sec.1.3 and Sec.3.1, respectively.

1.2.2.2 Electron Paramagnetic Spin Resonance (EPR) study of impurities in Ge

Among the various semiconductor defect characterization techniques, Electron Paramagnetic Spin Resonance (EPR) spectroscopy is a very powerful characterization tool whenever applicable.[70] The EPR technique provides microscopic information about impurities and defects such as their symmetry, the value of the nuclear spin of the impurity atom, the nuclear spins of neighboring host lattice atoms, the radius of the localized wave functions, the effect of external stress, etc. In general, most semiconductor crystals are macroscopically diamagnetic. However, if impurities or defects in semiconductors contain an unpaired electron the crystals become paramagnetic. The paramagnetic unpaired electrons associated with impurities or defects are the subject of EPR studies.

The stable isotopes in natural Si, Ge, and GaAs are shown in Table 3.1. Among them, isotopes with nuclear spins are ^{29}Si (I=1/2), ^{73}Ge (I=9/2), ^{69}Ga (I=3/2), ^{71}Ga (I=3/2) and ^{75}As (I=3/2). The rest does not have nuclear spins. Because of the superhyperfine interaction it is desirable for atoms of the host crystal not to have a nuclear spin when donors or acceptors are studied with EPR.[70] This problem has been apparent with natural Ge for it contains 7.8% of ^{73}Ge (I=9/2). The superhyperfine interaction of donor electrons with ^{73}Ge nuclear spins leads to strong line broadening preventing researchers from obtaining high resolution EPR spectra. However, this can be improved by growing Ge crystals with no ^{73}Ge. In 1964 Wilson [71] demonstrated a factor of three narrower EPR linewidths arising from Ge:As by using an isotopically enriched ^{74}Ge sample depleted of ^{73}Ge. He clearly showed that the arsenic spectrum obtained with natural Ge is broadened by the presence of ^{73}Ge whereas the spectrum of the ^{74}Ge crystal is very sharp. Therefore, isotopically controlled Ge with low ^{73}Ge content will be extremely useful in the EPR studies of a variety of defects in Ge.

1.2.2.3 Phonon Dispersion Relation Determination in CdTe

As was mentioned earlier, the inelastic neutron scattering technique is the only method which allows the determination of the phonon dispersion relation covering the entire Brillouin zone. However, natural cadmium based II-VI compound semiconductors including CdS, CdSe and CdTe cannot be evaluated with inelastic neutron scattering because of the extremely large thermal capture cross section of $^{113}_{48}$Cd. Rowe et al. grew a CdTe crystal depleted of $^{113}_{48}$Cd isotopes for a neutron scattering study.[72] In this manner the strong neutron absorption by $^{113}_{48}$Cd was minimized and the phonon dispersion relation of CdTe was determined for the first time. Measurements of the phonon dispersion relationships of CdS and CdSe with inelastic neutron scattering have not yet been performed.

1.2.3 Isotope Superlattices

Isotope superlattices, i.e., layered structures where each layer consists of a controlled isotopic composition, were first proposed by Haller [73] in the context of selective doping with the NTD technique. A few very interesting studies which involved such structures have been recently performed.

1.2.3.1 Phonons in Isotope Superlattices

Short period isotope superlattices consisting of layers each made up of a few atomic planes of ^{70}Ge and ^{74}Ge were grown by Schorer et al.[74] The electronic band offset between ^{70}Ge and ^{74}Ge layers is ~1.4meV which is negligibly small for all practical purposes. Because of this, the superlattice only affects the phonon dispersion while electrons behave just as if they were in a bulk crystal. Consequently these are new and ideal structures for the study of the effects of isotope mass distribution on phonon properties. (All commercially available superlattice structures such as AlGaAs/GaAs superlattices have large electronic band offsets and large changes in host atom masses. This makes it difficult to perform phonon studies using Raman spectroscopy.)

Before the growth of the ^{70}Ge/^{74}Ge superlattices, Fuchs et al. [38] performed a theoretical calculation regarding the effects of the dimensionality on the properties of phonons. Because of the additional periodicity introduced by short-period isotope superlattices, the Brillouin zone edges that occur at $k=\pm\pi/a$ in bulk crystals change in the growth direction in **k** space. This change leads to an effect known as Brillouin zone folding of the phonon dispersion curves. Fig.1.10 shows the calculated phonon dispersion for an isotopic superlattice with layers alternating between four planes of ^{70}Ge and four planes of ^{76}Ge along [001].[38] Folding leads to states at **k**=0 which do not exist in the bulk material, e.g., non-zero acoustic phonon modes etc. The vibrational modes for this $^{70}\mathrm{Ge}_4/^{76}\mathrm{Ge}_4$ [001] superlattice at **k**=0 were calculated using the simple planar force constant model. The same theoretical study also showed which of the **k**=0 modes are Raman active using the bond polarizability model.[75] The relative intensity of the Raman lines should reflect the densities of phonon states at **k**=0.

These theoretical predictions were recently tested by Spizer et al. [76] using the ^{70}Ge/^{74}Ge superlattices grown by Schorer et al.[74] The experimental and theoretical results are summarized in Fig.1.11. The shortest periods studied consisted of two atomic layers (n=2) each producing a single Raman line corresponding to the LO phonon in a crystal with

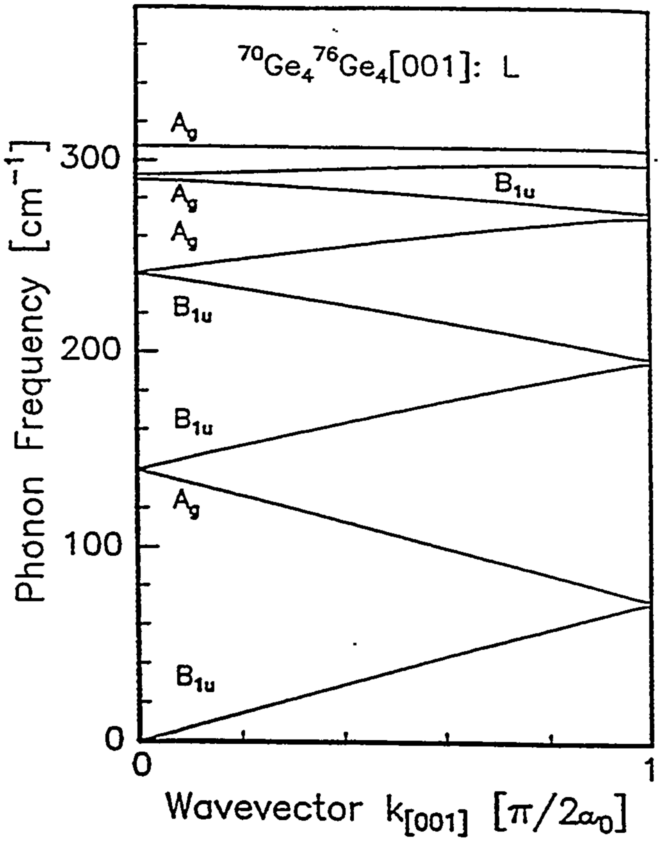

Fig.1.10 Calculated phonon dispersions for a $^{70}Ge_4/^{76}Ge_4$ isotope superlattice grown along [001].[38]

isotope mass A = 72, the linear average of the two masses. The n = 4 superlattice shows the Raman line predicted at ~290 cm^{-1} though at a slightly lower intensity than shown in Fig.1.11. In the n=12 superlattice we observe at least three strong Raman lines. For n=32 the Raman spectra begin to approach the structure we would expect to observe for to isotopically pure bulk crystals, one made up of ^{70}Ge, the other of ^{74}Ge. Localization of the different phonon modes in each layer is practically complete at this point.

These first Raman spectroscopy studies of isotope superlattices demonstrate Brillouin zone folding in a very pure form. They also show the impressive validity of the planar bond-charge and bond polarizability models. It is especially interesting to notice that the phonon properties of 30 atomic planes are already close to those of an infinitely large bulk crystal.

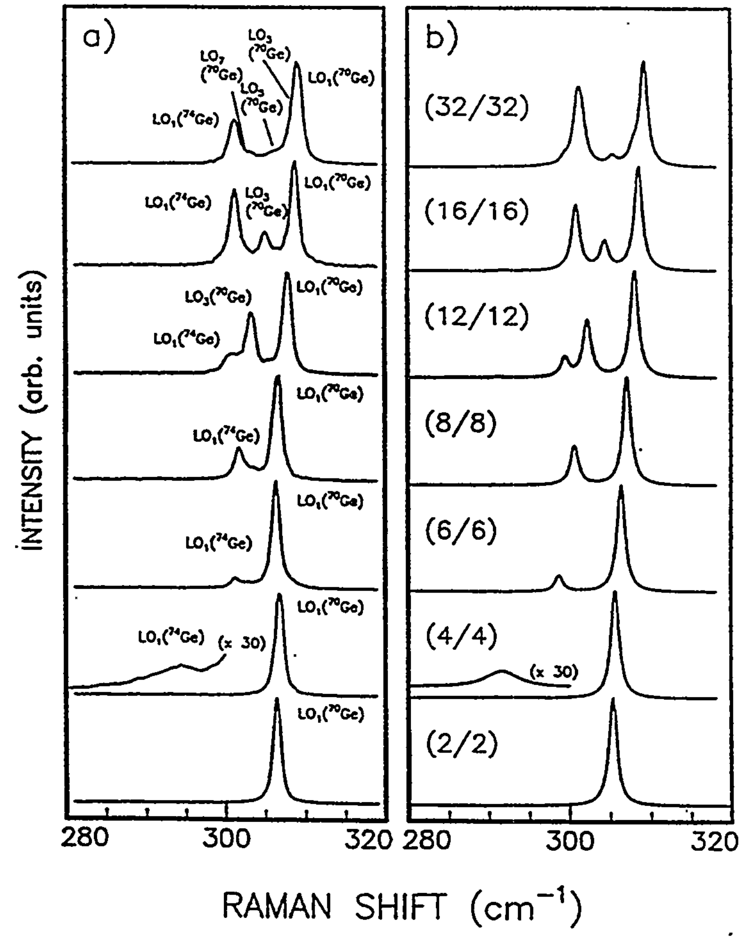

Fig.1.11 (a) Measured at T=10K and (b) calculated Raman spectra for a series of isotope superlattices $^{70}Ge_n/^{74}Ge_n$ grown along [001] with n = 2, 4, 6, 8, 12, 16, and 32.[76]

1.2.3.2 Diffusion Studies

Isotope superlattices are ideal structures to study diffusion of host atoms (self-diffusion) of semiconductors. Tan et al. [77] were the first to make use of a $^{69}Ga^{75}As/^{71}Ga^{75}As$ isotope supperlatice to study Ga self-diffusion. The ^{69}Ga and ^{71}Ga distribution profiles before and after a variety of annealing conditions were measured by secondary ion mass spectroscopy (SIMS). Even though Tan et al. [77] were able to obtain the Ga self-diffusivity, the data may not reflect the intrinsic Ga self-diffusion in GaAs since the superlattice was grown on a strongly Si doped substrate which will affect the Ga diffusion in the superlattice.

Ge self-diffusion has been studied recently by Fuchs et al. [78] who used bi-layers of ^{70}Ge and ^{74}Ge (each 1000 or 2000Å thick) which were grown by MBE on a natural Ge substrate.[74] They have chosen five diffusion temperatures and the times so as to obtain similar $\sqrt{Dt}$ products (D: diffusion coefficient). Fig.1.12 shows a SIMS result for the diffusion run at 586°C for 55.55 hrs. Because the isotopes are only enriched into the high 90 percentile range, one finds SIMS data from all of the residual minor Ge isotopes. The data analysis was performed as followings. Disregarding the small differences in diffusivity caused by different isotopes masses [79], the ^{70}Ge and ^{74}Ge isotopes are expected to diffuse symmetrically into each layer following complementary error functions. The individual profiles are described by:

$$[^{70}Ge]_x = 0.5[^{70}Ge]_o\{1 - \mathrm{erf}(x/2\sqrt{Dt})\} \tag{1.16}$$

$$[^{74}Ge]_x = 0.5[^{74}Ge]_o\{1 - \mathrm{erf}(- x/2\sqrt{Dt})\}. \tag{1.17}$$

The interface is located at $x = 0$ and $[^{70}Ge]_o = [^{74}Ge]_o = 4.4\times10^{22}\mathrm{cm}^{-3}$. The self-diffusivity of Ge for the 586°C-55.55hrs run was obtained by fitting the experimental profile of ^{70}Ge with Eq.1.16 (the solid curve in Fig.1.11). The results for the diffusivities determined at five temperatures are shown together with older published data [80, 81] (Fig.1.12). The Ge diffusivities obtained by Fuchs et al. [78] are in excellent agreement

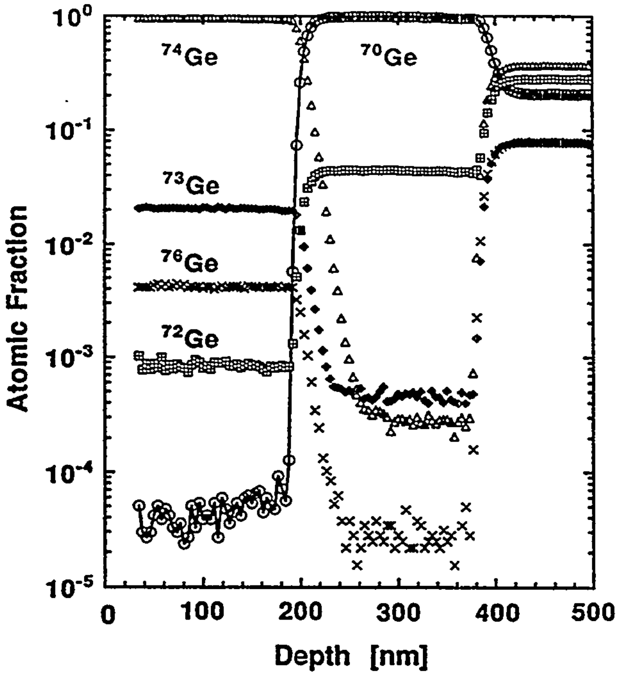

Fig.1.12 Experimental concentration-depth profiles obtained with SIMS of the atomic fractions of ^{70}Ge, ^{72}Ge, ^{73}Ge, ^{74}Ge and ^{76}Ge of a ^{74}Ge/^{70}Ge bi layer on a natural Ge substrate after annealing at 586 °C for 55.55 hrs. The solid line is a fit to the ^{70}Ge profile.[78]

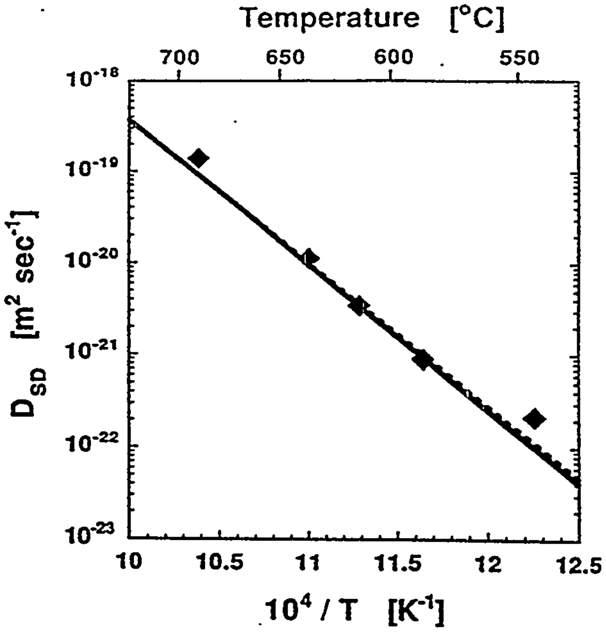

Fig.1.13 Arrhenius plot of the Ge self-diffusion coefficient as a function of temperature. The results obtained with the isotope bi layers (◆) compare most favorably with the most recent data by Vogel et al. [81] (solid line) and Werner et al. [80] (broken line).

with previously reported values.[80, 81] It should be pointed out that the bi-layers used by Fuchs et al. [78] contained residual boron concentrations as high as $10^{17}cm^{-3}$. The Ge self-diffusivity may be affected by these impurities, similar to the case of the Ga self-diffusion study by Tan et al's.[77] However, these two experiments [77, 78] clearly demonstrated for the first time the usefulness of isotope superlattices for the study of self-diffusion in semiconductors.

1.3. Neutron Transmutation Doped (NTD) Ge Thermistors

Germanium continues to be one of the most suitable materials for detection of nuclear radiation [82] because of the very high chemical purity and crystalline perfection that can be achieved. Large volume p-i-n Ge diodes which exhibit excellent electron and hole transport allow high resolution nuclear spectroscopy. The high-purity crystal growth technique has also been used to produce "purely" doped, far-infrared radiation photoconductor materials such as Ge:Ga, Ge:Be, Ge:Zn and Ge:Cu.[83-85] The highest purity regarding electrically active impurities which can be achieved in Ge lies in the range of 10^9cm^{-3} to 10^{10}cm^{-3} (compare with $4X10^{22}$ cm^{-3} Ge atoms!), while the purest Si and GaAs are normally found to contain on the order of several times 10^{11}cm^{-3} and 10^{12}cm^{-3} * , respectively.

After growing ultra-pure germanium crystals of natural isotopic composition (^{Nat}Ge), one can place the crystals into a nuclear reactor to obtain neutron transmutation doping (NTD). Upon thermal neutron irradiation, the five stable isotopes of ^{Nat}Ge may undergo the following nuclear reactions after neutron capture:

$$^{70}_{32}\text{Ge}\ (20.5\%) + n \rightarrow\ ^{71}_{32}\text{Ge} \xrightarrow[T_{1/2}\,=\,11.2\ d]{EC}\ ^{71}_{31}\text{Ga}$$

$$^{72}_{32}\text{Ge}\ (27.4\%) + n \rightarrow\ ^{73}_{32}\text{Ge}$$

$$^{73}_{32}\text{Ge}\ (7.8\%) + n \rightarrow\ ^{74}_{32}\text{Ge}$$

$$^{74}_{32}\text{Ge}\ (36.5\%) + n \rightarrow\ ^{75}_{32}\text{Ge} \xrightarrow[T_{1/2}\,=\,82.8\ min]{\beta^-}\ ^{75}_{32}\text{As}$$

$$^{76}_{32}\text{Ge}\ (7.8\%) + n \rightarrow\ ^{77}_{32}\text{Ge} \xrightarrow[T_{1/2}\,=11.3\ hrs]{\beta^-}\ ^{77}_{34}\text{As} \xrightarrow[T_{1/2}\,=38.8\ hrs]{\beta^-}\ ^{77}_{34}\text{Se}$$

---

* This result can only be achieved for liquid phase grown GaAs which leads to thin films only. [86, 87]

The abundance of each Ge stable isotope is shown in the parenthesis. The nuclear reaction symbols shown above will be explained in Sec.3.1.2.

Ge is unique because it is one of few semiconductors whose stable isotopes form both acceptors and donors after NTD: shallow acceptors Ga, shallow donors As and double donors Se. The ^{72}Ge and ^{73}Ge isotopes simply transmute into other stable Ge isotopes.

The isotopic abundance in ^{Nat}Ge and the thermal neutron capture cross sections yield p-type Ge crystals after NTD with the fixed compensation ratio K: [88]

$$K \equiv \frac{[\text{Minority Impurity}]}{[\text{Majority Impurity}]} = \frac{[\text{As}] + 2[\text{Se}]}{[\text{Ga}]} = 0.32. \tag{1.18}$$

Compared to other doping methods, NTD leads to a very homogeneous, perfectly random distribution of the dopants. This is because of the large neutron field produced by a nuclear reactor guaranteeing a homogeneous flux over the crystal dimensions, the small capture cross section of semiconductor isotopes for neutrons minimizing "self-shadowing" and the perfect random distribution of the stable isotopes in ^{Nat}Ge single crystals. Reproducibility of NTD is also excellent as long as the same irradiation site and the same power of a nuclear reactor are employed (since the "thermal" neutron capture cross sections of stable isotopes can vary depending on the neutron velocity distribution).

In recent years many low temperature thermistors for bolometric detection have been fabricated by doping ^{Nat}Ge with the NTD technique.[88, 89] NTD ^{Nat}Ge chips of typically (0.25 to 0.5mm)^3 volume have been used widely for phonon mediated detectors for dark matter searches and neutrino physics [90-92], as thermistors for a wide range of radioastronomical observations [83, 93, 94] and for cosmic ray microwave background measurements.[95] Fig.1.14 shows the temperature dependence of the resistivity ρ of ten selected NTD ^{Nat}Ge crystals. Table 1.2 contains information on each of the NTD Ge samples. Log ρ is plotted against $T^{-1/2}$ in Fig.1.14 because Shklovskii and Efros's theory of "variable range hopping conduction" , the hole transport mechanism dominant below ~1K, predicts the following temperature dependence of the resistivity ρ for doped Ge: [96]

$$\rho = \rho_0 \exp\left(\frac{T_0}{T}\right)^{1/2} \tag{1.19}$$

where ρ_0 and T_0 are parameters which depend on the net dopant impurity concentration ($N_{Net}=N_{Ga}-N_{As}-2N_{Se}$) and the compensation ratio K. For the interested readers Eq.1.19 is derived in Appendix C. Fig.1.14 shows that the resistivity of all NTD ^{Nat}Ge samples obeys the law given in Eq.1.19. Some degree of compensation is required for holes to be able to hop from neutral to ionized acceptors using the available thermal energy from the crystal environment (K>0).

A NTD Ge thermistor working as a particle (radiation) detector makes use of the well behaved dependence of the resistivity on temperature described above. The thermistor is maintained at a base temperature T_B by a thermal link connected to a thermal bath. The temperature increase of the thermistor due to energy dissipation of incident particles or radiation is detected via the change in the resistance. The sensitivity is defined by the temperature coefficient α:

$$\alpha = \frac{1}{R}\left(\frac{\partial \log R}{\partial \log T}\right)_{T_B} \tag{1.20}$$

where R is the resistance. Electronic amplifier noise considerations require an optimum thermistor resistance of 5×10^6 to 5×10^7 Ω. The larger the $\partial R/\partial T$, the larger is the signal for a given ΔT. If one wishes to design $\partial R/\partial T$ for a given T_B, appropriate control of the parameters ρ_0 and T_0 appearing in Eq.1.1 is required. Another critical issue for the thermistor performance is the current-voltage (I-V) characteristics at T_B. It has been reported that the linear I-V (Ohmic) region of the NTD ^{Nat}Ge is rather small and the resistance significantly decreases as the current is increase.[97] The linear I-V region may be extended by changing the compensation ratio K of the thermistor.

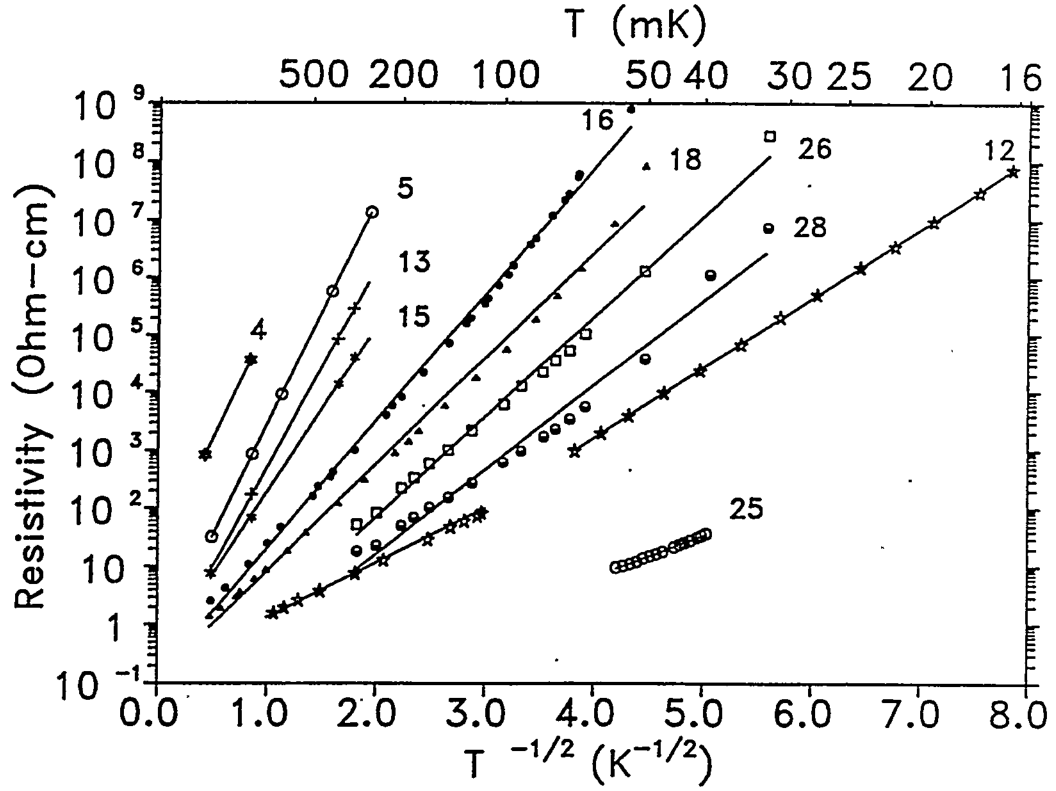

Fig. 1.14 A plot of the logarithm of ten selected NTD Ge samples as a function of $T^{-1/2}$. The linear dependence indicates variable range hopping conduction. Table 1.2 contains the neutron fluence and the various dopant concentrations for each sample (compiled by J. Beeman, Lawrence Berkeley Laboratory).

Table 1.2 NTD Ge thermistor data

NTD#	n Dose (cm^{-2})	N_{Ga} (cm^{-3})	N_{As} (cm^{-3})	N_{Se} (cm^{-3})	$N_{Ga} - \Sigma N_D$(cm^{-3})
4	3.38E+17	9.94E+15	2.83E+15	1.86E+14	6.74E+15
5	7.50E+17	2.21E+16	6.29E+15	4.13E+14	1.50E+16
13	1.24E+18	3.65E+16	1.04E+16	6.83E+14	2.47E+16
15	1.54E+18	4.53E+16	1.29E+16	8.49E+14	3.07E+16
16	2.07E+18	6.09E+16	1.73E+16	1.14E+15	4.13E+16
18	2.61E+18	7.67E+16	2.19E+16	1.44E+15	5.20E+16
26	2.82E+18	8.29E+16	2.36E+16	1.55E+15	5.62E+16
28	3.07E+18	9.03E+16	2.57E+16	1.69E+15	6.11E+16
12	3.33E+18	9.79E+16	2.79E+16	1.83E+15	6.64E+16
25	4.20E+18	1.23E+17	3.52E+16	2.31E+15	8.37E+16

As stated above, ρ_0 and T_0 depend on N_{Net} and K. Thus the ability to precisely control both N_{Net} and K is important for the development of improved thermistors.

Unfortunately there has been no method which allows independent control of N_{Net} and K for ^{Nat}Ge. Obtaining a crystal with highly uniform majority and minority impurity distributions using one of the conventional bulk doping technique is impossible. During Czochralski growth, for example, one cannot maintain a fixed concentration ratio of two or more impurities along the growth axes because of their different distribution coefficients. In addition non-uniform concentration fluctuations (called impurity striations) are caused by natural and forced convection of the melt during growth.[98] Since crystal growth from the melt is a high temperature process during which impurities remain mobile for prolonged time, it is possible that impurities with opposite charge attract each other causing further microscopic inhomogeneities.

The application of the NTD technique to ^{Nat}Ge only allows the control the net-concentration N_{MJ}-N_{MN} by adjusting the total neutron fluence. The compensation ratio $K(=N_{MN}/N_{MJ})$ however remains fixed at 0.32 and cannot be changed.

In this thesis I will introduce a new bulk doping method "neutron transmutation doping of isotopically engineered Ge" which allows the precise control of K for the first time. The concentration ratio of the NTD products, ^{71}Ga acceptors and ^{75}As donors, is controlled by adjusting the atomic fractions of ^{70}Ge and ^{74}Ge isotopes in the starting Ge crystals. The combination of isotopically enriched germanium and the neutron transmutation doping technique guarantees unprecedented doping uniformity and <u>independent</u> control of the majority and minority impurity concentrations. This is the only technique which allows simultaneous control of the net-impurity concentration and the compensation ratios in a bulk semiconductor. Our primary goal is to improve the performance of Ge thermistors by using NTD of isotopically engineered Ge. This topic will be covered extensively in Sec.4.3. The controllability of the compensation ratios allowed us to perform additional interesting basic studies for the first time.

1.4 Topics Addressed in this Thesis

As discussed in the last section, the independent control of the net-impurity concentration and the compensation ratios through NTD requires crystal growth of isotopically engineered Ge. Even under very favorable circumstances isotope separation remains costly and ways have to be found to minimize materials use. The following section (Sec. 2) describes the isotope separation process, zone purification, and crystal growth method which produces small, high quality Ge single crystals with volumes of the order of 1-2 cm^3. A description of the crystal characterization is rather brief since the same topic was extensively covered in my master's thesis [99] and several papers.[100, 101]

Sec. 3 contains an in-depth discussion of the neutron transmutation doping technique and its application to isotopically engineered Ge. It will be shown that our method indeed leads to precise control of the net-impurity concentrations and the compensation ratios. Thermal annealing of irradiation defects due to unavoidable fast neutron is also discussed.

NTD of isotopically controlled Ge for which both the carrier concentration and the compensation ratio can be adjusted are ideal crystals for the to study carrier transport properties in semiconductors. Sec. 4 contains a review of various carrier transport mechanisms in semiconductors and the results of our carrier transport studies. Topics to be discussed are free carrier transport in a neutral impurity scattering dominated regime, free carrier transport in a ionized impurity scattering dominated regime, carrier transport on the metallic side of the metal-insulator transition and hopping conduction.

In Sec. 5 we present our recent results of an infrared absorption line width study performed on NTD Ge:Ga,As with K=0.082-0.9. Because the ionized impurity concentration in the crystal is determined by the compensation ratio, one expects significant broadening of the gallium absorption lines in highly compensated materials due to inhomogeneous electric fields arising from the surrounding charged impurity centers. So far there have been very few quantitative study of infrared absorption linewidth because of the difficulty of controlling the compensation ratios using conventional doping techniques. Our quantitative study helps to clarify some of the unsolved issues of electric field broadening of absorption lines in semiconductors.

A summary and conclusions are given at the end the thesis.

Chapter 2 Crystal Growth of Isotopically Controlled Ge

2.1 The Isotope Separation Process

Growth of isotopically enriched crystals requires isotopically separated starting materials in elemental form in large enough quantities for zone refining. Ge isotope production in kilogram quantities was originally motivated by the search for the double β-decay in ^{76}Ge crystals.[102] The gas centrifuge system, which had been used in the former Soviet Union for the uranium isotope enrichment, was employed for the ^{76}Ge isotope separation.[103] An excellent review of this technique has been given by Olander.[25] In the past 11 years more than 26 kg of ^{76}Ge isotope with 85% enrichment (see Table 2.1) were produced at the Kurchatov Institute of Atomic Energy (now the Russian Science Center "Kurchatov Institute").

In the germanium isotope separation process volatile, chemically reactive germanium tetrafloride (GeF_4) was used as a working gas. Its molecular mass is 149 a.m.u. which is substantially smaller than that of uranium hexafluoride (353 a.m.u.). A special modification of the gas centrifuge was needed in order to accommodate these significantly lighter molecules.[103] Germanium tetrafloride enriched with the target isotope was transformed into germanium oxide GeO_2 followed by its reduction to the elemental form.

Enriched ^{70}Ge can be produced directly from natural Ge since it is the lightest stable isotope of Ge. On the other hand, the second heaviest stable isotope ^{74}Ge may be efficiently separated only from an isotope mixture with a minimal content of the heaviest ^{76}Ge component. After the removal of ^{76}Ge, the remaining mixture (^{76}Ge content of only about 1.2%) was used to separate the ^{74}Ge isotopes. Several hundred grams of ^{70}Ge and ^{74}Ge isotopes with enrichments shown in Table 2.1 have been produced at the Kurchatov Institute and have been made available to a number of research groups in Russia, the Ukraine and the United States.

Table 2.1 Isotopic composition of the Ge isotopes enriched at the Kurchatov Institute

Isotopic product \ Isotope	^{70}Ge	^{72}Ge	^{73}Ge	^{74}Ge	^{76}Ge
Natural Ge	20.5%	27.4%	7.8%	36.5%	7.8%
^{70}Ge	96.3%	2.1%	0.1%	1.2%	0.3%
^{74}Ge	0.5%	0.17%	2.2%	96.8%	0.33%
^{76}Ge	0.1%	0.1%	0.2%	14.5%	85.1%

2.2 Zone Purification

We started our zone purification process with 100g each of isotopically enriched granular powders of ^{70}Ge and ^{74}Ge. The donor concentration in the powder was so high that the Ge crystal grown from this material with no purification process exhibited metallic conduction (free electron concentration $>3\times10^{17}$cm^{-3}). In order to remove these donors each of the isotopically enriched ^{70}Ge and ^{74}Ge powders was placed in a boat of ultra-pure graphite. The boat was inserted in a quartz tube which allowed atmosphere control. After each powder was transformed into a very narrow continuous Ge polycrystalline bar (~50cm long, ~0.4cm^2 cross section area), by RF heating and melting a short molten zone (2.5cm long) was formed. The liquid zone traveled from one end of the bar to the other at a steady speed of 10cm/hr in a continuous flow of forming gas (90% N_2 and 10% H_2 mixture). Careful adjustment of the RF heater power and the tilt angle of the bar was necessary in order to keep the narrow Ge bar from breaking up into a string of drop shaped pieces. The removal of a small piece from the impure end of the bar after every 10 zone passes, decreased the total amount of impurities in the bar by 1~2 orders of magnitude. After completion of 25 zone passes, the net electrically active impurity concentration profile along the direction of the zone refined polycrystalline bar was determined via a resistivity measurement at 77K in the dark at 7cm intervals. The net impurity concentration $|N_A-N_D|$

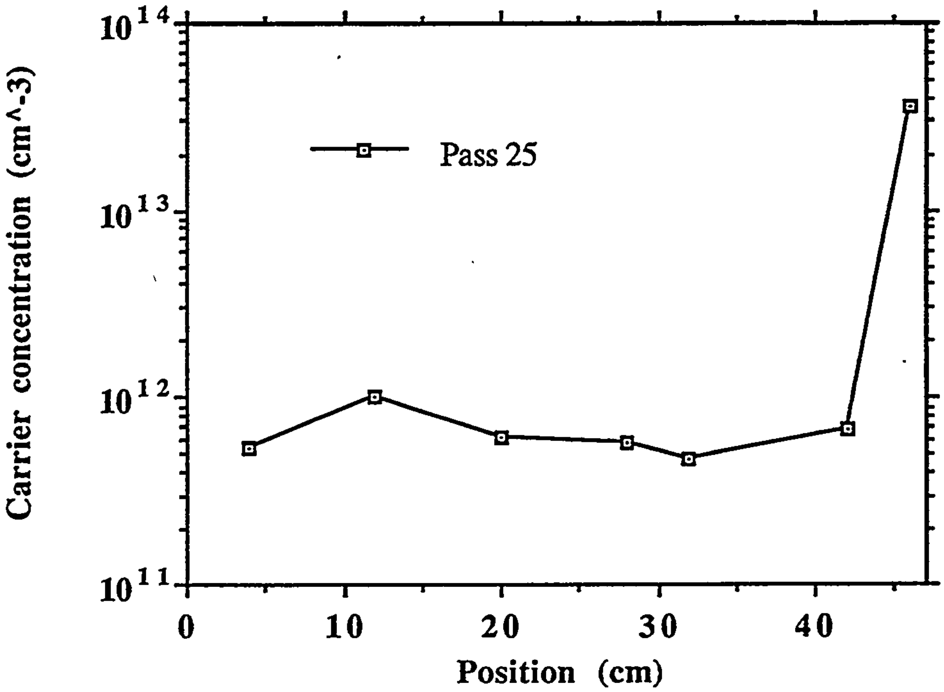

Fig. 2.1 Net carrier concentration profile of the 70-Ge bar after 25 zone refining passes

can be calculated with the relation $|N_A-N_D|=1/\rho\mu q$ where N_A and N_D are the ionized acceptor and donor impurity concentrations per cm^3, respectively, μ is the mobility (~40,000 $cm^2/Vsec$ for both electrons and holes in pure Ge at 77K) and q is the electron charge (-1.6×10^{-19}C). Fig.2.1 shows the net impurity concentration profile of the ^{70}Ge refined bar after 25 zone passes. More than 80% of the bar were purified to $|N_A-N_D| < 10^{12}$ cm^{-3}. This value corresponds to the highest degree of the purification one can measure due to defects and impurities at grain boundaries and dislocations. The net impurity concentration profile of the ^{74}Ge zone refined bar is almost identical to that of the ^{70}Ge bar. The measured net-concentrations are upper limits and the material could be purer.

2.3 Small Ge (~4g) Crystal Growth System

The crystal growth system developed in this work allows us to grow Ge single crystals of ~4 grams in weight. It is specifically designed for easy handling and rapid high purity growth. This system is designed such that it requires no seed crystal in order to preserve the isotopic purity of the starting material. The growth direction of the crystal cannot be chosen. The ability to control some important parameters for crystal growth (growth rate, interface temperature gradient, etc.) is limited because of the small dimension of the system. Nevertheless, after careful "trial and error" calibrations the system can reliably produce high purity single crystals. For high purity starting materials the net impurity concentration of $\sim 2\text{X}10^{12}\text{cm}^{-3}$ is achieved in crystals grown with this system. This purity is very good especially for such a small crystal having a volume to surface ratio that is unfavorable for the exclusion of impurities. Besides the growth of high purity crystals, this method may be also used for the growth of crystals doped with various impurities. Whereas many expensive, large crystal growers must be dedicated to the growth of certain crystals in order to avoid cross-contaminations, this system can be inexpensively cleaned by simply changing one pair of quartz tubes and the graphite crucible. Taking advantage of this system we have grown various types of oxygen doped mono-isotopic Ge crystals (^{70}Ge, ^{73}Ge, ^{74}Ge, and ^{76}Ge) for the local vibrational mode study [32] mentioned in Sec. 1.1.

Fig.2.2 (a) shows the specially designed ultra-pure graphite crucible in the disassembled state. It consists of one pair of split molds and a cap. The crystal resides inside the molds which are machined in the shape shown in Fig. 2.2 (a). In Fig.2.2 (b) we see the assembled crucible. In order to grow high purity crystals, the purity of the graphite plays a crucial factor. The graphite crucible used in this work was annealed at ~3000°C in a chlorine atmosphere to reduce the metal impurity contamination as far as possible [*]. Prior to the crystal growth, the interior of the split-off molds is coated with a thick carbon soot layer by using an oxygen-butane (C_4H_{10}) flame. The soft carbon layer acts as an cushion which provides the extra space of expansion when the molten Ge solidifies. Carbon is a neutral impurity in Ge and the solubility of C in Ge is $\sim 10^{14}$ cm^{-3} near the melting point.[104]

---

[*] The crucible was made and cleaned by Carbon USA, Ultra Carbon Division, USA.

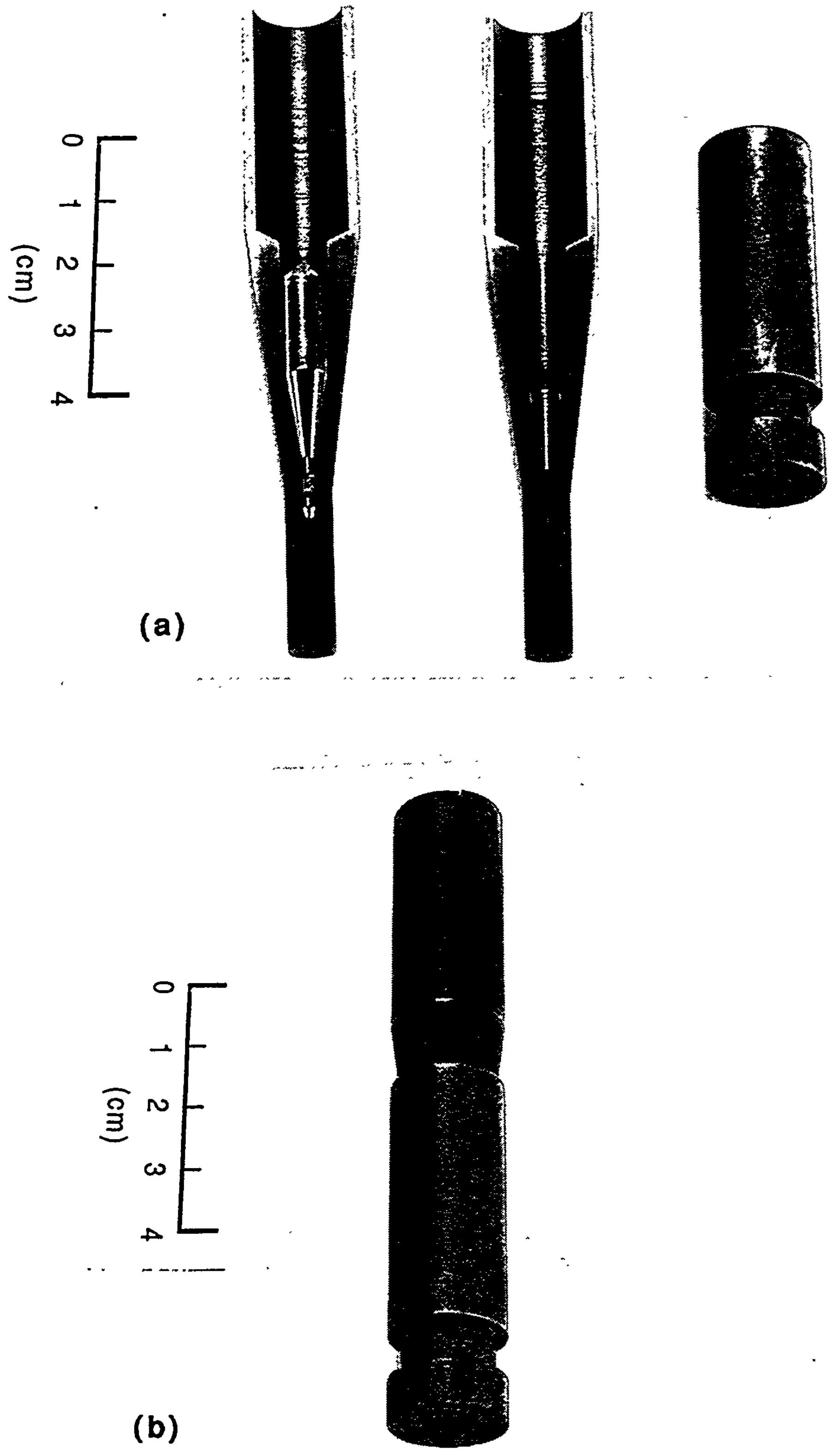

Fig. 2.2 Ultra-pure graphite crucible for a high purity Ge crystal growth.
(a) disassembled and (b) assembled.

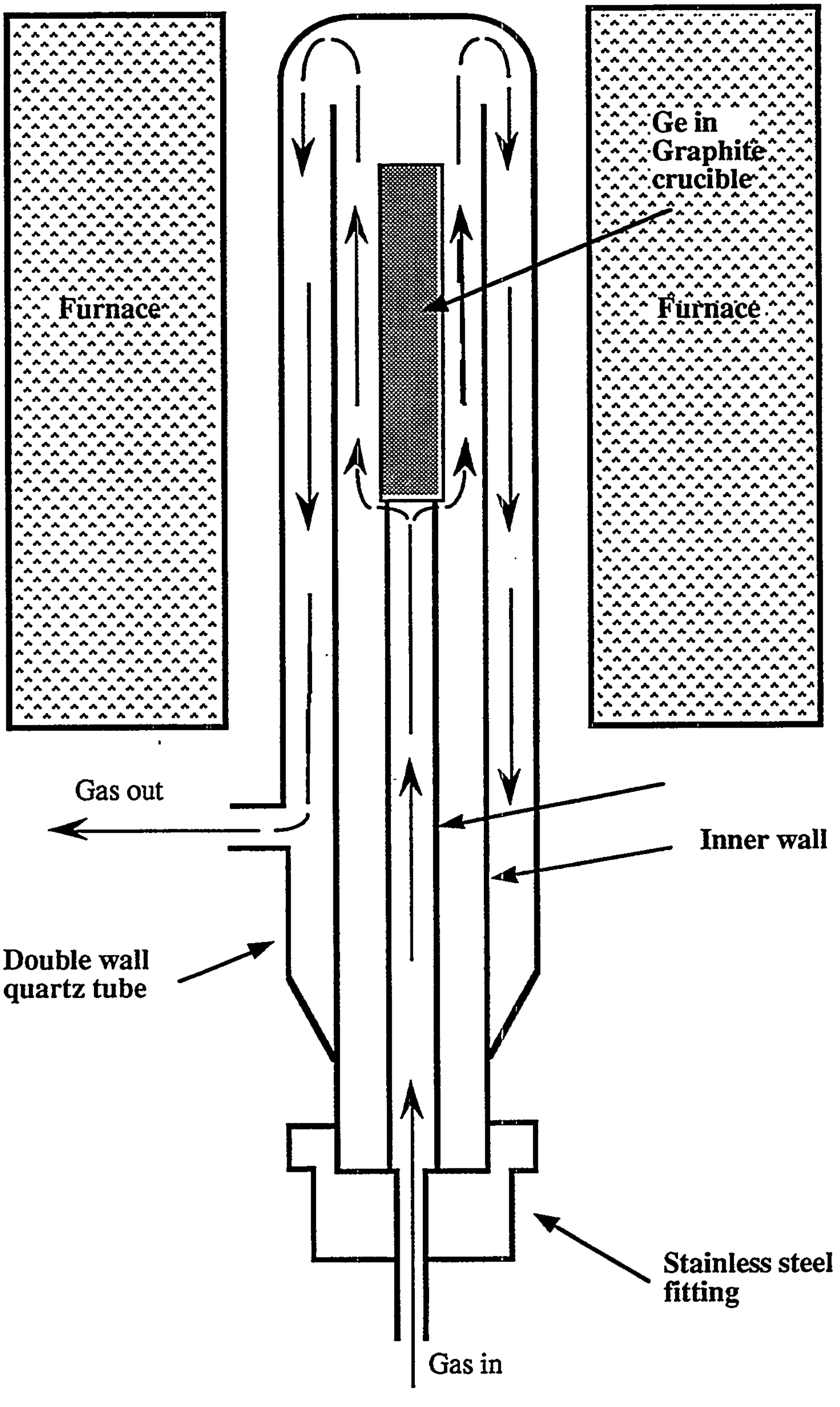

Fig. 2.3 Modified vertical Bridgman Ge crystal growth system

Therefore carbon in direct contact with molten Ge is of no concern regarding purity. Fig. 2.3 shows the system developed for the crystal growth of isotopically enriched Ge crystals. The graphite crucible containing Ge starting material (zone-refined poly-crystals of typical impurity concentrations $<10^{12}$ cm^{-3}) is placed inside the double-wall quartz tube. One end of the tube is closed, and crucible loading and gas feeding is performed through the open end. The diameter of the outer tube is roughly 3cm. The open end of the quartz tube is sealed by an "Ultra-torr" stainless steel fitting manufactured by Swagelock cooperation, USA. The crucible rests on the inner quartz support which is standing on the stainless steel fitting. The quartz tube is positioned inside the vertical furnace such that the crucible sits at a well calibrated position of the furnace. During heating nitrogen gas (~1l /min) is fed through the gas inlet valve in order to avoid oxidation. The gas travels along the path shown by arrows in the figure and exits through the gas outlet valve. When the germanium inside the crucible is completely melted, the furnace temperature is slowly lowered. At the same time the flow rate of the gas is increased so that the gas hitting the bottom of the crucible creates a temperature gradient necessary for the single crystal growth. Consequently, a single crystal grows gradually from the bottom. Fig 2.4 is a photograph of typical isotopically engineered crystals we grew using this system. A U.S. dime (ten-cent coin) is shown to give a scale. Each crystal is about 4 grams in weight, 6.5mm in diameter and 4.5cm in length.

2.4 Characterization of Isotopically Engineered Single Crystals

Isotopically engineered single crystals preserve the isotopic compositions of the starting materials very well because of our seed-less crystal growth system. This result was confirmed using secondary ion mass spectrometry (SIMS). Crystal orientation measurements on more than 70 crystals grown in our random-seeding system revealed that <113> is the statistically preferred growth direction. Typical net-impurity concentration profiles of isotopically engineered crystals are shown in Fig. 2.5. Two different crystal

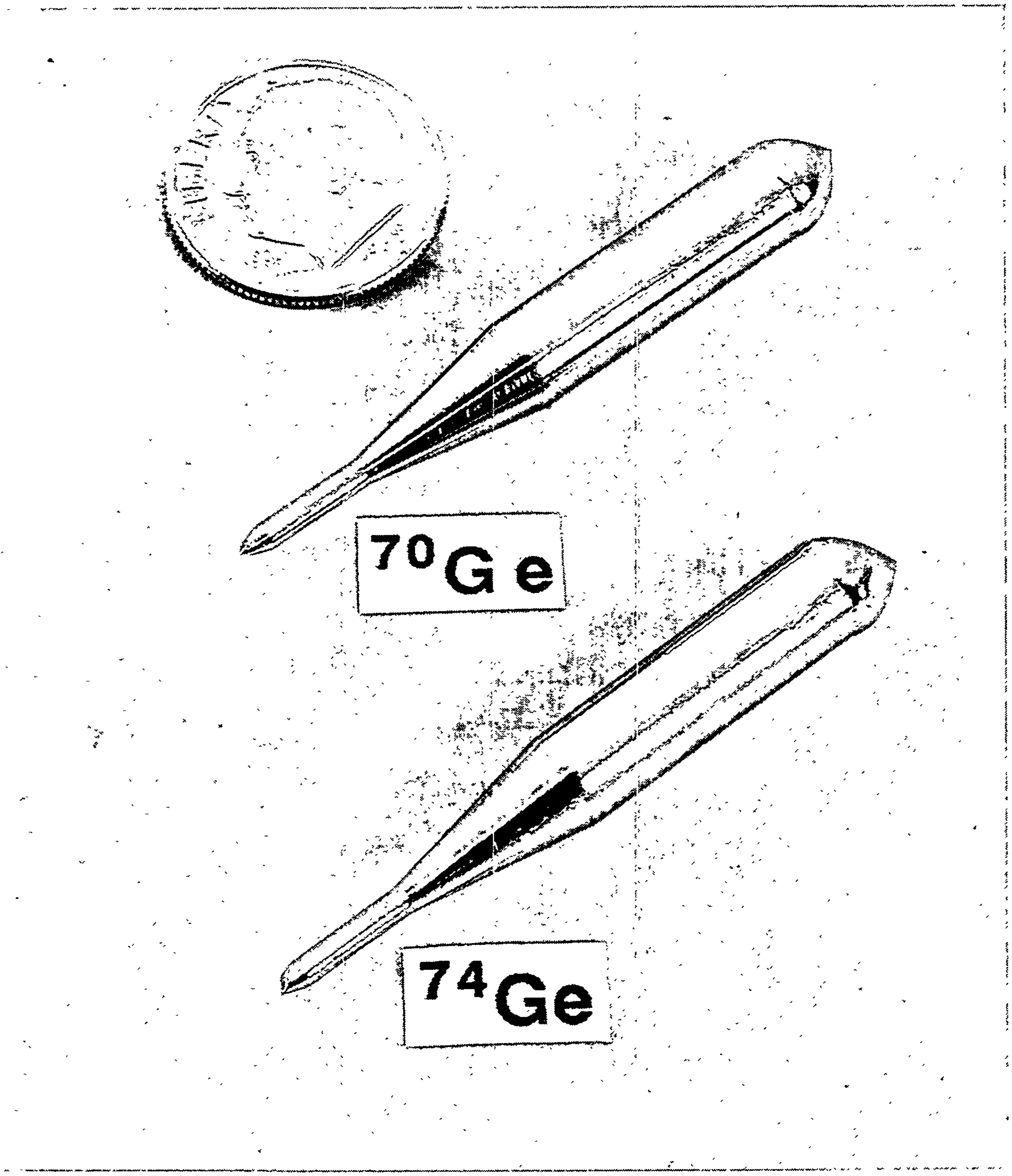

Fig. 2.4 Isotopically engineered Ge single crystals

profiles are shown as examples. Net-impurity concentrations as a function of position are found from resistivity measurements at T=77K described in the previous zone refining section (Sec. 2.2). Two profiles show that more than 70% of each crystal have a net-impurity concentration of the order of 10^{12} cm^{-3}. Note that one profile is entirely p-type while the other contains a p-n junction and is p-type near the growth tail end. The chemical identities of the residual impurities were determined from photothermal ionization spectroscopy (PTIS) measurements.[105] It was found that phosphorus and copper are dominant residual impurities in n and p-type regions of crystals, respectively.[99, 100] The dislocation density in typical crystals lies between 10^2 and 10^3 cm^{-2}.

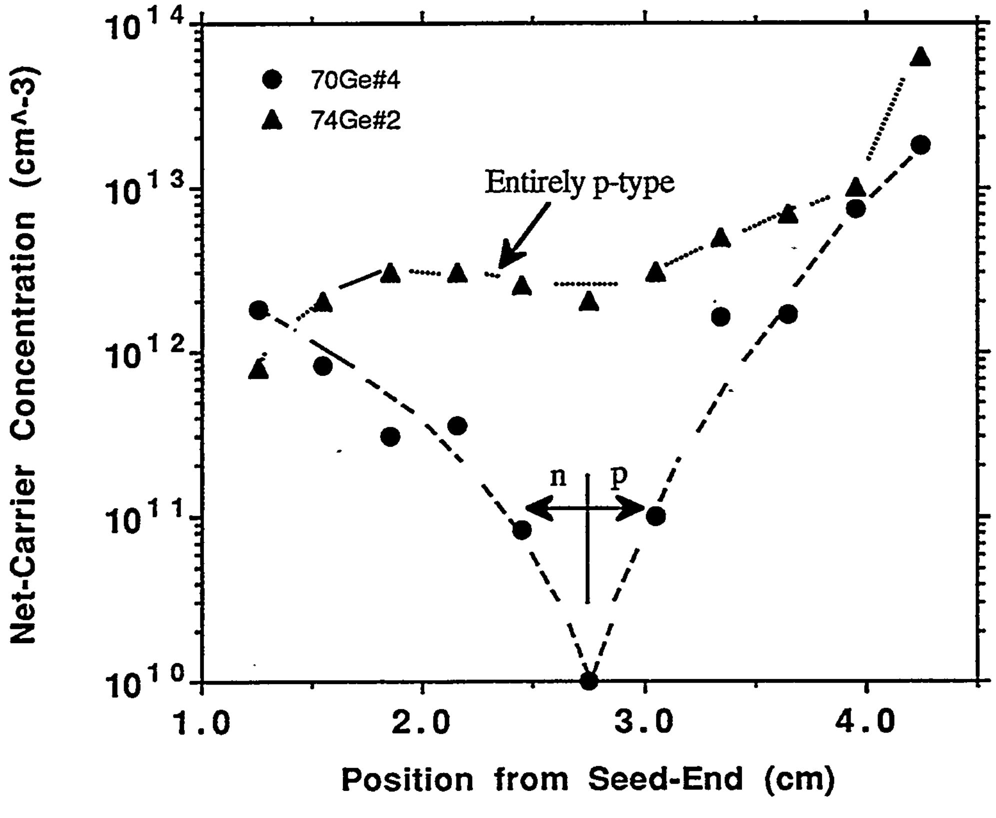

Fig. 2.5 Net-impurity concentration profiles in two isotopically engineered single crystals

Chapter 3 Neutron Transmutation Doping of Isotopically Engineered Ge

3.1 Neutron Transmutation Doping (NTD) of Semiconductors

3.1.1 Overview

The idea of producing semiconductors with perfectly uniform dopant distribution by neutron transmutation doping (NTD) was originally described by Lark-Horowitz in 1951.[106] As mentioned in section 1.3 the unrivaled doping uniformity is a result of the extent of the neutron field produced by a nuclear reactor which is many orders of magnitude larger than the typical semiconductor samples, the small capture cross section of semiconductor isotopes for neutrons minimizing "self-shadowing" and the perfect random distribution of the stable isotopes in the host semiconductor crystals. Nine years after Lark-Horowitz's paper Frizsche and Cuevas [107] produced NTD Ge of various net-impurity concentrations and performed a comprehensive electronic conductivity study on these materials. In order to change compensation, Cuevas [108] resorted to a combination of chemical doping and NTD thereby using some of the advantages offered by NTD. In 1974 the first technological application of NTD of Si was reported by Schnöller.[109] He demonstrated that the breakdown behavior of high voltage, high power rectifiers occurred over a much narrower range of voltages for NTD Si:P than in melt doped crystals. This improved performance was a result of the uniform phosphorus dopant distributions due to the reasons mentioned above. Today NTD of Si is still the dominating doping method for the fabrication of high-power, high-voltage rectifiers and thyristor devices. Approximately 150 tons of high-purity floating zone (FZ) silicon is doped by NTD every year for power device fabrication.[110] The current status and the future of Si NTD technology are presented in the recent review paper by von Ammon.[110]

As it was discussed in Sec.1.3, NTD has been extensively used for doping of Ge used in the fabrication of thermistors.[88, 89] NTD is the only doping technique which leads to low temperature Ge thermistors with reproducible properties, the most important aspect in the formation of thermistor arrays.

NTD compound semiconductors are yet to find their technological applications. NTD has been applied to GaAs [111-117], InP [114], and GaP [118, 119] for a number of basic studies.

Table 3.1 lists selected isotopes of interest for semiconductor research and technology with their thermal neutron capture cross sections and their neutron transmutation products. As one can see almost every semiconductor can be doped with NTD. Because of the limited number of stable isotopes and their nuclear reactions after thermal neutron capture, certain semiconductors can be doped with one type (n- or p-type) of dopants only. This is the case for Si and GaAs whose stable isotopes only decay to n-type dopants after capturing neutrons. The maximum phosphorus concentration in ^{Nat}Si produced by NTD is limited to ~10^{15}cm^{-3} due to the small abundance and thermal neutron capture cross section of the ^{30}Si isotopes. This maximum [P] can be increased by a factor of 33 by doping isotopically pure ^{30}Si crystals by NTD. NTD of isotopically controlled Ge allows the independent adjustment of the concentration of majority and minority dopants as will be described in Sec.3.3. Therefore, NTD of semiconductors becomes especially interesting and practical when isotopic control of the target materials is performed to control the resulting types of dopants.

Table 3.1 Abundances [120], thermal neutron capture cross sections [16] and neutron transmutation products of isotopes [16] related to semiconductor science and technology. (Data compiled by E.E. Haller, Lawrence Berkeley Laboratory and University of California)

Isotope	**Abundance (%)**	**Thermal neutron capture Cross section (10^{-24} cm^2)**	**Neutron transmutation product**
${}^{10}_{5}\mathrm{B}$	19.8	3838 (n,α) 0.52	${}^{7}_{3}\mathrm{Li} + {}^{4}_{2}\mathrm{He}$ ${}^{11}_{5}\mathrm{B}$
${}^{11}_{5}\mathrm{B}$	80.2	0.005	${}^{12}_{6}\mathrm{C}$
${}^{12}_{6}\mathrm{C}$	98.89	0.0034	${}^{13}_{6}\mathrm{C}$
${}^{13}_{6}\mathrm{C}$	1.11	9×10^{-4}	${}^{14}_{7}\mathrm{N}$
${}^{14}_{7}\mathrm{N}$	99.63	0.076	${}^{15}_{7}\mathrm{N}$
${}^{15}_{7}\mathrm{N}$	0.37	4×10^{-5}	${}^{16}_{8}\mathrm{O}$
${}^{16}_{8}\mathrm{O}$	99.76	1.78×10^{-4}	${}^{17}_{8}\mathrm{O}$
${}^{17}_{8}\mathrm{O}$	0.038	0.235 (n,α)	${}^{14}_{6}\mathrm{C} + {}^{4}_{2}\mathrm{He} \rightarrow {}^{14}_{7}\mathrm{N}$
${}^{18}_{8}\mathrm{O}$	0.204	1.58×10^{-4}	${}^{19}_{9}\mathrm{F}$
${}^{27}_{13}\mathrm{Al}$	100	0.231	${}^{28}_{14}\mathrm{Si}$
${}^{28}_{14}\mathrm{Si}$	92.23	0.17	${}^{29}_{14}\mathrm{Si}$
${}^{29}_{14}\mathrm{Si}$	4.67	0.10	${}^{30}_{14}\mathrm{Si}$
${}^{30}_{14}\mathrm{Si}$	3.10	0.11	${}^{31}_{15}\mathrm{P}$
${}^{31}_{15}\mathrm{P}$	100	0.18	${}^{32}_{16}\mathrm{S}$
${}^{32}_{16}\mathrm{S}$	95.02	0.53	${}^{33}_{16}\mathrm{S}$
${}^{33}_{16}\mathrm{S}$	0.75	0.095 (n,α)	${}^{30}_{14}\mathrm{Si} + {}^{4}_{2}\mathrm{He}$
${}^{34}_{16}\mathrm{S}$	4.21	0.24	${}^{35}_{17}\mathrm{Cl}$
${}^{36}_{16}\mathrm{S}$	0.017	0.15	${}^{37}_{17}\mathrm{Cl}$
${}^{64}_{30}\mathrm{Zn}$	48.6	0.78	${}^{65}_{29}\mathrm{Cu}$
${}^{66}_{30}\mathrm{Zn}$	29.7	1.0	${}^{67}_{30}\mathrm{Zn}$
${}^{67}_{30}\mathrm{Zn}$	4.1	7.0	${}^{68}_{30}\mathrm{Zn}$

$^{68}_{30}$Zn	18.8	0.88	$^{69}_{31}$Ga
$^{70}_{30}$Zn	0.62	0.098	$^{71}_{31}$Ga
$^{69}_{31}$Ga	60.1	1.7	$^{70}_{30}$Zn (0.2%) $^{70}_{32}$Ge (99.8%)
$^{71}_{31}$Ga	39.9	4.7	$^{72}_{32}$Ge
$^{70}_{32}$Ge	20.5	3.25	$^{71}_{31}$Ga
$^{72}_{32}$Ge	27.4	1.0	$^{73}_{32}$Ge
$^{73}_{32}$Ge	7.8	15.0	$^{74}_{32}$Ge
$^{74}_{32}$Ge	36.5	0.36	$^{75}_{33}$As
$^{76}_{32}$Ge	7.8	0.16	$^{76}_{34}$Se
$^{75}_{33}$As	100	4.4	$^{76}_{34}$Se
$^{74}_{34}$Se	0.89	52	$^{75}_{33}$As
$^{76}_{34}$Se	9.36	85	$^{77}_{34}$Se
$^{77}_{34}$Se	7.63	42	$^{78}_{34}$Se
$^{78}_{34}$Se	23.78	0.7	$^{79}_{35}$Br (very long half life ~6.5×10^{4} years)
$^{80}_{34}$Se	49.61	0.68	$^{83}_{36}$Kr
$^{106}_{48}$Cd	1.25	1.0	$^{107}_{47}$Ag
$^{108}_{48}$Cd	0.89	1.2	$^{109}_{47}$Ag (long half life 453 days)
$^{110}_{48}$Cd	12.49	11	$^{111}_{48}$Cd
$^{111}_{48}$Cd	12.80	24	$^{112}_{48}$Cd
$^{112}_{48}$Cd	24.13	2	$^{113}_{48}$Cd
$^{113}_{48}$Cd	12.22	1.98×10^{4}	$^{114}_{48}$Cd
$^{114}_{48}$Cd	28.73	0.34	$^{115}_{49}$In (95%) $^{115}_{50}$Sn (5%)
$^{116}_{48}$Cd	7.49	0.075	$^{117}_{50}$Sn
$^{113}_{49}$In	4.3	10.8	$^{114}_{50}$Sn (94.8%) $^{114}_{48}$Cd (5.2%)
$^{115}_{49}$In	95.7	202	$^{116}_{50}$Sn
$^{121}_{51}$Sb	57.36	6.2	$^{122}_{52}$Te (97%) $^{122}_{50}$Sn (3%)

$^{123}_{51}\mathrm{Sb}$	42.64	4.0	$^{124}_{52}\mathrm{Te}$ (20%) $^{124}_{50}\mathrm{Sn}$ (80%)
$^{120}_{52}\mathrm{Te}$	0.096	2.3	$^{121}_{51}\mathrm{Sb}$
$^{122}_{52}\mathrm{Te}$	2.603	3	$^{123}_{52}\mathrm{Te}$
$^{123}_{52}\mathrm{Te}$	0.908	400	$^{124}_{52}\mathrm{Te}$
$^{124}_{52}\mathrm{Te}$	4.816	6.7	$^{125}_{52}\mathrm{Te}$
$^{125}_{52}\mathrm{Te}$	7.139	1.6	$^{126}_{52}\mathrm{Te}$
$^{126}_{52}\mathrm{Te}$	18.95	1.0	$^{127}_{53}\mathrm{I}$
$^{128}_{52}\mathrm{Te}$	31.69	0.22	$^{129}_{53}\mathrm{I}$ (decays into $^{129}_{54}\mathrm{Xe}$ with a half life of 1.6×10^{7} years)
$^{130}_{52}\mathrm{Te}$	33.80	0.23	$^{131}_{54}\mathrm{Xe}$
$^{196}_{80}\mathrm{Hg}$	0.15	3120	$^{197}_{79}\mathrm{Au}$
$^{198}_{80}\mathrm{Hg}$	9.97	0.018	$^{199}_{80}\mathrm{Hg}$
$^{199}_{80}\mathrm{Hg}$	16.87	2000	$^{200}_{80}\mathrm{Hg}$
$^{200}_{80}\mathrm{Hg}$	23.10	<60	$^{201}_{80}\mathrm{Hg}$
$^{201}_{80}\mathrm{Hg}$	13.18	<60	$^{202}_{80}\mathrm{Hg}$
$^{202}_{80}\mathrm{Hg}$	29.86	5.0	$^{203}_{81}\mathrm{Tl}$
$^{204}_{80}\mathrm{Hg}$	6.87	0.4	$^{205}_{81}\mathrm{Tl}$

3.1.2 Fundamental Interactions of Thermal Neutrons with Materials

A neutron is a neutral particle with mass of 1.008665 amu (0.13% heavier than a proton). A free neutron is radioactive with a half-life of ~12.8 minutes and splits up into a proton, an electron and an electronic anti-neutrino. The most common type of nuclear reactor is so called fission reactor in which fissioning of $^{235}\mathrm{U}$ works as a neutron source. About 84% of all neutrons captured by $^{235}\mathrm{U}$ lead to fissioning of the uranium with emission of 2.5 neutrons on the average. The fission neutrons are fast neutrons with an average energy of about 2 MeV. These fast neutrons collide with the reactor materials, in particular the "moderator," and through loss of energy at each collision are slowed down to very slow or "thermal" neutrons which bounce around in thermal equilibrium with the environment. Thermal neutrons may be considered analogous to a gas in thermal equilibrium with the environment, with a Maxwellian velocity distribution n(v):

$$n\,(v) = 4\,\pi\,n_0 \left(\frac{m}{2\,\pi\,k_B\,T}\right)^{3/2} v^2 \exp\left(-\frac{m\,v^2}{2\,k_B\,T}\right) \qquad (3.1)$$

where n_0=total thermal neutron density and m=mass of a neutron. With this distribution the most probable neutron velocity at T=293K is 2198 m/sec which corresponds to 0.0253eV in energy. It is these thermal neutrons we make use of in neutron transmutation doping of semiconductors. Fast-neutrons, on the other hand, are unwanted since they create radiation damage and long life radio-active species which may interfere with some of the particle detections using NTD Ge bolometers.

Because neutrons have no electric charges they are very penetrating particles and are readily captured by the nuclei of atoms, i.e., neutrons are not subject to the repulsive electrostatic forces in the neighborhood of a positively-charged nucleus. Upon absorbing a neutron, a nucleus may become radioactive and decay into an isotope of a different element or simply become an isotope of the same element heavier by one neutron. From the NTD point of view there are three nuclear reactions of interest: α-decay, orbital electron capture, and β^- decay. *

Examples are:

$^{10}_{5}B + ^{1}_{0}n \rightarrow ^{4}_{2}He + ^{7}_{3}Li + 2.79MeV$ (α-decay)

$^{70}_{32}Ge + ^{1}_{0}n \rightarrow ^{71}_{32}Ge + e \rightarrow ^{71}_{31}Ga + \text{x-ray (Max.9.24keV)} + \nu_e$ (electron capture)

$^{74}_{32}Ge + ^{1}_{0}n \rightarrow ^{75}_{32}Ge + \gamma \rightarrow ^{75}_{33}As + \beta^- + \overline{\nu_e}$ (β^- decay).

where $^{1}_{0}n$ is the neutron, γ is the gamma ray, β^- is the beta particle, and ν_e and $\overline{\nu_e}$ are the electronic neutrino and anti-neutrino, respectively. In the case of the electron capture reaction, an electron from the K-orbital is absorbed with the largest probability by the Ge nucleus so that the reaction within a nucleus can be written as $p+e^- \rightarrow n+\nu_e$ where p is the

---

* β^+ decay is neglected since the elctron capture is the dominant $_{Z}X$ to $_{Z-1}X$ decay process in most NTD reactions.

proton, e^- is the electron, ν_e is the electronic neutrino. Similarly, the reaction within a nucleus for the case of β^- decay can be written as $n \rightarrow p + \beta^- + \overline{\nu_e}$.

Each stable isotope has a characteristic thermal capture cross section σ_c whose value depends on the incident neutron energy. Because thermal neutron spectra vary between different positions and different powers for each reactor, it is important to determine σ_c of a particular isotope for a fixed position and power of a reactor. After this is done one can reliably predict the concentration (N_0) of a nuclear reaction product:

$$N_0 = \rho\, \sigma_c\, n \qquad (3.2)$$

where ρ is the number of the particular isotope in a unit volume (cm^{-3}) and n is the thermal neutron fluence (cm^{-2}).

Assuming that a concentration N_0 of radioactive isotopes has been formed at time t=0, the concentration of isotopes N that have decayed by the time $t=t_1$ is given by:

$$N = N_0\,(1 - \exp(-\lambda\, t_1)) \qquad (3.3)$$

where λ is the decay rate of this particular unstable isotope. We now introduce the "half-life $T_{1/2}$" which is the time that takes for a half of the N_0 isotopes to decay after t=0, i.e.,

$$0.5\, N_0 = N_0\,(1 - \exp(-\lambda\, T_{1/2})) \qquad (3.4)$$

and

$$T_{1/2} = \ln 2 / \lambda. \qquad (3.5)$$

Thus Eq.3.3 becomes,

$$N = N_0\,(1 - \exp(-\ln 2\, t_1 / T_{1/2})). \qquad (3.6)$$

In actual semiconductor NTD processes, dopants are formed from the decay of N_0 unstable host semiconductor isotopes, i.e., the doping concentration as a function of the time after irradiation is given by Eq.3.6.

3.1.3 Fast Neutron Defect Creation During NTD of Semiconductors

So far I have discussed the transmutation of isotopes in materials due to low energy thermal neutrons. However, there are also fast neutrons that cannot be completely eliminated even with the aid of a moderator. A fast neutron with its high energy can cause structural defects in materials. Obviously we would like to minimize the defect production during our neutron transmutation doping of semiconductors. The simplest kind of defects produced by fast neutrons are the Frenkel (vacancy-interstitial) pairs. The number of Frenkel pairs formed per primary knock-on atom (PKA) ν can be estimated using the Kinchin-Pease model: [121]

$$\nu = \langle E_p \rangle / 2\, E_d \tag{3.7}$$

where $\langle E_p \rangle$ is the average energy transferred from the incident neutron to the struck atom and E_d is the displacement energy required to remove a host atom from its lattice site. Taking typical values for 2-MeV fast neutrons entering Ge ($\langle E_p \rangle \sim 0.05$MeV and $E_d \sim 27.5$eV), we find the number of Frenkel pairs per PKA to be ~900. This translates to a formation of ~10^{14} Frenkel pairs/cm^{-3} sec in Ge during our typical NTD process assuming a fast neutron flux of ~10^{11} cm^{-2} sec^{-1}. The time required to dope ^{70}Ge crystals with 10^{17}cm^{-3} Ga impurities is ~40 hours, i.e., ~10^{19} Frenkel pairs/cm^3 are produced in this NTD process. Note that the concentration of defects so far quoted neglects recombination of Frenkel pairs, a very efficient process at room temperature. It is also unlikely that all the fast neutrons which travel through a moderator have an energy of 2MeV. The actual defect density in our Ge after the NTD process will be significantly smaller. Also, damage created by neutrons is known to be far more extended than simple Frenkel defects due to the heavy mass of neutrons. This in turn leads to microscopically amorphous regions.

Fast neutron radiation defects in Ge have been studied by a number of researchers.[122-132] Many of the studies involved deep level transient spectroscopy (DLTS) [133] of defects in which the concentration and the electronic energy levels of defects were found without direct structural information.[124, 126, 129, 131, 132] It is the general consensus [123-125] that radiation-induced defects in Ge are vacancy related as opposed to interstitial related. Interstitials have high mobility so that recovery is fast even below room temperatures.[134] Evidence for donor-vacancy (D-V) complexes (hole traps at E_v+0.10eV) has been found in Ge γ-irradiation experiments.[122] There are a few additional studies which support the existence of the D-V complexes. In an infrared absorption study on NTD Ge, Park and Haller [127] have shown that the gallium acceptor levels appears at full concentration with no annealing after NTD while it takes at least 1 hour annealing at 450 °C for the arsenic donor levels to appear at full concentration. They showed that this is due to donor-radiation-defect complex formation. An electron-trap at E_c-0.36eV probably due to D-V complexes was also found by Nagesh and Farmer.[128] Erchak et al. [130] have studied the electron wavefunction symmetry of fast neutron defects in heavily doped ($2x10^{18}$-$3x10^{19}cm^{-3}$) Ge:Sb, Ge:P, and Ge:As using electron paramagnetic spin resonance (EPR). There spectra strongly suggest that donor-monovacancy pairs are dominant defects in n-type Ge irradiated with fast neutrons. Therefore many As donors in NTD Ge do not become electrically active due to the formation of D-V complexes. Thus appropriate thermal annealing is necessary to break those D-V complexes in order to activate As donors.

Although D-V pairs in irradiated Ge are quite well characterized, the structure of other more complicated defects caused by fast neutrons are not as well defined as in the case for most neutron damaged semiconductors. Park [135] has observed a two-dimensional disordered region, 10x10 atomic spacings in size, in NTD Ge using high resolution transmission electron microscopy (HREM). However, the electronic properties of these extended defects observed by Park are still unknown. Nagesh and Farmer [128] performed one of the few studies which focused on both the structure and the energy level of the neutron induced defects. By applying uniaxial stress to their samples during DLTS measurements, they have determined the symmetry of the electron trap at E_c-0.09eV, and proposed the defect to be a planar tetravacancy. To my knowledge, all the other micro-structural assignments of traps found in DLTS contain little structural information and the assigned defect structures are rather speculative. DLTS studies miss structural defects which are electrically neutral. Thus our understanding of fast neutron induced defects in Ge is far from complete.

It is not the aim of this thesis to identify various fast neutron induced defects in Ge. The main emphasis is on finding the necessary annealing condition such that the carrier transport in NTD isotopically engineered Ge is not affected by scattering due to the radiation defects. Such thermal annealing studies of fast neutron defects in Ge after NTD have been investigated by Palaio et al. [126] using mobility measurements at 77K and DLTS. They have measured the concentration of electronically active defects by DLTS after 400°C annealing of different durations (isothermal annealing). After 400°C-6hr annealing of NTD Ge with $1x10^{17}cm^{-2}$ thermal neutron fluence ($\sim 7x10^{15}cm^{-2}$ fast neutron fluence), they observed full recovery of the carrier mobility at 77K and found a concentration $\sim 10^{13}cm^{-3}$ of one type of major deep hole traps. This concentration of the defect is more than two order of magnitude smaller than the NTD produced net-impurity concentration ([Ga]-[As]-2[Se]) $\sim 2x10^{15}cm^{-3}$ in their samples. Annealing of the same NTD Ge at the same temperature (400°C) but for much shorter duration (3 hours) did not completely remove radiation defects and the mobility did not fully recover. A similar study arriving at the same conclusions was performed by Park.[135]

In this thesis I discuss samples of isotopically engineered Ge which received thermal neutron fluences as high as $4x10^{18}$ cm^{-2} which is factor of 14 larger than the samples discussed by Palaio et al. In these high dose cases, annealing temperatures much higher than 400°C (maximum 800°C) are necessary according to our experimental findings. We employed the rapid thermal annealing process ($t \leq 10sec$) for annealing temperature higher than 600°C, in order to suppress (i) indiffusion of undesirable impurities and (ii) diffusion of already uniformly distributed impurities created by NTD. The results of our annealing study will be presented in Sec.3.2.2.

3.2 Neutron Transmutation Doping of Isotopically Enriched ^{70}Ge and ^{74}Ge Crystals

The most interesting isotopes of Ge from the NTD point of view are ^{70}Ge and ^{74}Ge, since they decay into the well understood shallow impurities Ga and As, respectively. The objectives of this section are to:

(1) show that isotopically enriched ^{70}Ge and ^{74}Ge crystals can be doped with Ga and As, respectively, with small compensation ratios,

(2) determine precise neutron capture cross section σ_c for ^{70}Ge and ^{74}Ge isotopes for our specific irradiation condition, i.e., precise control of Ga and As concentrations becomes possible by using Eq. 3.2, and

(3) establish annealing conditions which remove the fast neutron damage to a level low enough for our various carrier transport studies.

3.2.1 Experimental

We have doped ~40 wafers of ^{70}Ge and ~20 wafers of ^{74}Ge over the past three years. Here we show NTD results of eight ~1mm thick wafers (four from crystal "^{70}Ge#7" and four from crystal "^{74}Ge#2") as typical examples. All wafers were irradiated at the University of Missouri Research Reactor. The thermal to fast neutron flux ratio is estimated to be 13:1. Low neutron dose samples (^{70}Ge#7-1 and ^{74}Ge#2-1) were annealed for 90 minutes at 450°C in flowing N_2 ambient, and the higher dose samples were rapidly annealed for 10 seconds at 650°C after the irradiation. The following section (3.2.2) describes our method for determining these annealing conditions in detail. Fig.3.1 shows the free hole concentration as a function of the time after irradiation of the sample ^{70}Ge-2.66. Each point (black square) was determined by a Hall effect measurement at 77K. Park et al. [127] have shown that all ^{71}Ga atoms transmuted from ^{71}Ge are electrically active at this low doping level after NTD. Thus assuming each newly formed ^{71}Ga atom contributes one free hole to the valence band and that there are no compensating donors, the time dependence of the free hole concentration N_h can be expressed by Eq.3.6:

$$N_h = N_{Ga} = N_{71Ge}\,[1- \exp(-t\ln 2 / T_{1/2})] \qquad (3.8)$$

where N_{Ga} is the concentration of ^{71}Ga created from ^{71}Ge decays, N_{71Ge} is the initial concentration of ^{71}Ge after irradiation, T is the time after the irradiation and $T_{1/2}$ is the half life of ^{71}Ge. Using Eq.3.8, the excellent theoretical fit to the experimental data shown in Fig.3.1 was obtained with $N_{71Ge}=(9.600\pm0.024)\times10^{14}$ cm^{-3} and $T_{1/2}=11.157\pm0.060$ days. The value of $T_{1/2}$ obtained is in remarkably good agreement with the published value of 11.2 days for ^{71}Ge→^{71}Ga decay.[16] This is a strong indication that ^{71}Ga atoms are the sole source of free holes in NTD ^{70}Ge samples.

Fig.3.2 (a) and (b) show the temperature dependence of the free carrier concentration in a series of NTD ^{70}Ge and ^{74}Ge samples measured by variable temperature Hall effect.

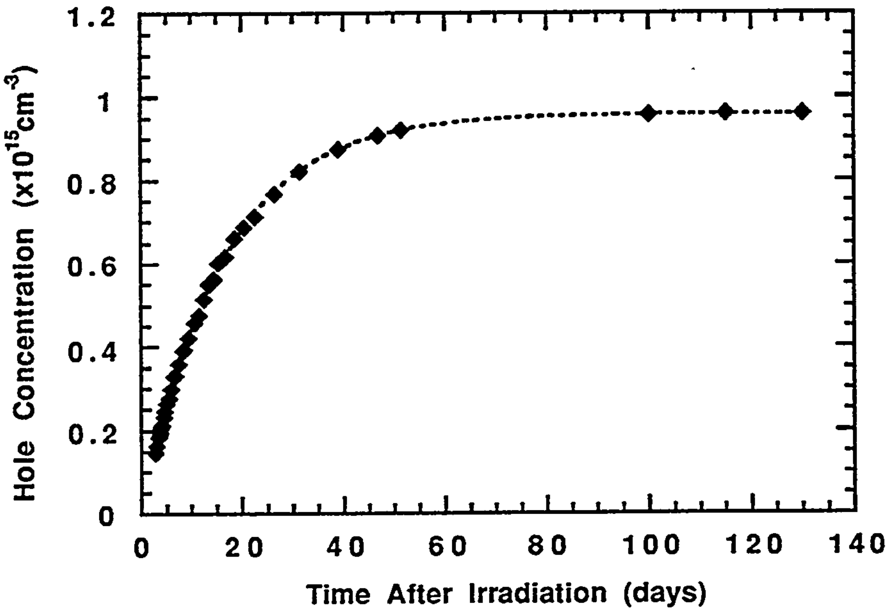

Fig.3.1 Free hole concentration in ^{70}Ge#7-2.66 as a function of time after irradiation

All NTD ^{70}Ge samples had completed >98% of the decay at the time of the measurement. The net-carrier concentrations and compensation levels for the lower concentration samples were determined by fitting the theoretical curves to the experimental data. We use standard semiconductor statistics which describes the temperature dependence of the free carrier concentration in semiconductors doped by shallow majority impurities and compensated by minority impurities: [136]

$$n(T) = 2\,(N_{MJ} - N_{MN}) \Big/ \Big\{ [1+(N_{MJ}/gN_B)\exp(E_{MJ}/k_BT)] + \sqrt{[1+(N_{MN}\, gN_B)\exp(E_{MJ}/k_BT)]^2+(4/gN_B)(N_{MJ}-N_{MN})\exp(E_{MJ}/k_B T)} \Big\} \quad (3.9)$$

where n(T) is the free electron (hole) concentration, N_{MJ} and N_{MN} are the majority and minority impurity concentration, respectively, N_B is the effective conduction (valance) band density of states, g=1/2 (g=4) is the spin degeneracy for a donor (acceptor), and E_{MJ} are the experimentally determined ionization energies: 14meV and 11.07meV for As and Ga, respectively. For the low dose samples (^{70}Ge#7-1 and ^{74}Ge#2-1), 450°C for 1.5 hour annealing was sufficient to remove the radiation defects to the point where good theoretical fits were obtained for our Hall data. However, it was only after 650°C, 10 seconds rapid thermal annealing that good fits were obtained for the higher dosage samples, ^{70}Ge#7-2 and ^{74}Ge#2-2. Higher free carrier concentration samples could not be fitted with Eq.3.9 because additional conduction mechanisms began to play a role (ε_2 or hopping*). This made it impossible to determined the compensation level in these samples. Table 3.2 shows the neutron fluence and resulting dopant concentration measured by Hall effect in eight samples studied in this section.

The typical compensation ratio in NTD ^{70}Ge:Ga and ^{74}Ge:As is less than 0.01 for Ga or As doping concentrations between 10^{14} and 10^{16} cm^{-3}. Compared to the residual impurity concentration before NTD ([P]~2x10^{12}cm^{-3} and [Cu]~2x10^{12}cm^{-3}), the residual donor concentration in ^{70}Ge:Ga samples increases by a factor of 2-3 after NTD and

---

* See Sec.4.1 for the review of these conduction mechanisms.

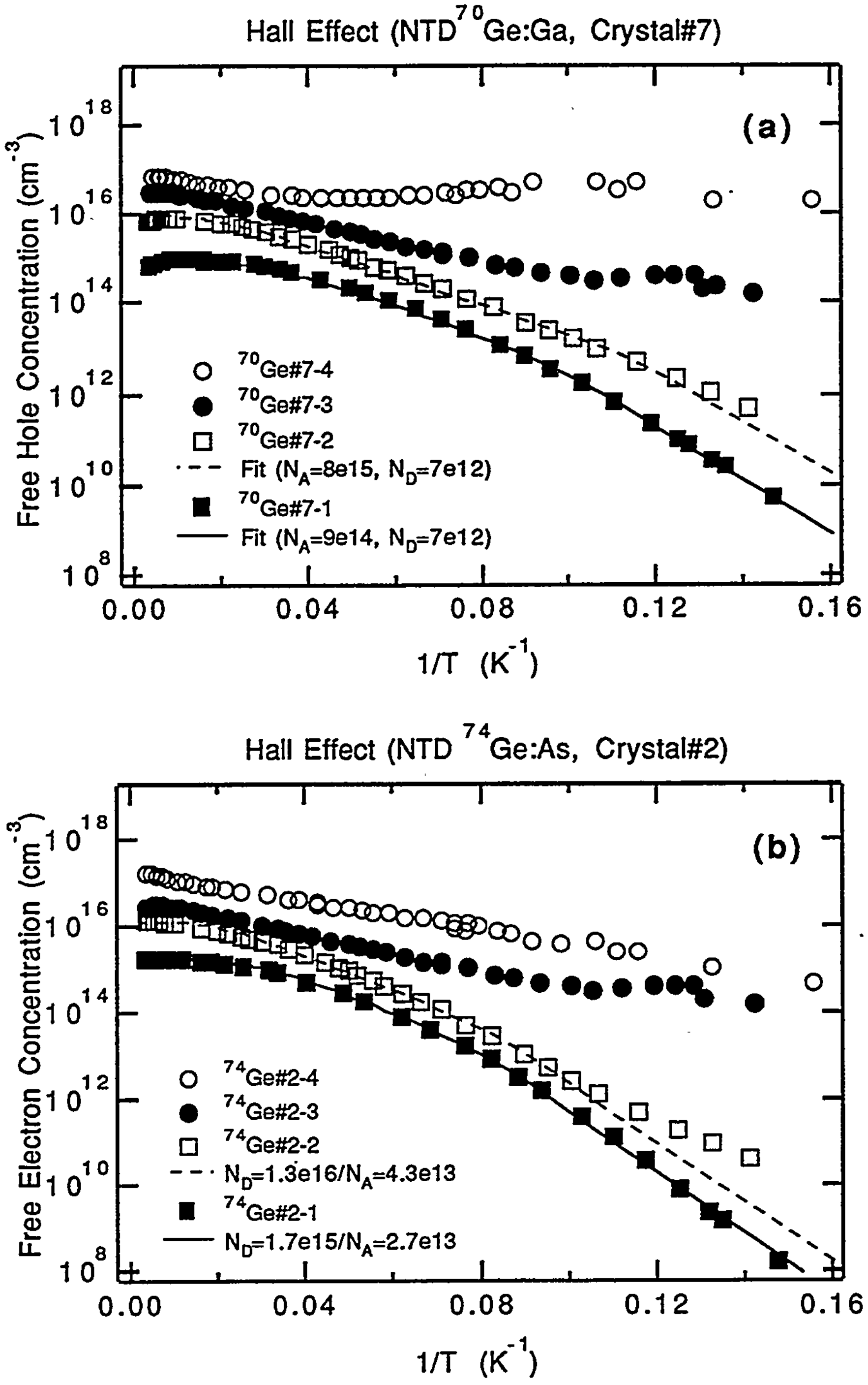

Fig.3.2 Temperature dependence of free carrier concentration in a series of (a) four NTD ^{70}Ge:Ga and (b) four NTD ^{74}Ge:As samples.

Table 3.2 Summary of NTD ^{70}Ge and ^{74}Ge samples

Sample	Thermal neutron fluence (cm^{-2})	Dopant concentration after irradiation (cm^{-3})
^{70}Ge#7-1	7.407×10^{15}	9.60×10^{14}
^{70}Ge#7-2	7.431×10^{16}	8.28×10^{15}
^{70}Ge#7-3	2.963×10^{17}	3.02×10^{16}
^{70}Ge#7-4	7.407×10^{17}	8.00×10^{16}
^{74}Ge#2-1	6.018×10^{16}	1.60×10^{15}
^{74}Ge#2-2	6.018×10^{17}	1.43×10^{16}
^{74}Ge#2-3	2.454×10^{18}	6.10×10^{16}
^{74}Ge#2-4	6.064×10^{18}	1.80×10^{17}

annealing, and the residual acceptor concentration in the ^{74}Ge:As samples increases by a factor of 2 or more after NTD and annealing. Further investigations have shown that the compensation level in various NTD ^{70}Ge:Ga samples increases with neutron fluence while that of various ^{74}Ge:As samples is almost independent of the fluence. Because our 650°C, 10sec rapid thermal annealing process usually introduces ~$1\text{-}3\times10^{12}$cm^{-3} Cu triple acceptors, the compensating centers in NTD ^{74}Ge:As are most likely copper impurities that are introduced during the post NTD thermal annealing. On the other hand the nature of the compensating donor centers in NTD ^{70}Ge:Ga is not understood.

Fig.3.3 (a) and (b) show far infrared transmission spectra of ^{70}Ge#7-1 and ^{74}Ge#2-1. All absorption lines exactly correspond to ground state to bound excited state transitions of Ge:Ga and Ge:As, respectively.[137] No other shallow impurity absorption line was observed within our detection limit of ~10^{12}cm^{-3}. The transmission measurements were repeated under continuous band edge light illumination of the samples in order to identify the minority shallow impurities in both samples. However, no minority shallow impurities could be detected in either sample at a concentration >10^{12} cm^{-3}. Thus the compensating centers in both samples must be relatively deep, and may be copper or radiation damage related.

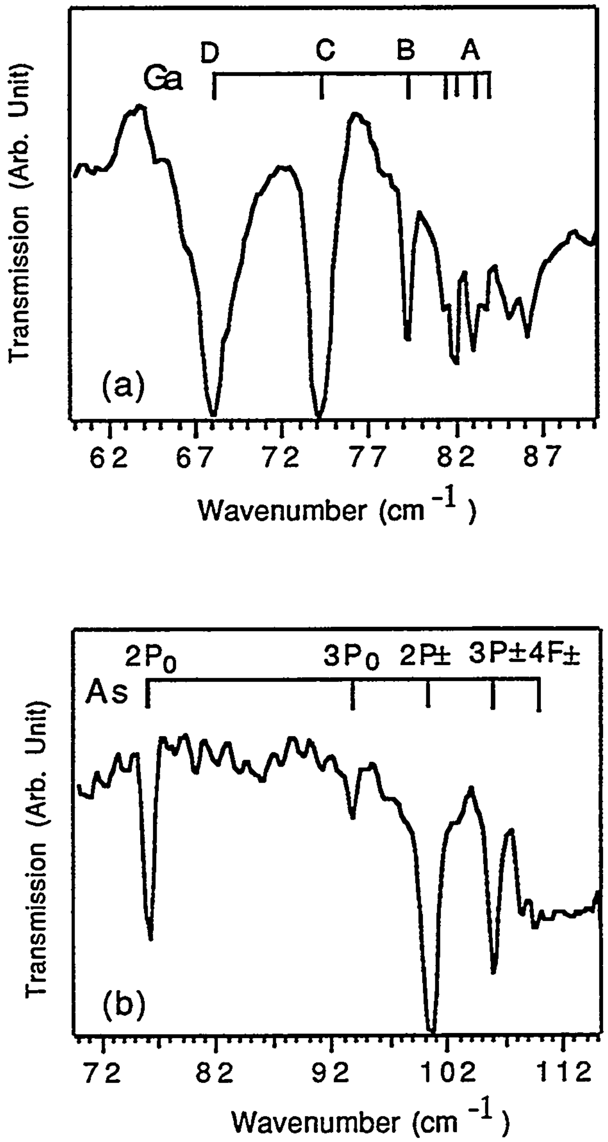

Fig.3.3 Infrared transmission spectra of samples (a) ^{70}Ge:Ga [sample#7-1] and (b) ^{74}Ge:As [sample #2-1]

Finally the thermal neutron capture cross section σ_c of ^{70}Ge and ^{74}Ge isotopes for our specific irradiation condition is statistically determined by evaluating more than 40 NTD ^{70}Ge:Ga and 20 ^{74}Ge:As samples. Using Eq.3.2 with $\rho=4.38\times10^{22}\times$(fraction of ^{70}Ge or ^{74}Ge isotopes) we obtain:

$$\sigma_c\,(^{70}\mathrm{Ge}) = 2.74\pm0.08\times10^{-24}\ \mathrm{cm}^2 \qquad (3.10)$$

$$\sigma_c\,(^{74}\mathrm{Ge}) = 4.82\pm0.03\times10^{-25}\ \mathrm{cm}^2. \qquad (3.11)$$

The average σ_c for ^{70}Ge and ^{74}Ge listed in Ref.16 are 3.25 and 0.52×10^{-24}cm^2, respectively. The σ_c we measured differ from these reported values by 10-20%. This demonstrates the importance of the determining thermal neutron cross-sections for each irradiation condition. The cross-sections given by Eq.3.10 and 3.11 are used in Sec.3.3 where we discuss studies of crystals of ^{70}Ge and ^{74}Ge isotopes that are mixed to control the compensation ratio.

3.2.2 Annealing of Fast Neutron Induced Defects in NTD ^{70}Ge:Ga and ^{74}Ge:As

Defects of concern in this thesis are those which affect carrier transport properties. Results of a DLTS study are reported first since they show the concentration and the energy levels of deep centers. NTD ^{70}Ge:Ga and ^{74}Ge:As samples with a majority impurity concentration ~10^{15}cm^{-3} were used for this study. In general, it is difficult to perform DLTS on Ge with net-impurity concentration larger than 5×10^{15} cm^{-3} due to large leakage current through the rectifying contacts. Therefore low temperature conductivity measurements were used to probe the annealing of compensating centers in the higher concentration samples. Conductivity due to banding of the dopant wavefunctions (ε_2)* in nearly uncompensated materials is known to be very sensitive to the material's compensation level.

---

* A description of the ε_2 conduction mechanism will given in Sec.4.1.

Fig.3.4 shows the DLTS spectra of two NTD Ge samples after 650°C-10sec annealing in a flowing N_2 atmosphere. One sample is NTD ^{70}Ge:Ga with [Ga]~$1x10^{15}cm^{-3}$ with the compensation ratio K~0.01 and the other is NTD ^{74}Ge:As with [As]~$1x10^{15}cm^{-3}$ with K~0.01. The ^{70}Ge:Ga and ^{74}Ge:As received ~$8.7x10^{15}cm^{-2}$ and ~$4.9x10^{16}cm^{-2}$ fluence of thermal neutrons, respectively. The fast neutron fluence is 1/13 of the thermal neutron fluence. Because of our normal reverse bias DLTS condition, we are probing only the same type (p- or n-type) of defects as the majority shallow impurities, i.e., deep electron-traps in ^{74}Ge:As and deep hole traps in ^{70}Ge:Ga. A detailed description of the DLTS technique is given elsewhere.[133, 138] In Fig.3.4 there is only one distinctive peak in the ^{74}Ge:As spectrum while there are two in the ^{70}Ge:Ga spectrum. The concentration and the energy of the deep donor centers in ^{74}Ge:As are ~$5x10^{12}cm^{-3}$ and E_c-0.38eV, respectively. This energy level of the donor-like defect corresponds to that of well characterized D-V pairs. Therefore about 0.5% of the As impurities are electrically inactive as shallow donors due to As-V pair formation. The lager peak in the ^{70}Ge:Ga spectrum is

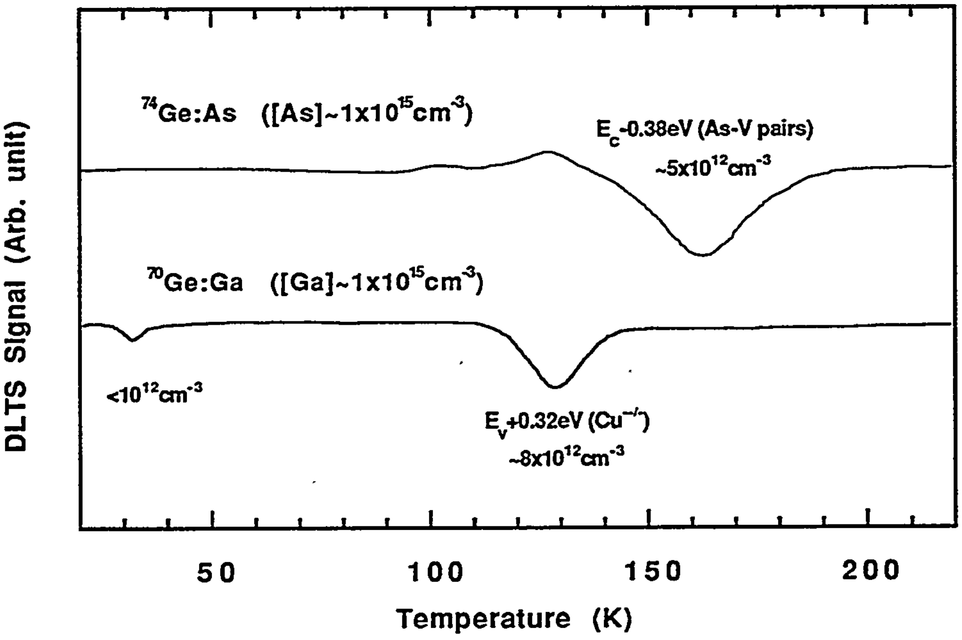

Fig.3.4 DLTS spectra of NTD ^{70}Ge:Ga and ^{74}Ge:As samples after 650°C, 10 seconds annealing

due to a deep acceptor with a concentration of ~8×10^{12}cm^{-3} and an energy level E_v+0.32. This energy corresponds precisely to that of substitutional Cu impurities (Cu$^{-/--}$). Typically this concentration of Cu impurity is introduced during our rapid thermal annealing at 650°C for 10 seconds. Unfortunately we could not obtain the energy level of the shallower peak which corresponds to a concentration less than 10^{12}cm^{-3}. However this defect concentration is less 0.1% of the Ga concentration and will be neglected. We are yet to perform DLTS measurements under the forward bias condition to probe the presence of compensating deep defects. It is expected that the ^{74}Ge:As sample contains a similar amount of Cu impurities after rapid thermal annealing. On the other hand we do not expect a significant concentration of D-V pairs in the ^{70}Ge:Ga sample for there are less than 10^{13}cm^{-3} shallow donors in this sample. Rapid thermal annealing at various temperatures was also performed and the same peaks as in Fig.3.4 were found for annealing above 600°C. However the concentration of the Cu increases almost exponentially with the temperature above T=650°C. The DLTS spectra of samples with T<600°C-10sec annealing show a superposition of many unresolved peaks indicating many different deep levels. An annealing temperature larger than 600°C is necessary to remove these levels when one employs short annealing times of the order of 10 seconds.

Now we shall review the low temperature resistivity behavior of NTD Ge. Fig.3.5 (a) and (b) show the temperature dependent resistivities of NTD ^{70}Ge:Ga and ^{74}Ge:As samples, respectively, after two different annealing procedures: 550°C for 2 hours and 650°C for 10 seconds. The thermal neutron fluence of 7×10^{17}cm^{-2} produced 8×10^{16}cm^{-3} Ga impurities in the ^{70}Ge:Ga sample while 3.4×10^{19}cm^{-2} thermal neutrons produced 7×10^{16}cm^{-3} As in the ^{74}Ge:As sample. The difference in the resistivity due to the two annealing conditions appears only at low temperatures. The low temperature resistivity after 650°C-10sec annealing is lower than that of after 550°C-2hr annealing in both the ^{70}Ge:Ga and the ^{74}Ge:As samples. Because both samples have extremely small

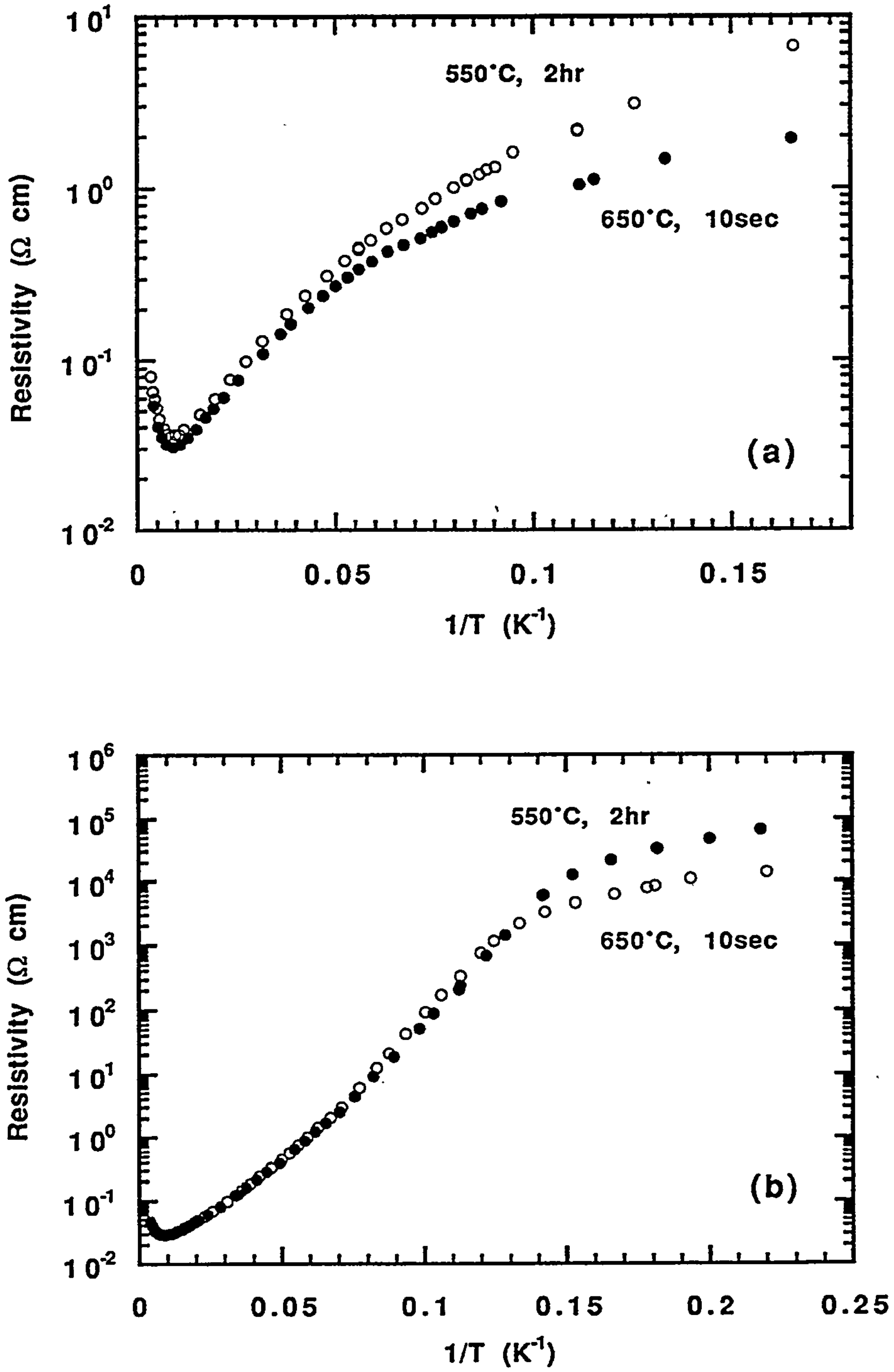

Fig.3.5 Temperature dependent resistivity in (a) NTD ^{70}Ge:Ga and (b) NTD ^{74}Ge:As samples after two different annealing processes: 550°C for 2 hours and 650°C for 10 seconds.

compensations (K<1%), so called "ε_2 conduction" * is the most likely the dominant conduction mechanism in the low temperature regime shown in Fig.3.5. As I will explain in Sec.4.1, the ε_2 resistivity decreases when the compensation becomes small. Therefore, from the lowering of the low temperature resistivity, we conclude that the 650°C-10sec annealing removed more compensating centers than the 550°C,-2hr annealing. Further annealing of the same samples at higher temperatures and/or longer durations does not lead to any further significant change of the resistivity. Fig.3.6 compares the resistivity of the NTD ^{Nat}Ge:Ga,As sample #11 ($1.7\mathrm{x}10^{18}\mathrm{cm}^{-2}$ thermal neutron fluence) after two different annealing conditions: 400°C for 6 hours and 650°C for 10 seconds. The former annealing condition was found to be appropriate for NTD ^{Nat}Ge:Ga,As by Palaio et al.[126] Both resistivity curves agree very well even in the lowest temperature regime. This result can be understood when one considers the effect of the compensation ratio on the carrier transport. The dominant low temperature conduction mechanism in NTD ^{Nat}Ge is "hopping conduction" rather than "ε_2 conduction" because of the high compensation ratios (K~0.32). The change in the hopping resistivity ρ as a function of the compensation K at K~0.32, i.e., $(d\rho/dK)_{K=0.32}$, is very small.[139] Therefore, the difference between two annealing processes does not appear in the resistivity even if the 650°C-10sec annealing removes more compensating centers than the 400°C-6hr annealing. On the other hand the annealing of the NTD ^{70}Ge:Ga and ^{74}Ge:As samples at 400°C for 6 hours leads to much higher low temperature resistivities than those of the 650°C-10sec annealing. This is due to the large $(d\rho/dk)_{K\sim0}$ of ε_2 conductivity. Therefore the 400°C-10sec annealing is insufficient for NTD ^{70}Ge:Ga and ^{74}Ge:As with small compensation ratios.

We thus conclude that the 650°C-10sec rapid thermal annealing is the optimum choice for elimination of defects in NTD Ge of all kinds. Annealing at higher temperature does not further reduce damage related centers but it introduces larger amount of detrimental triple acceptors Cu in the sample.

---

* A description of the ε_2 conduction mechanism will given in Sec.4.1.

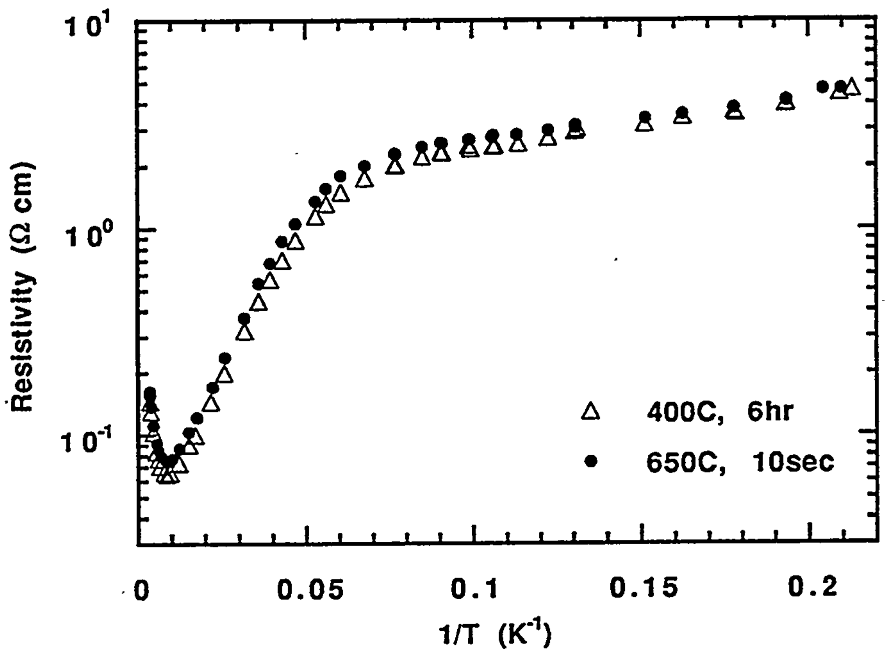

Fig.3.6 Temperature dependent resistivity of NTD ^{Nat}Ge #11

3.3 NTD of Isotopically Engineered Ge - Independent Control of the Net-Impurity Concentrations and the Compensation Ratios

Many solid state experiments require extremely homogeneous doping and precise control of both majority and minority impurity concentrations (N_{MJ} and N_{MN}). The ability to precisely control both the net-impurity concentration $N_{Net}=N_{MJ}-N_{MN}$ and the compensation ratio $K=N_{MN}/N_{MJ}$ in bulk Ge is also important for the development of the NTD Ge thermistors as discussed in Sec.1.2. (It is important to recognize that controlling N_{Net} and K is equivalent to controlling N_{MJ} and N_{MN}.)

In this section I describe the production of p-type Ge samples of various compensation ratios as a natural extension of the previous section. N-type samples of K between 0 and 1 can be produced simply by choosing the concentration of ^{74}Ge accordingly.

The experimental procedure is the following. Crystals consisting of controlled mixtures of ^{70}Ge and ^{74}Ge were grown from pieces cut from zone refined isotopically enriched ^{70}Ge and ^{74}Ge bars of isotopic compositions given in Table 2.1. A detailed description of our crystal growth method has been discussed in Sec.2.3. The mass ratio of the ^{70}Ge and ^{74}Ge starting charges determines the [^{74}Ge]/[^{70}Ge] ratio in our crystals:

$$\frac{[^{74}\mathrm{Ge}]}{[^{70}\mathrm{Ge}]}=\frac{5.13\ \mathrm{g/cm^3}\times(\text{Mass of the }^{74}\text{Ge piece})\times 96.3\%}{5.43\ \mathrm{g/cm^3}\times(\text{Mass of the }^{70}\text{Ge piece})\times 96.8\%}\ . \tag{3.12}$$

Volume densities 5.13 and 5.43 g/cm^3 for our ^{70}Ge and ^{74}Ge bars, respectively, are used in accordance with the composition shown in Table 2.1. We also assume that the number of Ge atoms per unit volume is the same for ^{70}Ge and ^{74}Ge, because the measured isotope shift of the Ge lattice constant is negligibly small.[63] Prior to growth, the ^{70}Ge and ^{74}Ge pieces were melted together in a RF heated ultra-pure graphite boat, in order to assure complete mixing of the different isotopes. After growing seven Ge crystals with different [^{74}Ge]/[^{70}Ge] ratios, a 1mm thick wafer was cut from each crystal (samples A~G in Table 3.3) and their isotopic compositions were measured by secondary ion mass spectroscopy (SIMS). Uniform isotope distribution throughout the crystals was confirmed by comparing the isotopic composition at both ends of several crystals. All wafers were then thermal neutron irradiated for exactly the same duration, four hours, at University of Missouri Research Reactor. The thermal neutron flux at the irradiation position was $6.43\mathrm{x}10^{12}$ cm^{-2} sec^{-1}. The irradiated wafers were annealed for 10 seconds at 650°C in a N_2 atmosphere to eliminate electrically active radiation defects formed by unavoidable fast neutrons. After seven half-lives of the ^{71}Ge to ^{71}Ga decay reaction, the temperature dependence of the free hole concentration was measured by Hall effect in order to determine the Ga and As concentrations in each sample.

Table 3.3 shows the isotopic composition measurement results obtained by SIMS. The [^{74}Ge]/[^{70}Ge] ratios in the range from 0 to 4.34 agree well with the values we estimated with Eq.3.12. We can predict the concentration N_0 (cm^{-3}) of Ga and As for a given thermal neutron fluence n (cm^{-2}) for each sample by inserting the measured isotopic composition values into Eq.3.2. The thermal neutron capture cross section values used for the ^{70}Ge and ^{74}Ge isotopes are the same as Eq.3.10 and 3.11, respectively. The predicted concentrations, shown in Table 3.3, are to be compared with the [Ga] and [As] measured by the Hall effect.* Fig.3.7 shows the temperature dependence of the free hole concentration in samples A~G. A magnetic induction of 3000 Gauss was used for all measurements and a Hall factor of unity (high magnetic field limit) is assumed for T<100K. Eq.3.9 is used to fit freeze out each curve. E_{MJ} of Ga in Ge is 11.07meV for [Ga]<10^{15}cm^{-3} samples, but it decreases when [Ga]>10^{15}cm^{-3}.[140] Therefore, in the first step of our fitting procedure, we set N_{MJ} and N_{MN} equal to the [Ga] and [As], respectively as given by our SIMS results. E_{MJ} is used as a fitting parameter in Eq.3.9. By this method, excellent fits are obtained for samples A, D, and E with E_{MJ}=9meV, 9.7meV, and 9.8meV, respectively, as shown in Fig.3.7. Deviations of the experimental results for T>100K and for the very low temperature region are due to deviations of the Hall factor from 1 and the onset of hopping conduction, respectively. The predicted net-acceptor values [Ga]-[As] also agree very well with the Hall measurements in samples F and G. However, in the T<20K region the freeze-out curve can not be fitted, possibly due to hopping conduction or again to the deviation of the Hall factor from 1. In the case of samples B and C, the predicted values of [Ga] and [As] needed to be modified slightly in order obtain a good fit. It appears that sample B has received ~30% more thermal neutrons than the other samples, i.e., [Ga]-[As] is 30% larger than the predicted value. Nevertheless the compensation ratio of sample B precisely matches with the prediction.

---

* See Appendix D for a description of the Hall effect measurement.

Table 3.3 Summary of SIMS composition measurement and predicted and measured impurity concentrations after a 4 hour neutron irradiation

Sample	Isotope composition measured by SIMS (in At.%)						Predicted concentrations after NTD based on SIMS results (in x10^{15} cm^{-3})				Fitted concentrations after NTD (in x10^{15} cm^{-3})			
	^{70}Ge	^{72}Ge	^{73}Ge	^{74}Ge	^{76}Ge	$\frac{[^{74}\mathrm{Ge}]}{[^{70}\mathrm{Ge}]}$	[Ga]	[As]	[Ga]-[As]	K	[Ga]	[As]	[Ga]-[As]	K
A	96.3	3.7	--	--	--	0	17.0	--	17.0	~0	17.0	0.2	16.8	0.012
B	65.8	2.6	0.7	30.7	0.2	0.47	7.30	0.60	6.70	0.082	9.41	0.77	8.64	0.082
C	32.9	1.5	1.4	64.0	0.2	1.94	3.65	1.25	2.40	0.34	3.95	1.35	2.6	0.34
D	29.5	1.2	1.5	67.6	0.2	2.29	3.27	1.32	1.95	0.40	3.27	1.32	1.95	0.40
E	25.5	1.1	1.8	71.3	0.3	2.80	2.83	1.39	1.49	0.49	2.83	1.39	1.49	0.49
F	21.8	0.9	1.7	75.4	0.2	3.46	2.42	1.47	0.95	0.61	2.42	1.47	0.95	0.61
G	18.2	0.8	1.7	79.0	0.3	4.34	2.02	1.54	0.48	0.76	2.02	1.54	0.48	0.76

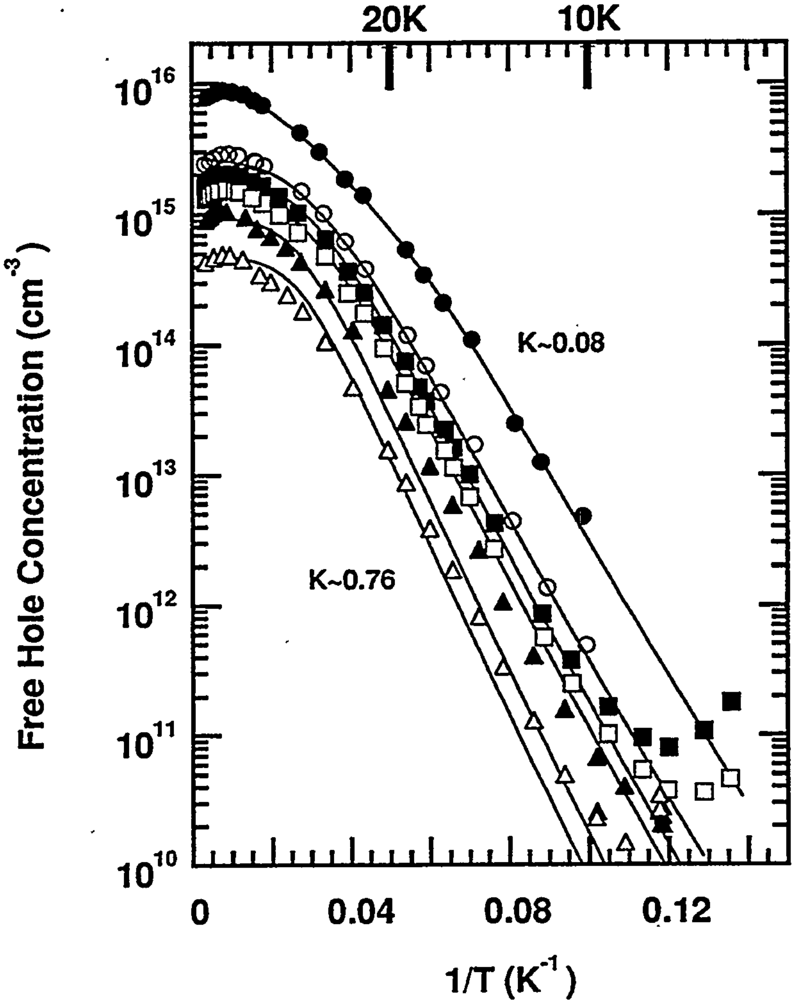

Fig.3.7 Temperature dependence of the free hole concentration in samples B(●), C(○), D(■), E(□), F(▲), and G(△). Solid curves are fits obtained from Eq.3.9.

After the modification fits were obtained for samples B and C with E_{MJ} of 9meV and 9.3meV, respectively. Because the effect of hopping conduction is very small even at 10K, the measurement error in N_{MJ} and N_{MN}, i.e., [Ga] and [As] obtained by fitting is minimal for samples B and C.

Values of [Ga] and [As] obtained by fitting the Hall results after NTD are listed in Table 3.3. The predicted compensation ratios from the SIMS results agreed perfectly with the measured compensation after NTD for all samples except for Sample A. There is a large uncertainty in the [As] of Sample A obtained from the fit due to the effect of hopping conduction. The values of [Ga] and [As] calculated from Eq.3.12 agree very well with the fitted values obtained from Hall measurements. Thus our proposed method, the neutron transmutation doping of isotopically controlled Ge, is proven to be an effective approach of controlling both N_{Net} and K in Ge.

In summary, we have shown that the combination of neutron transmutation doping and isotopic control of Ge leads to predictable and highly uniform majority and minority dopant concentrations in Ge. The measured temperature dependence of the free hole concentration curves in all p-type samples agree very well with the theoretical fits, i.e., all samples doped by NTD in this section must have extremely homogeneous majority and minority impurity distributions. This new approach to obtain precise and uniform dopant concentrations is promising for a range of solid state studies that will be discussed in Sec.4.

Chapter 4 Transport Studies

4.1 Carrier Transport in Semiconductors

One differentiates between three distinctive conduction mechanisms in semiconductors: free carrier conduction, ε_2 conduction, and hopping conduction. Which mechanism becomes dominant depends on the temperature and the type of a sample (dopant species, concentration, compensation level, etc.). Dominant conduction mechanisms in different temperature ranges can be found by inspecting the temperature dependent resistivity ρ. In the following two sections (Sec.4.1.1 and Sec.4.1.2) I will describe basic free carrier transport theories and other conduction mechanisms.

4.1.1 Free Carrier Transport in Semiconductors

Fig.4.1 (a) and (b) schematically show examples of the temperature dependence of the carrier concentration and resistivity of a moderately doped and compensated semiconductor. For simplicity we shall discuss a semiconductor which contains a shallow

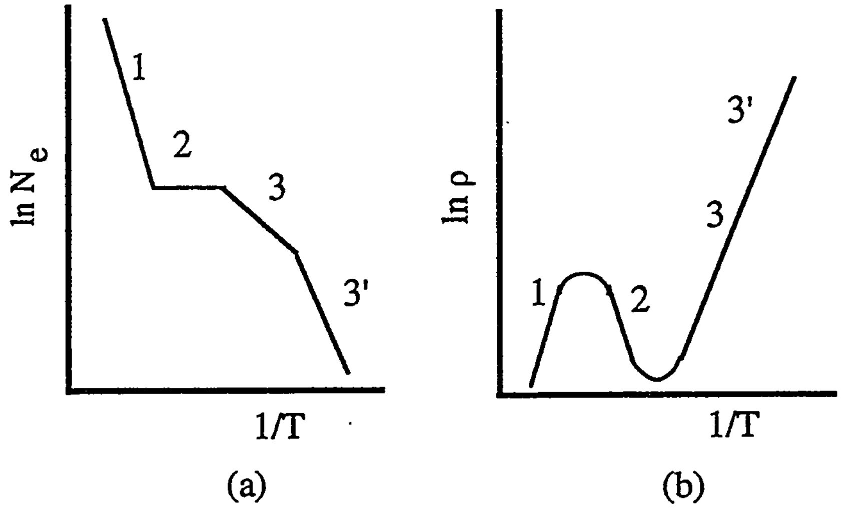

Fig.4.1 Temperature dependence of the (a) carrier concentration and (b) resistivity of a moderately doped and compensated semiconductor.

donor impurity concentration N_D with a lower concentration of compensating acceptors N_A. The compensation ratio is defined as N_A/N_D. The inverse ratio is used for p-type semiconductors.

Segment 1 in Fig.4.1: High temperature region ($k_BT>E_g$, E_g: energy gap)

This is the intrinsic region where the temperature is high enough to excite electrons from the valence band to the conduction band to create free electrons and holes in excess of the dopant related electrons. The number of free electrons and holes overwhelm the number of extrinsic carriers, and the slope of ln N_e vs. 1/T in Fig.F.1 (a) is proportional to $E_g/2k_B$.

The resistivity ρ is given by;

$$\rho = (N_e\, e\, \mu_e)^{-1} + (N_h\, e\, \mu_h)^{-1} \tag{4.1}$$

where N_e and N_h are the free electron and hole concentrations, e is the charge and $\mu_{e,h}$ are the mobilities of electrons and holes, respectively. Due to the rapid decrease in the free carrier concentration, the resistivity increases as the temperature decreases.

Segment 2-3' in Fig.4.1: Extrinsic region

Temperature dependence of the free carrier concentration in this region is quantitatively given by well known semiconductor statistics Eq.3.9. The qualitative description of the important features in a freeze-out curve is given here.

The plateau of segment 2 in ln N vs. 1/T is due to the extrinsic carrier concentration which exceeds the intrinsic free carrier concentration. The temperature is too low to create a large concentration of intrinsic free carriers but sufficient to ionize the net-donor impurities ($k_BT>E_D$, E_D: donor ionization energy ~10meV for Ge). Thus the carrier concentration stays constant at N_D-N_A.

In segment 3 the temperature becomes so low that the thermal energy is no longer sufficient to maintain the ionization of all donor impurities ($k_BT\leq E_D$). As the temperature is lowered, the carrier concentration decreases. The behavior of the ln N_e vs.1/T curve strongly depends on compensation level. If the material is uncompensated, the slope is proportional to $E_D/2k_BT$ throughout segment 3. If the material is compensated ($N_A \neq 0$), the slope is proportional to $E_D/2k_BT$ in the temperature range for which $N_e > N_A$. For $N_e < N_A$ the slope is proportional to E_D/k_BT. In Fig. F.1 (a) segment 3 has a half slope ($\propto E_D/2k_BT$) while 3' has a full slope ($\propto E_D/k_BT$). The change in slope occurs at the minority impurity concentration level N_A.

Because $N_D >> N_A$ in segment 2-3', the second term in Eq.4.1 becomes negligibly small, i.e., resistivity is simply given by:

$$\rho = (N_e\, e\, \mu_e)^{-1}. \tag{4.2}$$

Therefore measurements of N_e and ρ as a function of temperature (typically by Hall effect) allows us to find a parameter of this thesis's interest the "low field mobility* μ_e as a function of temperature". The free electron mobility in n-type Ge at T=300K is limited by a combination of many different scattering mechanisms: optical deformation potential, acoustic deformation potential, intervalley, and ionized impurity scattering. Theoretical calculation of the mobility at room temperature is quite involved since some of the scattering processes are inelastic. At low temperatures (T<100K) only three elastic scattering mechanisms play important roles: acoustic deformation potential, ionized impurity, and neutral impurity scattering. In this case one can calculate the mobility with a relatively straight forward method called "relaxation time approximation". A mathematical description of the three scattering mechanisms and relaxation time approximation is given in Appendix B.

Fig.4.2 (a) shows three typical mobility curves that are due to acoustic deformation potential (μ_{AC}), ionized impurity (μ_I), and neutral impurity (μ_N) scattering in a *highly compensated sample*. The temperature segments shown at the top correspond to those in Fig.4.1. μ_{AC} is one of the intrinsic properties of a semiconductor and does not depend on

---

* The term "mobility" refers to the low-field mobility in this thesis.

impurity concentrations ($\mu_{AC} \propto T^{-3/2}$ at all T). Values of μ_I and μ_N, on the other hand, are strongly affected by the nature and the concentration of impurities.

In <u>segment 2</u>, the neutral impurity concentration N_N is zero (since all donors are ionized), i.e., μ_N is infinitely large. The ionized impurity concentration N_I is constant ($\sim N_D+N_A$), i.e., μ_I decreases with T ($\mu_I \propto T^{3/2}$) since slower electrons are scattered more efficiently*. However, μ_{AC} stays much lower than μ_I and μ_N. Therefore acoustic phonon deformation potential scattering is always the dominant scattering mechanism in segment 2.

In <u>segment 3</u> carriers start to freeze-out and N_N which is given by $N_D-N_A-N_e$ increases due to the decrease in N_e, i.e., μ_N decreases. On the other hand N_I that is given by N_e+2N_A decreases with T due to decrease in N_e, i.e., μ_I increases. The values of μ_{AC} and μ_I become comparable. μ_N is significantly larger than μ_{AC} and μ_I.

In <u>segment 3'</u> N_e becomes negligibly small ,i.e.,N_N becomes constant at N_D-N_A. Neutral impurity scattering is an isotropic scattering process and its rate in the first order approximation does not depend on the velocity of electrons, i.e., μ_N becomes temperature independent. N_I also becomes constant at $2N_A$ since $N_e<<N_A$,i.e., $\mu_I \propto T^{3/2}$ as in segment 2. Unless the semiconductor is very pure, $\mu_{AC} >> \mu_I$ and μ_N in this lowest temperature segment. The relative contributions of μ_I and μ_N again are determined by the value of N_A; when N_A is large μ_I becomes smaller than μ_N which is the case shown in Fig.4.2 (a).

Fig.4.2 (b) shows the total mobility μ_T in the system when the three independent mobilities shown in Fig.4.2.(a) are combined using Matthiessen's rule: [141]

$$\mu_T^{-1} = (\mu_{AC}^{-1} + \mu_I^{-1} + \mu_N^{-1})^{-1}. \tag{4.3}$$

Segment 2 of the total mobility curve has a slope proportional to $T^{-3/2}$ because phonon scattering dominates in this temperature range. On the other hand segment 3' is dominated by ionized impurity scattering ($\mu_T \propto T^{3/2}$) since the sample in this particular example is highly compensated. Because of the large N_A, the number of N_I is larger than N_N in

---

* Electrons in our case are in thermal equilibrium with the system, i.e., lower the temperature, smaller is the drift velocity of these electrons.

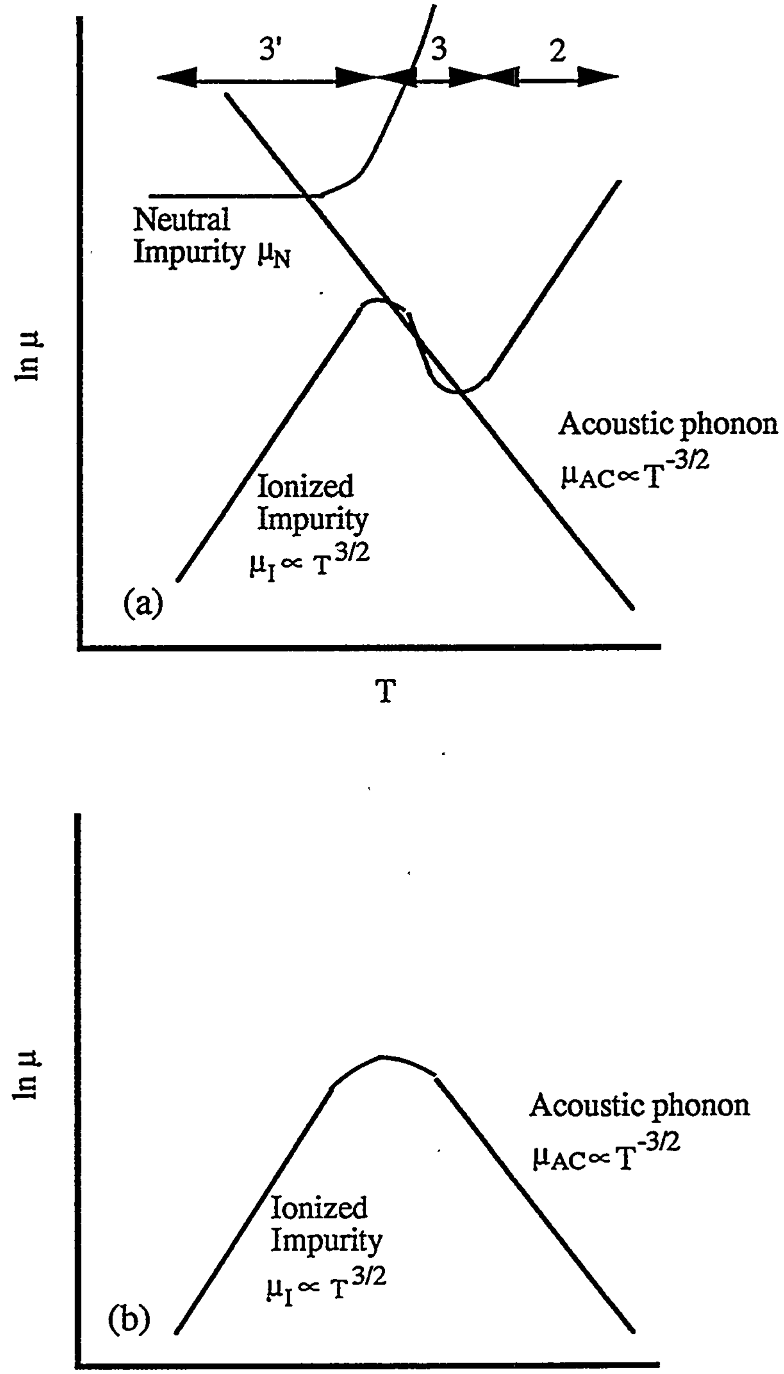

Fig.4.2 (a) Three mobility curves due to acoustic deformation potential, ionized impurity, and neutral impurity scattering, and (b) total mobility curves obtained from combining the three mobility curves in (a).

segment 3, i.e., μ_I dominates over μ_N. When a sample is nearly uncompensated, N_A is small enough so that the condition $\mu_N<\mu_I$ is established in segment 3'. This particular case is shown in Fig.4.10. μ_T keeps increasing with decreasing T following μ_{AC} of $\propto T^{-3/2}$ until μ_N limits the mobility at the lowest T. One can see from the above discussion that the low temperature mobility is very sensitive to the compensation level N_A. Therefore the ability to control the compensation ratio K ($=N_A/N_D$) is crucial for a study of low temperature carrier transport properties.

4.1.2 ε_2 and Hopping Conduction

When the dopant concentration in a semiconductor is relatively low, the thermal excitation of carriers from the donor levels to the conduction band generates the conducting electrons. However, when a semiconductor is moderately to highly doped ($>10^{15}$cm^{-3} for Ge), completely different conduction mechanisms begin to dominate at very low temperatures. In these transport mechanisms, electrons (holes) do not get excited to the conduction (valance) band; instead they conduct between states that are in the energy gap. Since they are not "free" carriers, N_e or N_h become irrelevant parameters for these

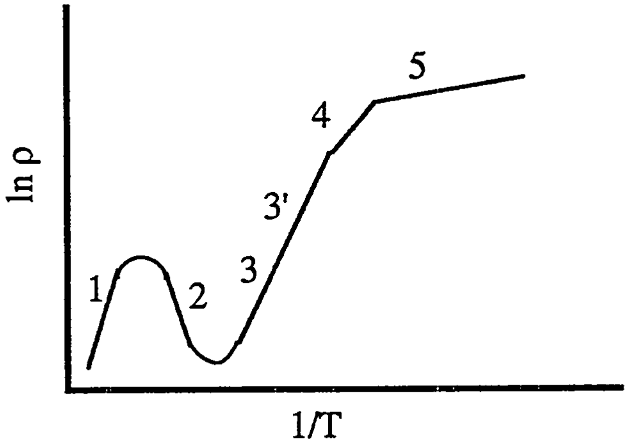

Fig.4.3 Resistivity vs. 1/T in doped semiconductors

conduction mechanisms. Thus we shall only look into the temperature dependent resistivities ρ . Fig.4.3. is same as Fig.4.1 (b) except we now have new segment 4 and 5 in the lower temperature end.

Segment 4 in Fig.4.3: ε_2 conduction.

When a semiconductor contains a relatively large concentration of impurities ($3\times10^{17}>N_D-N_A\geq10^{16}cm^{-3}$ for Ge) with very little compensation, so called "ε_2 conduction" dominates. Electrical conduction in this case is no longer due to free carriers in the conduction band, but is due to electrons excited to the so called "upper Hubbard" band. Gershenzon et al. [142] showed that neutral donors in Ge can bind a second electron (the D^- state) with a binding energy of the order of $0.1E_D$. This is analogous to the formation of H^-. Because the binding energy of the state is small, the D^- state has a very large Bohr radius. The overlap of D^- wavefunctions leads to an energy band at the energy between the donor levels and conduction band minima (CB) as shown in Fig.4.4. Since $\varepsilon_2<E_D$, this conduction mechanism dominates at lower temperatures at which normal freeze

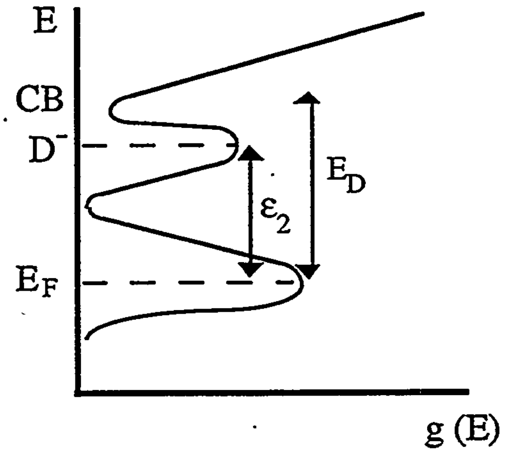

Fig.4.4 Density of states of the D^- band and the activation energy for the ε_2 conduction

out would occur otherwise. In order for this ε_2 conduction to occur, the donor concentration must be high enough so that D^- states can overlap. Also the low compensation ratio is favorable for the ε_2 conduction since compensation reduces the number of electrons in the donor states and decreases the probability for D^- state formation.

Segment 5 in Fig.4.3: Hopping conduction regime.

Further decrease in temperature may lead to the occurrence of hopping conduction. Whether or not it occurs depends on the donor and acceptor impurity concentrations. When these impurity concentrations are sufficiently high ($3X10^{17}>N_D-N_A\geq10^{15}cm^{-3}$ for Ge), electrical conduction is due to hopping of electrons between donor impurity sites. The resistivity slope changes in segment 5 of Fig.4.3 are due to hopping conduction.

At the high temperature side of the hopping conduction regime, one usually observes "nearest neighbor hopping."

Hopping of electrons occurs between an occupied and an unoccupied donor sites. Fig.4.5 shows the example of electrons hopping from occupied sites to the nearest unoccupied sites. In order to create a number of unoccupied donor sites, it is necessary to have compensating acceptors. Electrons prefer the lowest possible energy states hence electrons at donor sites choose to "fall" into all available acceptor sites. This is the essence of "compensation". Once unoccupied states are created, electrons are able to jump into them from the nearest occupied states. This is called nearest-neighbor hopping conduction. Notice that donor states next to each other take slightly different energy levels due to the Pauli exclusion principle and the fluctuation of the potential arising from the compensating centers. The resistivity can be expressed as

$$\rho = \rho_0 \exp\left(\frac{E_A}{k_B T}\right) \tag{4.4}$$

where E_A is the activation energy for the hopping, ρ_0 the constant pre-factor.

In the lowest temperature regime, where the available thermal energy is less than the nearest-neighbor hopping activation energy E_A, electrical conduction occurs by electrons

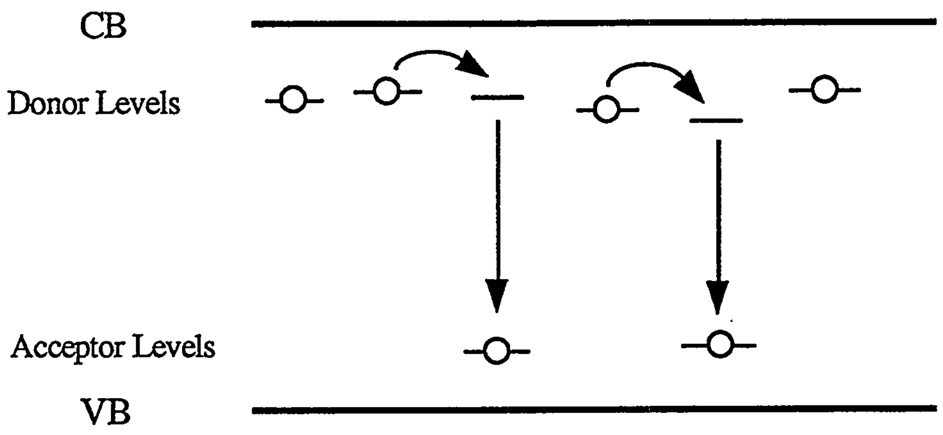

Fig.4.5 Nearest neighbor hopping conduction in n-type semiconductors

jumping to sites which are energetically in reach, though they may be much further away. This is called variable range hopping conduction. The mechanism is shown in Fig.4.6. Each electron sitting on the donor site "looks" for an empty donor site into which the electron can hop with the available thermal energy k_BT. In Fig.4.6 the electron at site 1 finds the state at site 6 to be within energy k_BT; so it can hop from site 1 to 6, whereas site 5 is out of the available k_BT range even though it is closer than site 6. The theory of variable range hopping conduction predicts the following temperature dependence of resistivity: [96, 143]

$$\rho = \rho_0 \exp\left(\frac{T_0}{T}\right)^n \quad \text{where } n = \frac{1}{4} \text{ or } \frac{1}{2} \tag{4.5}$$

n = 1/4 or 1/2 is determined by the shape of the impurity band density of states g(E) around the Fermi level E_F. Fig.4.7 (a) shows Mott's original assumption that the density of states around E_F is nearly constant.[143, 144] In this case n=1/4. Efros and Shklovskii [96, 145] later proposed the presence of a "Coulomb gap E_{CG}" which is parabolic around E_F with density of states being zero at E_F (Fig.4.7.(b)). E_{CG} arises due to long range Coulomb interactions between electrons. With $g(e) \sim |E-E_F|^2$, Efros and Shklovskii obtained n=1/2. A derivation of Mott's and Efros-Shklovskii's equations is given in Appendix C. Variable range hopping conduction of both n=1/4 and 1/2 have been observed in various semiconductor systems. It is generally believed now that the parabolic Coulomb gap is always present in every doped semiconductors. n=1/4 is observed when the hopping (or thermal) energy is larger than E_{CG} so that the presence of the gap can be neglected. Only the n=1/2 behavior has been observed in n- and p-type Ge, showing a strong effect of the Coulomb gap. It is therefore important to understand the shape and width of the Coulomb gap in doped Ge semiconductors for thermistor development.

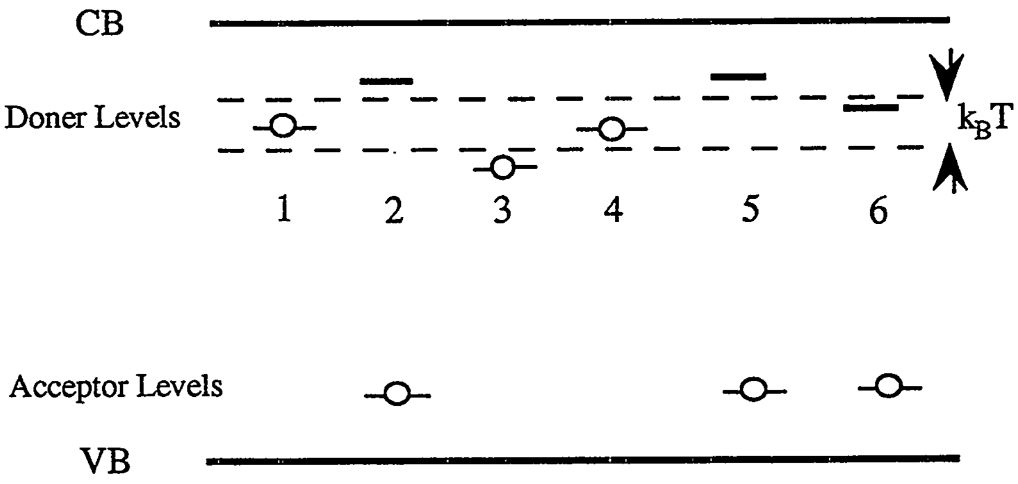

Fig.4.6 Variable range hopping conduction in n-type semiconductors

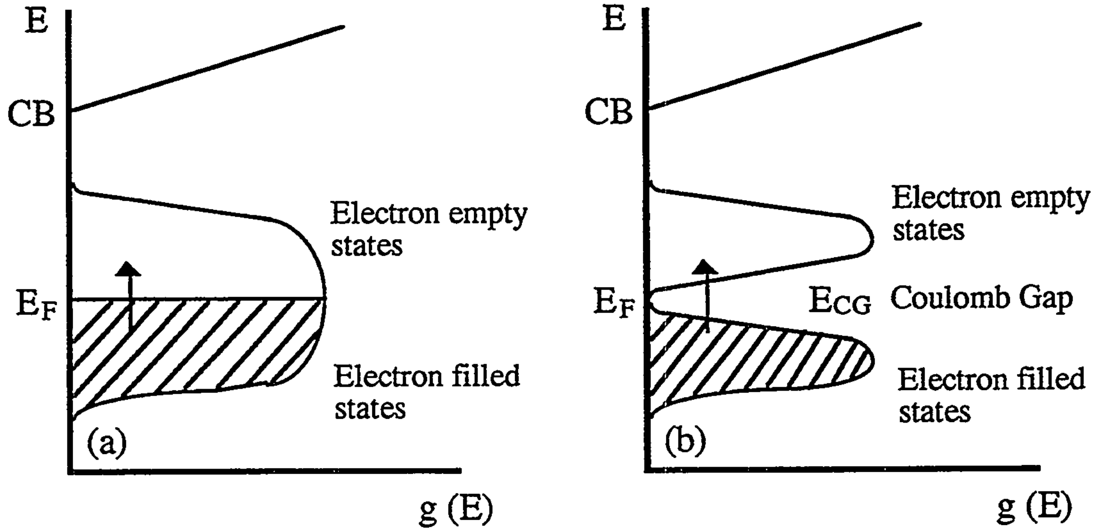

Fig.4.7 Two models of the donor impurity band density of states proposed (a) by Mott and (b) by Efros and Shklovskii. .

4.2 Neutral impurity scattering

4.2.1 Introduction

As explained in the previous section the low temperature mobility of free carriers in semiconductors is mainly determined by ionized and neutral impurity scattering. The ionized impurity scattering mechanism in semiconductors has been extensively studied [146], and various aspects of this process especially in lightly compensated semiconductors are now quite well understood. Scattering by neutral impurities is much less effective than by ionized centers, i.e., its contribution is significant only in crystals with low compensation and at very low temperatures where most of the free carriers are frozen on the impurity sites.

Good examples of devices in which the neutral impurity scattering mechanism becomes important are extrinsic semiconductors for infrared photoconductors (Ge:Ga, Ge:Zn, Ge:Be, Ge:Cu, Si:B, etc. [83, 147]) that are widely used by astrophysicists [148] and condensed matter scientists.[149] Because photoconductor materials are typically nominally uncompensated and are operated at low temperatures (T<10K), understanding of the mobility dominated by neutral impurity scattering is crucial for the development and modeling of these infrared detectors.

Theoretical research on neutral impurity scattering has been active since 1950. [150-155] Following the progress of the theory, a few experimental studies probing the nature of neutral impurity scattering were published.[156-159] However, for these experiments it was necessary to introduce adjustable parameters to obtain good agreement between the experimental results and theory. Consequently, there still exists no solid experimental verification for the theoretical models of the neutral impurity scattering rate.

In order to clearly discern the effects of neutral impurities on the carrier mobility, one has to reduce or eliminate the much more efficient ionized impurity scattering. This can be realized only in uncompensated materials. Furthermore, since the standard scattering models assume a random distribution of scattering centers, it is very important that the impurities are uniformly distributed in the samples. These conditions are not easily achievable with standard doping techniques where considerable compensation and / or non-uniform impurity distributions are frequently observed.

In this work, in order to satisfy the very strict materials requirements for our neutral impurity scattering experiment, we have applied the NTD technique to isotopically enriched ^{70}Ge and ^{74}Ge samples. As previously explained the NTD method leads to very uniform impurity distributions down to the atomic level. This homogeneous dopant distribution turns out to be a crucial factor for the success of the neutral impurity scattering experiment as I will show in the results and discussion section.

The main objective of this section is to compare directly experimentally measured Hall mobilities with theoretical mobilities calculated without any adjustable parameters.

4.2.2 Theory

A. Neutral Impurity Scattering

In 1950 Erginsoy [150] was first to realize that the neutral impurity scattering cross sections in semiconductors can be derived by taking electron-hydrogen (e^--H) scattering cross sections in free space and modifying them to semiconductors by scaling the electron mass and the dielectric constant. Unfortunately the exact e^--H cross sections in free space were not available to Erginsoy at the time. He took approximate e^--H results of Massey and Moiseiwitsch [160] and calculated the inverse relaxation time τ^{-1}, the scattering rate, for neutral impurity scattering using the phase shift method: [150]

$$\tau_{\text{neutral}}^{-1} = \frac{20\,\kappa\,N_N\,\hbar^3}{m^{*2}\,e^2} \qquad (4.6)$$

where κ is the dielectric constant, e is the electron charge, N_N is the neutral impurity concentration, and m^* is the electron effective mass. A description of the phase shift method and a derivation of Eq.4.6 are given in Appendix B. Eq.4.6 can be considered only as a first order approximation because the pre-factor 20 is an empirically determined constant and only the lowest order s-partial-wave is taken into account in the phase shift calculation. Anselm [151] and Sclar [152] later attempted to improve Erginsoy's calculation by including over-charged H^- state which might become important at low temperatures. Sclar also derived an expression which relates τ^{-1} in semiconductors to the phase shifts of e^--H scattering: [161]

$$\tau^{-1}_{\text{neutral}} = 2\pi N_N v \frac{2}{k^2} \sum_{l=0}^{\infty} (l+1) \sin^2(\delta_l - \delta_{l+1}) \tag{4.7}$$

where v is the velocity of an incident electron, k is the wavenumber, and δ_l is the *l*th partial phase shift. Nearly exact phase shift calculations of e^--H scattering were finally performed in 1961 by Tamkin and Lamkin [162] and Schwartz.[163] These calculations included scattering for singlet and triplet states. Blagosklonskaya et al. [159] scaled these results to semiconductors and obtained cross sections which turned out to be appropriate only when the incident electron energy was less than 1/100 of the binding energy of a scattering center. McGill and Baron [160] used the results of Sclar (Eq.4.7) in the form:

$$\tau^{-1}_{\text{neutral}} = \frac{4\pi N_N \hbar\ e^2}{2\kappa m^* E_B} \sum_{l=0}^{\infty} \frac{(l+1)}{4 w^{1/2}} \left[3 \sin^2(\delta_l^- - \delta_{l+1}^-) + \sin^2(\delta_l^+ - \delta_{l+1}^+)\right] \tag{4.8}$$

where E_B is the binding energy of the scattering centers, $w \equiv E/E_B$ where E is the incident electron energy, and δ_l^+ and δ_l^- are the *l*th partial phase shift for the singlet and triplet states, respectively. By inserting δ_l^+ and δ_l^- (l =0-2) of e^--H scattering calculated by Tamkin and Lamkin [162] into Eq.3, McGill and Baron graphically showed the accurate τ^{-1} as a function of w for neutral impurity scattering in semiconductors.[154] McGill and Baron's result has been considered as an appropriate model for neutral impurity scattering in semiconductors and has been discussed in detailed in many standard text books.[164] Later Meyer and Bartoli reevaluated the problem and provided an analytical expression that is essentially the same as the graphical solution of McGill and Baron but covering a wider incident electron energy range: [155]

$$\tau_{\text{neutral}}^{-1} = \frac{A(w)\,\kappa\,N_N\,\hbar^{3}}{m_H^{*2}\,e^2} \tag{4.9.a}$$

$$\text{with}\quad A(w) = \frac{35.2}{w^{1/2}}\frac{(1+e^{-50w})(1+80.6w+23.7w^2)}{(1+41.3w+133w^2)}\left[\frac{1}{w}\ln(1+w)-\frac{(1+0.5w-1.7w^2)}{(1+w)^3}\right]. \tag{4.9.b}$$

Here m_H^* is the hydrogenic effective mass given by:

$$m_H^* = \frac{E_B\,\kappa^2\,m_0}{E_{Hy}} \tag{4.10}$$

where m_0 is the electron rest mass and E_{Hy}=13.6eV is the binding energy of hydrogen. In their original treatment Meyer and Bartoli used square conductivity effective mass m_{con}^{*2} instead of m_H^{*2} in the denominator of Eq.4.9.a. The two effective masses in the denominator of Eq.4.9.a. have two different origins: one is the mass of an incident electron and the other is the mass of a bound electron at the scattering center. For this reason it may look appropriate to use m_{con}^* times m_H^* instead of m_H^{*2}. However because we are adopting the results of e^--H scattering in free space in which the masses of incident and bound electrons are the same, we must keep the two masses in the denominator the same in order for our scaling to semiconductors to be valid. Therefore appropriate parameters to use are m_H^{*2} for scaling of the Bohr radius in Eq.4.9.a. and $w=E/E_B$ for the scaling of the incident electron energy in Eq.4.9.b. One should also be careful with the choice E_B for this calculation. All previous studies cited above employed experimentally determined E_B which included contributions from central cores of impurities. Because we are only interested in the Bohr radius of scattering centers, a theoretically calculated E_B of a perfect hydrogenic impurity without any central cell corrections should be used. This approach is appropriate since the central cell potential is highly localized and therefore, although it can affect the binding energy, it does not significantly change the size of the neutral impurity which is mainly determined by the long range Coulomb interactions.

B. Total mobility calculation for doped Ge at low temperatures

In our total mobility calculation we employ a standard relaxation time approximation*. This approach is valid because we are limiting ourselves to low temperatures ($T<25K$) where the inelastic optical phonon deformational potential scattering is negligible. Three scattering mechanisms are considered: neutral impurity, ionized impurity, and acoustic phonon deformation potential scattering.

The neutral impurity scattering contribution is calculated using both Eq.4.6 and Eq.4.9 so we can compare Erginsoy's and Meyer and Bartoli's models to our experiment. The concentration of neutral impurity centers as a function of temperature $N_N(T)$ in each sample is given by:

$$N_N(T) = N_{MJ} - N_{MN} - n(T) \qquad (4.11)$$

where N_{MJ}, N_{MN}, and $n(T)$ are the majority impurity, minority impurity, and free carrier concentrations, respectively.

For the ionized impurity scattering, we employ the Brooks-Herring expression: [165-168]

$$\tau_{ion}^{-1} = \frac{\pi N_I e^4 (k_B T)^{-3/2} x^{-3/2}}{\left(2 m_{con}^*\right)^{1/2} \kappa^2} \left[\ln\left(1+\frac{4x}{a}\right) - \frac{4x/a}{1+4x/a}\right] \quad \text{where} \quad a = \frac{2 \pi \hbar^2 e^2 n}{m^* \kappa k_B^2 T^2}, \qquad (4.12)$$

$x=E/k_BT$ (E: incident electron energy), m^*_{con} is the average conductivity effective mass, and N_I is the ionized impurity concentration. The temperature dependent N_I in each sample is given by:

$$N_I(T) = n(T) + 2N_{MN}. \qquad (4.13)$$

For the acoustic phonon deformation potential scattering: [169]

$$\tau_{ac}^{-1} = B_{ac} \left(m_{con}^* T\right)^{3/2} x^{1/2} \qquad (4.14)$$

where the constant B_{ac} has well established values for n and p-type Ge as shown in Table 4.1. (In our case we use the values of B_{ac} that are determined experimentally using ultra pure n- and p-type Ge of $N_{MJ}-N_{MN} \sim 3\times10^{11}cm^{-3}$.)

---

* A detailed description of the relaxation time approximation and derivations of the Brooks-Herring equation (Eq.4.12) and the acoustic deformation potential scattering equation (Eq.4.14) are given in Appendix B.

Having found τ^{-1} of all three scattering mechanisms, we calculate an average $<\tau>$ using the Maxwell-Boltzman integration:

$$<\tau> = \frac{4}{3\sqrt{\pi}} \int_0^\infty \frac{x^{3/2} \exp(-x)}{\tau_{ac}^{-1} + \tau_{ion}^{-1} + \tau_{neutral}^{-1}} dx. \qquad (4.15)$$

Finally the total mobility μ_{total} is then given by

$$\mu_{total} = e <\tau> / m^*_{con}. \qquad (4.16)$$

All the parameters required for the mobility calculations are well known in Ge (Table 4.1). The only unknown material parameters at this point are sample dependent N_{MJ}, N_{MN}, and n(T) in Eq.4.11 and Eq.4.13. However as it is shown later all three parameters can be determined precisely for each sample by performing variable temperature Hall effect measurements. Consequently all mobility calculations are performed without any adjustable or scaling parameters.

Table 4.1 Parameters used in the total mobility calculations

	Ge:As (n-type)	Ge:Ga (p-type)
κ	16	16
m_{con}^*	$0.12m_0$	$0.28m_0$
B_{ac}	1.08×10^{10} $g^{3/2}K^{-3/2}$	9.50×10^{8} $g^{3/2}K^{-3/2}$
E_B (Theoretical)	12.5meV [170]	11.2meV [171]

4.2.3 Experiment

Our growth method of isotopically enriched ^{74}Ge and ^{70}Ge crystals has been described in detail in Sec.2. Wafers were cut from each ingot and thermal neutron irradiated at University of Missouri Research Reactor facility. After the irradiation, the ^{74}Ge wafers became As doped, i. e., n-type due to the $^{74}\text{Ge}+\text{n}\rightarrow{}^{75}\text{Ge}\rightarrow{}^{75}\text{As}$ β^- decay reaction, while the ^{70}Ge wafers turned p-type due to the $^{70}\text{Ge}+\text{n}\rightarrow{}^{71}\text{Ge}\rightarrow{}^{71}\text{Ga}$ electron capture reaction. Unavoidable fast neutron radiation damage was removed by thermal annealing at 650°C for 10sec in a N_2 atmosphere. A series of ^{74}Ge:As and ^{70}Ge:Ga wafers of net-carrier concentrations in the range 10^{14}~10^{16}cm^{-3} and less than 1% compensation were produced in this manner. A detailed description of neutron transmutation doping of ^{70}Ge and ^{74}Ge crystals was given in Sec.3.2. Hall and resistivity measurements were performed in order to determine the free carrier concentration and the mobility as a function of temperature. A description of the Hall effect method is given in Appendix D. Disc-shape (~6mm diameter, ~0.5mm thick) samples with the van der Pauw contact configuration were used in all measurements. Phosphorus and boron were implanted to NTD ^{74}Ge:As and NTD ^{70}Ge:Ga samples, respectively, for the formation of ohmic contacts. A magnetic induction of 3000 Gauss was used in all Hall measurements.

4.2.4 Results and Discussion

Our first experimental step is the determination of n(T), N_{MJ}, and N_{MN} in each sample performing Hall effect measurements. Fig.4.8 (a) and (b) show the temperature dependent free carrier concentrations n(T) in four ^{74}Ge:As and two ^{70}Ge:Ga samples, respectively. The experimental curves are fitted with the standard semiconductor statistics (Eq.3.9). All fits we obtained using Eq.3.9 are very good (see Fig.4.8) and N_{MJ} and N_{MN} are accurately determined for each sample as shown in Table 4.2.

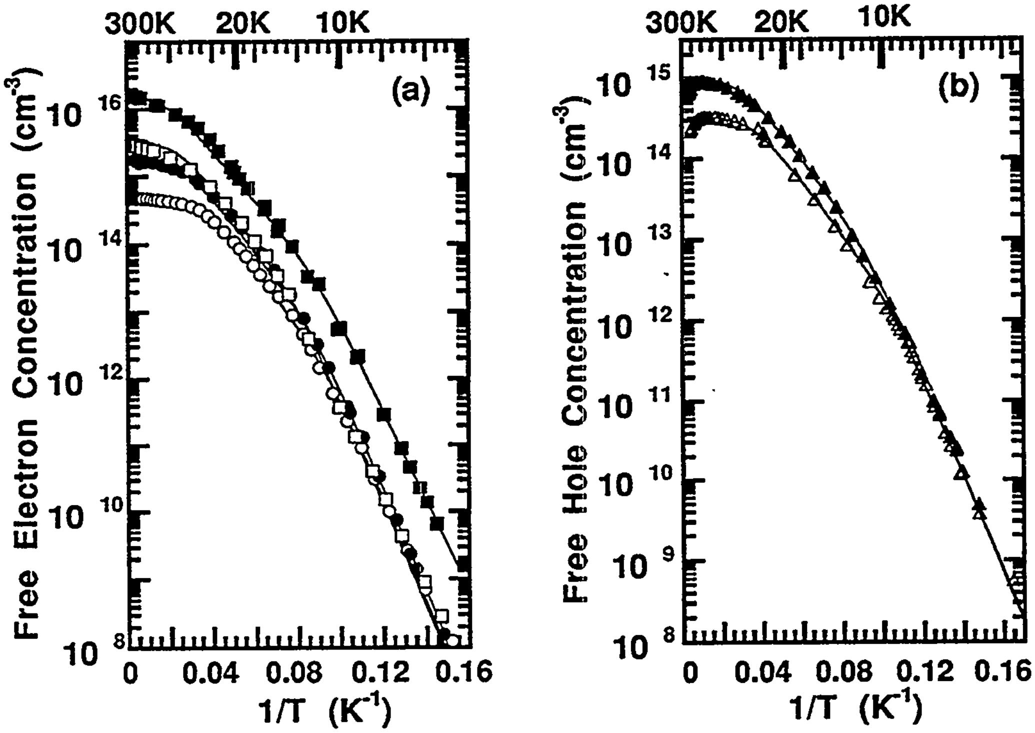

Fig.4.8 Temperature dependence of free carrier concentration in (a) four ^{74}Ge:As and (b) two ^{70}Ge:Ga samples: ^{74}Ge:As-1 (○), ^{74}Ge:As-2 (●), ^{74}Ge:As-3 (□), ^{74}Ge:As-4 (■), ^{70}Ge:Ga-1 (△), and ^{70}Ge:Ga-2 (▲).

Table 4.2 N_{MJ} and N_{MN} obtained from the Hall curve fittings

Sample	N_{MJ} (cm^{-3})	N_{MN} (cm^{-3})
^{74}Ge:As-1	4.5x10^{14}	2.5x10^{12}
^{74}Ge:As-2	1.8x10^{15}	6.0x10^{12}
^{74}Ge:As-3	2.9x10^{15}	2.1x10^{13}
^{74}Ge:As-4	1.5x10^{16}	4.2x10^{13}
^{70}Ge:Ga-1	3.2x10^{14}	1.0x10^{12}
^{70}Ge:Ga-2	8.8x10^{14}	5.1x10^{12}

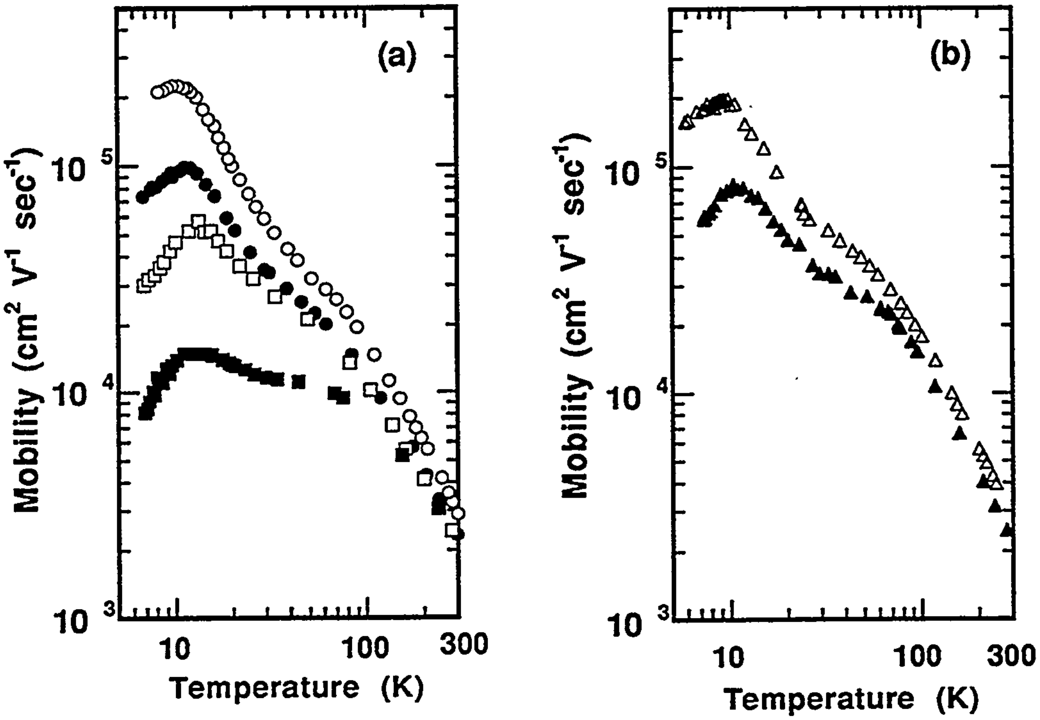

Fig.4.9 Experimentally measured carrier mobility in (a) four ^{74}Ge:As and (b) two ^{70}Ge:Ga samples. The symbols representing different samples are same as those in Fig.4.8.

Fig.4.9 (a) and (b) show the temperature dependent Hall mobility for all samples in the temperature range T=6-300K. We have demonstrated in our recent paper that the mobility in the high (T>80K), intermediate (T=20-80K), and low (T<20K) temperature regimes is dominated by phonon, ionized impurity, and neutral impurity scattering, respectively.[172] Fig.4.10 shows the comparison of the experimentally measured mobility in sample ^{70}Ge:Ga-1 with two theoretically calculated mobility curves. Fig.4.10 also shows the contributions of the three scattering mechanisms ($\mu_{neutral}$, $\mu_{ionized}$, and $\mu_{lattice}$) to the total mobility. One theoretical curve (solid line) with a label "Full integration" was calculated using a relaxation time approximation method described in the previous theory

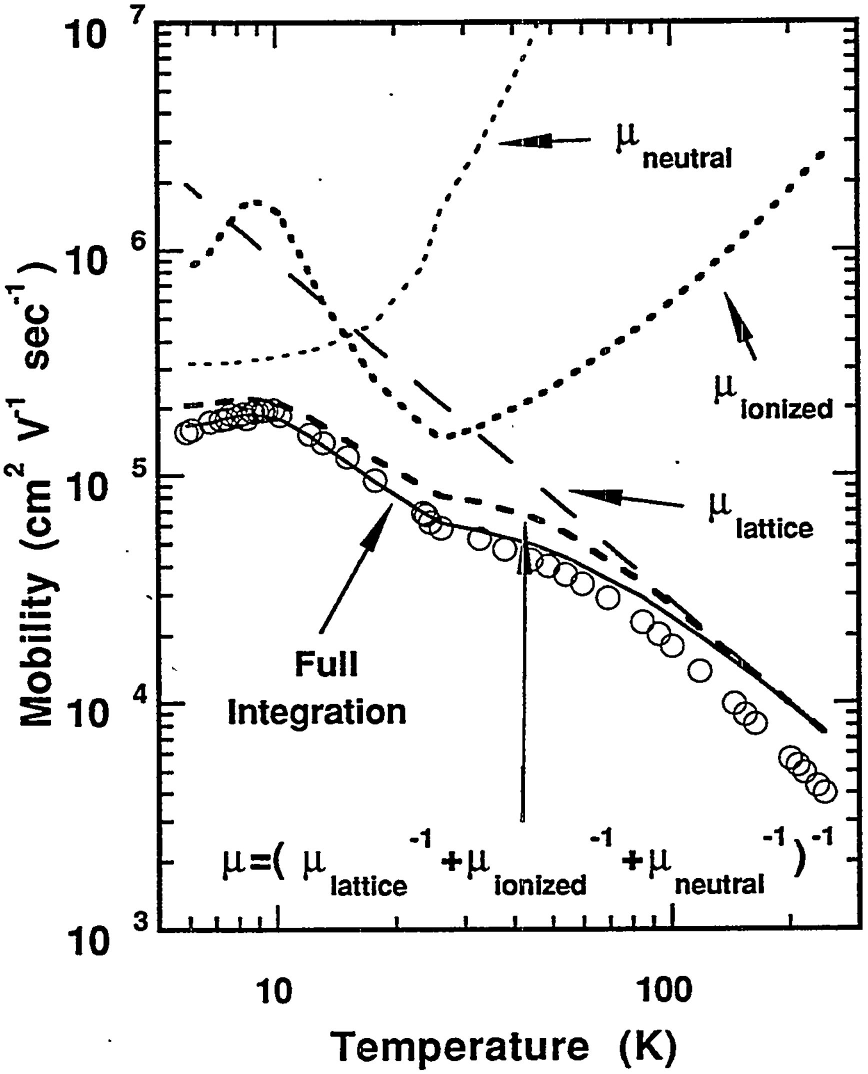

Fig.4.10 A direct comparison of experimentally measured mobility in sample ^{70}Ge:Ga-1 with two theoretically calculated mobility curves. See the main text for details of this figure.

section 4.2.2. The other theoretical curve (dashed line) was calculated using Matthiessen's rule (Eq.4.3). Both theoretical curves deviate from the experimental curves at high temperatures due to neglecting the inelastic scattering mechanisms in our calculation. At low temperatures (T<30K) we obtained an excellent agreement of the experimental curve with a relaxation time approximation (solid curve) but not with Matthiessen's rule (dashed curve). Although Matthiessen's rule has been considered to be a standard method to approximate theoretical mobilities, this example clearly shows the necessity of using a relaxation time approximation for a more rigorous mobility calculation.

We now turn our attention to the low temperature regime where mobilities are dominated by neutral impurity scattering. Fig.4.11 (a) and (b) show a direct comparison of our experimental results with theoretical total mobility curves calculated using the procedure described in Sec.4.2.2. For each sample two theoretical total mobility curves are calculated: one using Eq.4.6 (Erginsoy) and the other using Eq.4.9 (Meyer and Bartoli). A strikingly good agreement was obtained between the experimental and theoretical mobilities calculated with the Meyer and Bartoli model for all samples. In the temperature range of interest (T<25K), the condition $\mu B>1$ of the high magnetic induction limit is met for all samples, i. e., the Hall factor r_H is unity.* Thus our data points in Fig.4.11 should represent the drift mobility μ_d. The contribution of hopping conduction to the measured mobility is negligible because, as seen in Fig.4.8, there is no difference between the experimental points and the fitted curves for all samples even at the lowest T. For completeness, we have also calculated the Hall factor r_H using $r_H=<\tau^2>/<\tau>^2$. As a result we have found that r_H was in the range 1.05 to 1.1 for all data points shown in Fig.4.11. Therefore, even if our Hall results were affected by r_H, the 5-10% upward shift of each curve calculated with the Meyer and Bartoli's theory would still be in good agreement with our experimental results while it would lead to further deviation from Erginsoy's theory. Also shown in Fig.4.11 (b) are the contributions of different scattering mechanisms to the total mobility in ^{70}Ge:Ga-1 which contains the least amount of Ga impurities as seen in Table II. Even with this small amount of the neutral impurity concentration, neutral Ga become the dominant scattering centers below 16K. Mobilities in other samples with higher Ga and As concentrations are dominated by neutral impurity scattering up to higher

---

* See Appendix D for a descripton of the Hall factor r_H.

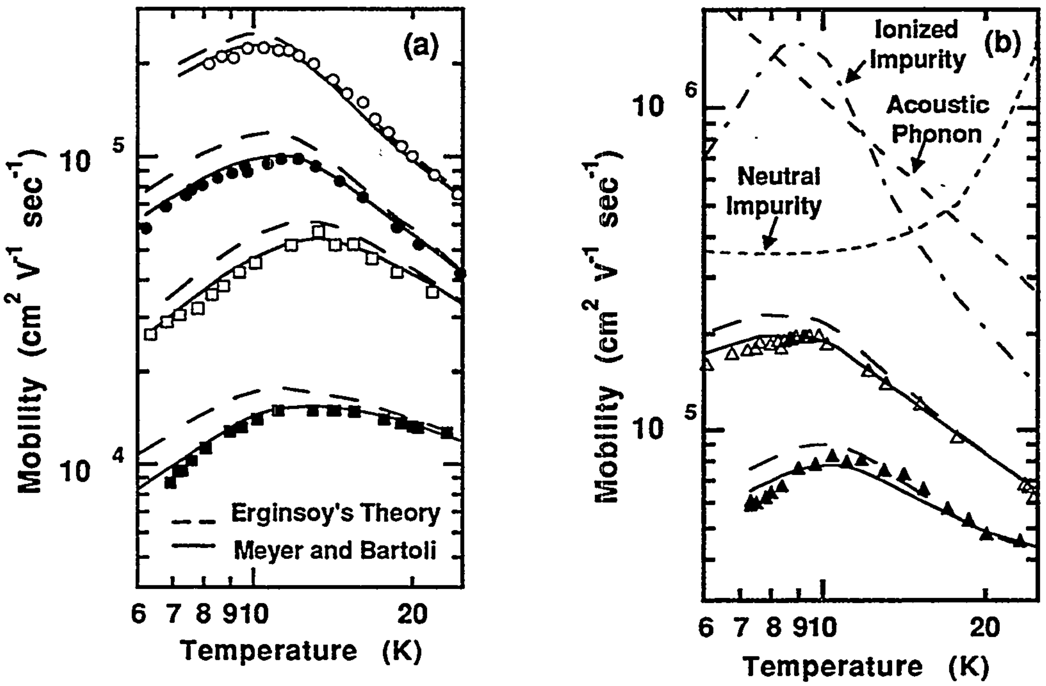

Fig.4.11 Data points represent experimentally measured carrier mobility in (a) four ^{74}Ge:As and (b) two ^{70}Ge:Ga samples. The symbols representing different samples are same as those in Fig.4.8. For a direct comparison the theoretically calculated mobilities using Erginsoy's model (broken line) and Meyer and Bartoli's model (solid line) are shown for each sample. The contributions of the different scattering mechanisms to the total mobility of the ^{70}Ge:Ga-1 sample are shown in the upper half of Fig.4.11.(b).

temperatures. For example neutral impurity scattering dominates up to T~21K in highly doped ^{74}Ge:As-4.

In order to demonstrate the importance of the homogeneous dopant distribution, we have perform the same study on samples cut from Ge:Ga crystals grown by the conventional Czochralski (Cz) method. Compared to our NTD ^{74}Ge:As and NTD ^{70}Ge:Ga, we expect these samples to have less homogeneous Ga impurity distributions since Ga impurities were introduced to the Ge melt during the crystal growth. We have measured four Cz-Ge:Ga samples cut from four different ingots. All samples had

[Ga]~1.5x10^{14}cm^{-3} and N_{MN}~2x10^{11}cm^{-3}. Among these four samples, mobilities of only two samples showed fair agreement with the theoretically calculated mobility. However mobilities in two other samples as shown in Fig.4.12 (a) and (b) substantially deviate from the theory. These observed deviations of the measured mobility from the theoretical calculations are most likely due to inhomogeneous Ga impurity distributions in melt doped Ge. Only the use of the neutron transmutation doped semiconductors with randomly distributed dopants allows an accurate test of the neutral impurity scattering models.

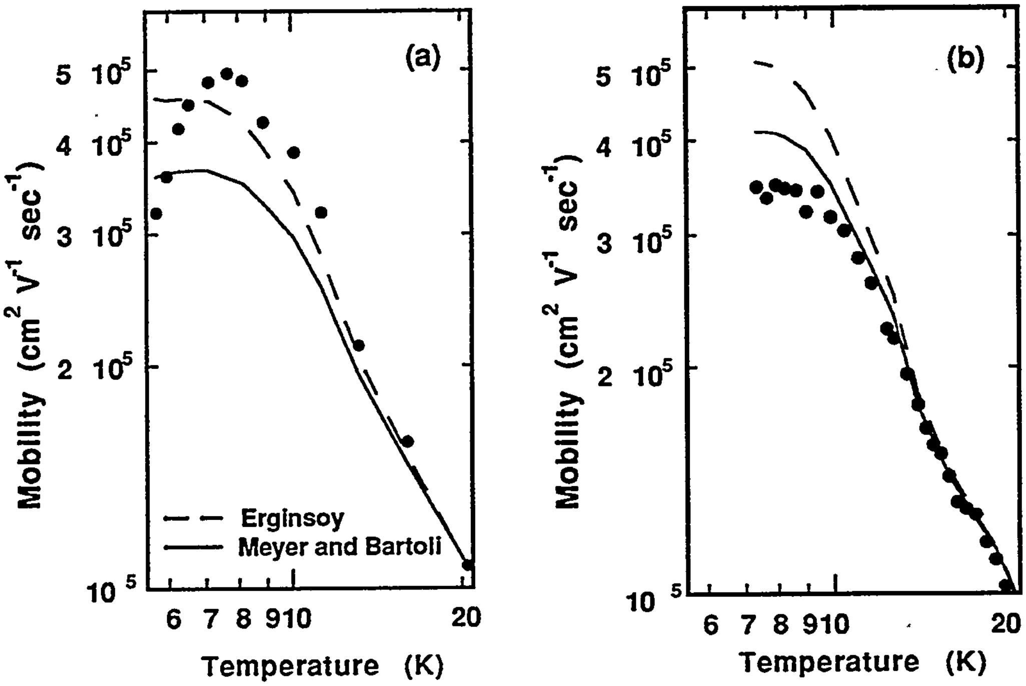

Fig.4.12 (a) and (b) A direct comparison of theoretically calculated mobilities to experimentally measured mobilities in two conventional Ge:Ga samples.

4.2.5. Summary and Conclusions of the Neutral Impurity Scattering Experiment

We have performed a detailed study of neutral impurity scattering by measuring the free carrier mobility in Ge:As and Ge:Ga samples. The application of the neutron transmutation doping technique to isotopically enriched ^{74}Ge and ^{70}Ge crystals allowed preparation of samples with controlled compensation and truly randomly distributed dopants. We have shown that the low temperature mobility is accurately described by the phase shift based scattering model of hydrogen atoms scaled to hydrogenic impurities in semiconductors.

4.3 Ionized Impurity Scattering

4.3.1 Introduction

Because of its technological importance, there has been a large number of papers published regarding ionized impurity scattering in semiconductors*. With a few exceptions, most aspects of ionized impurity scattering are now well understood. One of the few topics that requires further research is the ionized impurity scattering mechanism in highly compensated semiconductors. Although the Brooks-Herring expression (Eq.4.12) describes the ionized impurity scattering rate in non-degenerate lightly compensated ($K<0.2$) semiconductors very well, the expression was found to over-estimate the mobilities significantly when semiconductors are highly compensated. This discrepancy was experimentally demonstrated by Cuevas [108] in 1967. Since the work of Cuevas there has been no experimental work which explicitly attempted to study ionized impurity scattering as a function of the compensation. The main reason for Cuevas's work being the only experimental contribution is due to, again, the difficulty of fabricating samples with controlled compensation ratios. Cuevas has grown As doped Ge crystals (n-type) using

---

* An excellent review on this subject was given by Chattopadhyay and Queisser. [146]

the Czochralski method and has counter-doped them with Ga acceptors by NTD. This method developed by Fritzsche and Cuevas [107] allowed production of a series of n-type Ge samples with well defined K between ~0 and 0.96. However, the homogeneity of their n-type dopant distribution was questionable since As impurities were introduced during melt crystal growth.

In this section I shall describe our on going effort of understanding the ionized impurity scattering mechanism in highly compensated semiconductors. In order to improve the data taken by Cuevas [108] we use a series of NTD $^{70/74}$Ge:Ga,As samples of p-type with K between 0.4 and 0.95. Our samples should contain extremely uniform distribution of both the majority and minority concentration. It is very difficult to theoretically solve the problem of ionized impurity scattering in highly compensated semiconductors as I will show in the next section. Our experimental approach may point out some of problems associated with the existing theories.

4.3.2 Theory

Here, I shall describe two theories that are going to be used to compare with our experimental results. One is by Falicov and Cuevas [173], and the other is by Stern.[174] Both theories consider ionized impurity scattering in highly compensated semiconductors. Because they are extensions of the Brooks-Herring theory, we shall start by writing down the Brooks-Herring expression. (See Appendix B for a complete derivation.) Brooks [167] and Herring assumed a potential V(r) due to a point charge in semiconductor described by:

$$V(r) = \frac{(Ze)\,e}{\varepsilon r} \exp(-r/L_D) = \frac{Z e^2}{\varepsilon r} \exp(-r/L_D) \tag{4.17}$$

where Ze is the charge of the scattering center and L_D is known as the screening length. According to the form of Eq.4.17, the smaller the L_D, the more effective the screening is. There are two different screening mechanisms in doped semiconductors: (1) screening of ionized impurity centers by free carriers, and (2) screening of ionized impurity centers by other surrounding ionized centers (self-screening).

The expression for L_D for the former mechanism is given by Eq.B.33:

$$L_D(\text{free carrier}) = \frac{1}{e}\left(\frac{\varepsilon k_B T}{4\pi}\right)^{1/2} n^{-1/2} \tag{4.18}$$

where n is the free carrier concentration. As T→0, n→0, i.e., L_D(free carrier)→∞. Therefore, screening due to free carriers is significant only at high temperatures where there is a large concentration of free carriers to screen point charges.

The screening length L_D(ion) due to ionized impurity self-screening is given by:

$$L_D(\text{ion}) = \frac{1}{e}\left(\frac{\varepsilon k_B T}{4\pi}\right)^{1/2}\left[\frac{(N_{MJ}-N_{MN}-n)(N_{MN}+n)}{N_{MJ}}\right]^{-1/2}. \tag{4.19}$$

When the semiconductor is in the temperature range called "impurity saturation region" (segment 2 in Fig.4.1), $L_D(\text{ion})=0$ because $N_{MJ}-N_{MN}=n$. Therefore, the effect of the self-screening becomes significant only in the low temperature carrier freeze-out region. When $n<<N_{MJ}$ and N_{MN}, Eq.4.20 becomes:

$$L_D(\text{ion}) = \frac{1}{e}\left(\frac{\varepsilon k_B T}{4\pi}\right)^{1/2}\left[\frac{(N_{MJ}-N_{MN})(N_{MN})}{N_{MJ}}\right]^{-1/2}, \tag{4.20}$$

i.e., the degree of screening is determined only by the concentration of majority and minority impurities at very low temperature.

The general expression for L_D is obtained by adding Eq.4.18 and Eq.4.19:

$$L_D = \frac{1}{e}\left(\frac{\varepsilon k_B T}{4\pi}\right)^{1/2}\left[n + \frac{(N_{MJ}-N_{MN}-n)(N_{MN}+n)}{N_{MJ}}\right]^{-1/2}. \tag{4.21}$$

Therefore, L_D given by Eq.4.21 should be used in Eq.17 according to Brooks.[167]

The scattering rate (or inverse relaxation time) τ_{ion}^{-1} given by Brooks [167] and Herring [168] is expressed as (Eq.B.38 in Appendix B):

$$\tau_{\text{ion}}^{-1} = \frac{\pi N_I Z^2 e^4}{(2\,m^*)^{1/2}\,\varepsilon^2}\left[\ln(1+\gamma^2) - \frac{\gamma^2}{1+\gamma^2}\right]E^{-3/2} \tag{4.22}$$

with

$$\gamma^2 = 8\,m^*\,E\,L_D^2/\hbar^2, \tag{4.23}$$

where E is the energy of an incident electron.

Now we shall describe a modification of Brooks-Herring theory proposed by Falicov and Cuevas.[173] In the course of deriving the screened potential (Eq.4.17), Brooks and Herring linearized the source term in Poisson's equation assuming that $eV(\mathbf{r})/k_BT$ is much smaller than unity.[167] Falicov and Cuevas [173] explicitly pointed out that this condition is satisfied only in two cases:

(1) at high enough temperatures for any kind of impurity concentration;

(2) at all temperatures for semiconductors doped with only one kind (donors or acceptors) of impurities.

In the latter case, as the temperature goes down the thermal energy decreases exponentially with T, so that the ratio $eV(\mathbf{r})/k_BT$ remains always small. However, when the compensation is high, $V(\mathbf{r})$ remains large even at low temperatures so that the assumption $eV(\mathbf{r})/k_BT \ll 1$ made by Brooks and Herring breaks down. Therefore, Falicov and Cuevas tried to get around the problem by solving Poisson's equation without resorting to an expansion in a series of $eV(\mathbf{r})/k_BT$. Because there are very few carriers at low temperatures, Brooks and Herring's original proposal is that the screening arises no longer from free carriers but from the random distribution of ionized impurities (Eq.4.20). However, Falicov and Cuevas argued that the ionized impurity distribution at low temperature is not random but is correlated, i.e., it is "frozen" in the state of minimum potential energy. Falicov and Cuevas tested their idea by using a simple temperature independent exponential correlation function between acceptors and donors. As a result Falicov and Cuevas [173] obtained the scattering rate as:

$$\tau_{ion}^{-1} = \frac{\pi N_I Z^2 e^4}{(2\, m^*)^{1/2}\, \varepsilon^2} \left[\ln(1+\gamma_{FC}^2) + \frac{\gamma_{FC}^2}{1+\gamma_{FC}^2} \right] E^{-3/2} \tag{4.24}$$

with
$$\gamma_{FC}^2 = 8\, m^*\, E\, a_c^2/\hbar^2, \tag{4.25}$$

and
$$a_c = [8\,\pi\,(N_{MJ} - N_{MN})]^{-1/3}. \tag{4.26}$$

Eq.4.21 differs from the Brooks-Herring expression (Eq.4.22) only in that the sign of the last term within large parentheses is positive and that the temperature dependent L_D is replaced by the static temperature independent inverse correlation length a_c. The form of the correlation function a_c (Eq.4.23) proposed by Falicov and Cuevas [173] turned out to be too simple to obtain good agreement with experimentally measured mobilities of Cuevas.[108] For deriving a_c, Falicov and Cuevas did not use a rigorous form of Coulomb interactions between ionized impurities. This point is obvious from the fact that Eq.2.23 does not contain parameters such as the electronic charge e and dielectric constant ε. Therefore, even though Falicov and Cuevas were able to point out the problem associated with the assumption $eV(\mathbf{r})/k_BT<<1$, they could not actually find out at what temperature this assumption breaks down. They relied on their physical intuition that $eV(\mathbf{r})/k_BT>1$ for T<40K for Ge moderately doped with shallow impurities.

Another approach to solve the problem of ionized impurity scattering in highly compensated semiconductors has been proposed by Stern.[174] He did not take into account the correlation effect proposed by Falicov and Cuevas, but included the effect of the impurity level broadening due to the Coulomb fields arising from randomly distributed ionized impurities. Kane [175] proposed that the linearization of Poisson's equation, i.e., the Brooks-Herring expression, is valid when the number of screening sites within a sphere of radius L_D be greater than unity. Stern [174] showed that this criterion is barely satisfied for most semiconductors even at low temperature. Based on this finding, Stern argued that the Brooks-Herring expression is valid even at low temperature without taking the correlation effect into account. He self-consistently calculated the modified screening length L_{DS} at T=0 due to the level broadening as a function of the compensation:

$$L_{DS} = s\,(8\,\pi^2 N_{MN})^{-1/3} \tag{4.27}$$

where s is the proportional factor graphically given in Fig.4.13. Thus, L_D in Eq.4.23 should be replaced by Eq.4.27 according to Stern. Then the scattering rate τ_{ion}^{-1} is according to Stern is calculated by the standard Brooks-Herring formula Eq.4.22.

The theories of Falicov and Cuevas and of Stern both assumed that the screening of charged impurities by free carriers at low temperatures is negligibly small. It will be shown in the following section that this may not be the case.

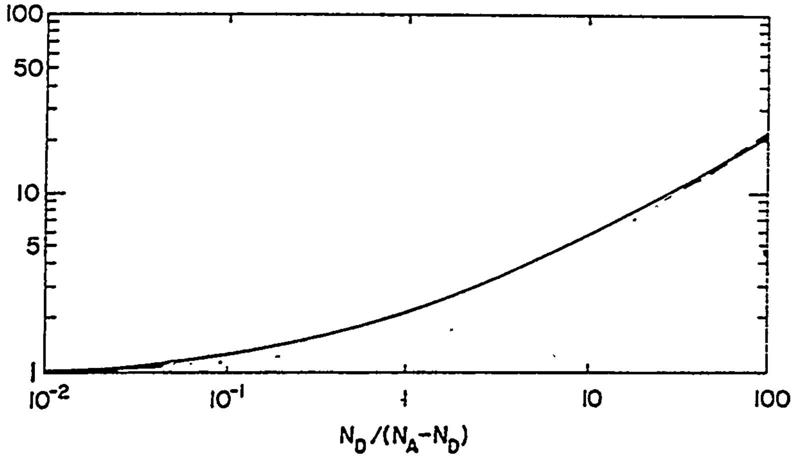

Fig.4.13 Modified screening length parameter s given by Stern.

Lastly, I should mention the series of recent ionized impurity scattering papers published by Meyer and Bartoli.[176-178] They have developed a self-consistent "multi-ion screening" formalism which, unlike conventional treatments mentioned above [167, 173, 174], explicitly assures that no electron state contributes more than one electron charge to the net charge screening the ionized impurities. Their key finding is that formal consistency can be achieved only when neighboring ion potentials overlap to a certain degree. Therefore, Meyer and Bartoli proposed that ionized-impurity scattering in a semiconductor is intrinsically a multi-ion process, and the tightly screened, isolated-impurity regime is unphysical. At the point of this thesis writing, we are still in the process of developing a computer program to self-consistently solve the "multi-ion scattering" equations given by Meyer and Bartoli. As I will show further down, the traditional theories do not agree very well with our experimental results when samples are highly compensated. Because the "multi-ion screening theory" is derived from a more realistic physical assumption than the traditional one electron scattering pictures, we are hoping to obtain a good agreement between our experimental results and the "multi-ion scattering theory" in the near future.

4.3.3 Results and Discussions

Fig.4.14 shows the experimentally measured Hall mobilities in p-type $^{70/74}$Ge:Ga,As samples with three different compensation ratios: K=0.4, K=0.76, and K=0.95. The concentration of Ga and As in each sample is shown in Table 4.3. One can see from Table 4.3 that the three samples have approximately the same As contents, i.e., the ionized impurity concentration at low temperatures (which is given by 2[As]) is constant in all three samples. Therefore the difference in the low temperature mobilities we observed in Fig.4.14 comes from the difference in the screening length L_D rather than the difference in the ionized impurity concentrations. By inspecting the low temperature L_D given by Brooks and Herring (Eq.4.20), one finds that the difference in N_{MJ} (i.e., [Ga]) is the main cause of the mobility differences at low temperatures. However, before we reach this conclusion, we should examine the validity of the Brooks-Herring expression by comparing it to our experimental results

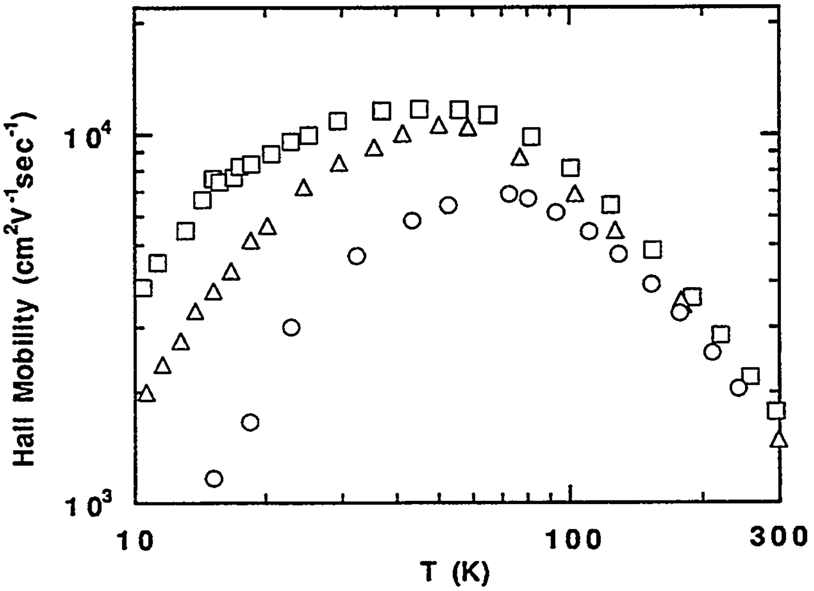

Fig.4.14 Experimentally measured Hall mobilities in p-type $^{70/74}$Ge:Ga,As samples with K=0.4 (□), K=0.76 (△), and K=0.95 (○).

Table 4.3 Ga and As concentrations in the samples shown in Fig.4.13

K	[Ga] (cm^{-3})	[As] (cm^{-3})
0.4	3.30×10^{15}	1.32×10^{15}
0.76	2.03×10^{15}	1.54×10^{15}
0.95	1.63×10^{15}	1.54×10^{15}

Fig.4.15 shows the comparison of our experimental results to the following four different theoretical calculations.

(1) Brooks-Herring's results (Eq.4.22) with L_D given by Eq.4.21. The result of this calculation is represented by curves labeled "BH" in Fig.4.15.

(2) Brooks-Herring's results (Eq.4.22) with modified L_D proposed by Stern (Eq.4.27). The result of this calculation is represented by curves labeled "FS" in Fig.4.15.

(3) Falicov-Cuevas's results (Eq.4.24) with a_c given by Eq.4.26. The result of this calculation is represented by curves labeled "FC" in Fig.4.15.

(4) Brooks-Herring's results (Eq.4.22) with L_D obtained by considering the free carrier screening only (Eq.4.18). The result of this calculation is represented by curves labeled " BH ' " in Fig.4.15.

The theoretical mobility calculation procedure is the same as the one explained in Sec.4.2.2.B, i.e., the calculation includes acoustic deformation potential scattering, ionized impurity scattering and neutral impurity scattering mechanisms. However, there is one extra step in the calculation in this study compared to the one we used in the neutral impurity scattering study. In the neutral impurity scattering study, the drift mobility μ_d was equal to the Hall mobility μ_H because the high field Hall effect criterion of $\mu B>1$ was satisfied throughout the measurement *. On the other hand all mobilities we measure with a magnetic induction of 3000 Gauss in this study are less than $10^4 cm^2 V^{-1} sec^{-1}$, i.e., the Hall measurements are now in the low magnetic field regime ($\mu B << 1$) of the Hall effect theory (see Appendix D). In this case the Hall mobility μ_H is given by Eq.D.15:

$$\mu_H = r_H \mu_d \tag{4.28}$$

where the Hall coefficient r_H is given by Eq.D.14:

$$r_H = <\tau_m{}^2> / <\tau_m>^2. \tag{4.29}$$

The value of r_H depends on the temperature so that, for each calculated drift mobility μ_d, we calculate r_H to find the theoretical Hall mobility μ_H. The values of r_H are found to lie betwen 1.5 and 1.8 for the measurements shown in Fig.4.15.

In Fig.4.15.(a) we compare our experimentally measured Hall mobility in the K=0.4 sample to calculated curves. For the sample with K as small as 0.4, Brooks-Herring (BH) and Stern (FS) theories already overestimate the experimental Hall mobilities by a factor of two. The FS theory which supposedly is the improvement of BH theory actually deviates more than BH theory from the experimental points. The FC theory on the other hand agrees reasonably well with the experimental curve. Because Eq.4.29 is the r_H expression for carriers associated with simple spherical conduction band, the 20% difference between FC theory and the experimental curve could have been introduced during our r_H calculation. The BH' curve also seems to agree with the experimental curve quite well.

In Fig.4.15.(b) we show the same comparison for the K=0.76 sample. The agreement of BH, FS, and FC theories with the experimental curve becomes worse. Even the closest of the three theories (FC) overestimates the experimental mobilities by a factor of 2.5 (notice the scale change from Fig.4.15.a). This difference can no longer be explained by the error in r_H. The BH' curve on the other hand lies only 20% above the experimental curve, well within the error introduced by r_H.

---

* See Appendix D for the description of the Hall effect theory.

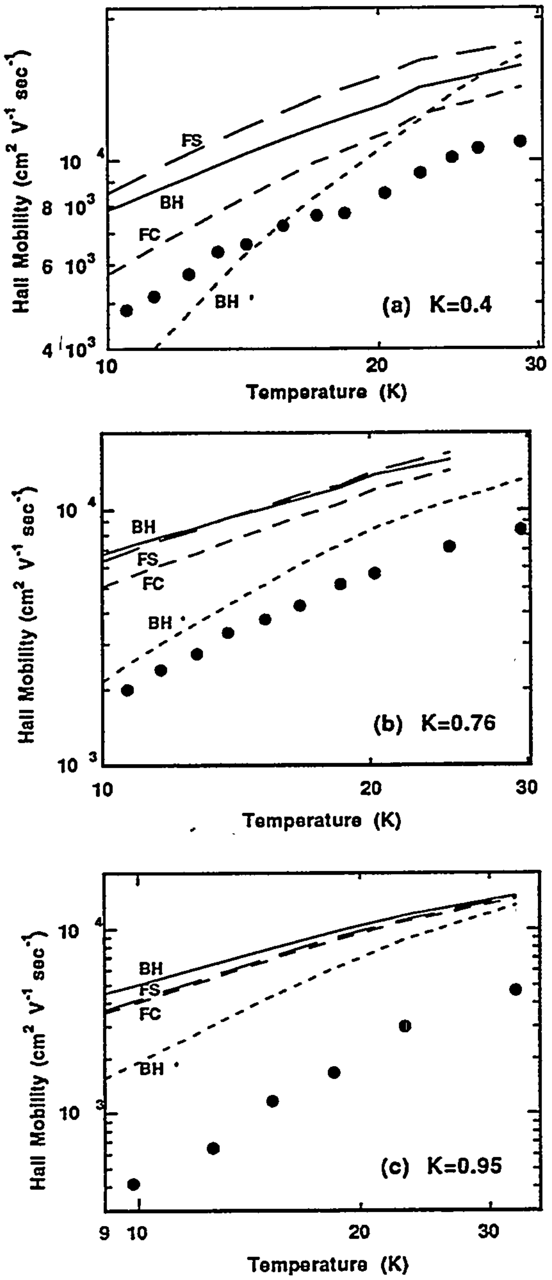

Fig.4.15 The comparison of the experimental mobilities (●) to the four different theoretical calculations. See the main text for detail.

For the K=0.95 sample (Fig.4.15.c) the situation becomes even worse. BH, FS, and FC theories all overestimate the experimental mobilities by a factor of ten. The BH' result, which shows good agreement with the experimental curves in the K=0.4 and K=0.76 samples, now deviates by a factor of ~3.

It is interesting to note that the BH' curves are in better agreement overall with the experimental curves than BH, FS, and FC theories. Brooks [167] clearly stated that L_D of the form given by Eq.4.20 should be used, i.e., the BH' curves which only consider the screening due to free carriers are physically wrong according to Brooks. In fact all BH, FS, and FC theories take into account only the screening due to distributed of ionized impurities. Physically the screening due to ionized impurities occurs by the local rearrangement of the ionized impurity distribution. Because impurities themselves cannot diffuse at such low temperature, this local rearrangement can happen only by moving holes that are bound to neutral impurities. For example, the local charge distribution can be changed by moving one hole from one Ga neutral center to another Ga ionized center (hopping conduction). However, this hopping process is much more inefficient and slower than the rearranging the free carrier distribution. Consequently, it may be the case that the screening due to ionized impurity distribution is not as efficient as Brooks, Falicov and Cuevas, and Stern have estimated. In fact, even though the carrier concentration is extremely small at low temperature, the free carrier screening (Eq.4.18) may dominate over ionized impurity self-screening (Eq.4.18). If this is the case, we should simply use Eq.4.18 to calculate the Brooks-Herring mobility, as we did to calculate BH' curves in Fig.4.15. For the K=0.95 sample, none of the approaches we took agrees with the experimentally measured mobilities. In such a high K sample, it is possible that the valance band edge in real space is no longer flat but consists of large abrupt potential fluctuations due to the extremely high concentration of ionized impurities. This type of band edge fluctuations in K>0.9 samples has been predicted by Shklovskii and Efros.[96] In this case, holes traveling in the valance band edge will be scattered significantly more than the estimation of simple ionized impurity scattering theory.

4.3.4 Summary

It has been shown that the traditional ionized impurity scattering treatments significantly overestimate the low temperature mobility in highly compensated semiconductors. We speculate that the free carrier screening of ionized impurities is important even at low temperature. However, we cannot provide any theoretical justifications to support our speculations at this point. We hope that our future work will provide a better understanding of the ionized impurity scattering mechanism in highly compensated semiconductors.

4.4 Hopping Conduction

It has already been mentioned in Sec.1 that the understanding of the low temperature hopping conduction mechanism is important for the development of the bolometric detectors for astrophysics and condensed matter experiments. The basic concept of the hopping process was discussed in Sec.4.1.2, and the following variable-range-hopping (VRH) expression has been derived in Appendix C:

$$\rho = \rho_0 \exp\left(\frac{T_0}{T}\right)^n \quad \text{where } n = \frac{1}{4} \text{ or } \frac{1}{2}. \tag{4.30}$$

The value of n is determined by the shape of the density of states around the Fermi level. Both the Mott [143, 144] (n=1/4 for Si:P, Si:As,etc.) and Efros-Shklovskii [96] (n=1/2 for n=1/2 for Ge:Ga, Ge:As, Si:B, etc.) VRH have been observed in doped semiconductors.[179] It is generally assumed that the n=1/2 behavior is observed when the energy E_{hop} of the hopping electron is less than the Coulomb gap E_{CG} shown in Fig.4.7.(b), while n=1/4 occurs when $E_{hop} > E_{CG}$.

For the n=1/4 case the Mott characteristic temperature T_0', the mean hopping distance $<R'_{hop}>$ and the mean hopping energy $<E'_{hop}>$ are given by [143]:

$$T_0' \approx 18 / k_B\, g(E_F)\, \xi^3(N), \tag{4.31.a}$$

$$<R'_{hop}> \approx 3\, \xi^3(N)\, (T_0' / T)^{1/4} / 8, \tag{4.31.b}$$

$$<E'_{hop}> \approx k_B\, T^{3/4}\, T_0'^{1/4} / 4, \tag{4.31.c}$$

where $g(E_F)$ is the density of the states at the Fermi level and $\xi(N)$ is called "localization length". In lightly doped semiconductors in which the average distance between impurities is much larger than the Bohr radius, $\xi(N)$ is given by the average distances . As the doping concentration increases, the degree of the wavefunction overlaps increases, i.e., $\xi(N)$ also increases. When the doping concentration exceeds the metal-insulator transition critical concentration N_c, $\xi(N)$ becomes infinity large since there are no more localized carriers.

The n=1/2 dependence arises from the parabolic Coulomb gap whose shape according to Efros and Shklovskii is given by: [96]

$$g(E)=3\varepsilon^3(E-E_F)^2/e^6, \tag{4.32}$$

where ε is the dielectric constant. Efros and Shklovskii's characteristic temperature T_0, the mean hopping distance $<R_{hop}>$, the mean hopping energy $<E_{hop}>$, and the width of the Coulomb gap E_{CG} are given by: [96]

$$T_0 \approx \beta\, e^2 / k_B\, \varepsilon(N)\, \xi(N), \tag{4.33.a}$$

$$<R'_{hop}> \approx \xi(N)\, (T_0 / T)^{1/2} / 4, \tag{4.33.b}$$

$$<E'_{hop}> \approx k_B\, T^{1/2}\, T_0^{1/2} / 2, \tag{4.33.c}$$

$$E_{CG} \approx e^3\, g_0(E_F) / \varepsilon^{3/2} \tag{4.33.d}$$

where the prefactor β according to Efros and Shklovskii [96] is 2.8 and $g_0(E_F)$ is the density of states at the Fermi level given by Mott. The dielectric constant $\varepsilon(N)$ also diverges to infinity as $N \rightarrow N_c$.

Because all our Ge samples show $\ln\rho \propto T^{-1/2}$, we shall concentrate on the theories which yield the n=1/2 dependencies for the rest of this thesis. It is generally agreed that there is a parabolic Coulomb gap around the Fermi level of every semiconductors.

However, the question remains how wide the gap is. Eq.4.33.d proposed by Efros and Shklovskii has been criticized by Pollak and Ortuno [180] on the basis that the method used for deriving Eq.4.32 accounted only for stabilization of the ground state by one-particle excitation. Rather than the sequential transitions of one electron considered by Efros and Shklovskii, Pollak and Ortuno [180] introduced the concept of simultaneous multielectron transitions with which the value of E_{CG} becomes much smaller than the prediction of Efros and Shklovskii (Eq.4.33.d). This in turn leads to a smaller T_0, i.e., the prefactor $\beta=2.8$ in Eq.4.33.a is reduced. Experimentally the reduced $\beta=0.2$ has been observed by Zabrodskii and Zinov'eva [181] in Ge:As with $[As]\sim0.5N_c$. Shklovskii and Efros argued that this reduction of the prefactor is due to the overlaps of wavefucntions in highly doped semiconductors rather than due to the multi-electron hopping. Therefore, the true test of the Coulomb gap may be performed by inspecting the value of β, using lightly doped samples whose ξ and ε are given by the average distance between impurities and static dielectric constant, respectively.

In this section I shall show the hopping resistivity data taken with two sets of p-type Ge:Ga samples. The first set was prepared by doping ^{Nat}Ge with NTD, i.e., the compensation ratio $K\approx0.32$. The second set was prepared by doping isotopically enriched ^{70}Ge single crystals with NTD, i.e., $K<0.001$. We have selected to inspect a series of small K samples because of the recent observation of the $\ln\rho\propto T^{-1}$ hopping conductivity in nominally uncompensated Si:B between T=50 and 100mK. Compared to the normal $T^{-1/2}$ dependence, the T^{-1} dependence would increase the sensitivity of thermistors significantly according to the sensitivity defined by Eq.1.20. We study the hopping resistivities as a function of the net-impurity concentration N_{Net} within each set. Hopping conduction studies require random distributions of the majority and minority dopant distributions. Our NTD isotopically controlled Ge should provide excellent opportunities to probe the hopping conduction mechanism.

A typical size of our sample was 2x2x0.5mm^3. The ohmic contacts for two-point measurements were formed on the opposing 2x2mm^2 faces of each sample by the B$^+$ 3×10^{14}cm^{-2} implantation. 200Å thick Pd and 4000Å Au pads were sputtered on the implanted layer. The samples were annealed again at 300°C for one hour to remove the implantation damage and stress in the metal film. Cu wires were attached to the Au pads. The Cu wires heat sink the samples and provide electrical currents through the ohmic contacts during measurements. The samples were suspended from the contact wires in a Cu box in order to avoid any stress. All low temperature resistivity measurements were performed using the Oxford Model-75 dilution refrigerator in collaboration with the members of Professor Sadoulet's group at University of California at Berkeley. A two point resistivity measurement was selected because of the high resistance of the five samples measured in this work. An I-V curve of each sample was recorded on a X-Y plotter by slowly changing the bias voltage. The linear (ohmic) part of I-V curve starting from the origin was used to calculate the resistivity of each sample.

Fig.4.16 shows the temperature dependence of the resistivity of five NTD ^{70}Ge:Ga and of eight NTD ^{Nat}Ge samples. Excellent fits with Eq.4.30 are obtained for all resistivity curves. Table 4.4 lists basic sample parameters such as [Ga], [As], [Se], and the net-hole concentration N_{Net}, compensation ratio K, and the parameters, ρ_0 and T_0, fitted with Eq.4.30.

For cosmic ray microwave background ^{95} and other measurements performed in ^{3}He refrigerators near 300mK, we first note that NTD ^{70}Ge-1.90 is more sensitive than NTD5 for T>300mK by a factor of 2.6. ^{70}Ge-1.90 has a T_0 which is a factor 2.6 larger than T_0 of NTD5 while maintaining the resistivity in the optimum range of 10^5~$10^7\Omega$ cm at T=300~500mK.* The effect of compensation to the hopping conduction can be recognized by comparing the resistivity curves of NTD18 with ^{70}Ge-2.98 and ^{70}Ge-2.15 in Fig.4.16.

---

* Recall discussion of the NTD thermistors in Sec.1.3.

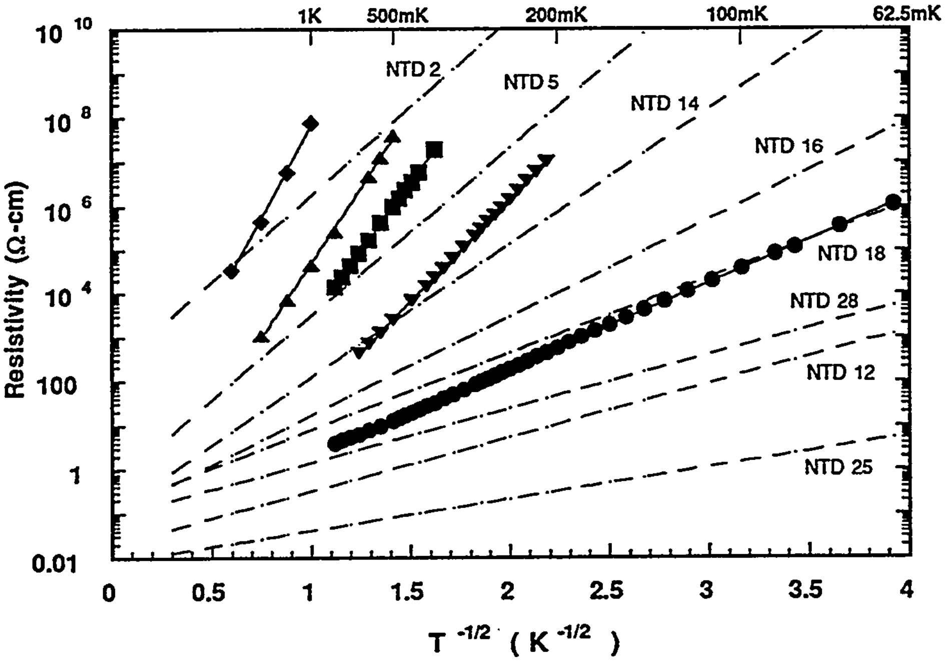

Fig.4.16 Temperature dependence of resistivity of various NTD ^{Nat}Ge:Ga and NTD ^{70}Ge:Ga samples: ^{70}Ge-3.30 (◆), ^{70}Ge-2.98 (▲), ^{70}Ge-1.90 (■), ^{70}Ge-1.65 (▼), and ^{70}Ge-2.15 (●)

Table 4.4 Basic parameters of the NTD Ge samples studied in this work

	Concentration $(\mathrm{x}10^{16}\mathrm{cm}^{-3})$						
Sample	[Ga]	[As]	[Se]	Net Hole	K	ρ_0 (Ω cm)	T_0 (K)
NTD 2	0.044	0.013	0.001	0.03	0.32	200	82.9
NTD 5	2.2	0.63	0.041	1.5	0.32	0.47	77.6
NTD 14	3.9	1.1	0.073	2.7	0.32	0.11	49.0
NTD16	6.1	1.7	0.11	4.2	0.32	0.1	26.5
NTD 18	7.7	2.2	0.14	5.3	0.32	0.15	15.9
NTD 28	9.0	2.6	0.17	6.3	0.32	0.09	7.84
NTD 12	9.8	2.8	0.18	6.8	0.32	0.02	7.84
NTD 25	12.3	3.52	0.23	8.6	0.32	0.008	2.74
^{70}Ge-3.30	3.02	<0.003		3.02	<0.001	0.34	364.8
^{70}Ge-2.98	8.00	<0.008		8.00	<0.001	0.0074	247.6
^{70}Ge-1.90	9.36	<0.009		9.36	<0.001	0.0019	201.4
^{70}Ge-1.65	14.5	<0.01		14.5	<0.001	0.0006	100.3
^{70}Ge-2.15	17.7	<0.01		17.7	<0.001	0.0215	20.7

Although ^{70}Ge-2.98 has a slightly higher net-hole concentration than NTD18, ρ of ^{70}Ge-2.98 is almost 4 orders of magnitude larger than ρ of NTD18 around 1K. The NTD 18 and ^{70}Ge-2.15 resistivity curves are similar, but the net-hole concentration of ^{70}Ge-2.15 is three times larger than NTD18. The resistivity of ^{70}Ge:Ga samples with $K<0.001$ is significantly larger because there are not enough empty Ga acceptor states into which holes can hop. On the other hand 32% of Ga sites in NTD ^{Nat}Ge are ionized (i.e., without a hole) so that hole hopping occurs more readily.

In Fig.4.17 (a) and (b) we compare the ρ_0 and T_0 values of NTD ^{Nat}Ge:Ga and NTD ^{70}Ge:Ga, respectively, as a function of the net-hole concentration. Despite the difference in K, ρ_0 of the NTD ^{Nat}Ge and NTD ^{70}Ge in Fig. 2 (a) for concentrations up to $\sim 10^{17}$cm^{-3} coincide and continuously decrease until a net-hole concentration of 1.5×10^{17}cm^{-3} is reached. The higher concentration points of ^{70}Ge rise again. Although a similar dependence was reported for the Si:P system [182], confirmation of this increase in ρ_0 requires further investigation. For T_0 significant differences exist between NTD ^{Nat}Ge and NTD ^{70}Ge as shown in Fig.4.17 (b). It was predicted by Efros and Shklovskii [96] that the value of T_0 approaches zero as the net-hole concentration N_{Net} approaches the metal-semiconductor transition critical concentration N_c with a form:

$$T_0 = A\,(1 - N_{Net}/N_c)^{\zeta} \tag{4.34}$$

where A and ζ are constants. Using Eq.4.34, a good fit to the T_0 of NTD ^{70}Ge (solid line in Fig.4.17 (b)) is obtained with:

$$T_0\,(\text{NTD }^{70}\text{Ge}) = 437.3\pm16\ \left(1 - N_{Net}\,/\,1.89\times10^{17}\text{cm}^{-3}\right)^{1.06\pm0.12}. \tag{4.35}$$

Eq.4.35 allows us to estimate the amount of Ga doping necessary to obtain a specific value of T_0 for our future NTD ^{70}Ge doping. Knowing the value of β also allows us to estimate the other important parameters such as the hole localization length ξ and dielectric constant ε.[179] However, this will be discussed in a future publication because more T_0 data points are necessary to obtain a truly reliable fit. We also attempted to fit T_0 of NTD ^{Nat}Ge with Eq.4.34 but were unsuccessful. N_c of NTD ^{Nat}Ge must be larger than N_c of NTD ^{70}Ge

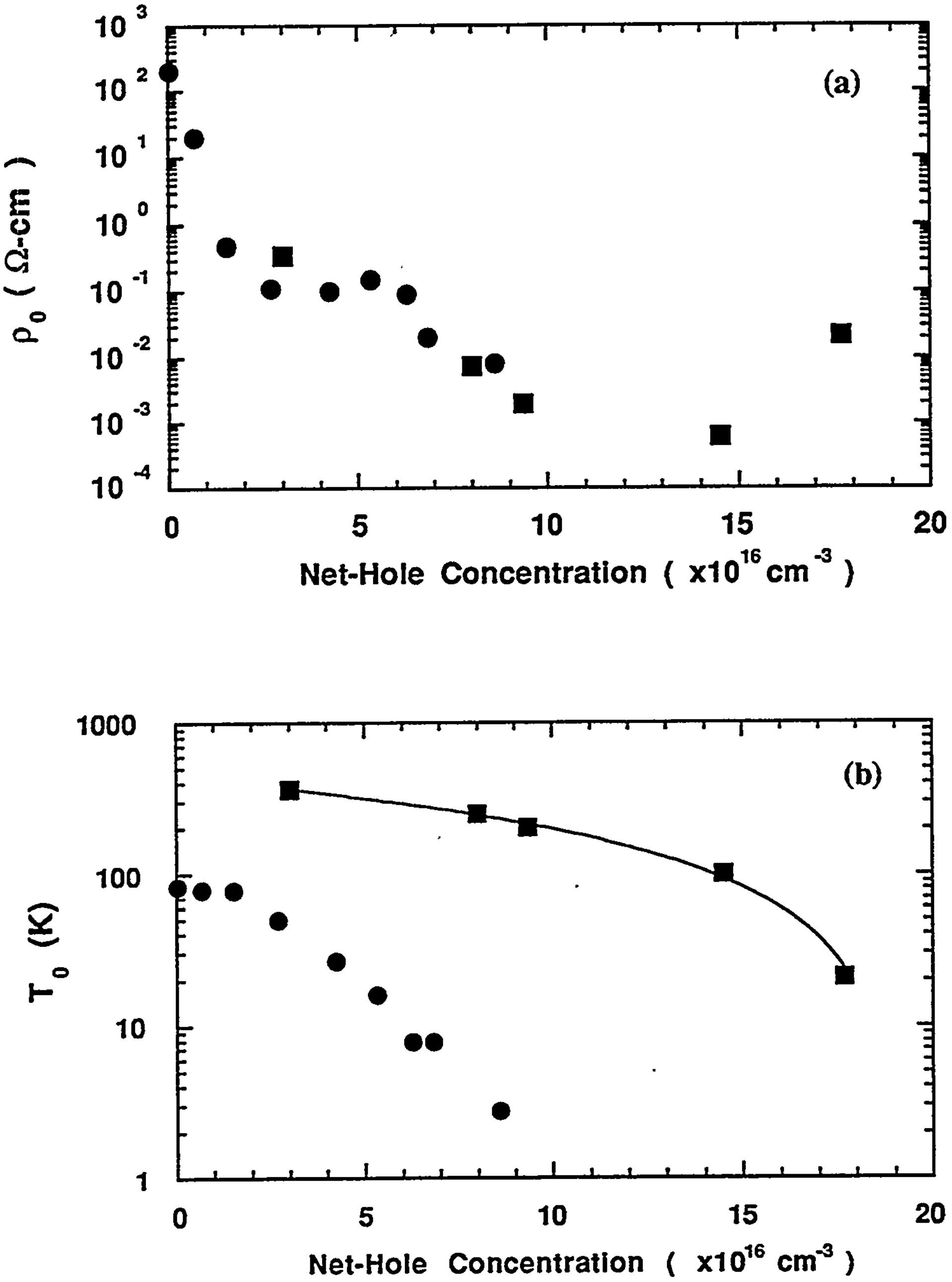

Fig.4.17 Net-hole concentration dependence of (a) ρ_0 and (b) T_0 of NTD ^{Nat}Ge:Ga (●) and NTD ^{70}Ge:Ga(■)

because NTD ^{Nat}Ge has a significantly higher compensation. However, it is impossible to fit T_0 of NTD ^{Nat}Ge with N_c larger than $1.89\times10^{17}cm^{-3}$.

Unfortunately we have not found any NTD ^{70}Ge:Ga samples that can be used for T=20mK range thermistor operations (the resistivities of all NTD ^{70}Ge:Ga samples shown in Fig.4.16 are too high at 20mK). The main difficulty has been the prediction of the appropriate Ga doping level which leads to the resistivities 10^7-$10^8\Omega$cm at 20mK. As shown in Fig.4.17, the appropriate doping level turned out to be situated in an extremely narrow Ga concentration window of $1.77x10^{17}cm^{-3}$ and $1.89x10^{17}cm^{-3}$. The low temperature resistivities of NTD ^{70}Ge:Ga containing such Ga concentrations will be measured soon.

In summary, the temperature dependence of the variable range hopping resistivity of NTD ^{70}Ge:Ga was found to be significantly different from that of NTD ^{Nat}Ge due to the difference in the compensation ratio. The NTD ^{70}Ge:Ga thermistors were found to have more than a factor of two higher sensitivity than NTD ^{Nat}Ge devices for temperatures T>300mK. Although the Efros-Shklovskii's theory of the variable range hopping conduction successfully predicts the $T^{-1/2}$ dependence of ln ρ, their predictions regarding T_0 disagree with our experimental findings. It may be possible that the multi-electron hopping proposed by Pollak and Ortuno is important. Further study is clearly necessary to improve our understanding of the hopping conduction process.

4.5 Metal-Insulator Transition

Increase of the dopant concentration in semiconductors eventually leads to an overlap of impurity electron wavefunctions. The overlap allows electrons to move rather freely from one impurity site to another without special excitation, resulting in a resistivity which is independent of the temperature. This is called "metallic conduction" in semiconductors. The subject of the interest is how the transition from semiconductor to metallic state occurs. Is the conductivity changing continuously or abruptly across the transition ? At what impurity concentration should the transition occur ? These common questions in the field of "metal-insulator (MI) transition" have been intensively studied with various semiconductor systems.[143] As I will show, very controversial experimental results regarding the MI transition has been published recently by Stupp et al.[183] A subtle feature found by Stupp et al. in the conductivity-[P] curve in Si:P samples was immediately criticized by Rosenbaum et al. [184] claiming that the result is most likely due to the inhomogeneous phosphorus distribution in Stupp et al's samples. I believe that the MI transition experiment using NTD doped semiconductor will most likely settle this controversy.

4.5.1 Mott vs. Anderson MI transition in doped semiconductors

In 1949, Mott [185, 186] considered an ensemble of neutral hydrogen atoms held rigidly in a simple cubic lattice. If the lattice spacing is small compared to the Bohr radius then in the ground state the 1s electron band is half filled and the system is a metal at T=0. Thus the system undergoes an MI transition as a function of the density of H atoms on account of electron correlation. He predicted that a discontinuous, abrupt MI transition with varying concentration should occur when

$$n^{1/3} a_H = 0.2 \tag{4.36}$$

where n is the number of electrons per unit volume and a_H the hydrogen radius. Mott proposed that one can apply the same type of equation for the case of a semiconductor which is doped with hydrogen-like shallow impurities. Experimentally measured MI transition critical concentrations N_c in a wide variety of semiconductor systems indeed found the following equation: [143]

$$N^{1/3} a = 0.27 \tag{4.37}$$

where N is the concentration of shallow dopants and a is the Bohr radius of the shallow impurity center. Clearly the main driving force for the Mott transition is the electron wavefunction overlap, i.e., electron-electron interactions.

Anderson [41] in 1958 showed that the presence of a sufficiently large random potential, even in the absence of electron-electron interactions, leads to localized electron states and hence an insulator at T=0. In such non-interacting systems, the MI transition is viewed not as a formation of metallic bands, but closing of the energy gap for electrons known as a "mobility gap". The mobility gap is the distance of the Fermi level from a mobility edge at which the one-electron states become delocalized. The relevance of Anderson's idea for doped semiconductors becomes clear if the shallow impurities are distributed not on a sublattice, but randomly, leading to an effective random potential in which carriers move.

Which of the two effects, electron interactions or disorder, is dominant near the MI transition is an issue which has been debated many times. It is now believed that the both of them are necessary to describe the experimental results.[187]

The metallic phase is defined by a finite T=0 dc conductivity $\sigma(0)$, while $\sigma(0)=0$ in the insulator. $\sigma(0)$ in the metallic phase is given by the Boltzmann transport theory. Assuming a spherical Fermi surface $\sigma(0)$ is expressed by:

$$\sigma(0)=\left(\frac{\pi}{3}\right)^{1/3}\frac{e^2}{\pi\hbar d}\frac{l}{d} \tag{4.38}$$

where l is the mean free path of carriers and $d{\sim}n^{-1/3}$ is the distance between scattering centers. Ioffe and Regel [188] pointed out that for the Boltzmann theory to be valid, *l* must be larger than d, i.e., Eq.4.38 has a lower limit:

$$\sigma_{IR} \approx e^2 / 3\,\hbar\, d. \tag{4.39}$$

Mott [189] in 1972 formalized this idea into the concept of a "zero temperature minimum metallic conductivity", σ_M. As N_c is approached from the metallic side, $\sigma(0)$ decreases with *l*, till $l \approx d$, and then the system becomes insulating with an abrupt drop in $\sigma(0)$, from σ_M to zero (Fig.4.18.a).

In 1979, Abrahams et al. [190] introduced a scaling theory of localization for non-interacting electrons in disordered systems. Their picture is based on the assumption that conductance is the only relevant parameter describing the phenomenon of localization close to the transitions. In three dimensional systems, their results show that the dc conductivity near the MI transition is given by a form like Eq.4.39, but d is replaced by the localization length ξ. Thus $\sigma(0)$ in the barely metallic sample is given by,

$$\sigma(0) \approx C'(e^2 / 3 \hbar \xi) \tag{4.40}$$

where c' is the constant. ξ diverges at the transition, $\xi \sim (n-N_c)^{-\alpha}$, so that $\sigma(0)$ as the transition is approached from the metallic side is described by the form:

$$\sigma(0) = \sigma_0 \left(\frac{n - N_c}{N_c}\right)^{\alpha} \tag{4.41}$$

where $\sigma_0 \sim \sigma_M$ within a factor of two is the prefactor, n is the carrier concentration, and $\alpha=1$ is the critical exponent. Thus, the Anderson MI transition is a continuous transition as seen in Fig.4.18.b. It is interesting to note that recent numerical calculations of the Anderson transition, i.e., driven purely by disorder without interaction, have suggested controversial critical exponents $\alpha=1.3$ to 1.5 (Fig.4.18.c).[191-194]

As noted before, the MI transition in doped semiconductors is believed to contain contributions from both Mott's and Anderson's types. Currently theories which incorporate both types of transitions predicts the lower bound $\alpha=2/3$.[187, 195]

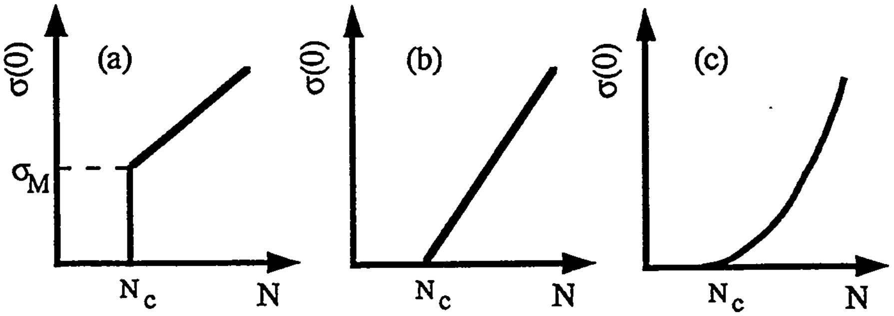

Fig.4.18 Various proposed scenarios for the conductivity onset: (a) Mott, (b) Anderson according to Abrahams et al., (c) Anderson according to MacKinnon et al.

Now we shall discuss how we may experimentally deduce the zero temperature conductivity $\sigma(0)$ in barely metallic semiconductors. The Coulomb interaction model with electron-electron and electron-hole scattering in the presence of random impurities predicts a $T^{1/2}$ correction to the finite temperature conductivity $\sigma(T)$: [196]

$$\sigma(T) = \sigma(0) + m\,T^{1/2} \tag{4.42}$$

where the slope m is either positive or negative. Usually, $m<0$ for samples very close to transitions.[187] Therefore, in order to find $\sigma(0)$ one needs to measure the conductivity as a function of the temperature. The y-axis intersect of a curve $\sigma(T)$ vs. $T^{1/2}$ gives $\sigma(0)$.

The MI transitions in doped semiconductors have been extensively studied by experimentalists in the past few decades. The exponent $\alpha=1$ predicted by Abrahams et al. has been observed with various compensated semiconductors such as Ge:Sb [197], Si:P,B [198], etc. However, the MI transition in uncompensated materials differs from the results of any theories; unpredicted values of $\alpha\sim1/2$ in Eq.4.41 have been observed in nominally uncompensated Si:P [199, 200], Si:As [201], Si:As, P [202], Si:B [203, 204] and Ge:Sb [197] Surprisingly, $\alpha=1/2$ is even smaller than the lower bound 2/3 set by the Mott-Anderson combined transition proposed by Chayes et al.[195] The most recent, very controversial experimental results regarding MI transition have been published by Stupp et al.[183] Fig.4.19 show the conductivity data taken by Stupp et al. in a series of Si:P samples of deferent P concentrations. The linear extrapolation of σ vs. $T^{1/2}$ curve gives $\sigma(0)$. Fig.4.20.(a) and (b) show the extrapolated $\sigma(0)$ vs. P concentration N. Fig.4.20.(a) is the traditional fit reported in all the previous literature which yields $\alpha\approx0.55$. Fig.4.20.(b), on the other hand, shows their newly proposed fit which is applied to a tail-off region between 3.4 and $4\times10^{18}\text{cm}^{-3}$. The fit was obtain with $\alpha\approx1.3$, supporting the recent calculation of the pure Anderson transition (Fig.4.18.c).[191-194] This subtle feature found by Stupp et al.[183] was immediately criticized by Rosenbaum et al.[184] claiming that the result is most likely due to the inhomogeneity in the phosphorus distribution. This problem, which is unsolved even today, is one of the most important issues in the field of the MI transition.

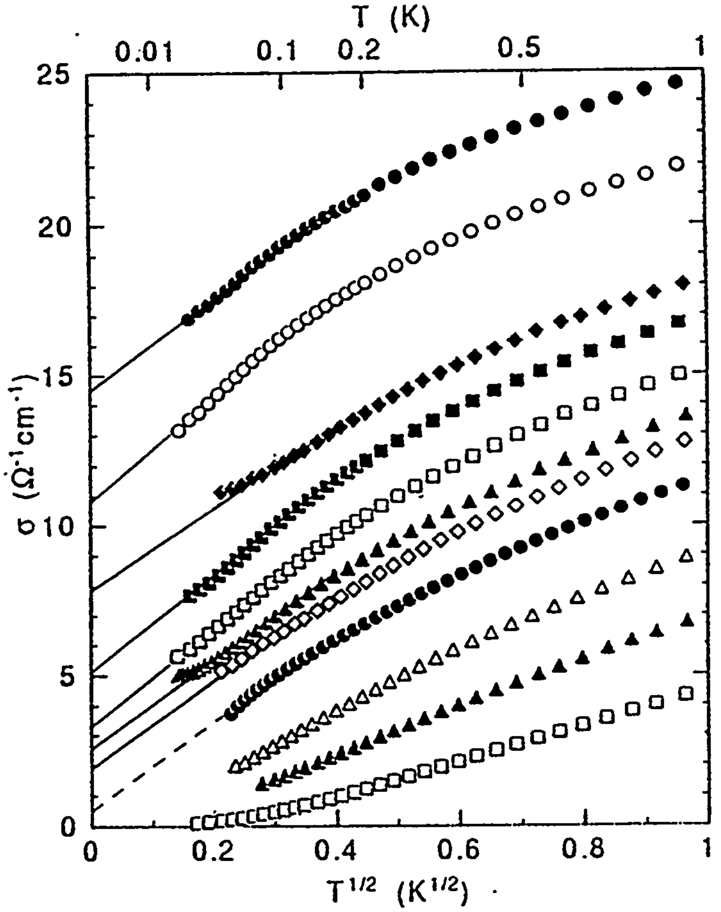

Fig.4.19 Conductivity vs.$T^{1/2}$ for Si:P samples with N close to the N_c. Solid lines indicate extrapolation to obtain $\sigma(0)$. The concentrations are (from top to bottom in units of $10^{18}cm^{-3}$): 3.69, 3.67, 3.63, 3.60, 3.58, 3.56, 3.55, 3.52, 3.50, 3.45, and 3.38.[183]

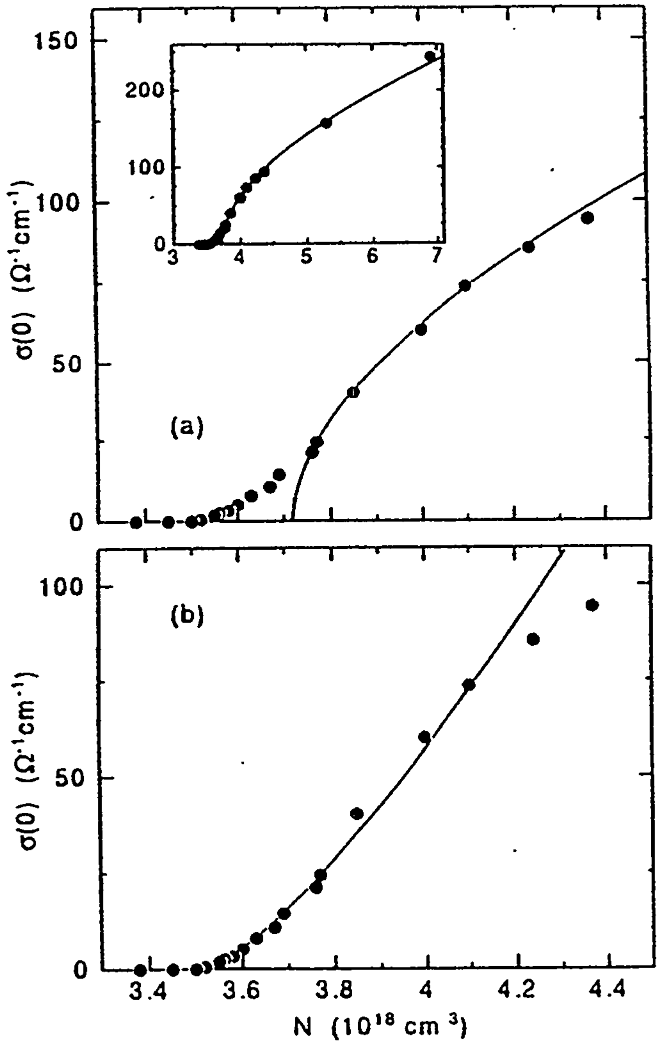

Fig.4.20 Extrapolated T=0 conductivity $\sigma(0)$ vs. P concentration N. (a) Fit with $\alpha=0.55$. Inset shows the same fit over an extended N range. (b) Fit with $\alpha=1.3$. [183]

4.5.2 Experimental Study of the Metal-Insulator Transition using NTD ^{70}Ge:Ga.

By applying NTD to isotopically enriched ^{70}Ge samples we prepared a series of barely metallic Ge:Ga samples. Each sample had a dimension, 8x0.6x0.3mm^3. Four strips of B implanted contacts for four-point resistivity measurements were placed on a 8x0.6mm^2 face of each sample. 200Å thick Pd and 4000Å Au pads were sputtered on the implanted contacts. The samples were annealed again at 300°C for one hour to remove the implantation damage and stress in the metal film. The Au wires heat sink the samples and provide electrical currents through the ohmic contacts during measurements. The samples were suspended from the contact wires in a Cu box in order to avoid any stress. As was the case for the study of hopping conduction, all low temperature resistivity measurements were performed using the Oxford Model-75 dilution refrigerator in collaboration with the members of Professor Sadoulet's group at University of California at Berkeley. Because of the low resistance of the samples, we employed four point resistivity measurements using a standard lock-in amplifier. Two different frequencies, 43 and 218Hz, in a contrast current mode with the power generated in the sample kept below 5x10^{-15}W were used.

Fig.4.21 shows the temperature dependent conductivities we measured in nine barely metallic NTD ^{70}Ge:Ga samples between T=20mK and 500mK. The Ga concentration in each sample given in the caption is estimated from the thermal neutron irradiation time. The estimated concentrations were also confirmed by Hall effect measurements. $\sigma(T)$ is plotted against $T^{1/2}$ because of the temperature dependence of σ predicted by Eq.4.42. All σ curves shown in Fig.4.21 obey Eq.4.42 much better than the σ curves measured by Stupp et al. in Si:P samples (Fig.4.19). Thus, our $\sigma(0)$ obtained by the extrapolation to T=0 should be more reliable than the results of Stupp et al. Fig.4.22 shows the zero temperature conductivity $\sigma(0)$ as a function of the Ga concentration [Ga] in the nine samples shown in Fig.4.21. A good fit to the data shown in Fig.4.22 is obtained by Eq.4.41 with $\alpha=0.430\pm0.015$, $N_c=1.90\pm0.01\times10^{17}\text{cm}^{-3}$,and $\sigma_0=25.48\pm0.01\Omega^{-1}\text{cm}^{-1}$.

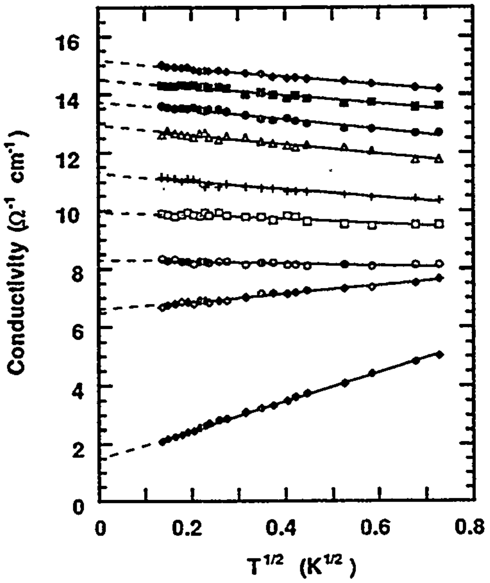

Fig.4.21 Conductivity vs.$T^{1/2}$ for Ge:Ga samples with [Ga] close to the N_c. Dashed lines indicate extrapolation to obtain $\sigma(0)$. The concentrations are (from top to bottom in units of $10^{17}cm^{-3}$): 2.49, 2.41, 2.34, 2.26, 2.20, 2.12, 2.05, 1.98, and 1.90.

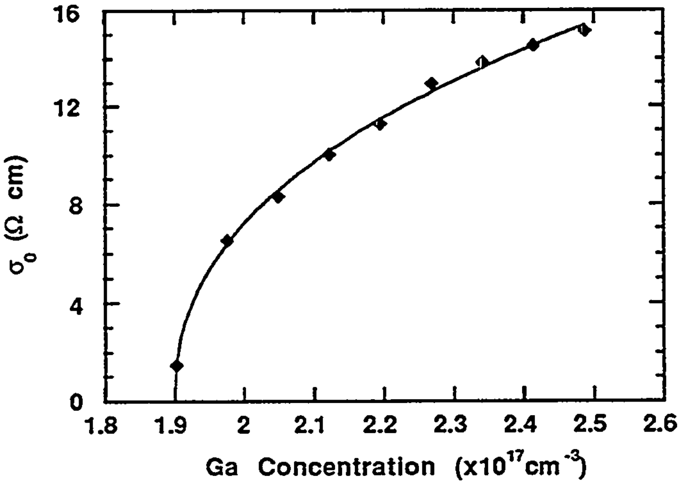

Fig.4.22 Extrapolated T=0 conductivity $\sigma(0)$ vs. [Ga] A fit with α=0.43 is shown.

The value of the critical exponent $\alpha=0.43$ we obtain is very close to $\alpha=0.55$ for Si:P obtained by Rosenbaum et al.[184], and different from $\alpha=1.3$ proposed by Stupp et al.[183] Even though more data points around N_c are necessary to draw a definite conclusion, the following two reasons supporting our fit with $\alpha=0.43$ are in order. First, Stupp et al. have made the strong statement that only the σ-$T^{1/2}$ curves which have positive slopes should be considered to be in the critical regime. However, two $\sigma(0)$ values obtained from the bottom two slopes in Fig.4.21 (which have positive slopes) agree with the $\alpha=0.43$ fit very well as shown in Fig.4.22. Second, the value of N_c we obtain from the fit agrees very well with the N_c we obtained from the critical exponent fit of T_0 (Eq.4.35) in the previous hopping conductivity study.

In summary, because our $\sigma(0)$ data taken with homogeneously doped Ge:Ga samples show $\alpha=0.43$ even down to N_c, we believe that the $\alpha=1.3$ observed by Stupp et al. is due to the inhomogeneous dopant distribution, supporting the claim of Rosenbaum et al.[184] Therefore, we shall still have to wait for the development of theories which explain $\alpha<2/3$ convincingly.

Chapter 5 Optical Studies

5.1 Infrared Absorption Spectroscopy Study of Highly Compensated Ge

5.1.1 Introduction

Highly compensated semiconductors have been important materials for both technological and fundamental basic research purposes. Semi-insulating GaAs used as substrates for high speed, high frequency electronic applications is an example of such a material of the technological importance. For fundamental research purposes, highly compensated semiconductors are ideal systems to study the effect of the disordered impurity distribution on the spatial fluctuations of the electronic potential.

A number of fundamental physical properties such as the free carrier mobility and the widths of optical transition lines (such as in impurity absorption spectra or photoluminescence) depend upon the spatial fluctuations of the electrostatic potential created by ionized donors and acceptors in the crystal. In this section we shall specifically discuss the broadening of ground state to bound excited state transition energies of hydrogenic acceptors in Ge due to the electric fields and field gradients arising from randomly distributed ionized impurities.

The four major broadening mechanisms of the impurity absorption lines have been treated theoretically some time ago. They are: (1) "phonon life-time broadening" due to interaction of bound electrons (holes) with phonons [205, 206], (2) "concentration broadening" due to overlap of the very extended hydrogenic impurity wavefunctions [207], (3) "strain broadening" due to strains resulting from the presence of dislocations and impurities [105], and (4) "Stark and quadrupole broadening" due to random electric fields produced by ionized impurities. [208-210]

In the past few decades a number of experiments have provided a good understanding of the first three broadening mechanisms. Navarro et al. [211] have used the extremely sharp absorptions lines of the stress-insensitive hydrogen-oxygen related shallow donors in ultra-pure Ge to demonstrate the quantitative validity of Barrie and Nishikawa's theory of "phonon life-time broadening".[205, 206] Colbow [212], Newman [213], and White [214] used Si:B, while Nisida and Horii [215] and Imateke [216] used Ge:Sb of a wide range of doping concentrations to measure the "concentration broadening" of the absorption lines. Most experimental results found good agreement with the semi-empirical theory of "concentration broadening" proposed by Baltensperger.[207] Artjemenko et al. [217] have observed a splitting in the gallium absorption lines in Ge due to stress caused by the presence of neutral barium impurities. Jagannath et al. [218] have studied all of the above mentioned broadening mechanisms by performing spectroscopic measurements on a wide variety of donors in Si (Si:P, Si:As, Si:Li, and Si:Li-O). Inspection of the extensive number of spectra given by Jagannath et al. [218] quantitatively confirmed the validity of the theories regarding the three broadening mechanisms.

Experiments have been also performed on the fourth broadening mechanism, "Stark and quadrupole broadening".[212, 214, 218, 219] However, only a few aspects of this subject are understood because of the difficulty in producing appropriate samples. Only a limited number of samples containing the narrow range of ionized impurity concentrations were employed in most of the previous studies. Their results were also complicated by the co-existence of "concentration broadening" in uncontrolled manners.

In order to understand how we have overcome these experimental difficulties, we shall begin with a brief description of the fabrication of suitable samples which allow the study of the "Stark and quadrupole broadening" mechanism. By using symbols N_{MJ} and N_{MN} for the majority and minority impurity concentrations, respectively, the net-impurity concentration N_{Net} is given by N_{MJ}-N_{MN} and the compensation ratio K is N_{MN}/N_{MJ}. A typical impurity absorption measurement is performed at low temperatures where a significant number of carriers are frozen-out, i.e., they are bound to the majority impurity sites. The concentration of the light absorbing neutral impurity centers N_0 is equal to $N_{Net}=N_{MJ}-N_{MN}$ and the concentration of the ionized impurity centers N_I is equal to

$2N_{MN}$. Assuming each of the N_{MN} minority centers compensates only one carrier (i.e., shallow impurities of the opposite types), a half of the $2N_{MN}$ ionized impurities are positively charged (donors) while the other half is negatively charged (acceptors). This shows that the number of ionized impurities can be controlled by adjusting the compensation ratio of a sample. However, random changes in the compensation ratios between different samples do not solve all of the problems associated with the study of the electric field broadening. As was pointed out, one has to somehow differentiate the effect of the electric-field broadening from that of other broadening mechanisms, especially, from the effect of the concentration broadening. It is impossible to completely eliminate the contribution of the "concentration broadening" when one tries to eliminate the relatively small contributions of the "phonon life-time" and "strain" broadening by doping the semiconductors to the level $N_{Net}a^3>5x10^{-6}$ (a is the Bohr radius of the impurity). However, one can at least maintain the same contribution of the "concentration broadening" between different samples by keeping the same concentration of the neutral impurities in all samples. Therefore, the ideal set of samples for this experiment is a series of semiconductors with the same N_{MJ}-N_{MN} but different compensation ratios K in the range between 0 and 1. Unfortunately it has been impossible to achieve the required level of precision of majority and minority impurity control with conventional bulk doping methods.

In this work, we have produced such a set of ideal samples by using neutron transmutation doping (NTD) of high purity Ge single crystals containing controlled atomic fractions of ^{70}Ge and ^{74}Ge isotopes.[220] This method allows independent control of the majority N_{MJ} and minority N_{MN} impurity concentration. Therefore, the independent control of the net-impurity concentration N_{MJ}-N_{MN} and the compensation ratio $K=N_{MN}/N_{MJ}$ became possible for the first time. The NTD method is also known to produce extremely homogeneous distributions of both the majority and minority impurities down to atomic levels.[88] Using this method, we have produced a series of p-type

Ge:Ga,As samples of constant $N_{Net}=[Ga]-[As]=5\times10^{14}cm^{-3}$ with K ranging between 0.082 and 0.93. In this paper, we shall quantitatively compare the widths of Ga absorption lines in this set of samples to theoretically predicted linewidths [208-210] due to the "Stark and quadrupole broadening" mechanism. Quantitative understanding of the electric-field broadening mechanism allows for the future application of infrared absorption spectroscopy for a determination of K in highly compensated semiconductors.

5.1.2 Theory

We shall first consider the energy shift of hydrogenic impurity bound levels in an external electric field. Choosing the neutral impurity center as the origin of spherical coordinates, the external potential V(r) evaluated at a point $\vec{r}$ near the neutral impurity is given as: [221]

$$V(r) = \sum_i \frac{e_i}{\kappa|\vec{R}_i - \vec{r}|}$$

$$= 4\pi \sum_i \frac{e_i}{\kappa R_i} \sum_{l=0}^{\infty} \sum_{m=-l}^{l} \frac{1}{(2l+1)} \left(\frac{r}{R_i}\right)^l Y^*_{lm}(\theta_i,\phi_i)\, Y_{lm}(\theta_i,\phi_i), \qquad (5.1)$$

where κ is the dielectric constant, e_i is the charge on the *i*th impurity ion, R_i, θ_i, ϕ_i denote the position of *i*th ion in the spherical coordinates, Y_{lm} is the spherical harmonics, and r, θ, ϕ are the spherical coordinates of $\vec{r}$. As pointed out by Larsen [208], the multipole expansion of V(r) is equivalent to a Taylor expansion of V(r) about the donor center (r=0). The $l=0$ terms in Eq.1 correspond to V(r) potential evaluated at r=0. Because $l=0$ terms do not depend on r, these terms simply shift all levels of the neutral impurity up or down and do not change the energy spacing between the levels, i.e., $l=0$ terms do not cause a shift in hydrogenic transition energies. $l=1$ terms on the other hand produce the well known Stark shift of the hydrogenic transition energies. These terms reduce to a simple potential $-\vec{E}(0)\cdot\vec{r}$ of the uniform electric field $\vec{E}(0)$. For weak electric fields the Stark shifted energy levels ε of the impurities with quantum numbers n, m, n_1 and n_2 are given by the familiar expression:

$$\varepsilon = \frac{e^2}{2\,a\,n^2} + \frac{3}{2}\,n\,(n_1\text{-}n_2)eEa - a^3\,[17n^2\text{-}3(n_1\text{-}n_2)^2\text{-}9m^2\text{+}19]\,\frac{E^2n^4}{16}\; + \ldots., \qquad (5.2)$$

where n is the principle quantum number, m is the magnetic quantum number, a is the effective Bohr radius, and n_1 and n_2 are integers greater than or equal to zero which obey:

$$n = n_1 + n_2 + |m| + 1. \qquad (5.3)$$

In Eq.5.2, the second term proportional to E is the linear Stark term while the third term proportional to E^2 is the quadratic Stark term. Finally, it can be shown that the l=2 terms in Eq.1 are linear in the electric field gradients, e.g., $\propto(\partial E/\partial z)_{r=0}$. The broadening due to l=2 terms is known as a quadrupole broadening.

From the preceeding discussion, we found three distinctive mechanisms that lead to electric field broadening of hydrogenic transition peaks: the linear Stark effect ($\propto$E), the quadratic Stark effect ($\propto E^2$), and the quadrupole interaction ($\propto\partial E/\partial z$). Extensive theoretical studies conclude that the increase of linewidths is proportional to:

(i) $(N_I/N_0)^{2/3}$ when the linear Stark effect dominates [209],

(ii) $(N_I/N_0)^{4/3}$ when the quadratic Stark effect dominates [209, 222],

(iii) N_I/N_0 when the quadruple interaction dominates [209, 222]

The quadrupole interaction is proposed to be dominant in the limit of small N_I while the quadratic Stark effect becomes most important in the other limit.[209, 222] The effect of the linear Stark terms turned out to be much smaller than the other two effects, i.e., it can be neglected to the first order.[209, 222] Thus, it is of significant interest to see whether linewidths in our samples obey one of the $\propto(N_I/N_0)^{4/3}$ or $\propto N_I/N_0$ dependencies. Neither of the dependencies has been experimentally demonstrated before.

The other point of interest is the quantitative comparison of our experimentally measured linewidths to theoretically predicted ones. For many years the electric field line broadening mechanism has been theoretically investigated by assuming a random distribution of frozen carriers among majority impurity centers.[208, 209, 212, 214, 223] The most in-depth and complete studies were performed by Larsen.[208, 209] After an extensive derivation of the relevant mathematical expressions, Larsen used the Monte Carlo technique to calculate the shape of the 1s-2p and 1s-3p transition absorption lines due to donors associated with a simple spherical conduction band. However, as Larsen himself has pointed out in his original paper [208], it has not been clear how appropriate it is to assume a random distribution of frozen carriers among neutral impurities. In reality, the frozen carrier distribution is likely to be correlated at low temperatures [173, 224], i.e., the carriers distribute themselves in such a way that the ionized impurity distributions are "frozen" in the state of minimum potential energy. It should be stressed here that the correlated ionized impurity distribution of interest to us is not the "technological" correlation introduced during the sample doping processes. Throughout this section we assume a completely random distribution of majority and minority impurities as in the case for our NTD $^{70/74}$Ge:Ga,As samples. The effect of the correlated ionized impurity distribution in the theory of the Stark and quadrupole broadening mechanism was first included in the paper by Kal'fa and Kogan for p-type Ge.[222] Later the same group [210] incorporated the correlation effect in their numerical calculation of the 1s-2p absorption line width due to donors associated with a simple spherical conduction band. According to Kogan and Van Lien [210] the correlation energy is of the same order of magnitude as the Coulomb interaction energy between majority impurities, i.e., $\sim e^2 N_{MJ}{}^{1/3}/\kappa$. Therefore, one would expect to see a strong effect of the correlation if the impurity absorption measurement is taken at temperatures $k_B T << e^2 N_{MJ}{}^{1/3}/\kappa$. On the other hand, one would expect Larsen's random distribution based result when $k_B T >> e^2 N_{MJ}{}^{1/3}/\kappa$. Thus the transition temperature T_t is given by:

$$T_t = e^2 N_{MJ}{}^{1/3} / k_B \, \kappa. \tag{5.4}$$

This transition of the linewidths was later observed by Baranovskii et al. in n-type GaAs at the corresponding transition temperature T_t=6K.[225, 226] The result of Baranovskii et al. is going to be discussed later in this section.

Unfortunately, no quantitative calculation has been reported regarding the impurity absorption linewidth arising from acceptors in semiconductors. Thus, in this section, we are going to quantitatively compare the linewidths of 1s-2p-like Ga absorption transitions to theoretically predicted linewidths of the 1s-2p transition in shallow donors. Our approach should be accurate to the first order, i.e., our experimental results should provide an opportunity to quantitatively examine the "random theory" of Larsen [209] and the "correlated theory" of Kogan and Van Lien.[210]

5.1.3 Experiment

Using the sample fabrication method described in Sec.3.3, eight p-type Ge:Ga,As samples of constant N_{Net}=[Ga]-[As]=5×10^{14}cm^{-3} but different K in the range between 0.082 and 0.93 were produced. Table 5.1 shows the Ga and As concentrations in each sample predicted from the combination of the isotopic composition and the thermal neutron irradiation time. Variable temperature Hall measurements were performed for all samples in order to confirmed the values of [Ga] and [As] listed in Table 5.1. All [Ga] and [As] were found to be accurate within error of 5%. The low temperature ionized impurity concentration $N_I = 2N_{MN} = 2[As]$, is also shown for each sample in Table 5.1.

Infrared absorption measurements were performed on a BOMEM DA.3 Fourier-transform spectrometer. An unapodized resolution of 0.054cm^{-1} was employed in all our measurements. A Si bolometer operating at 4.2K was used as the detector. A variable temperature stainless-steel optical cryostat was used for measurements over the desired temperature range. The temperature of the sample was monitored at the sample mount and controlled by an automatic temperature controller, allowing the sample to be maintained at any desired temperature between 1.8K and room temperature with an accuracy of 0.1K.

Table 5.1 Ga, As and ionized impurity concentrations in each sample

K	[Ga] (cm^{-3})	[As] (cm^{-3})	N_I (cm^{-3})
0.082	$5.5x10^{14}$	$4.5x10^{13}$	$9.0x10^{13}$
0.32	$7.4x10^{14}$	$2.4x10^{14}$	$4.8x10^{14}$
0.4	$8.3x10^{14}$	$3.3x10^{14}$	$6.6x10^{14}$
0.5	$1.0x10^{15}$	$5.0x10^{14}$	$1.0x10^{15}$
0.6	$1.3x10^{15}$	$7.5x10^{14}$	$1.5x10^{15}$
0.76	$2.1x10^{15}$	$1.6x10^{15}$	$3.2x10^{15}$
0.87	$3.9x10^{15}$	$3.4x10^{15}$	$6.8x10^{15}$
0.93	$7.1x10^{15}$	$6.6x10^{15}$	$1.3x10^{16}$

5.1.4 Results

Fig.5.1 shows four selected absorption spectra taken with samples of different compensation at T=4.6K in the wavenumber range 66-76cm^{-1}. Each spectrum shows two distinct peaks corresponding to C- and D-hole transitions in neutral Ga acceptors according to the notations introduced by Jones and Fisher.[227] We are going to concentrate on the linewidths of C- and D-transitions for the rest of the paper.

In the effective mass approximation, the ground state of a group III impurity in Ge has a symmetry Γ_8^+ of the cubic group O_h. The D-transition corresponds to the Γ_8^+ to Γ_8^- hole excitation, while the C-transition is the excitation from Γ_8^+ to the accidentally degenerate Γ_7^- and Γ_8^- state. The classification of the familiar hydrogenic spectroscopic notation of s,p,d... are given as: [228]

$$s \rightarrow \Gamma_8^+ \tag{5}$$

$$p \rightarrow \Gamma_7^- + \Gamma_6^- + 2\,\Gamma_8^-. \tag{6}$$

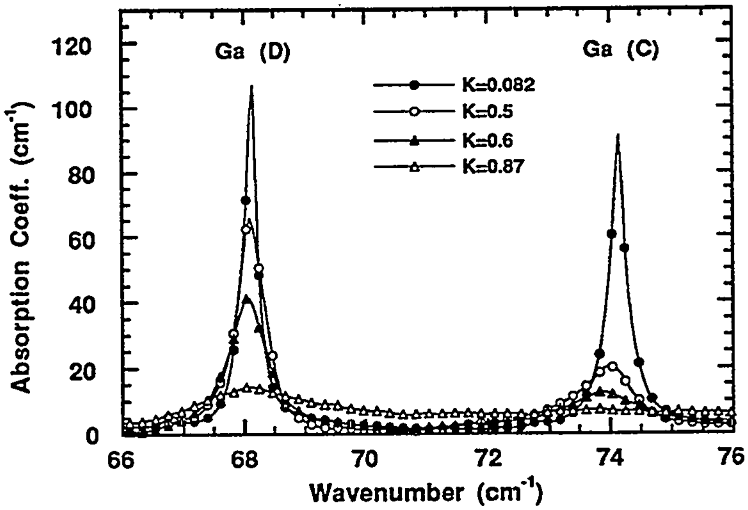

Fig.5.1 Absorption spectra of four Ge:Ga,As samples of different K taken with resolution $0.054\mathrm{cm}^{-1}$.

It can be shown that the final state Γ_8^- of the D-transition represents one of the two Γ_8^- of the 2p-like state. Similarly, the two final states Γ_7^- and Γ_8^- belong to 2p and 3p-like states, respectively. Therefore, one may classify the D-transition as a 1s-2p-like transition while the C-transition being a 1s-2p,3p-like transition:

D and C-transition linewidths broaden with an increase in compensation as shown in Fig.5.1. The area under D-transition-peaks in all samples remains approximately constant reflecting the same concentration of neutral Ga absorbing centers ($[\mathrm{Ga}^0]\sim5\mathrm{x}10^{14}\mathrm{cm}^{-3}$). The area under the C-transition-peaks, on the other hand, decreases rapidly with the increasing compensation. Because the excited states of the C-transition have a larger orbital than the excited states of the D-transition, it is likely that the excited states of the C-transition are more strongly affected by the surrounding random electric fields. Thus, the sharpness of the excited states of the C-transition tends to be washed out very quickly with the increasing compensation. However, the reason for the decrease in the area under the C-transition-peaks is not clear. All D-transition peaks seem to broaden symmetrically around the peak center while some of the C-transitions seem to broaden more towards lower wavenumbers. The asymmetric broadening is most likely due to the quadratic Stark effect. Note that the quadratic interaction broadens a peak towards lower energies as one can see from the negative sign of the third term in Eq.5.2.

The full width at half maximum (FWHM) of each peak is determined using standard Lorentzian fitting procedures:

$$\text{Absorption Coeff. (k)} = A \frac{\text{FWHM}/2}{(k-k_0)^2 + (\text{FWHM}/2)^2} \tag{5.7}$$

where k is the wavenumber, and A and k_0 are the amplitude and the position of the peak, respectively. The fitting results are shown in Fig.5.2 for the D-transitions of the selected samples. Good fits are obtained up to K~0.76. However, Eq.5.7 does not represent the shape of a peak very well when samples have a compensation K larger than 0.76. Therefore, FWHM of all K>0.76 samples are determined by directly measuring the width at the half maximum rather than by the Lorentzian fitting. FWHM of C lines is determined in the same manner.

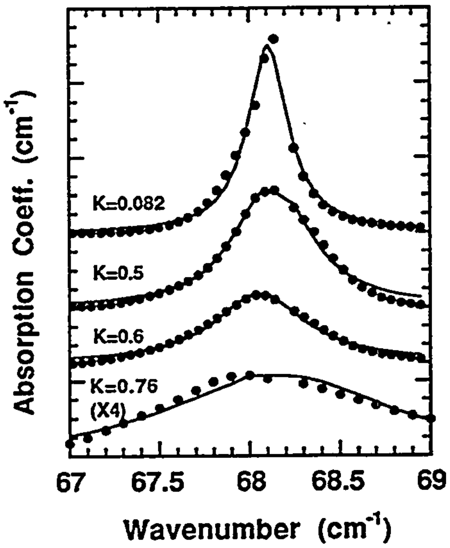

Fig.5.2 Full width at half maximum (FWHM) determination of the D-peaks using the Lorentzian fit:

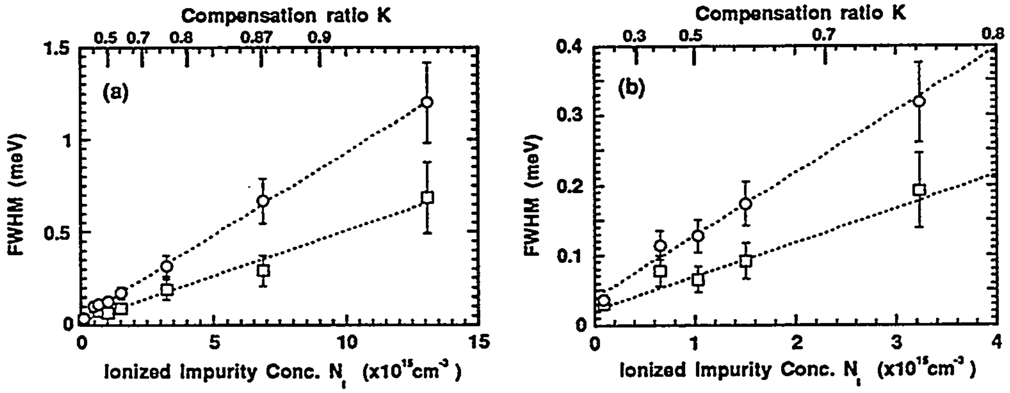

Fig.5.3 Experimentally measured FWHM of the C (○) and D (□) peaks in p-type Ge:Ga,As.

Fig.5.3.(a) shows our main experimental results, the FWHM as a function of the ionized impurity concentration at T=4.6K. The low ionized impurity concentration region (<4x10^{15}cm^{-3}) of Fig.5.3.(a) is expanded in Fig.5.3.(b). The linewidth of C- and D-transitions is temperature independent as long as the temperature is below 15K so that the thermal ionization of the neutral Ga centers is negligibly small. Thus the widths shown in Fig.3 represent characteristic FWHM of C- and D-transitions below T=15K.

The dependence of the C- and D-transition linewidths with respect to the ionized impurity concentration is linear within our experimental error. The best linear fits to the experimental points are represented by dashed lines. At $N_I=0$, both fits have non-zero values 44μeV and 22μeV for C- and D-transition linewidths, respectively. These small residual broadenings arise due to contributions of other broadening mechanisms ("concentration broadening", "phonon life-time broadening", etc.). As it was already discussed in section 5.1.2, the $FWHM \propto N_I/N_0$ relation has been predicted when the quadruple interaction is dominant. This experimentally determined linear dependence, which is shown for the first time, is theoretically predicted for lightly doped semiconductors. It appears, however, that the quadrupole interaction is the dominant broadening mechanism even in moderately doped Ge samples of $N_{Net}=5\times10^{14}cm^{-3}$ and K<0.93. It was pointed out previously that the C-transitions broaden asymmetrically to the lower wavenumbers, and that this may be due to the contribution of the quadratic Stark effect. However, the contribution of the third term in Eq.5.2 must be significantly smaller that $l=2$ terms in Eq.1 since we clearly observe the $\propto N_I/N_0$ dependence for C-transition linewidths in Fig.3.

Fig.4 (a) and (b) show the temperature dependence of the C- and D-transition linewidths in the K=0.082 and K=0.5 samples, respectively. The linewidths are constant in both samples when T<15K.

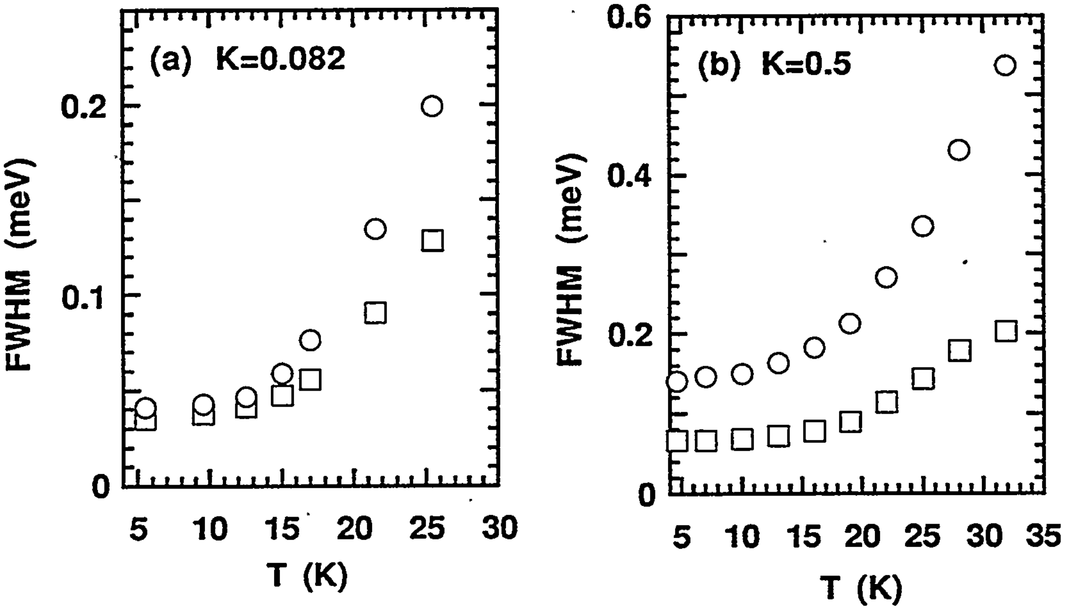

Fig.5.4 Temperature dependence of the C (O) and D (□) transition linewidths in the (a) K=0.082 and (b) K=0.5 samples

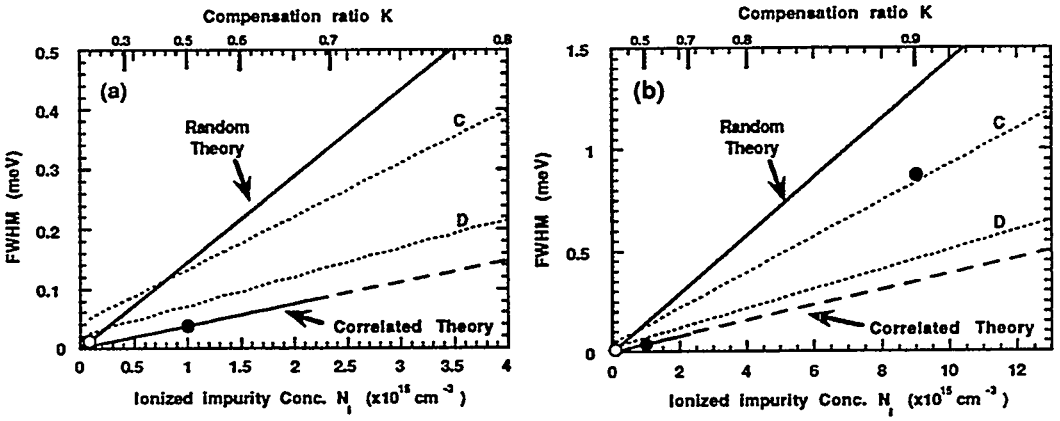

Fig.5.5 Comparison of the experimentally measured FWHM (dotted lines) to linewidths predicted by "random theory" of Larsen (○) [209] and "correlated theory" of Kogan and Van Lien (●) [210] Solid lines representing both theories are drawn following the procedures described in the main text. Fig.5.(b) shows a broader N_I region than Fig.5.(a).

5.1.5 Discussions

Fig.5.5.(a) shows the ionized impurity concentration dependencies of two theoretical linewidths of hydrogenic donor 1s-2p transitions representing the "random" ionized impurity distribution theory of Larsen [209] and the "correlated" distribution theory of Kogan and Van Lien [210] in the range $0 \leq N_I \leq 4 \times 10^{15} cm^{-3}$. Two dashed lines shown in the same plot represent the fits we obtained in Fig.5.3 for the experimental C- and D-linewidths. First, it is important to explain how these two theoretical curves were determined.

The "random" theory predicts that the linewidth is determined solely by the concentration of ionized impurity centers. Larsen's Monte Carlo result for $N_I a^3 = 5 \times 10^{-6}$ (Fig.2 in Ref.209) shows FWHM of 10.8×10^{-4}Ry* where Ry* is the effective Rydberg energy. Taking Ry*=11meV for Ga in Ge, we find one point, FWHM=12μeV at $N_I = 8 \times 10^{13} cm^{-3}$ in Fig.5.5. Based on our experimentally determined linewidths dependence $\propto N_I/N_O$, we simply draw a straight line (the solid line labeled "Random theory") which goes through both the origin and the point (denoted by an open circle in Fig.5.5) given by Larsen's calculation.

The linewidth predicted by the "correlated" theory also depends solely on the ionized impurity concentration when the compensation ratio K is smaller than 0.7.[210] However, when K>0.9, the potential fluctuations due to ionized impurities become much larger than the correlation energy, so that the effect of the correlation disappears. As a consequence, the width of the peaks becomes comparable with the prediction of the "random" theory when K>0.9. The compensation range 0.7<K<0.9 can be characterized as a "correlated" to "fluctuating potential" transition region. Kogan and Van Lien [210] performed a numerical calculation of the linewidth as a function of the majority impurity concentration N_{MJ} for two different compensations: K=0.5 and K=0.9. They assume the quadruple interaction to be dominant, i.e., the linewidths due to the given compensation scales linearly with N_{MJ} (see Table 1 of Ref.210). Therefore, we find two theoretically predicted points for our $N_{Net}=5\times10^{14}cm^{-3}$ condition in Fig.5.5 (two filled circles), one at $N_I=1\times10^{15}cm^{-3}$ (K=0.5) and the other at $N_I=9\times10^{15}cm^{-3}$ (K=0.9). With the K=0.5 point we can determine the prediction of the "correlated theory" for any compensations between 0 and 0.7 because of the $FWHM\propto N_I/N_0$ relation in this regime, i.e., we draw a straight line (the solid line labeled "Correlated theory" in Fig.5.5) which goes through both the origin and the K=0.5 point (denoted by an close circle) given by Kogan and Van Lien's calculation. On the other hand, we cannot determine the prediction of the "correlated theory" anywhere above K=0.7 except for the K=0.9 point given by Kogan and Van Lien.

It has been pointed out in the previous section that the D-transition has the characteristics of a 1s-2p-like transition in a hydrogenic impurity. Therefore, we compare our experimentally measured linewidths of the D-transitions to the theoretical results calculated for the 1s-2p electronic transition in donors. In the lower N_I regime (K<0.8) shown in Fig.5.5.(a), the linewidths of the D-transition agree much better with the "correlated" theory of Kogan and Van Lien than Larsen's "random" theory. We believe this to be the direct evidence for the correlated distribution of ionized impurities at low temperature. Larsen's theory which neglects the correlation effect clearly overestimates the width by 4-5 times.

Even though the "correlated theory" agrees well with experimental results in the low N_I range shown in Fig.5.5.(a), it is interesting to note the deviation of Kogan and Van Lien's theory from our experimental results at K=0.9 point in Fig.5.5.(b). In fact, although Kogan and Van Lien for K>0.7 samples predicted the deviation of the 1s-2p transition linewidths from $\propto N_I/N_0$, we observe the linear linewidth dependencies all the way up to K=0.93 for both C- and D-transitions. This implies that the quadruple interaction some how remains strong up to such high K.

Next we discuss our interpretation of the temperature dependent absorption linewidths shown in Fig.5.4. The experimental confirmation of Kogan and Van Lien's theoretically determined linewidths for K<0.7 at low temperature motivates us to search for the correlated to random (CR) ionized impurity distribution transition at elevated temperatures. Using Eq.5.4, we find T_t for the CR transition in the K=0.082 and K=0.5 samples shown in Fig.5.4 to be 8.5K and 10.4K, respectively. However, it can be seen in Fig.5.4 that the width of C- and D-peaks in the both samples stays temperature independent up to T=15K, and rapidly increases at temperatures larger than 15K. This increase may be due to thermal ionization of neutral Ga impurities rather than due to the CR transition. In order to confirm this, we first calculate the free hole concentration p(T) in these samples by solving the following semiconductor free carrier statistics equation: [136]

$$\frac{p\,(p+N_{MN})}{(N_{MJ}-N_{MN}-p)} = \frac{1}{\beta} N_g \exp\left(-R_y^*/k_B T\right) \tag{8}$$

where β is the degeneracy factor 4 for acceptors, $N_g=1.2\times10^{15}T^{3/2}\mathrm{cm}^{-3}$ is the effective density of states in the valance band, and R_y^* is the ionization energy of the majority (Ga) impurities, then we find the ionized impurity concentration N_I as a function of temperature:

$$N_I\,(T) = n\,(T) + 2N_{MN}. \tag{9}$$

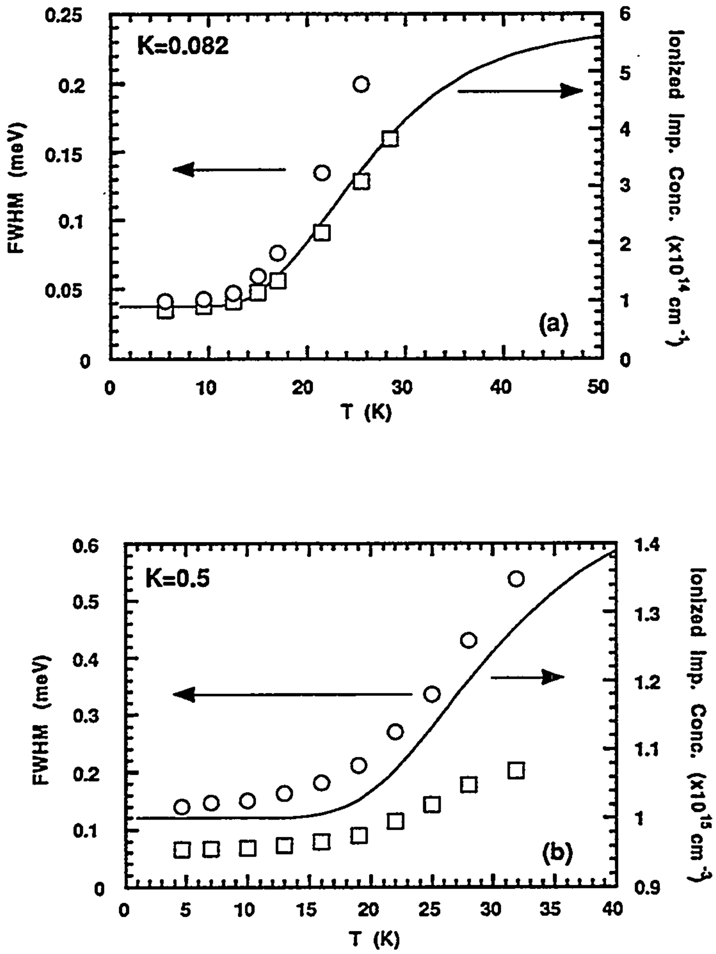

Fig.5.6 Temperature dependence of the C (○) and D (□) linewidth in the samples with (a) K=0.082 and (b) K=0.5. The solid curves are the calculated ionized impurity concentration in each sample.

The results for K=0.082 and 0.5 samples are shown in Fig.5.6 (a) and (b), respectively, together with the linewidths of C- and D-transitions as a function of temperature. We find that the temperature profiles of the C- and D-transition linewidth exactly match with those of N_I in both samples. Therefore, the widths increase above T=15K is due to the thermal ionization of Ga neutral impurities and we did not observed any signs of the CR transition at T_t as predicted by Kogan and Van Lien (Eq.5.4). It is somewhat puzzling not to observed the CR transition in our Ge, especially after obtaining good agreement between our experimentally measured linewidths and the "correlated theory". It may be possible that the predicted T_t is slightly too high so that the CR transition is hidden somewhere above T=15K.

In contrast to our result, Baranovskii et al. [225, 226] reported on the observation of the CR transition in n-type GaAs recently. They measured the temperature dependence of the 1s-$2p_0$ transition linewidth by performing photothermal ionization spectroscopy [105] (PTIS) with a variable magnetic induction. Fig.5.7 shows the results of Baranovskii et al. for one sample (N_{MJ}~$10^{14}cm^{-3}$ and K=0.23) together with the calculated equilibrium ionized impurity concentration N_I assuming zero external magnetic induction. The external magnetic induction causes the donor ionization energy to become larger [229], i.e., the onset of the thermal ionization may be at higher temperature than what is drawn in Fig.5.7. The CR transition observed at T_t=6K is clearly separated from the higher temperature region in which the thermal ionization becomes significant, i.e., unlike our results, this experimental evidence supports the CR transition predicted by Kogan and Van Lien.

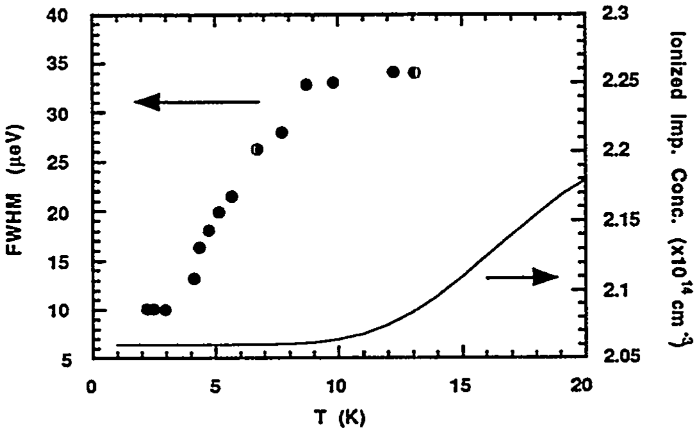

Fig.5.7 Temperature dependence of the 1s-$2p_0$ linewidth in n-type GaAs reported in Ref.226 The solid curve is the calculated ionized impurity concentration in zero magnetic field.

Lastly we shall discuss the possibility of determining the compensation ratio K using absorption spectroscopy. Baranovskii et al.[226] proposed that the comparison of the linewidth before and after the CR transition allows for the determination of K. This method obviously does not work for us since we do not observe the CR transition. From our point of view, K can be determined in a much simpler way using the following steps.

(1) Measure N_{Net} using Hall effect or capacitance-voltage measurements.

(2) Record one low-temperature absorption spectrum to find the chemical identity of the impurity (from the position of peaks) and the linewidth of the 1s-2p-like transition.

(3) The slope of Kogan and Van Lien's straight line between K=0 and 0.7 (in Fig.5.4) depends on N_{MJ}. We only know N_{Net} at this point, so that we find the slope of Kogan and Van Lien's theory that is consistent with experimentally measured linewidth and the relation $N_{Net} = N_{MJ} - N_{MN} = N_{MJ} - 0.5N_I$.

Our experimental results show that the FWHM is proportional to N_I even up to K=0.93. Thus it should be possible to find K of samples not only up to 0.7 but at least up to 0.93 with this method. However, at this point, the K determined by this method contains some error, partly because of the large error bars that accompany the linewidth measurement in high K samples, and partly because of the slight offset between the experimentally observed D-transition linewidths and those obtained from Kogan and Van Lien's theory. This offset may be due to the fact that we are comparing acceptor absorption spectra to the theoretical results for donors. Clearly, our study needs to be repeated using n-type semiconductors in order to draw more precise conclusions.

5.1.6 Summary

We have quantitatively shown for the first time that the FWHM calculation based on correlated electron distribution is the appropriate model for the quadrupole dominated electric field broadening of 1s-2p-like transitions. We did not, however, observe any signs of the correlated to random impurity distribution transition around temperatures predicted by theory. It is of great interest to repeat the same study using n-type samples of the similar net-impurity concentration. The quantitative understanding of the electric field broadening mechanism will allow us to determine the compensation ratio in any samples using infrared absorption spectroscopy.

Chapter 6 Summary and Conclusions

I have presented and discussed a wide variety of solid state experiments we have performed using neutron transmutation doped isotopically engineered Ge. The high quality of the Ge crystals grown by the modified vertical Bridgman system developed in this thesis has been the key for the success of the project. All Ge crystals before neutron transmutation doping had very high chemical purity (electrically active residual impurity concentrations $\sim 10^{12}cm^{-3}$). Our neutron transmutation doping process has been calibrated by detailed studies such as the determination of the thermal neutron cross-section of the ^{70}Ge and ^{74}Ge isotopes and annealing of fast neutron damage. The combination of the isotopically engineered Ge and the neutron transmutation doping method guaranteed unprecedented doping uniformity, and allowed for the independent control of the net-impurity concentrations and the compensation ratios. Previous difficulties in making appropriate samples for carrier transport and optical property studies have been overcome by the sample fabrication method developed in this thesis.

In the free carrier transport studies, our experimentally measured neutral impurity scattering rate in semiconductors have agreed very well with the theoretical rate estimated by scaling the phase shift calculations for the hydrogen atom to the impurity atoms in semiconductors. The experimentally measured rate of the ionized impurity scattering in highly compensated semiconductors, on the other hand, did not agree with any of the theories we tested. Our experimental results suggested that the screening due to ionized impurities centers is not as efficient as the predictions of the theories.

In the study of the hopping conduction, we have examined the temperature dependent resistivities in two sets of samples with different compensation ratios ($K<0.01$ and $K=0.32$). For the ^{3}He refrigerator temperature range bolometer applications ($T\sim300mK$), NTD ^{70}Ge:Ga samples with $K<0.01$ showed a factor of 2.6 higher sensitivity than NTD ^{Nat}Ge:Ga,As with $K=0.32$. Theoretically expected $\ln\rho \propto T^{-1/2}$ dependencies were observed in both sets of samples. However, some of the details of the resistivity behaviors could not be explained with a standard theory of the variable range hopping conduction. Further investigations of hopping conduction are necessary to achieve a better understanding of this process.

Our transport study with barely metallic NTD ^{70}Ge:Ga samples yielded a preliminary result which may put the end on the recent controversy in the field of metal-insulator transition. The critical exponent α of conductivity obtained with our homogeneously doped samples is ~0.43, i.e., the recently reported α~1.3 may be indeed due to non-uniform dopant distribution in the samples, as claimed by researchers who disagree with this result. It is necessary for us to perform a few more low temperature conductivity measurements in order to unambiguously establish the value of α in our NTD ^{70}Ge:Ga samples.

The infrared absorption spectroscopy of highly compensated Ge allowed a quantitative study of the electric field broadening mechanism of hydrogenic impurity absorption lines. We have found excellent agreement of our data with the theory which is based on the correlated distribution of ionized impurity centers. A new method to determine compensation ratios in highly compensated semiconductors has been proposed.

Chapter 7 Future Work

Many of the transport and optical studies described in this thesis should be considered as on-going investigations.

The success of our neutral impurity scattering study with hydrogenic impurities encourages us to inspect neutral impurity scattering by He- and Li-like dopants in semiconductors. The nature of neutral impurity scattering by double (Hg) and triple (Cu) acceptors in Ge has been studied by Blakemore [158] and Norton et al.[156], respectively, and they compared the experimentally measured mobilities to theoretical mobilities limited by hydrogen-like scattering centers. Both groups could not obtain satisfactory agreement between their experimental results and their calculations. Rather than this hydrogenic impurity approach, we believe that the electron-He and electron-Li scattering cross-sections in free space should be scaled to semiconductors for scattering by double and triple acceptors, respectively. We are in the process of making mobility measurements in Ge:Be and Ge:Zn samples, and of scaling the electron-He scattering cross-sections to semiconductors. In the future we hope to study neutral impurity scattering by Cu in Ge. The ground state of this triple acceptor, normally accommodating three 1s holes, can be reconfigurated into an atomic Li-like $1s^2 2s^1$ arrangement by the application of [100] stress larger than 4kbar.[233] Thus it is interesting to perform Hall effect measurements under stress to find the validity of scaling electron-Li scattering cross-sections to semiconductors.

The ionized impurity scattering study has raised many questions regarding the charged impurity screening mechanism in highly compensated semiconductors. In this thesis we have compared the experimentally measured Hall mobilities to existing theories without including detail corrections such as the warping and double degeneracy of the valance band. Our investigation has shown that the collection of one-electron scattering does not appropriately describe the experimental results. It seems that the successful introduction of the many-body effect (e.g., the correlated motion of carriers, etc.) is the key for the development of the ionized impurity scattering theory.

Our ability to dope semiconductor very uniformly may bring the studies of hopping conduction and metal-insulator transition (MIT) into new era. Inhomogeneity of the impurity distribution has been a issue that was raised many times in MIT studies especially when new experimental evidence was proposed. As was shown in Sec. 4.5.2, it is interesting to re-examine some of the controversial hopping and metal-insulator conductivity data that were previously published. Our ability to control the majority and minority impurity concentrations allows us to study the compensation dependencies of hopping conduction and metal-insulator transitions. Many different critical phenomena such as behaviors of the dielectric constant, specific heat, electron spin states, thermo-electric power, and optical properties around metal-insulator critical concentrations can be studied using isotopically controlled NTD Ge samples.

The infrared spectroscopy study of highly compensated p-type Ge has allowed us to find the nature of the electric-field broadening mechanism. As was stated in Sec.5.1.6, it is important to repeat the same study using n-type materials. It has been proposed [96] that the shallow impurities in highly compensated, non-degenerate semiconductors should form a number of H_2^+-like molecules due to correlations induced by long-range Coulomb interactions. Observation of new spectroscopic lines arising from impurity pairs or clusters may lead to determination of structures of such defects.

Germanium and diamond isotope engineering has enabled many new studies. There can be little doubt that we will see experiments with isotopically controlled Si bulk crystals and superlattices. The Si isotope superlattices should provide ideal structures for investigating Si self-diffusion. Isotopically controlled III-V and II-VI compound semiconductors and their alloys are most promising in the context of NTD. The selective doping of these semiconductors is made possible by the particular choice of host semiconductor isotopes. One can also study self- and impurity-diffusion in compound semiconductors by using isotope superlattices.

The end of the cold war five years ago has made highly enriched Ge isotopes more readily available to the western scientific community. We have had the fortune to be able to participate in the field of Ge isotope engineering from the beginning of this post cold war period. Isotopically engineered semiconductors offers almost countless possibilities for the advancement of semiconductor science and technology. Further understanding of the isotope effect becomes very important especially in the era of the atomic level control of semiconductor structures.

Appendix A: Semiconductor Characterization Techniques

Raman Spectroscopy

When light is scattered from the surface of a sample, the scattered light is found to contain mainly wavelengths that were incident on the sample (Raleigh scattering) but also different wavelengths at very low intensities (few parts per million) that represent an interaction of the incident light with the material. The interaction of the incident light with optical phonons is called Raman scattering. Since the intensity of Raman scattered light is very weak, Raman spectroscopy requires an intense monochromatic light source like a laser and very high resolution spectrometers.

Various properties of the sample can be characterized using this technique. One obvious one is the optical phonon frequencies and the phonon density of the states at **k**=0 in the E-k space (Fig.1.2). Impurity vibrational modes can also be studied. This study may allow for identification and concentration of defects. Raman spectroscopy is also sensitive to crystal or defect structures, since, for example, different crystal or defect orientations give slightly different Raman shifts.

Inelastic Neutron Scattering

It is possible to extract the detailed form of the normal-mode phonon dispersion relations (Fig.1.2) from experiments in which the lattice vibrations exchange energy with an incident beam of neutrons. One can view the energy lost (or gained) by a neutron while interacting with a crystal as being due to the emission (or absorption) of phonons, and by measuring the emergent angles and energies of the scattered neutrons one can extract direct information about the phonon spectrum covering the entire E-**k** space.

Photoluminescence Spectroscopy (PL)

This technique relies on the excitation of an electron (hole) across the band gap by incident radiation and subsequent radiative recombination photon emission. The emitted light is detected for analysis. Any non-radiative recombination events are not detected and detract from the PL signal. PL can be used to detect and identify impurities and defects in semiconductors. It also allows for determinations of phonon energies and band gaps as described in Sec.1.2.1.1 and Sec.1.2.1.4.

Secondary Ion Mass Spectroscopy (SIMS)

The technique relies on removal of material from a solid by sputtering and on mass spectroscopy analysis of the sputtered ionized species. One can find the depth profile of impurities and the isotopic or chemical composition of the material.

Electron Paramagnetic Spin Resonance (EPR)

Many point defects in a semiconductor have an unpaired electron spin. The electron spin produces a magnetic dipole moment and the orbit adds a further contribution. If such centers are present at low concentration so that they are non-interacting the crystal becomes paramagnetic. When an external magnetic field B_0 is applied there is alignment of the magnetic dipoles which have discrete energy levels determined by quantum mechanical principles. The crystal is then subjected to incident radiation of frequency ν and for particular values of B_0 the differences in the energy levels ΔE of the magnetic dipoles will be given by $h\nu = \Delta E$, where h is Planck's constant. When this happens there will be absorption of the radiation, and the process is known as electron paramagnetic resonance (EPR).

Many microscopic details of a defect can be found if an EPR spectrum is properly interpreted. More specifically, the symmetry is found, the value of the nuclear spin of a central atom, the nuclear spins of neighboring host lattice atoms, the extent of the localized wavefunction, the response to the system to external constraints such as a uniaxial stress, etc.

Infrared Absorption Spectroscopy

This technique relies on optical excitation of electrons (holes) within available states of donors (acceptors). Measurements are usually taken at low temperature, so that the incident light excites carriers from their ground states to bound excited states. The intensity of the transmitted light is reduced when such transitions occur. The position of absorption peaks as a function of energy can be analyzed and matched to known absorption energies for identification of impurities and defects. Impurity and defect concentrations can also be found by comparing to known absorption coefficients of impurities and defects. The ionization energy of impurities can be found by exciting an electron (hole) from its ground state to the conduction (valance) band continuum. Chapter 5 of this thesis discusses the possibility of determining the compensation ratio using infrared absorption spectroscopy.

Photothermal Ionization Spectroscopy (PTIS)

This is a variation of the infrared absorption technique. Bound donor electrons are optically excited from the ground state to one of the bound excited states, and subsequently thermally excited from the excited state to the conduction band. Electrons excited into the conduction band are free carriers, i.e., this excitation process changes the sample conductivity. It is this photothermal conductivity change that is detected as a function of wavelength. This technique is known for its extremely high sensitivity. It allows for detection of $<10^8 cm^{-3}$ shallow impurities in Ge. Infrared spectroscopy, on the other hand, requires $10^{12} cm^{-3}$ or larger impurity concentrations. One of the disadvantages of this technique is the need for ohmic contacts. It is also difficult to obtain impurity or defect concentrations with PTIS to the precision one obtains with infrared spectroscopy.

Deep Level Transient Spectroscopy (DLTS)

Measurement of the small-signal capacitance of a reverse-biased semiconductor p-n or Schottky junction, and of its transient change with bias reduction pulses and temperature, allows the determination of three properties of deep traps: binding energy, concentration and capture cross-section. The most commonly used technique of this kind is known as "deep level transient spectroscopy (DLTS)". A description of this technique is quite involved and interested readers should consult Ref.133.

Appendix B: Free Carrier Mobility Calculation using the Relaxation Time Approximation

Suppose one electron of conductivity effective mass m_{con}^* is accelerated in a semiconductor by an applied electric field **E**. This electron is accelerated until it collides with a scattering center. At the time of collision the electron completely loses its drift velocity v_d and is re-accelerated from v_d=0 by $\mathbb{E}$. Although v_d of electrons in real semiconductors never goes to zero by scattering, this simplified picture of free electron transport allows us to conceptually understand the relaxation time approximation. The force **F** on an electron of charge e when electric field **E** is applied is given by,

$$\mathbf{F} = e\,\mathbf{E} = m_{con}^* \frac{d\,v_d}{d\,t}. \tag{B.1}$$

We now introduce an average relaxation time $<\tau>$ which is an average time of the electron travel between two collisions. Then,

$$v_d = \frac{d\,v_d}{d\,t} <\tau> = \frac{e\,\mathbf{E}}{m_{con}^*} <\tau> = \mu\,\mathbf{E} \tag{B.2}$$

and we have defined the mobility as:

$$\mu = \frac{e\ <\tau>}{m_{con}^*}. \tag{B.3}$$

Eq.B.3 is the expression for the mobility in the context of the relaxation time approximation. Because m_{con}^* of electrons and holes is well known for most semiconductors, one needs to find $<\tau>$ in Eq.B.3 as a function of temperature to calculate the temperature dependence of μ. When carriers are in thermal equilibrium with an environment (i.e., low field mobility), one may find the average $<\tau>$ by assuming a Maxwellian velocity distribution of a non-degenerate electron gas:

$$<\tau> = \frac{4}{3\sqrt{\pi}} \int_0^{\infty} \frac{x^{3/2} \exp(-x)}{\sum_{j=1}^{n} \tau_j^{-1}}\, dx \tag{B.4}$$

where $x = E/k_BT$ (E: electron kinetic energy, k_B:Boltzmann's constant), and τ_j^{-1} is the inverse relaxation time due to j^{th} carrier scattering mechanism (total of n different scattering mechanisms are included). It should be noted that the relaxation time approximation is valid only when all carrier scattering events are elastic, i.e., it is valid only at low temperatures (T<100K for Ge) where the effect of inelastic scattering processes (optical deformation potential, intervalley scattering) is negligible. Thus we will now concentrate on the low temperature regime of Ge (T<100K), and see how we can calculate $<\tau>$ considering three major scattering mechanisms: acoustic phonon deformation potential, ionized impurity, and neutral impurity scattering. Eq.B.4 then becomes:

$$<\tau> = \frac{4}{3\sqrt{\pi}} \int_0^{\infty} \frac{x^{3/2} \exp(-x)}{\tau_{ac}^{-1} + \tau_{ion}^{-1} + \tau_{neutral}^{-1}} dx \tag{B.5}$$

where τ_{ac}^{-1}, τ_{ion}^{-1}, and $\tau_{neutral}^{-1}$ are the inverse of the relaxation time due to acoustic phonon, ionized impurity, and neutral impurity scattering. Now we shall see how we can find τ_{ac}^{-1}, τ_{ion}^{-1}, and $\tau_{neutral}^{-1}$. All the following mathematical treatments will be in c.g.s. units. Conversion to SI units can be done by simply replacing all the dielectric constant ε with $4\pi\varepsilon\varepsilon_0$ where ε_0 is the permittivity of the free space: 8.85×10^{-12} $A^2s^2N^{-1}m^{-2}$.

Acoustic phonon deformation potential (ADP) scattering :

A mathematical derivation of the relaxation time for ADP and ionized impurity scattering is based on the well known "Born approximation" in quantum mechanics*. The scattering process is considered to be a small perturbation of the electron wave by the potential V(r) of the acoustic phonon. Supposed an incoming electron wavefunction ψ has a wavevector **k** in a crystal of volume Ω.

$$\psi_n = \Omega^{-1/2} \exp\left[i\left(\mathbf{k}_n \cdot \mathbf{r}\right)\right] \tag{B.6}$$

is the solution of the time-dependent Schrödinger equation:

---

* A mathematical treatment of the Born approximation is taken from the book by Seeger. (Ref.230)

$$H \psi_n = \hbar \omega_n \psi_n; \quad n=0,1,2,3,....,\tag{B.7}$$

where H is the Hamiltonian and $\hbar \omega_n$ are the eigenvalues of the unperturbed problem. For the scattering process by scattering potential V(r) we solve the time-dependent Schrödinger equation of the perturbation problem:

$$[H + V(r)] \psi = i \hbar (\partial\psi/\partial t)\tag{B.8}$$

where ψ is expanded in a series of ψ_n:

$$\psi = \sum_n a_n \psi_n \exp(-i \omega_n t)\tag{B.9}$$

with unknown coefficients $a_n = a_n(t)$. Combining of Eq.B.8 and Eq.B.9 yields:

$$\sum_n a_n V(r) \psi_n \exp(-i\omega_n t) = i \hbar \sum_n (da_n/dt) V(r) \psi_n \exp(-i\omega_n t)\tag{B.10}$$

We multiplied Eq.B.10 by $\psi_m^* \exp(i\omega_m t)$, where m is an integer. Integrating over the crystal volume we obtain:

$$\sum_n a_n H_{mn} \exp(i\omega_{mn} t) = i \hbar (da_n/dt)\tag{B.11}$$

since the integral

$$\int \psi_m^* \psi_n d^3r = \frac{1}{\Omega} \int \exp[i(k_n - k_m) \cdot \mathbf{r}]\, d^3 r\tag{B.12}$$

is zero for m≠n and unity for m=n due to the normalization of ψ_n.The matrix element H_{mn} and the angular frequency difference ω_{mn} are given by:

$$H_{mn} = \int \psi_m^* V(r) \psi_n d^3r,\tag{B.13}$$

and

$$\omega_{mn} = \omega_m - \omega_n.\tag{B.14}$$

The integration of Eq.B.11 leads to

$$a_m(t) = -\frac{i}{\hbar} \sum_n H_{mn} \int_0^t a_n \exp(i \omega_{mn} t)\, dt.\tag{B.15}$$

The incoming electron is considered to be in an initial state k where a_k=1 and all other a's are zero. By denoting the final state by k',

$$|a_{k'}(t)|^2 = \hbar^{-2} |H_{k'k}|^2 t^2 \sin^2 (\omega_{k'k} t/2)/(\omega_{k'k} t/2)^2.\tag{B.16}$$

For t→∞ (i.e., long enough time for the scattering process to be completed),

$\sin^2(\omega_{k'k}\, t/2)/(\omega_{k'k}t/2)^2$ becomes a δ-function. Then the transition probability S per unit time is given by;

$$S(\mathbf{k},\mathbf{k}') = |a_{k'}(t)|^2/t = (2\pi/\hbar)\ |H_{k'k}|^2\ \delta\,[E(\mathbf{k}')-E(\mathbf{k})], \tag{B.17}$$

where E(k') and E(k) are the energy of the scattered and incoming electron. $\delta\,[E(\mathbf{k}')-E(\mathbf{k})]$ simply limits the scattering process to be elastic. Eq.B.17 is well known as a "Fermi's Golden Rule No.2"[231]

Finally the inverse momentum relaxation time τ^{-1} is given by:

$$\tau^{-1} = \sum S(\mathbf{k},\mathbf{k}')\ [1-(p'/p)\cos\theta\,] \tag{B.18}$$

where p' and p are the momentum of the scattered and incident electron, respectively, and θ is the scattered angle. We use Eq.B.13, B.17, B.18 to find τ^{-1} for ADP and ionized impurity scattering.

Now we shall start the describing ADP scattering which was originally developed by Bardeen and Shockley in 1950.[169] Consider the variation of the conduction band edge δE_c with a change in the lattice constant a:

$$\delta E_c \sim D_c(\delta a/a) \tag{B.19}$$

where D_c is a factor of proportionality known as the deformation potential constant. If we consider an elastic wave u(x,t):

$$u(x,t)=A\exp[i(\pm\beta x-\omega t)] \tag{B.20}$$

where A is the amplitude and β is the wavenumber, then a longitudinal acoustic phonon will have the scattering potential $V_{AP}(x,t)$:

$$V_{AP}(x,t) = D_c\,(\partial u/\partial x). \tag{B.21}$$

With Eq.B.20 and B.21,

$$V_{AP}(x,t)=\pm\, i\beta D_c u. \tag{B.22}$$

By inserting Eq.B.22 to B.13, we obtain:

$$|H_{k'k}|^2 = (D_A\beta A)^2. \tag{B.23}$$

We now have to find a quantum mechanical equivalent of the vibrational amplitude A. The energy E(β) of a phonon given by quantum mechanics is:

$$E(\beta) = (N_\omega + 1/2)\,\hbar\,\omega_s, \tag{B.24}$$

with $$N_\omega \sim k_B T/\hbar\,\omega \quad \text{when } \hbar\,\omega << k_B T \tag{B.25}$$

On the other hand the energy E given by classical physics is:

$$E = 1/2\ (\rho\,\Omega)\ |du/dt|^2 = 1/2\ \rho\Omega A^2\beta^2. \tag{B.26}$$

By equating Eq.B.24 and B.26, we obtain

$$A^2 = \frac{2\,(N_\omega + 1/2)\,\hbar}{2\,\rho\,\omega_s\,\Omega} \tag{B.27}$$

so Eq.B.23 becomes:

$$|H_{k'k}|^2 = \frac{2\,D_c^2\,\beta^2 (N_\omega + 1/2)\,\hbar}{\rho\,\omega_s\,\Omega} \approx \frac{2\,D_c^2\,\beta^2\,\hbar}{\rho\,\omega_s\,\Omega}\,\frac{k_B T}{\hbar\,\omega_s}. \tag{B.28}$$

Now we can calculate S(k,k') by inserting Eq.B.28 into B.17:

$$\begin{aligned} S(\mathbf{k},\mathbf{k}') &\approx \frac{2\,\pi\,D_c^2}{\rho\,v_s^2\,\Omega}\,\frac{k_B T}{\hbar}\,\{\delta\,[E(\mathbf{k}')-E(\mathbf{k})+\hbar\omega_s] + \delta\,[E(\mathbf{k}')-E(\mathbf{k})-\hbar\omega_s]\} \\ &\approx 2\,\frac{2\,\pi\,D_c^2}{\rho\,v_s^2\,\Omega}\,\frac{k_B T}{\hbar}\,\delta\,[E(\mathbf{k}')-E(\mathbf{k})] \end{aligned} \tag{B.29}$$

where emission and absorption of a phonon was considered and the velocity of the sound in the crystal $v_s = \omega/\beta$ was introduced.

Finally using the relation $k^2 dk = m^{*2} v \hbar^{-3} dE$ and Eq.B.18 we obtain

$$\tau_{ac}^{-1} = \frac{2^{1/2}\,m^{*3/2}\,k_B\,T\,D_c^2\,E^{1/2}}{\rho\,v_s^2\,\hbar^4\,\pi}, \tag{B.30}$$

in which the spherical band approximation $E = (\hbar k)^2/2m^*$ was used (i.e., the conductivity effective mass is same as the density of states effective mass). If we insert Eq.B.30 into Eq.B.4, we obtain the mobility which is limited by ADP scattering only:

$$\mu_{ac} = \frac{2^{3/2}\,e\,\rho\,v_s^2\,\hbar^4\,\pi^{1/2}}{3\,m^{*5/2}\,D_c^2\,(k_B\,T)^{3/2}} \tag{B.31}$$

which is proportional to $T^{-3/2}$ as shown in Fig.4.2.

Ionized impurity scattering :

The following theory of ionized impurity scattering was independently developed by Brooks [166, 167], Herring [168], and Dingle.[165] They assumed a potential V(r) due to a point charge in semiconductor was given by:

$$V(r) = \frac{(Ze)\,e}{\varepsilon\, r} \exp(-r/L_D) = \frac{Z\,e^2}{\varepsilon\, r} \exp(-r/L_D) \qquad (B.32)$$

with

$$L_D = \frac{1}{e}\sqrt{\frac{\varepsilon\, k_B\, T}{4\,\pi\, n}} \qquad (B.33)$$

where Ze is the charge of the scattering center and n is the free carrier concentration. Eq.B.32 is now well known as a screened (or Yukawa) potential with L_D being the Debye length. The idea behind L_D is that the electrostatic field of the individual ionized impurity is screened by the surrounding carrier gas. Inserting Eq.B.32 into Eq.B.13 gives:

$$|H_{k'k}| = \frac{Z\,e^2}{\Omega\,\varepsilon} \int \exp(-i\,\mathbf{k'}\bullet\mathbf{r})\, \frac{\exp(-r/L_D)}{r} \exp(i\,\mathbf{k}\bullet\mathbf{r})\, d^3r$$

or

$$|H_{k'k}| = \frac{Z\,e^2}{\Omega\,\varepsilon} \int_0^{2\pi}\!\int_0^{\pi}\!\int_0^{\infty} \exp(-r/L_D)\, \exp[i(\mathbf{k}-\mathbf{k'})\bullet\mathbf{r}]\; r\, \sin\theta\; dr\, d\theta\, d\phi . \qquad (B.34)$$

If we set $\beta = k - k' = 2|k|\sin(\alpha/2)$ where α is the scattering angle, Eq.B.34 becomes:

$$|H_{k'k}| = \frac{Z\,e^2}{\Omega\,\varepsilon} \int_0^{\infty}\!\int_0^{2\pi}\!\int_{-1}^{+1} r \exp(-r/L_D)\, \exp(i\,\beta\, r\cos\theta)\; d(\cos\theta)\, d\phi\, dr$$

which simplifies to:

$$|H_{k'k}| = -\frac{Z\,e^2}{\Omega\,\varepsilon}\, \frac{1}{\beta^2 + 1/L_D^2} . \qquad (B.35)$$

Now with Eq.B.17:

$$S(\mathbf{k}, \mathbf{k'}) = -\frac{2\,\pi}{\hbar} \left(\frac{Z\,e^2}{\Omega\,\varepsilon}\right)^2 \frac{\delta(E'-E)}{\left(\beta^2 + 1/L_D^2\right)^2} . \qquad (B.36)$$

Eq.B.36 is the scattering rate for one ionized impurity in a unit volume,i.e.,we now multiply B.36 by the ionized impurity concentration N_I and the volume Ω:

$$S(\mathbf{k}, \mathbf{k'}) = -\frac{2\,\pi}{\hbar} \frac{N_I}{\Omega} \left(\frac{Z\,e^2}{\varepsilon}\right)^2 \frac{\delta(E'-E)}{\left(4\,k^2 \sin^2(\alpha/2) + 1/L_D^2\right)^2} . \qquad (B.37)$$

Finally by inserting Eq.B.37 into B.18 we obtain:

$$\tau_{ion}^{-1} = \frac{\pi N_I Z^2 e^4}{(2 m^*)^{1/2} \varepsilon^2}\left[\ln(1+\gamma^2) - \frac{\gamma^2}{1+\gamma^2}\right] E^{-3/2} \tag{B.38}$$

with

$$\gamma^2 = 8 m^* E L_D^2/\hbar^2. \tag{B.39}$$

We can now calculate the mobility which is limited by ionized impurity scattering by inserting Eq.B.39 into B.4. This numerical integration is very simple with today's personal computer technology. However we shall introduce an approximation due to Brooks [166, 167] and Herring [168] here to illustrate the ionized impurity scattering limited mobility*. We replace E in γ (Eq.B.39) by that value for which the integrand $x^{3/2}\exp(-x)$ is a maximum; this is true for $E=3k_BT$. We then denote γ by γ_{BH} where B and H are the initials of Brooks and Herring:

$$\gamma_{BH} = 2\frac{m^*}{\hbar}\left(\frac{2}{m^*} 3 k_BT\right)^{1/2} L_D \tag{B.40}$$

and the mobility is given by:

$$\mu_{ion} = \frac{2^{7/2}\varepsilon^2 (k_BT)^{3/2}}{\pi^{3/2} Z^2 e^3 m^{*1/2} N_I\left[\ln(1+\gamma_{BH}^2) - \gamma_{BH}^2/(1+\gamma_{BH}^2)\right]} \tag{B.41}$$

which has $T^{3/2}$ proportionality when N_I is constant as shown in Fig.4.2.

Neutral Impurity Scattering:

A mathematical derivation of the relaxation time for neutral impurity scattering is based on the "phase shift method" in quantum mechanics. Because neutral impurity scattering becomes dominant only at low temperatures, the phase shift method must be used since it is known to be a better approximation than the Born approximation in the limit of the small incident wave energy.[231] A scattered wave is spherically symmetric around the scattering center as shown in Fig.B.1. The wave function ψ is given by:

$$\psi(r,\theta) = \psi_{incident} + \psi_{scattered} = e^{ikz} + \frac{e^{ikr}}{r} f(\theta) \tag{B.42}$$

---

* All integrations in the research described in this thesis were solved numerically without any approximations.

where r is the radial distance from the scattering center and $f(\theta)$ is the amplitude function. The flux of the incident wave I is:

$$I = v\,|\psi_{incident}| = v\,e^{ikz}\,e^{-ikz} = v \tag{B.43}$$

where v is the velocity of the incident wave. The flux of the scattered wave through small area dA shown in Fig.B.1 is given by:

$$dA = v\,|f(\theta)|^2 dA/r^2 = S(\theta)d\Omega \tag{B.44}$$

where $S(\theta)$ is the total flux spherically scattered. Using Eq.B.43 and B.44 we find the differential scattering cross section $\sigma(\theta)$:

$$\sigma(\theta) = d\sigma(\theta)/d\Omega = S(\theta)/I = |f(\theta)|^2. \tag{B.45}$$

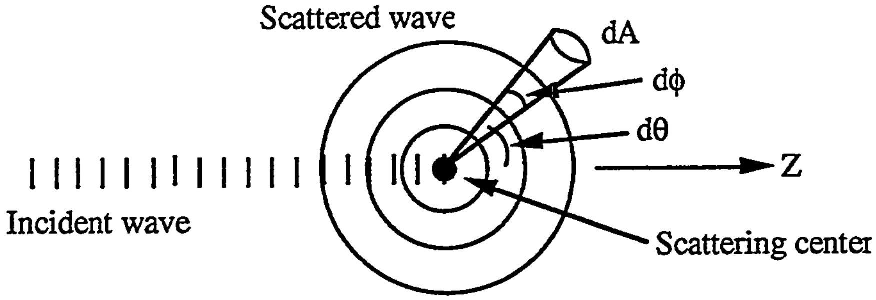

Fig.B.1 Scattering model of the phase shift analysis

The main trick of the partial wave analysis is to regard the incident plane wave as a solution of a hydrogen-like wavefunction in the limit of r→∞ and V(r)→0. Then the incident wave function becomes:

$$\psi_{incident} = e^{ikz} = e^{ikr\cos\theta} = \sum_{l=0}^{\infty} i^l(2l+1)\frac{\sin kr - l\,\pi/2)}{kr} P_j(\cos\theta) \tag{B.46}$$

where l is the angular momentum quantum number and $P_j(\cos\theta)$ is the Legendre polynomials. Now a cross section of the incident wave is divided according to l as shown in Fig.B.2. The wave that is inside the area of a circle at the core is due to the l=0 term in Eq.B.46 and is known as s-partial-wave. The torus just outside of the s-partial wave is l=1 the p-partial wave, and the other torus just outside of l=1 is the l=2 d-partial wave, and so on. The radius of the circle d is given by:

$$d = [l\,(l+1)]^{1/2}/k \tag{B.47}$$

so that one needs to determine how many incident partial waves are necessary to obtain good approximation depending on the size and the potential of the scattering center. Very often one considers the number of partial waves sufficient when the d of the highest order wave is slightly lager than a_0 (Bohr radius) of the scattering center. Using Eq.B.47 this condition can be written as:

$$[l\,(l+1)]^{1/2} > k\,a_0. \tag{B.48}$$

However, this inequality was derived by completely neglecting the potential due to the scattering center. A determination of how many partial waves to employ is somewhat difficult.

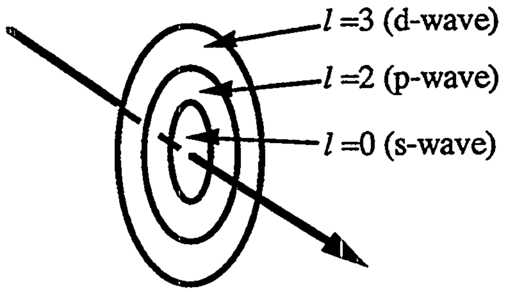

Fig.B.2 Partial incident waves in the phase shift analysis

Having deconvoluted the incident wave into partial waves, we now need to find the differential cross section $\sigma(\theta)$, i.e., an expression for $f(\theta)$ in Eq.B.45. I shall just show the final result because this process is mathematically quite involved: [231]

$$f(\theta) = \sum_{l=0}^{\infty} \frac{2l+1}{k}\, e^{i\delta_l} \sin\delta_l \, P_j(\cos\theta) \tag{B.49}$$

where δ_l is the phase shift of the scattered wave with respect to that of the incident wave. Exact calculation of δ_l for an arbitrary scattering potential is impossible except for the one case; a free electron scattering by a hydrogen atom in free space. Approximation of δ_l for scattering by other arbitrary potential is very difficult and usually involves simplification of the potential to a solvable one. If we are able to find δ_l then we can find $\sigma(\theta)$ by putting Eq.B.49 into B.45. The total momentum scattering cross section σ_T is given by:

$$\sigma_T = 2\pi \int_0^{\pi} \sigma(\theta)\ (1-\cos\theta)\ \sin\theta\ d\theta, \tag{B.50}$$

and the inverse of relaxation time τ^{-1} is finally obtained as:

$$\tau^{-1} = N\sigma_T v = 2\pi N v \int_0^{\pi} \sigma(\theta)\ (1-\cos\theta)\ \sin\theta\ d\theta \tag{B.51}$$

where N is the concentration of the scattering center and v is the velocity of the incident wave.

Now we shall calculate $\tau_{\text{neutral}}{}^{-1}$ due to neutral impurity scattering in semiconductors. The following calculation is due to Erginsoy [Erginsoy, 1013 #112] who has considered only s-wave scattering. ka_0 of shallow levels in Ge at 10K is about 0.8 so that the l=0 wave should be sufficient to approximate the cross section according to the condition Eq.B.48. Erginsoy has adopted the calculated s-wave phase shift of electron-hydrogen scattering in free space published by Massey and Moiseiwitsch: [154]

$$k^2\ \sigma_T \approx\ 20\ k\ a_0. \tag{B.52}$$

$\sigma(\theta)$ for l=0 is obtained by Eq.B.45 and B.49:

$$\sigma(\theta) = (1/k^2)\ \sin^2 \delta_l. \tag{B.53}$$

Now using Eq.B.51 and B.53,

$$\begin{aligned}\tau^{-1}_{\text{neutral}} &= N_N\sigma_T v = 2\pi N_N v \int_0^{\pi} \sigma(\theta)\ (1-\cos\theta)\ \sin\theta\ d\theta \\ &= N_N\ v\ (4\pi/k^2)\ \sin^2\delta_l \\ &= N_N\ v\ \sigma_T.\end{aligned} \tag{B.54}$$

With $a_0 = \varepsilon\hbar^2/m^* e^2$, $v = k\hbar/m^*$ and Eq.B.52, Eq.B.54 becomes:

$$\tau^{-1}_{\text{neutral}} = \frac{20\ a_0}{k} = \frac{20\ \varepsilon\ N_N\ \hbar^3}{m^{*2}\ e^2} \tag{B.55}$$

where a_0 is the Bohr radius of the scattering center, k is the wavenumber of the incident electron, and N_N is the neutral impurity concentration. The significance of Erginsoy's result Eq.B.55 can be understood by calculating the mobility limited only by neutral impurity scattering:

$$\mu_{neutral} = \frac{e\,\tau_{neutral}}{m^*} = \frac{m^*\,e^3}{20\,\varepsilon\,N_N\,\hbar^3} \tag{B.56}$$

which is independent of the temperature when N_N is constant. This result is demonstrated in the low temperature regime of Fig.4.2.a where N_N becomes a constant.

Erginsoy's s-wave only calculation approximates the experimentally measured neutral impurity scattering mobility quite well but not exact as it is shown in Sec.4.1 of this thesis. A more precise $\tau_{neutral}^{-1}$ can be obtained by considering the contribution from higher order partial waves (l=1, 2, 3....). When one does this, $\tau_{neutral}$, i.e., $\mu_{neutral}$ is found to have weak temperature dependencies as shown in Sec.4.1.1.

Appendix C: Derivation of the Variable Range Hopping Resistivity Equations

C.1 Mott's low

We shall consider an electronic transition between localized donor states (from states i to j) near the Fermi level (E_F) as shown in Fig.C.1. There is a slight shift in energies of these states due to a long-range Coulomb interaction in-between them. If we denote the energy difference between states i and j by E_{ij}, only resistances having very small values of E_{ij} will contribute to conduction at low temperatures. This means that energies E_i and E_j of the relevant states must lie in a narrow band between E_F-E_0 and E_F+E_0 in order for these states to be involved in the conduction process. E_0 decreases as T goes to zero.

Mott's formula (Eq.4.5 with n=1/4) can be derived by calculating the optimum width $2E_0$ of the band by the following method. The resistance ρ between two localized states is given by:

$$\rho = \rho_0 \exp\left(\frac{2\, r_{ij}}{a_0} + \frac{E_{ij}}{k_B\, T}\right) \tag{C.1}$$

where r_{ij} is the distance between two states and a_0 is the Bohr radius. $2r_{ij}/a_0$ is the

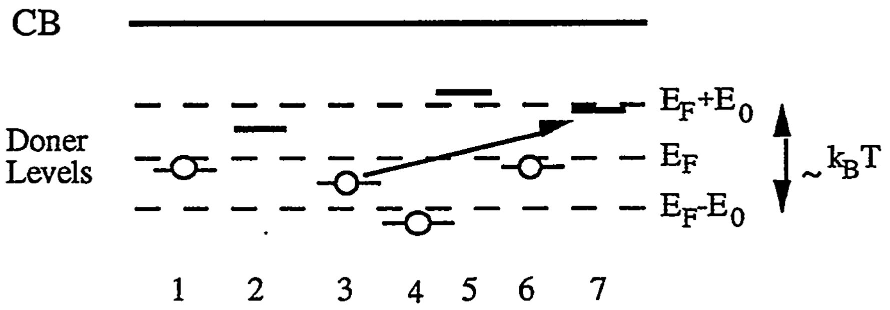

Fig.C.1 Energies of donor states around the Fermi level. Only the states whose energies lie within the band of width $2E_0$ contribute to conduction electron wavefunction overlap term and E_{ij}/k_BT is the activation term. To estimate the resistance corresponding to hopping between two states in the band, Mott substituted $[N_b(E_0)]^{-1/3}$ for r_{ij} and E_0 for E_{ij} (N_b: concentration of donor states in the band). $N_b(E_0)$ is given by the following equation assuming a constant density of states $g(E_F)$ around E_F (as shown in Fig.4.7.a):

$$N_b(E_0) = 2\, g(E_F)\, E_0. \tag{C.2}$$

Eq.C.1 then becomes,

$$\rho = \rho_0 \exp\left[\frac{1}{[g(E_F)\, E_0]^{1/3}\, a_0} + \frac{E_0}{k_B T}\right]. \tag{C.3}$$

Now we shall find a value of E_0 which minimizes ρ. By inspecting Eq.C.3, one easily finds the minimum ρ for the following condition:

$$\frac{1}{[g(E_F)\, E_0]^{1/3}\, a_0} = \frac{E_0}{k_B T} \tag{C.4}$$

i.e.,

$$E_0 = \frac{(k_B T)^{3/4}}{\left(g(E_F)\, a_0^3\right)^{1/4}} \,. \tag{C.5}$$

Finally by inserting Eq.C.5 into C.3 we find the hopping resistivity $\ln\rho \propto T^{-1/4}$ which is the famous Mott's law for variable range hopping conduction.

C.2 Efros-Shklovskii's law

Mott has assumed a constant density of states around E_F. However Efros and Shklovskii (ES) have shown that this is not the case. Due to a Coulomb interaction between electron occupied (i) and electron empty (j) states, the energy difference E_{ij} between these states according to ES is given by:

$$E_{ij} = E_j - E_i - \frac{e^2}{\varepsilon\, r_{ij}} > 0 \tag{C.7}$$

where ε is the dielectric constant. It follows from the inequality Eq.C.7 that states close to E_F must be located considerable distances apart. This restriction is the physical origin of the Coulomb gap in the density of states as shown Fig.4.7.b. Let us consider the band of width $2E_0$ around E_F. We now set the Fermi level as a reference point in the energy scale, i.e., $E_F=0.$, and the energies of the upper and lower bound of the band are $+E_0$ and $-E_0$, respectively. According to Eq.C.7, any two donors in this band with energies on opposite side of E_F must be separated by a distance not less than $e^2/\varepsilon E_{ij}$. This condition implies a symmetric position of states i and j around E_F, i.e., $E_j=0.5E_{ij}$ and $E_i=-0.5E_{ij}$ with respect to E_F. The concentration of donor states N_b in the band is now given by:

$$N_b < r_{ij}^{-3} \approx E^3\,\varepsilon^3 / e^6 \tag{C.8}$$

where E is the energy in respect to E_F. The density of states g(E) in the band then becomes:

$$g(E) = \frac{dN}{dE} \approx \frac{A\,\varepsilon^3 E^2}{e^6} \tag{C.9}$$

where A is a numerical constant. Eq.C.9 clearly shows existence of a parabolic "Coulomb gap" ($\propto E^2$) around E_F as shown in Fig.4.7.b.

Now we shall derive the variable range hopping resistivity when electronic transitions take place within the Coulomb gap. By substituting $N_b^{-1/3}$ of Eq.C.8 for r_{ij} in Eq.C.1, we obtain:

$$\rho = \rho_0 \exp\left[\frac{1}{\left(\frac{\alpha\,\varepsilon^3 E_0^3}{e^6}\right)^{1/3} a_0} + \frac{E_0}{k_B T}\right] \tag{C.10}$$

where α is a numerical constant. The value of E_0 which minimizes the hopping resistivity can be found by taking the same step as Eq.C.7:

$$E_0 = \frac{(k_B T)^{1/2}}{\alpha\,(\varepsilon\, a)^{1/2}} \tag{C.11}$$

Finally, insertion of Eq.C.11 to C.10 gives $\ln\rho \propto (T_0/T)^{1/2}$ with $T_0 \approx \beta e^2/\varepsilon a_0$ where $\beta \approx 2.8$ is the simulation calculated constant.

Appendix D: Hall Effect

In the experimental arrangement shown in Fig.D.1, carriers moving in x the direction are deflected from the direction of motion by the Lorentz force due to a perpendicular magnetic field B_z. This deflection causes a Hall voltage V_y:

$$V_y = R_H I_x B_z / d \tag{D.1}$$

where R_H is the Hall coefficient and d is the thickness of the sample. V_x is proportional to B_z if R_H is assumed to be constant. This is true only for a condition $\mu B_z<1$ as we shall see below. The Hall field E_y is given by:

$$E_y = R_H j_x B_z. \tag{D.2}$$

For a calculation of R_H, we have to determine the energy distribution function $f(v)$ of the carriers under the influence of electric field and magnetic field. Solving the Boltzmann equation:

$$\frac{df(v)}{dt} + \frac{f(v) - f_0(v)}{\tau_m(v)} = 0 \tag{D.3}$$

where $f_0(v)$ is the thermal-equilibrium distribution, i.e., without any external fields, we obtain a general form of $f(v)$ with external **B** and **E**: [232]

$$f=f_0-f_0' e\hbar^{-1}\nabla_k E\tau_m \frac{\mathbf{F}-e[\mathbf{B}\times m^{-1}\tau_m\mathbf{F}]+\alpha\mathbf{B}\cdot(\mathbf{F}\cdot\mathbf{B})}{1+(\mathbf{B}\cdot\alpha\mathbf{B})} \tag{D.4}$$

where **F** is the force and α is the coefficient to be determined. For the calculation of the conductivity without any magnetic field, for example, we set **B**=0 and **F**=**E**, i.e., Eq.D.4 becomes:

$$f=f_0-f_0' e\tau_m(v\cdot\mathbf{E}) \tag{D.5}$$

from which a familiar result of conductivity σ_0 is obtained as:

$$\sigma_0 = (N_c e^2/m)<\tau_m> \tag{D.6}$$

where N_c is the carrier concentration. Now we shall show solutions of Eq.D.4 for (1) the small magnetic field condition $B\mu<<1$ and (2) the large magnetic field condition $B\mu>>1$.

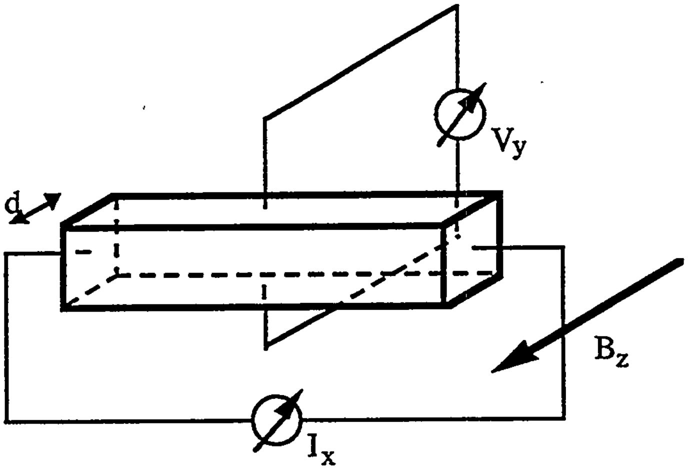

Fig.D.1 Hall effect measurement configuration

Small magnetic field $B\mu<<1$

Current components j_x and j_y in the small field condition are given by:

$$j_x = (\sigma_0+\beta_0 B_z^2)E_x + \gamma_0 B_z E_y \qquad (D.7)$$

$$j_y = \gamma_0 B_z E_x + (\sigma_0+\beta_0 B_z^2)E_y \qquad (D.8)$$

where

$$\beta_0 = -(N_c e^4/m^3)<\tau_m^3> \qquad (D.9)$$

$$\gamma_0 = (N_c e^3/m^2)<\tau_m^2> \qquad (D.10)$$

and $\omega_c=|e|B/m$ is the cyclotron frequency. For the steady state the component j_y vanishes, i.e., from Eq.D.8,

$$E_x = \frac{\sigma_0 + \beta_0 B_z^2}{\gamma_0 B_z} E_y. \qquad (D.11)$$

Using Eq.D.10 we eliminate E_x form Eq.D.7:

$$E_y = \frac{\gamma_0}{(\sigma_0 + \beta_0 B_z^2)^2 + \gamma_0^2 B_z^2} j_x B_z. \qquad (D.12)$$

By comparing with Eq.D.2, we find R_H as:

$$R_H = \frac{\gamma_0}{(\sigma_0 + \beta_0 B_z^2)^2 + \gamma_0^2 B_z^2} \approx \frac{\gamma_0}{\sigma_0^2} = \frac{r_H}{N_c e} \qquad (D.13)$$

where the so called Hall factor r_H stands for:

$$r_H = <\tau_m^2> / <\tau_m>^2. \qquad (D.14)$$

The value of r_H is usually between 1 and 2 and depends strongly on a dominating scattering mechanism e.g., $r_H=1.18$ for deformation potential acoustic phonon scattering, 1.93 for ionized impurity scattering and 1 for neutral impurity scattering. In a normal Hall effect set up, we measure R_H to determine the concentration and type of majority carriers. The combination of the two independently measured parameters, carrier concentration and resistivity, allows for the determination of the mobility using Eq.4.2. Because of r_H involved in the Hall effect, the mobility deduced with this method, Hall mobility μ_H, is different from the drift mobility μ_d by r_H:

$$\mu_H = R_H \sigma_0 = (r_H/N_c e) N_c e \mu_d = r_H \mu_d. \qquad (D.15)$$

High magnetic field Bμ>>1

In a very strong B field, one can approximate σ, γ, and β by the following expressions:

$$\sigma \approx (N_c e^2/m\omega_c^2)\langle\tau_m^{-1}\rangle \qquad (D.16)$$

$$\gamma \approx N_c e^3/m^2\omega_c^2 \qquad (D.17)$$

$$\beta \approx - (N_c e^4/m^3\omega_c^2)\langle\tau_m\rangle, \qquad (D.18)$$

then j_x and J_y are given by:

$$j_x = \sigma E_x + \gamma B_z E_y \qquad (D.19)$$

$$j_y = - \gamma B_z E_x + \sigma E_y. \qquad (D.20)$$

From $j_y=0$,

$$E_x = (\sigma / \gamma B_z) E_y, \qquad (D.21)$$

and we eliminate E_x from Eq.D.19:

$$E_y = \frac{\gamma}{\sigma^2 + \gamma^2 B_z^2} j_x B_z = R_H j_x B_z. \qquad (D.22)$$

Now R_H in the strong B field is approximated by:

$$R_H = \frac{\gamma}{\sigma^2 + \gamma^2 B_z^2} \approx \frac{1}{N_c e} \qquad (D.23)$$

in which the Hall coefficient r_H becomes unity. Therefore $\mu_H=\mu_d$ in a $B\mu>>1$ Hall effect condition.

References

1. E. Rutherford, *Phil. Mag.* **21**, 669 (1911).
2. J. J. Thomson, *Phil. Mag.* **24**, 209, 669 (1912).
3. M. E. Weeks and H. M. Leicester, in "*Discovery of the Elements*" , 7 Ed., (Journal of Chemical Education, Eaton, 1968), pp. 775-809.
4. H. N. McCoy and W. H. Ross, *J. Am. Chem. Soc.* **29**, 1907 (1907).
5. F. Soddy, *Nature* **105**, 516 (1920).
6. F. Soddy, in "*Interpretation of Radium*" , 4 Ed., (Putnam's Sons, New York, 1922), pp. 134 and pp. 260.
7. T. W. Richards and M. E. Lembert, *J. Am. Chem. Soc.* **36**, 1329 (1914).
8. M. E. Hönigschmid and S. Horovitz, *Compt. rend.* **158**, 1796 (1914).
9. M. Curie, *Compt. rend.* **158**, 1976 (1914).
10. F. W. Aston, *Phil. Mag.* **38**, 707 (1919).
11. F. W. Aston, in "*Mass Spectra and Isotopes*". (Edward Arnold and Co., London, 1942).
12. E. Rutherford, *Proc. Roy. Soc.* **97**, 374 (1920).
13. J. Chadwick, *Nature* **129**, 312 (1932).
14. J. Chadwick, *Proc. Roy. Soc.* **A136**, 692 (1932).
15. D. Iwanenko, *Comptes Rendus* **195**, 439 (1932).
16. "*Table of Isotopes* ", 7 Ed., edited by C. M. Lederer and V. S. Shirley (John Wiley & Sons. Inc., New York, 1978).
17. I. Kaplan, in "*Nuclear Physics*". (Addison-Wesley, Cambridge, 1956).
18. B. G. Harvey, in "*Introduction to Nuclear Physics and Chemistry*". (Prentice-Hall, New Jersey, 1969).
19. K. Fajans, *Physik. Z.* **16**, 456 (1915).
20. H. C. Urey, F. G. Brickwedde, and G. M. Murphy, *Phys. Rev.* **40**, 1 (1932).
21. G. Herzberg, in "*Infrared and Raman Specta of Polyatomic Molecules*". (Van Nostrand Reinhold, New York, 1945).
22. G. Herzberg, in "*Spectra of Diatomic Molecules*". (Van Nostrand Reinhold, New York, 1950).

23. K. Clusius and G. Dickel, *Naturwiss* **26**, 546 (1938).

24. L. O. Love, *Science* **182**, 343 (1973).

25. D. R. Olander, *Sci. Am.* **239**, 37 (1978).

26. E. Maxwell, *Phys. Rev.* **78**, 477 (1950).

27. C. A. Reynolds, B. Serin, W. H. Wright, and L. B. Nesbitt, *Phys. Rev.* **78**, 487 (1950).

28. J. Bardeen, C. N. Cooper, and J. R. Schrieffer, *Phys. Rev.* **108**, 1175 (1957).

29. T. H. Geballe and G. W. Hull, *Phys. Rev.* **110**, 773 (1958).

30. D. R. Bosomworth, W. Hayes, A. R. L. Spray, and G. D. Watkins, *Proc. Royal Soc. (London)* **A317**, 133 (1970).

31. B. Pajot, in Proc. of "*The 18th Intl. Conf. on the Physics of Semiconductors*", edited by O. Engsröm, (World Sientific, 1987), pp. 911.

32. A. J. Mayur, M. Dean Sciacca, M. K. Udo, A. K. Ramdas, K. M. Itoh, J. Wolk, and E. E. Haller, *Phys. Rev. B* **49**, 16293 (1994).

33. A. A. Berezin, *J. Phys. Chem. Solids* **50**, 5 (1989).

34. G. Nilsson and G. Nelin, *Phys. Rev. B* **3**, 364 (1971).

35. H. D. Fuchs, C. H. Grein, C. Thomson, M. Cardona, W. L. Hansen, K. Itoh, and E. E. Haller, *Phys. Rev. B* **43**, 4835 (1991).

36. H. D. Fuchs, C. H. Grein, R. I. Devlen, and J. Kuhl, *Phys. Rev. B* **44**, 8633 (1991).

37. H. D. Fuchs, C. H. Grein, M. Cardona, W. L. Hansen, K. Itoh, and E. E. Haller, *Sol. State Comm.* **82**, 225 (1992).

38. H. D. Fuchs, P. Etchegoin, M. Cardona, K. Itoh, and E. E. Haller, *Phys. Rev. Lett.* **70**, 1715 (1993).

39. M. Cardona, C. H. Grein, H. D. Fuchs, and S. Zollner, *J. Non-Cryst. Solid* **141**, 257 (1993).

40. M. Cardona, P. Etchegoin, H. D. Fuchs, and P. Molinas-Mata, *J. Phys. Condens. Matter* **5**, A61 (1993).

41. P. W. Anderson, *Phys. Rev.* **109**, 1492 (1958).

42. G. Davies, J. Hartung, V. Ozhogin, K. Itoh, W. L. Hansen, and E. E. Haller, *Semic. Sci. and Technol.* **8**, 127 (1993).

43. G. Davies, E. C. Lightowlers, V. Ozhogin, K. Itoh, W. L. Hansen, and E. E. Haller, in Proc. of "*The 5th Intl. Conf. on Shallow Impurities in Semiconductors*",

edited by T. Taguchi, **117 & 118** (Trans Tech Publications, Kobe, Japan, 1993), pp. 111.

44. P. Etchegoin, J. Weber, M. Cardona, W. L. Hansen, K. Itoh, and E. E. Haller, *Sol. State. Comm.* **83**, 843 (1992).

45. P. Etchegoin, H. D. Fuchs, H. Weber, M. Cardona, L. Pintschovius, K. Itoh, and E. E. Haller, *Phys. Rev. B* **48**, 12661 (1993).

46. G. Davies, E. C. Lightowlers, K. Itoh, W. L. Hansen, E. E. Haller, and V. Ozhogin, *Semic. Sci. and Technol.* **7**, 1271 (1992).

47. W. F. Banholzer and T. R. Anthony, *Thin Solid Films* **212**, 1 (1992).

48. K. C. Hass, M. A. Tamor, T. R. Anthony, and W. F. Banholzer, *Phys. Rev. B* **44**, 12046 (1991).

49. K. C. Hass, M. A. Tamor, T. R. Anthony, and W. F. Banholzer, *Phys. Rev. B* **45**, 7171 (1992).

50. F. Yonezawa, in *"The Structure and Properties of Matter"*, vol. 28, Ed., edited by T. Matsubara, (Springer, Berlin, 1982), pp. 383.

51. A. T. Collins, S. C. Lawson, G. Davies, and H. Kanda, *Phys. Rev. Lett.* **65**, 891 (1988).

52. A. T. Collins, G. Davies, H. Kanda, and G. S. Woods, *J. Phys. C. Solid State Phys.* **21**, 1363 (1988).

53. N. W. Ashcroft and N. D. Mermin, in *"Solid State Physics"*, (Saunders College, Philadelphia, 1976), pp. 458.

54. I. Pomeranchuk, *J. Phys. (Moscow)* **6**, 237 (1942).

55. H. B. G. Casimir, *Physica* **5**, 495 (1938).

56. J. Callaway, *Phys. Rev.* **113**, 1046 (1959).

57. T. R. Anthony, W. F. Banholzer, J. F. Fleischer, L. Wei, P. K. Kuo, R. L. Thomas, and R. W. Pryor, *Phys. Rev. B* **42**, 1104 (1990).

58. J. R. Olson, R. O. Pohl, J. W. Vandersande, A. Zolton, T. R. Anthony, and W. F. Banholzer, *Phys. Rev. B* **47**, 4850 (1993).

59. L. Wei, P. K. Kuo, R. L. Thomas, T. R. Anthony, and W. F. Banholzer, *Phys. Rev. Lett.* **70**, 3764 (1993).

60. T. H. Geballe, *Science* **250**, 1194 (1990).

61. L. E. Berman, J. B. Hatings, D. P. Siddons, M. Koike, V. Stojanoff, and S. Sharma, *Synchr. Rad. News.* **6**, 21 (1993).

62. G. A. Slack, *J. Phys. Chem. Solids* **34**, 321 (1973).

63. R. C. Buschert, A. E. Merlini, S. Pace, S. Rodriguez, and M. H. Grimsditch, *Phys. Rev. B* **38**, 5219 (1988).

64. H. Holloway, K. C. Hass, M. A. Tamor, and T. R. Anthony, *Phys Rev. B* , 7123 (1991).

65. A. K. Ramdas, S. Rodriguez, M. Grimsditch, T. R. Anthony, and W. F. Banholzer, *Phys. Rev. Lett.* **71**, 189 (1993).

66. W. A. Wooster, *Rep. Progr. Physics* **16**, 62 (1953).

67. S. Zollner, M. Cardona, and S. Gopalan, *Phys. Rev. B* **45**, 3376 (1991).

68. G. Davies, E. C. Lightowlers, T. S. v. Hui, V. Ozhogin, K. M. Itoh, W. L. Hansen, and E. E. Haller, *Semic. Sci. and Technol.* **8**, 2201 (1993).

69. C. Parks, A. K. Ramdas, S. Rodriguez, K. M. Itoh, and E. E. Haler, *Phys. Rev. B* **49**, 14244 (1994).

70. R. C. Newman, in "*Growth and Characterisation of Semiconductors*" , edited by R. A. Stradling and P. C. Klipstein, (Adam Hilger, Bristol, 1990), pp. 119.

71. D. K. Wilson, *Phys. Rev.* **134**, A265 (1964).

72. J. M. Rowe, R. M. Nicklow, D. L. Price, and K. Zanio, *Phys. Rev. B* **10**, 671 (1993).

73. E. E. Haller, *Semic. Sci. Technol.* **5**, 319 (1990).

74. R. Schorer, W. Dondl, and G. Abstreiter, unpublished, (1993).

75. B. Jusserand and M. Cardona, in "*Light Scattering in Solids*" , vol. 5, edited by M. Cardona and G. Güntherodt, (Springer, Heidelberg, 1989), pp. 49.

76. J. Spitzer, T. Ruf, M. Cardona, W. Dondl, R. Schorer, G. Abstreiter, and E. E. Haller, *Phys. Rev. Lett.* **72**, 1565 (1994).

77. T. Y. Tan, H. M. You, S. Yu, U. M. Gösele, W. Jäger, D. W. Boeringer, F. Zypman, R. Tsu, and S. T. Lee, *J. Appl. Phys.* **72**, 5206 (1992).

78. H. D. Fuchs and E. E. Haller, *Submitted to Phys. Rev. Lett.*,

79. D. R. Campbell, *Phys. Rev. B* **12**, 2318 (1975).

80. M. Werner, H. Mehrer, and H. Siethoff, *J. Phys. C* **16**, 6815 (1983).

81. G. Vogel, G. Hettich, and H. Mehrer, *J. Phys. C* **16**, 6197 (1983).

82. E. E. Haller, and F. S. Goulding, in "*Handbook of Semiconductors*" , vol. 4, 2 Ed., edited by C. Hilsum, (North-Holland, Amsterdam, 1993), pp. 937-963.

83. E. E. Haller, *Infrared Phys. Technol.* **35**, 127 (1994).

84. N. M. Haegel, E. E. Haller, and P. N. Luke, *Int. J. IR MM Waves* **4**, 945 (1983).

85. N. M. Haegel, M. R. Hueschen, and E. E. Haller, *Infrared Phys.* **25**, 273 (1985).

86. T. Amano, S. Kondo, H. Nagai, and S. Maruyama, *Jpn. J. Apl. Phys.* **32**, 3692 (1993).

87. I. Silier, S. Subramanian, E. Dießel, H.-J. Queisser, and E. Bauser, *Submitted to Appl. Phys. Lett.* ,

88. E. E. Haller, N. P. Palaio, M. Rodder, W. L. Hansen, and E. Kreysa, in "*Neutron Transmutation Doping of Semiconductor Materials*" , edited by R. D. Larrabee, (Plenum, New York, 1984), pp. 21.

89. E. E. Haller, K. M. Itoh, J. W. Beeman, W. L. Hansen, and V. I. Ozhogin, in Proc. of "*The SPIE Symposium on Instrumentation in Astronomy VIII*", **2198** (SPIE, Kona, Hawaii, 1994), pp. 630.

90. B. Sadoulet, T. Shutt, N. Wang, A. Commings, P. Barnes, J. Beeman, J. Emes, Y. Giraud-Heraud, E. E. Haller, A. Lange, J. Rich, and R. Ross, in "*Low Temperature Detectors for Neutrino and Dark Matter III*" , edited by L. Brogiato, D. V. Camm, and E. Fiorini, (Editions Frontiers, Gifsur Yvette, 1990), pp. 227.

91. T. Shutt, B. Ellman, P. D. Barnes, A. Cummings, A. Da Silvia, J. Emes, Y. Giraud-Heraud, E. E. Haller, A. E. Lange, R. R. Ross, J. Rich, B. Sadoulet, G. Smith, W. Stockwell, C. Stubbs, N. Wang, S. White, B. A. Young, and D. Yvon, *Phys. Rev. Lett.* **69**, 3425 (1992).

92. T. Shutt, N. Wang, B. Ellman, Y. Giraud-Heraud, C. Stubbs, P. D. Barnes, A. Cummings, A. Da Silvia, J. Emes, E. E. Haller, A. E. Lange, J. Rich, R. R. Ross, B. Sadoulet, G. Smith, W. Stockwell, S. White, B. A. Young, and D. Yvon, *Phys. Rev. Lett.* **69**, 3531 (1992).

93. C. R. Cunningham and W. K. P. Gear, in Proc. of "*SPIE Instrumentaion in Astronomy VII*", **1235** 1990), pp. 515.

94. E. Kreysa, in Proc. of "*Intl. Symp. of Photon detectors for Space Instrumentation*", edited by T. D. Guyennes, (ESA/ESTEC, Noordwijk, 1993).

95. A. E. Lange, E. Kreysa, S. E. McBride, P. L. Richard, and E. E. Haller, *Int. J. IR MM Waves* **4**, 689 (1983).

96. B. I. Shklovskii and A. L. Efros, in "*Electronic Properties of Doped Semiconductors*". Solid State Series , vol. 45 (Springer-Verlag, Berlin Heidelberg, 1984).

97. N. Wong, F. C. Wellstood, B. Sadoulet, E. E. Haller, and J. Beeman, *Phys. Rev. B*, (1990).

98. W. A. Tiller, in "*The Science of Crystallization - Macroscopic Phenomena and Defect Generation*". (Cambridge University Press, Cambridge, 1992).

99. K. Itoh, "*Growth and Characterization of Isotopically Enriched* ^{70}*Ge and* ^{74}*Ge Single Crystals*", Master's Thesis, University of California at Berkeley (1992).

100. K. Itoh, W. L. Hansen, E. E. Haller, J. W. Farmer, V. I. Ozhogin, A. Rudnev, and A. Tikhomirov, *J. Mater. Res* **8**, 1341 (1993).

101. K. Itoh, W. L. Hansen, E. E. Haller, J. W. Farmer, and V. I. Ozhogin, in Proc. of "*The 5th Intl. Conf. on Shallow Impurities in Semiconductors*", edited by T. Taguchi, **117 & 118** (Trans Tech Publications, Kobe, Japan, 1993), pp. 117.

102. A. A. Vasenko, Y. I. Vereshchagin, I. V. Kirpichnikov, V. A. Kuznetsov, V. N. Prusakov, A. I. Rudnev, A. S. Starostin, and A. V. Tikhomirov, *Instrum. Exp. Tech.* **32**, 312 (1989).

103. E. I. Abbakumov, V. A. Bazhenov, Y. V. Verbin, A. A. Vlasov, A. S. Dorogobed, A. K. Kaliteevskii, V. F. Kornilov, D. M. Levine, E. I. Mikerin, A. A. Sazykin, V. I. Sergeev, and G. S. Soloviev, *Sov. J. At. Energy* **67**, 739 (1989).

104. E. E. Haller, W. L. Hansen, P. N. Luke, R. McMurray, and B. Jarrett, *IEEE Trans. Nucl. Sci.* **NS-29**, 745 (1982).

105. S. M. Kogan and T. M. Lifshifts, *Phys. Stat. Solidi A* **39**, 11 (1977).

106. K. Lark-Horowitz, in Proc. of "*Conf. on Semi-Conducting Materials*", edited by H. K. Henish, (Butterworth Sci. Publ., London, 1951), pp. 47.

107. H. Fritzsche, and M. Cuevas, *Phys. Rev.* **119**, 1238 (1960).

108. M. Cuevas, *Phys. Rev.* **164**, 1021 (1967).

109. M. S. Schnöller, *IEEE Trans Electr. Dev.* **ED-23**, 797 (1976).

110. W. von Ammon, *Nucl. Instr. Meth. B* **B63**, 95 (1992).

111. S. M. Mirianashvili and D. I. Nanobashvili, *Sov. Phys. Semicond.* **4**, 1612 (1971).

112. M. A. Vesaghi, *Phys. Rev. B* **25**, 1982 (1982).

113. J. Garrido, J. L. Castano, J. Piqueras, and V. Alcober, *J. Appl. Phys.* **57**, 2186 (1985).

114. S. P. Najda, S. Holmes, R. A. Stradling, and F. Kuchar, *Semicnd. Sci. Technol.* **4**, 791 (1989).

115. M. Satoh, K. Kuriyama, and T. Kawakubo, *J. Appl. Phys.* **67**, 3542 (1990).

116. M. Satoh, K. Yokoyama, and K. Kuriyama, *J. Appl. Phys.* **68**, 363 (1990).

117. K. Kuriyama, K. Yokoyama, and K. Tomizawa, *J. Appl. Phys.* **70**, 7315 (1991).

118. A. Huber, F. Kuchar, and J. Casta, *J. Appl. Phys.* **55**, 353 (1984).

119. B. J. Heijmink, M. Godlewski, T. Gregorkiewicz, and C. A. J. Ammerlaan, *J. Appl. Phys.* **69**, 689 (1991).

120. J. R. DeLaeter, K. G. Henmann, and K. J. R. Rosman, *J. Phys. Chem. Ref. Data* **20**, 1327 (1991).

121. G. H. Kinchin and R. S. Pease, *Repts. Prog. in Phys.* **18**, 1 (1955).

122. T. V. Mashovets, and V. V. Emtsev, in "*Lattice Defects in Semiconductors*" , edited by F. A. Huntley, (The Institue of Physics, London, 1974), pp. 103.

123. A. Seeger, H. Föll, and W. Frank, *Inst. Phys. Conf. Ser.* **59**, 1977 (1977).

124. J. C. Bourgoin, P. M. Mooney, and F. Poulin, in Proc. of "*ICDRES-11*", **59**, (Insitute of Physics, Oiso, Japan, 1980), pp. 33.

125. L. C. Kimerling, *Physica* **116B**, 1 (1983).

126. N. P. Palaio, S. J. Pearton, and E. E. Haller, *J. Appl. Phys.* **55**, 1437 (1984).

127. I. S. Park and E. E. Haller, *J. Appl. Phys.* **64**, 6775 (1988).

128. V. Nagesh and J. W. Farmer, *J. Appl. Phys.* **63**, 1549 (1988).

129. N. Fourches, A. Huck, G. Walter, and J. C. Bourgoin, in Proc. of "*15th Intl. Conf. on Defects in Semiconductors*", edited by G. Ferencz, **38-41** (Trans. Tech. Publ., Budapest, Hungary, 1988), pp. 1233.

130. D. P. Erchak, V. S. Kosobutskii, and V. F. Stel'makh, *Sov. Phys. Semicond.* **23**, 955 (1989).

131. N. Fukuoka and H. Saito, *Physica* **116B**, 343 (1982).

132. N. Fukuoka, M. Honda, K. Atobe, H. Yamaji, M. Ide, and M. Okada, *Jpn. J. Appl. Phys.* **31**, 2534 (1992).

133. D. V. Lang, *J. Appl. Phys.* **45**, 3014 (1974).

134. H. Saito, N. Fukuoka, and H. Yoshida, *Inst. Phys. Conf. Ser.* **59**, 45 (1980).

135. I. S. Park, "*Characterization and Applications of Neutron Transmutation Doped Germanium*", Ph. D. Thesis, University of California at Berkeley (1988).

136. J. S. Blakemore, in "*Semiconductor Statistics*". (Dover, New York, 1987).

137. M. S. Skolnick, in "*Semiconductors: Impurities and Defects in Group IV Elements and III-V Compounds*" , vol. 22b, edited by O. Madelung, M. Schulz, (Springer Verlag, Berlin, 1989), pp. 466-489.

138. D. W. Palmer, in "*Growth and Characterisation of Semiconductors*" , edited by R. A. Stradling and P. C. Klipstein, (Adam hilger, Bristol, 1991), pp. 187.

139. E. A. Davis and W. D. Compton, *Phys. Rev.* **A140**, 2183 (1965).

140. D. M. Brown and R. Bray, *Phys. Rev.* **127**, 1593 (1962).

141. N. W. Ashcroft and N. D. Mermin, in "*Solid State Physics*", (Saunders College, Philadelphia, 1976), pp. 323.

142. E. I. Gershenzon, G. N. Gol'tsman, and A. P. Mel'nikov, *JETP Lett.* **14**, 185 (1971).

143. N. F. Mott, in "*Metal-Insulator Transition*". (Taylor&Francis, London, 1990).

144. N. F. Mott, *J. Non-Crystal. Solids* **1**, 1 (1968).

145. A. L. Efros and B. I. Shklovskii, *J. Phys. C* **8**, L49 (1975).

146. D. Chattopadhyay and H. J. Queisser, *Rev. Mod. Phys.* **53**, 745 (1981).

147. P. R. Bratt, in "*Semiconductors and Semimetals*", edited by R. K. Willardson and A. C. Beer, (Academic Press, New York, 1977), pp. 67.

148. S. E. Church, M. J. Griffin, P. A. R. Ade, M. C. Price, P. J. Emery, and B. M. Swinyard, *Infrared Phys.* **34**, 389 (1993).

149. J. A. Wolk, M. B. Kruger, J. N. Heyman, W. Walukiewicz, R. Jeanloz, and E. E. Haller, *Phys. Rev. Lett.* **66**, 774 (1991).

150. C. Erginsoy, *Phys. Rev.* **79**, 1013 (1950).

151. A. L. Anselm, *Zh. Eksp. Teor. Fiz.* **24**, 85 (1953).

152. N. Sclar, *Phys. Rev.* **104**, 1559 (1956).

153. L. E. Blagosklonskaya, E. M. Gershenzon, Y. P. Ladyzhinskii, and A. P. Popova, *Sov. Phys. Solid State* **11**, 2402 (1970).

154. T. C. McGill and R. Baron, *Phys. Rev. B* **11**, 5208 (1975).

155. J. R. Meyer and F. J. Bartoli, *Phys. Rev. B* **24**, 2089 (1981).

156. P. Norton, T. Braggins, and H. Levinstein, *Phys. Rev. B* **8**, 5632 (1973).

157. R. Baron, M. H. Young, and T. C. McGill, in Proc. of "*The 13th Intl. Conf. on Physics of Semiconductors*", edited by F. G. Fumis, (North-Holland, Rome, 1976), pp. 1158.

158. J. S. Blakemore, *Phys. Rev. B* **22**, 743 (1980).

159. J. R. Meyer and F. J. Bartoli, *Solid State Commun.* **41**, 19 (1982).

160. H. S. W. Massey and B. L. Moiseiwitsch, *Phys. Rev.* **78**, 180 (1950).

161. N. Sclar, *Phys. Rev.* **104**, 1548 (1956).

162. A. Temkin and J. C. Lamkin, *Phys. Rev.* **121**, 788 (1961).

163. C. Schwartz, *Phys. Rev.* **124**, 1468 (1961).

164. For examples, R. A. Smith, in "*Semiconductors*", (Cambridge University Press, Cambridge, 1978) and B. K. Ridley, in "*Quantum Processes in Semiconductors*", (Claredon Press, Oxford, 1993).

165. R. B. Dingle, *Philos. Mag.* **46**, 831 (1955).

166. H. Brooks, *Phys. Rev.* **83**, 879 (1951).

167. H. Brooks, *Electron. Electron. Phys.* **7**, 85 (1955).

168. C. Herring, *Unpublished*.

169. J. Bardeen and W. Shockley, *Phys. Rev.* **80**, 72 (1950).

170. M. Altarelli, W. Y. Hsu, and R. A. Sabatini, *J. Phys. C* **10**, (1977).

171. A. Baldereschi, and N. O. Lipari, in Proc. of "*The 13th Intl. Conf. on Physics of Semiconductors*", edited by F. G. Fumi, (North-Holland, Rome, 1976), pp. 1158.

172. H. D. Fuchs, K. M. Itoh, and E. E. Haller, *Philos. Mag. B* , **70**, 661 (1994).

173. L. M. Falicov and M. Cuevas, *Phys. Rev.* **164**, 1025 (1967).

174. F. Stern, *Phys. Rev. B* **9**, 4597 (1974).

175. E. O. Kane, *Phys. Rev.* **131**, 79 (1963).

176. J. R. Meyer and F. J. Bartoli, *Phys. Rev. B* **30**, 1026 (1984).

177. J. R. Meyer and F. J. Bartoli, *Phys. Rev. Lett.* **57**, 2568 (1986).

178. J. R. Meyer and F. J. Bartoli, *Phys. Rev. B* **36**, 5989 (1987).

179. T. G. Castner, in "*Hopping Transport in Solids*" , edited by M. Pollak and B. Shklovskii, (North-Holland, Amsterdam, 1991), pp. 1.

180. M. Pollak, and M. Ortuno, in "*Electron-Electron Interactions in Disordered Systems*", edited by A. L. Efros and M. Pollak, (North-Holland, Amsterdam, 1985), pp. 287.

181. A. G. Zabrodskii and K. N. Zinov'eva, *Sov. Phys.-JETP Lett.* **59**, 425 (1983).

182. W. N. Shafarman, D. W. Koon, and T. G. Castner, *Phys. Rev. B* , 1216 (1989).

183. H. Stupp, M. Hornung, M. Lakner, O. Madel, and H. v. Löhneysen, *Phys. Rev. Lett.* **71**, 2634 (1993).

184. T. F. Rosenbaum, G. A. Thomas, and M. A. Paalanen, *Phys. Rev. Lett.* **72**, 2121 (1994).

185. N. F. Mott, *Proc. Camb. Phil. Soc.* **32**, 281 (1949).

186. N. F. Mott, *Proc. Phys. Soc. London* **A62**, 416 (1956).

187. D. Belitz and T. R. Kirkpatrick, *Rev. Mod. Phys.* **66**, 261 (1994).

188. A. F. Ioffe and A. R. Regel, *Prog. Semicond.* **4**, 237 (1960).

189. N. F. Mott, *Phil. Mag.* **26**, 1015 (1972).

190. E. Abrahams, P. W. Anderson, D. C. Licciardello, and T. V. Ramakrishnan, *Phys. Rev. Lett.* **42**, 693 (1979).

191. A. MacKinnon and B. Kramer, *Phys. Rev. Lett.* **47**, 1546 (1981).

192. M. Schreiber, B. Kramer, and A. MacKinnon, *Phys. Scr.* **T25**, 67 (1988).

193. T. Ohtsuki, B. Kramer, and Y. Ono, *Solid State Commun.* **81**, 477 (1992).

194. E. Hofstetter and M. Schreiber, *Europhys. Lett.* **21**, 933 (1993).

195. J. Chayes, L. Chayes, D. S. Fisher, and T. Spencer, *Phys. Rev. Lett.* **57**, 2999 (1986).

196. B. L. Altshuler, and A. G. Aronov, *Soviet. Phys. JETP* **50**, 968 (1979).

197. G. A. Thomas, Y. Ootsuka, S. Katsumoto, S. Kobayashi, and W. Sasaki, *Phys. Rev. B* **25**, 4288 (1982).

198. M. J. Jirsch, U. Thomanschefsky, and D. F. Holcomb, *Phys. Rev. B* **37**, 8257 (1988).

199. T. F. Rosenbaum, K. Andres, G. A. Thomas, and R. N. Bhatt, *Phys. Rev. Lett.* **45**, 1723 (1980).

200. T. F. Rosenbaum, R. F. Milligan, M. A. Paalanen, G. A. Thomas, R. N. Bhatt, and W. Lin, *Phys. Rev. B* **27**, 7509 (1983).

201. P. F. Newman and D. F. Holcomb, *Phys Rev. B* **28**, 638 (1983).

202. P. F. Newman and D. F. Holcomb, *Phys. Rev. Lett.* **51**, 2144 (1983).

203. P. Dai, Y. Zhang, and M. P. Sarachik, *Phys. Rev. Lett.* **66**, 1914 (1991).

204. P. Dai, Y. Zhang, and M. P. Sarachik, *Phys. Rev. Lett.* **67**, 136 (1991).

205. K. Nishikawa and R. Barrie, *Can. J. Phys.* **41**, 1135 (1963).

206. R. Barrie and K. Nishikawa, *Can. J. Phys.* **41**, 1823 (1963).

207. W. Baltensperger, *Philos. Mag.* **44**, 1953 (1953).

208. D. M. Larsen, *Phys. Rev. B* **8**, 535 (1973).

209. D. M. Larsen, *Phys. Rev. B* **13**, 1976 (1976).

210. S. M. Kogan and N. Van Lien, *Sov. Phys. Semicond.* **15**, 26 (1981). [Fiz. Tekh. Poluprovodn. **15**, 44 (1981).]

211. H. Navarro, E. E. Haller, and F. Keilmann, *Phys. Rev. B* **37**, 10822 (1988).

212. K. Colbow, *Can. J. Phys.* **41**, 1801 (1963).

213. R. Newman, *Phys. Rev.* **103**, 103 (1956).

214. J. J. White, *Can. J. Phys.* **45**, 2792 (1967).

215. Y. Nisida and K. Horii, *J. Phys. Soc. Jpn.* **26**, 388 (1969).

216. A. Imatake, *J. Phys. Soc. Jpn.* **35**, 164 (1973).

217. S. N. Artjemenko, A. A. Kal'fa, S. M. Kogan, and V. I. Sidorov, *Sov. Phys. Semicond.* **8**, 1405 (1975). [Fiz. Tekh. Poluprovoda **8**, 2164 (1974).]

218. C. Jagannath, Z. W. Grabowski, and A. K. Ramdas, *Phys. Rev. B* **23**, 2082 (1981).

219. T. Ohyama, *Phys. Stat. Sol. A* **98**, 373 (1980).

220. K. M. Itoh, W. L. Hansen, J. W. Beeman, E. E. Haller, J. W. Farmer, A. Rudnev, A. Tikhomirov, and V. I. Ozhogin, *Appl. Phys. Lett.* **64**, 2121 (1994).

221. J. D. Jackson, in "*Classical Electrodynamics*" , 2 Ed., edited by (Wiley, New York, 1975), pp. 102.

222. A. A. Kal'fa and S. M. Kogan, *Sov. Phys. Semicond.* **6**, 1839 (1973). [Fiz. Tekh. Poluprovodn. **6**, 2175 (1972).]

223. G. L. Bir, E. I. Butikov, and G. E. Pikus, *J. Phys. Chem. Sol.* **24**, 1475 (1963).

224. B. I. Shklovskii and A. L. Efros, *Sov. Phys.-JETP* **33**, 468 (1971). [Zh. Eksp. Tor. Fiz. **60**, 867 (1971)]

225. S. D. Baranovskii, B. L. Gel'mont, V. G. Golubev, V. I. Ivanov-Omskii, and A. V. Osutin, *JETP Lett.* **46**, 511 (1987). [Pis'ma Ah. Eksp. Teor. Fiz. **46**, 405 (1987).]

226. S. D. Baranovskii, B. L. Gel'mont, V. G. Golubev, V. I. Ivanov-Omskii, and A. V. Osutin, *Sov. Phys. Semicond.* **23**, 891 (1989). [Fiz. Tech. Poluprovodn. **23**, 1434, (1989).]

227. R. L. Jones and P. Fisher, *J. Phys. Chem. Solids* **26**, 1125 (1965).

228. D. H. Dickey and J. O. Dimmock, *J. Phys. Chem. Solids* **28**, 529 (1967).

229. S. Narita and M. Miyao, *Solid State Commun.* **9**, 2167 (1971).

230. K. Seeger, in "*Semiconductor Physics*" , 5 Ed., (Springer-Verlag, Berlin, 1991), pp.159-169.

231. L. I. Schiff, in "*Quantum Mechanics*". (McGraw-Hill, New York, 1968).

232. K. Seeger, in "*Semiconductor Physics*" , 5 Ed., (Springer-Verlag, Berlin, 1991), pp. 55-61.

233. O. D. Dubon, J. W. Beeman, L. M. Falicov, H. D. Fuchs, E. E. Haller, and C. Wang, *Phys. Rev. Lett.* 72, 2231 (1994).